UNIVERSITY OF SOUTHAMPTON
SCHOOL OF PHYSICS AND ASTRONOMY
FACULTY OF PHYSICAL AND APPLIED SCIENCES

Cosmological Evolution of Supermassive Black Holes in the Centres of Galaxies

Anna Danuta Kapińska
Submitted for the degree of Doctor of Philosophy

June 10, 2012

Supervision:

Dr. Phil Uttley
Dr. Christian R. Kaiser
Dr. Thomas J. Maccarone

Viva voce examination lead by:

Dr. Somak Raychaudhury (University of Birmingham, U.K.)
Dr. Anna M. M. Scaife (University of Southampton, U.K.)

April 13th, 2012

UNIVERSITY OF SOUTHAMPTON

ABSTRACT

FACULTY OF PHYSICAL AND APPLIED SCIENCES

SCHOOL OF PHYSICS AND ASTRONOMY

Physical Sciences: Astrophysics

Doctor of Philosophy

COSMOLOGICAL EVOLUTION OF SUPERMASSIVE BLACK HOLES IN THE CENTRES OF GALAXIES

by Anna Danuta Kapińska

Radio galaxies and quasars are among the largest and most powerful single objects known and are believed to have had a significant impact on the evolving Universe and its large scale structure. Their jets inject a significant amount of energy into the surrounding medium, hence they can provide useful information in the study of the density and evolution of the intergalactic and intracluster medium. The jet activity is also believed to regulate the growth of massive galaxies via the AGN feedback.

In this thesis I explore the intrinsic and extrinsic physical properties of the population of Fanaroff-Riley II (FR II) objects, i.e. their kinetic luminosities, lifetimes, and central densities of their environments. In particular, the radio and kinetic luminosity functions of these powerful radio sources are investigated using the complete, flux limited radio catalogues of 3CRR and BRL. I construct multidimensional Monte Carlo simulations using semi-analytical models of FR II source time evolution to create artificial samples of radio galaxies. Unlike previous studies, I compare radio luminosity functions found with both the observed and simulated data to explore the best-fitting fundamental source parameters. The Monte Carlo method presented here allows one to: (i) set better limits on the predicted fundamental parameters of which confidence intervals estimated over broad ranges are presented, and (ii) generate the most plausible underlying parent populations of these radio sources. Moreover, I allow the source physical properties to co-evolve with redshift, and I find that all the investigated parameters most likely undergo cosmological evolution; however these parameters are strongly degenerate, and independent constraints are necessary to draw more precise conclusions. Furthermore, since it has been suggested that low luminosity FR IIs may be distinct from their powerful equivalents, I attempt to investigate fundamental properties of a sample of low redshift, low radio luminosity density radio galaxies. Based on SDSS-FIRST-NVSS radio sample I construct a low frequency (325 MHz) sample of radio galaxies and attempt to explore the fundamental properties of these low luminosity radio sources. The results are discussed through comparison with the results from the powerful radio sources of the 3CRR and BRL samples.

Finally, I investigate the total power injected by populations of these powerful radio sources at various cosmological epochs and discuss the significance of the impact of these sources on the evolving Universe. Remarkably, sets of two degenerate fundamental parameters, the kinetic luminosity and maximum lifetimes of radio sources, despite the degeneracy provide particularly robust estimates of the total power produced by FR IIs during their lifetimes. This can be also used for robust estimations of the quenching of the cooling flows in cluster of galaxies.

CONTENTS

LIST OF TABLES

LIST OF FIGURES

DECLARATION

I hereby declare that this thesis entitled COSMOLOGICAL EVOLUTION OF SUPERMASSIVE BLACK HOLES IN THE CENTRES OF GALAXIES is my own work and has been generated by me as a result of my own original research. The research was carried out in close collaboration with my successive supervisors, Dr. C.R. Kaiser, Dr. P. Uttley and Dr. T.J. Maccarone.

I confirm that the work presented here has been done wholly while in candidature for a research degree at the University of Southampton, U.K. I declare that no part of this thesis has been accepted, or is being submitted, for any degree, diploma or any other qualification in this University or elsewhere.

Any consulted or quoted work of others is always clearly stated and the source is given. Parts of this work have been published, or have been submitted for publishing, as a number of journal articles and conference proceedings (detailed in adequate chapters):

Kapińska, Uttley, Best & Maccarone, MNRAS, *in preparation*
Kapińska & Uttley, MNRAS, 2012, *to be submitted*
Kapińska, Uttley & Kaiser, 2012, MNRAS, *in press*
Kapińska, Uttley & Kaiser, 2010a, ASCP 427, 337
Kapińska, Uttley & Kaiser, 2010b, HEAD 11.0707, 661
Kapińska & Kaiser, 2009, AN 330, 279

Anna Danuta Kapińska, June 10, 2012

ACKNOWLEDGEMENTS

This work has been done as a result of my interaction with my three successive supervisors without whom it would not be possible to achieve what I achieved during my doctorate candidature. I would like to thank my first supervisor, Christian, with whom I started this project; although it had been only one year it was my pleasure to have a chance to work with you. It definitely strengthen my appreciation for theoretical work! My honest thanks go also to my second supervisor, Phil, who adopted me and my project in its early stages. Although the relationship was not an easy one (let's admit, there were ups and downs) I would not be able to proceed with this project so far and so well without your constant questions, curiosity, ideas and criticism (although, I have to admit, all those things caused so much more work!). Finally, sincere thanks to my third supervisor, Tom, who agreed on adopting me as a student for the last six months of my PhD. Many thanks Tom for spending all that time for reading, understanding and commenting on all my written work, for those chats and discussions that kept me sane (well, as much as it was possible at that point) before submitting this thesis, and for taking care of all the required bureaucratic paperwork. Also, given the particular situation with my doctorate I would like to thank all those who I met and chatted with at various conferences, meetings and workshops as often ideas have been born then, and the work may have not came to such a fruition without this.

I am really happy I had a chance to spend the whole four years of my PhD in the Astronomy Group at the University of Southampton; all of you guys, whether you already left to other places or are staying around for much longer, have made this place a particularly fun to work in. So maybe let's go for some good pints to celebrate!

Many thanks go also to my parents. Chciałabym także podziękować moim rodzicom, Danucie i Markowi, za wsparcie i wiarę we mnie przez te wszystkie lata odkąd wymyśliłam sobie, że to właśnie astronomia jest czymś co chciałabym robić w życiu. And finally, I would like to say a big and incomparable thank you to Peter for simply being always here.

As a final note, I acknowledge all the institutes and people involved in creation and production of all software, databases and telescopes (and running observations on them too) I have used to carry out this project (and I wonder whether it should be slightly worrying that this list seems to be nearly as long as my personal acknowledgements). The Westerbork Synthesis Radio Telescope is operated by the Netherlands Institute for Radio Astronomy ASTRON, with support of NWO (WENSS survey). This work made use of the FIRST, NVSS and VLSS NRAO VLA surveys, and the NRAO AIPS software. The National Radio Astronomy Observatory is a facility of the National Science Foundation operated under cooperative agreement by Associated Universities, Inc. This publication makes use of the Sloan Digital Sky Survey. Funding for the SDSS and SDSS-II has been provided by the Alfred P. Sloan Foundation, the Participating Institutions, the National Science Foundation, the US Department of Energy, the National Aeronautics and Space Administration, the Japanese Monbukagakusho, and the Max Planck Society, and the Higher Education Funding Council for England. The SDSS Web site is http://www.sdss.org/. This research has use of the NASA/IPAC Extragalactic Database (NED) which is operated by the Jet Propulsion Laboratory, California Institute of Technology, under contract with the National Aeronautics and Space Administration. In this work I also used of the following: the VizieR catalogue service which is a joint effort of CDS (Centre de Donnes astronomiques de Stras-

bourg) and ESA-ESRIN (Information Systems Division), the Sky View Virtual Observatory which is a service of the Astrophysics Science Division at NASA/GSFC and the High Energy Astrophysics Division of the Smithsonian Astrophysical Observatory (SAO), and the TOPCAT software developed by M.B. Taylor, Bristol University, U.K. This work made an extensive use of the Iridis Compute Cluster maintained by the University of Southampton, Southampton, U.K., and in later stages of my doctorate also of the Sciama High Performance Compute Cluster maintained by the University of Portsmouth, Portsmouth, U.K. and SEPNet, the South East Physics Network. Finally, I am also thankful for the Leverhulme Trust for providing me with the financial support over the four years of my doctorate through the Leverhulme Trust Research Project Grant.

ANNA

Anna Danuta Kapińska, June 10, 2012

A great pleasure in life is doing what people say you cannot do.

WALTER BAGEHOT (1826 – 1877)

ABBREVIATIONS

3CRR	3rd Cambridge Revised Revised Catalogue
AGN	Active Galactic Nucleus
BH	Black Hole
BRL	Best *et al.* (1999)
BRW99	Blundell *et al.* (1999)
CMB	Cosmic Microwave Background
CSS	Compact Steep Spectrum sources
dof	degrees of freedom
FIRST	Faint Images of the Radio Sky at Twenty-centimeters Survey
FR	Fanaroff-Riley morphology class
GoF	Goodness-of-Fit
GPS	GHz-Peaked Spectrum sources
HEG	High-Excitation radio Galaxy
HYMROS	Hybrid Morphology Radio Sources
ICM	Intracluster Medium
IGM	Intergalactic Medium
ISM	Interstellar Medium
KA97	Kaiser and Alexander (1997)
KDA97	Kaiser *et al.* (1997)
LEG	Low-Excitation radio Galaxy
LOFAR	Low Frequency Array
ΛCDM	Λ Cold Dark Matter (cosmology)
MCMC	Markov Chain Monte Carlo
MHD	MagnetoHydroDynamics
MK02	Manolakou and Kirk (2002)
MLE	Maximum Likelihood Estimator
MLM	Maximum Likelihood Method
MNRAS	Monthly Notices of the Royal Astronomical Society
NVSS	NRAO VLA Sky Survey
RG	Radio Galaxy
SED	Spectral Energy Distribution
SKA	Square Kilometer Array
SMBH	Supermassive Black Hole
WENSS	Westerbork Northern Sky Survey
VLA	Very Large Array
VLSS	VLA Low-frequency Sky Survey

SYMBOLS

Symbol	Description	Reference
α	radio spectral index	§2.3.4
$\alpha_{\rm s}$	exponent of the kinetic luminosity distribution	§2.3.1
$\alpha_{\rm sig}$	significance	§2.4.2
β	power-law index of the radial external gas density distribution	§2.3.2
$\Gamma_{\rm b}$	adiabatic index of the magnetic field energy density	§2.3.8
$\Gamma_{\rm ICM}$	adiabatic index of intracluster medium	§6.3.2
$\Gamma_{\rm l}$	adiabatic index of the radio lobes	§2.3.8
$\Gamma_{\rm x}$	adiabatic index of the IGM	§2.3.8
γ	Lorentz factor	§2.1.1
$\gamma_{\rm min}$	minimum Lorentz factor of relativistic particles	§2.3.4
$\gamma_{\rm max}$	maximum Lorentz factor of relativistic particles	§2.3.4
θ	multidimensional parameter vector	§2.5
$\theta_{\rm jet}$	jet half opening angle	§2.3.5
$\theta_{\rm res}$	angular resolution	§1.4
$\theta_{\rm size}$	angular size	§1.4
ϑ	projection angle	§2.3.9
λ	wavelength	§1.4
ν	frequency	§1.4
μ	molecular weight of gas particles	§6.1
$\rho_{\rm crit}$	critical density of the evolving Universe	§3.7, §E.1
ρ_o	mean central density in which source expands	§2.3.2
$\rho_{\rm m}$	mean of log-normal distribution of radio sources' central densities	§2.3.2
ρ_x	ambient medium gas density	§2.1.2
σ_{ρ_o}	standard deviation of log-normal distribution of radio sources' central densities	§2.3.2
$\sigma_{t_{\rm max}}$	standard deviation of log-normal distribution of radio sources' maximum ages	§2.3.3
$\sigma_{\rm T}$	Thomson cross section	§2.1.1
$\phi(L)$	radio luminosity function	§2.2
$\psi(Q)$	kinetic luminosity function	§2.3.1
Ω	density parameter	§E.1
$\Omega_{\rm k}$	spatial curvature density parameter	§E.1
Ω_λ	vacuum density parameter	§1.7, §E.1
$\Omega_{\rm m}$	matter density parameter	§1.7, §E.1
$\Omega_{\rm R}$	radiation density parameter	§E.1

Symbol	Description	Reference
$\mathcal{A}$	slope of the kinetic luminosity – radio lobe luminosity density scaling relation	§5.2
a_o	core radius	§2.3.2
$a(t)$	scale factor at the time t	§E.1
B	magnetic field strength	§2.1.1
ΔC	'delta C' statistics of maximum likelihood method	§2.4.3
D	radio source total projected linear size	§2.3.9
$D_{\rm baseline}$	length of an interferometer baseline	§1.4
$D_{\rm lobe}$	radio lobe length of an extended radio source	§2.1.2
$D_{\rm o}$	characteristic length scale	§2.1.2
d	distance	§4.3.1
$d_{\rm L}$	luminosity distance	§1.4,§E.2
$d_{\rm LR}$	likelihood ratio test	§2.4.2
H_0	Hubble parameter at redshift $z = 0$	§1.7, §E.1
$H(z)$	Hubble parameter at redshift z	§E.1
K	gas entropy index	§6.1.2
$K_{\rm ent}$	gas 'entropy'	§6.1.2
k'	ratio of thermal to electron energy densities in the jet	§2.3.6
$k_{\rm B}$	Boltzmann constant	§6.1
$\mathcal{L}$	maximum likelihood	§2.4.1
$L_{\rm cool}$	cooling flow power	§6.3.2
L_ν	radio lobe luminosity density at frequency ν	§2.1.3
$L_{\rm x}$	bremsstrahlung luminosity density	§6.3.2
$\dot{M}_{\rm cool}$	mass inflow rate of the cooling flow	§6.3.2
$\dot{M}_{\rm o}$	rest-mass transport rate in the jet	§2.1.2
m	power-law exponent of the relativistic particles' energy distribution	§2.3.4
$m_{\rm p}$	proton mass	§6.3.2
$\mathcal{N}$	normalisation of the kinetic luminosity – radio lobe luminosity density scaling relation	§5.2
$N(E)$	energy distribution of relativistic particles	§2.3.4
$n(\gamma)$	number density of relativistic particles with Lorentz factors contained within γ and γ+dγ	§2.1.1
$n_{\rm e}$	gas number density (electrons)	§6.3.2
n_i	data counts in bin i	§2.2
$n_{\rm I}$	gas number density (ions)	§6.3.2
$n_{\rm p}$	gas number density (protons)	§6.3.2
$n_{\rm q}$	strength of the kinetic luminosity break redshift evolution	§3.4.2

Symbol	Description	Reference
n_r	strength of the central density redshift evolution	§3.4.2
n_t	strength of the maximum source's lifetime redshift evolution	§3.4.2
P	total radio power	§2.1.1
P_ν	radio power at frequency ν	§2.1.1
$p_{\rm bowshock}$	bow shock pressure	§2.1.2
$p_{\rm hotspot}$	hot spot pressure	§2.1.2
$p_{\rm lobe}$	radio lobe pressure	§2.1.2
$p-$value	probability	§2.4.2
Q	kinetic luminosity	§2.3.1
$Q_{\rm B}$	kinetic luminosity break	§2.3.1
$Q_{\rm max}$	maximum kinetic luminosity	§2.3.1
$Q_{\rm min}$	minimum kinetic luminosity	§2.3.1
$\mathcal{R}$	radio loudness	§1.2
$R_{\rm T}$	aspect ratio	§2.3.5
r	radial distance form the core (of AGN, cluster, etc.)	§2.1.2
S	gas entropy	§6.1.2
S_ν	flux density at frequency ν	§1.4
t	source current age	§2.3.3
$t_{\rm max}$	source maximum age	§2.3.3
$t_{\rm max_m}$	mean of log-normal distribution of radio sources' maximum ages	§2.3.3
$U_{\rm B}$	magnetic field energy density	§2.1.1
$U_{\rm par}$	particle energy density	§2.1.1
$U_{\rm tot}$	total energy density	§2.1.1
V	volume	§2.1.1
$V_{\rm lim}$	maximum co-moving volume in which a source of a given luminosity density and given survey's flux limit would be included on the sample	§2.2
$V_{\rm lobe}$	radio lobe volume	§2.1.2
$V_{\rm max}$	maximum co-moving volume at redshift z	§2.3.10
$V_{\rm min}$	minimum co-moving volume at redshift z	§2.3.10
$V_{\rm survey}$	volume of a survey	§2.2
$v_{\rm adv}$	maximum allowed head advance speed	§2.3.7
$v_{\rm j}$	jet speed	§2.3.7
z	redshift	§2.3.10

They’ve done studies you know, 60% of the time it works every-time.
PAUL RUDD (1969 –), AS BRIAN FANTANA

The most exciting phrase to hear in science, the one that heralds the most discoveries, is not ‘Eureka!’ but ‘That’s funny...’
ISAAC ASIMOV (1920 – 1992)

Reports that say that something hasn't happened are always interesting to me, because as we know, there are known knowns; there are things we know we know. We also know there are unknowns; that is to say we know there are things we do not know. But there are also unknown unknowns - the ones we don't know we don't know.

DONALD RUMSFELD (1932 –)

1 Introduction

The following chapter gives an introduction to the background of active galaxies, and radio galaxies and radio-loud quasars in particular. Their basic characteristics, influence on the expanding Universe and hence their importance is discussed. Major previous studies are summarised and the aims of this work are presented.

1.1 Where the story begins: the nuclei of active galaxies

Remarkable advances in extragalactic astronomy have been made since the discovery of active galaxies – the galaxies that harbour supermassive black holes (SMBH) in their nuclei (active galactic nucleus, hereafter AGN; e.g. Curtis *et al.*, 1918; Baade and Minkowski, 1954; Schmidt, 1963; Smith, 1967; Schmidt, 1968; Rowan-Robinson, 1972; Fabian *et al.*, 1976; Hutchings and Campbell, 1983; Begelman, 1986; Shlosman *et al.*, 1990; Richstone *et al.*, 1998; Di Matteo *et al.*, 2005; Cattaneo *et al.*, 2009, among many others). Early investigations of the origin of the extraordinary luminosity of these sources in the 1960s led to the present belief that most, if not all, galaxies contain a supermassive black hole in their centres, whether violently active, dormant or dead (Kormendy and Richstone, 1995; Richstone *et al.*, 1998; Magorrian *et al.*, 1998). In simple models an AGN is powered by accretion onto the central supermassive compact object. The total energy produced by the AGN is enormous, reaching 10^{50} J Mpc^{-3} (e.g. Soltan, 1982), and the mass of the central compact object is of order of $10^6 - 10^9$ M$_\odot$ (e.g. Burbidge and Perry, 1976; Sargent *et al.*, 1978; Yu and Tremaine, 2002).

In the general picture the central black hole (BH) is surrounded by an accretion disc composed of cold matter and, further away, by an obscuring torus composed of dust and matter (Figure 1.1). Dissipative processes, such as viscosity and turbulence, transport the matter falling onto the BH inwards, causing the disc to heat up and the angular momentum to be transferred outwards. Sometimes the angular momentum is efficiently lost via the so-called jets, that is twin, perpendicular to the accretion disc, collimated outflows of energetic matter most probably coming from the vicinity of the SMBH. However, the jet production mechanism on small scales, and even the jet composition, is rather poorly known (e.g. Rees *et al.*, 1982; Begelman *et al.*, 1984; Wardle *et al.*, 1998; Ferrari, 1998; Meier *et al.*, 2001; Sikora *et al.*, 2005; Ferrari *et al.*, 2009).

All of the above processes give rise to the AGN luminosity causing it to radiate significantly in most bands of the electromagnetic spectrum. An example of the spectral energy distribution (SED) of quasars is reproduced in Fig. 1.2. In particular, for quasars the accretion disc radiation peaks in the optical and ultraviolet part of the spectrum (however, for low-luminosity AGN the peak of the radiation tends to be in the near infrared, see e.g. Ho 1999). If the accretion disc is obscured by gas and dust, the emission is absorbed by the dust and then re-emitted in the infrared; this is the so-called reprocessing and since it produces a thermal spectrum it is easily distinguished from any jet or disc related components. Further, the strong gravitational gradient produced by the SMBH will increase the frictional heating which will then cause emission in X-rays close to the event horizon. The photons can be also scattered up to X-ray energies (producing power-law spectrum) through the inverse Compton scattering in the corona of hot material formed around the accretion disc, which is suggested to be the dominant emission process in the X-ray energy range (e.g. Jovanović *et al.*, 2008). The overall X-ray spectrum originates from, among

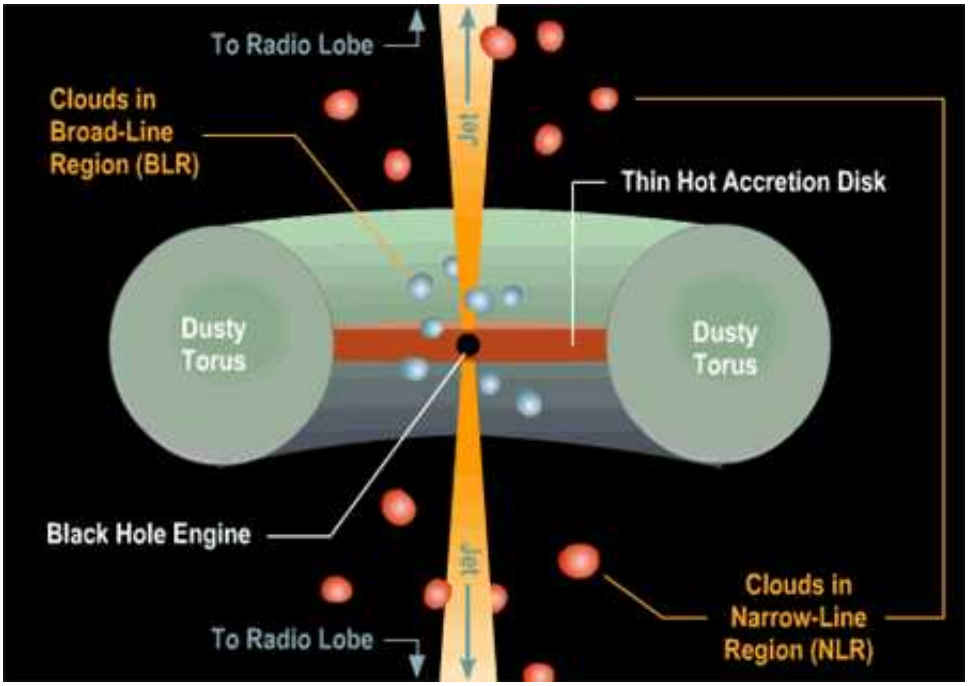

Figure 1.1: A schematic model of an AGN. Credits: Brooks/Cole Thomson Learning.

others, thermally Comptonized soft photons, thermal black body emission (in the case of optically thick accretion discs) and X-ray reflection from the disc (see e.g. Fabian, 2006; Jovanović and Popović, 2009, and references therein). In the optical and ultraviolet part of the spectrum one may distinguish broad and narrow emission lines. The broad emission lines originate from the cold material which orbits around the BH at high speeds, hence photons at various Doppler shifts are produced, while the lines with narrow widths[1] are produced by slower moving clouds of gas that can be found beyond the torus. The jets and the outflow created so-called radio lobes are prominent predominantly at radio frequencies due to the synchrotron radiation from relativistic particles. The synchrotron radiation produces a non-thermal spectrum, which again is easily distinguishable. The extended emission of energy transported to the radio lobes is often spectacularly visible at MHz frequencies, while the compact radio core and jets may be detected at GHz radio frequencies due to the relativistic beaming as well as de-beaming effects of the jets. Interestingly, jets may be sometimes observed at optical and X-ray wavelengths (e.g. M87: Kinman *et al.*, 1974; Schreier *et al.*, 1982; Lelievre *et al.*, 1984; Stiavelli *et al.*, 1991; Biretta *et al.*, 1991; Marshall *et al.*, 2002). Fundamentally, the release of the gravitational energy is the origin of the AGN's luminosity; however, it is important to note that if the SMBH is spinning, extra energy may be extracted electro-magnetically from the BH itself, contributing to its enormous energetic output (e.g. Blandford and Znajek, 1977; Rees *et al.*, 1982; Meier *et al.*, 1997, 2001; Meier, 2002).

[1]Note, that the forbidden emission lines always come from the narrow line region.

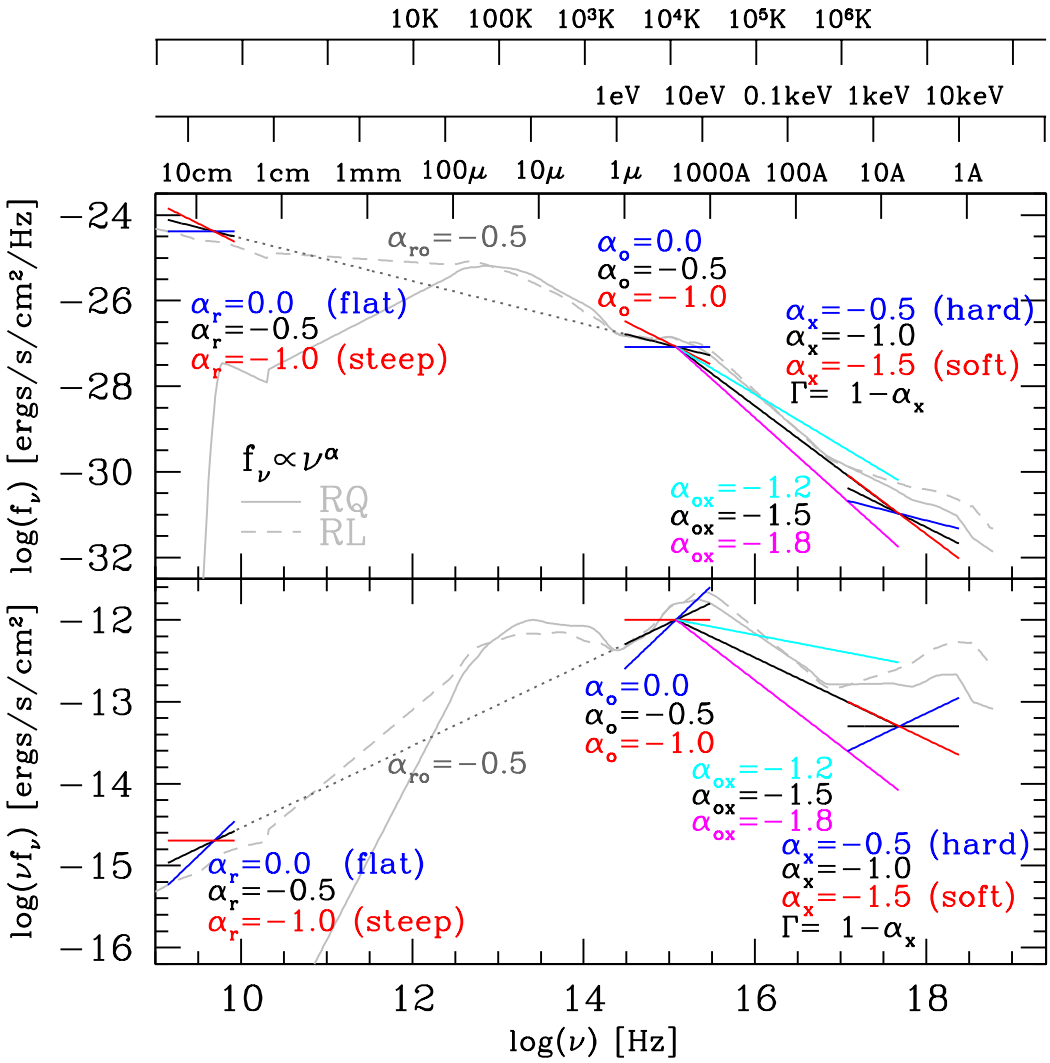

Figure 1.2: Mean broadband spectral energy distribution of radio-loud (grey, dashed) and radio-quiet (grey, solid) low redshift quasars as modelled by Elvis *et al.* (1994). The coloured solid lines represent the typical spectral indices in optical, radio and X-ray regime (α_o, α_r, and α_x respectively), as well as typical radio-to-optical spectral index for radio-loud quasars (α_{ro}), and typical optical-to-X-ray spectral indices (α_{ox}). The *x*-axis shows frequency $\log_{10}(\nu/\mathrm{Hz})$ (bottom axis), and its corresponding wavelength, energy, and temperature (top axis). Credits: Richards *et al.* (2006).

1.2 Menagerie of AGN

Despite the existence of a whole zoo of different AGN types (see e.g. Urry and Padovani, 1995, for a review), one can introduce some systematics to its classification. AGNs are often divided into two types depending on their radio loudness: the radio-quiet and radio-loud classes. Radio loudness of an AGN is often defined as a ratio ($\mathcal{R}$) of its radio flux density measured at 5 GHz to the optical *B*-band (4400 Å) flux density (Kellermann *et al.*, 1989), and for radio-loud AGN it is expected that

$$\mathcal{R} = \frac{S_{5\,\mathrm{GHz}}}{S_B} \geqslant 10. \tag{1.1}$$

Only approximately $10-20$ per cent of AGNs are radio-loud (Sramek and Weedman, 1980; Strittmatter *et al.*, 1980; Kellermann *et al.*, 1989). However, through recent studies this ratio is believed to increase with optical luminosity density (e.g. $20-50$ per cent of quasars which have $\mathrm{M_B} < -24.5$ are radio-loud, while only $16-20$ per cent them are radio loud for $\mathrm{M_B} < -21.5$: Padovani, 1993; Hooper *et al.*, 1996), as well as X-ray luminosity density (e.g. della Ceca *et al.*, 1994; La Franca *et al.*, 2010). Moreover, it has been suggested that radio loudness may be related to the type of the AGN host galaxy (see e.g. Smith *et al.* 1986, but cf. Dunlop *et al.* 2003), BH mass (Laor e.g. 2000; Dunlop *et al.* e.g. 2003; McLure and Jarvis e.g. 2004, but cf. Ho 2002b) and/or the black hole spin (e.g. Wilson and Colbert 1995; Moderski *et al.* 1998; Sikora *et al.* 2007; Chiaberge and Marconi 2011, but cf. Broderick and Fender 2011).

In this project I focus only on radio-loud AGN, which are further divided into radio-loud quasars, blazars and radio galaxies. It is important to note here that although historically only quasars, blazars and radio galaxies are considered radio loud, there is growing evidence that some low-luminosity AGN should be included in this class (see Ho and Peng, 2001; Ho, 2002a,b). Nevertheless, the latter will not be considered in this work.

1.2.1 Quasars, Blazars and Radio Galaxies

Quasars (quasi-stellar sources) were originally identified in optical images as extremely luminous point-like objects resembling stars. Quickly it became evident that they are at high redshifts and hence must be extragalactic (Greenstein and Matthews, 1963; Schmidt, 1963). They are ones of the most luminous AGN classes with luminosities reaching $10^{39}-10^{40}$ W. As with all active galaxies they can be detected across the entire electromagnetic spectrum and they often show broad and narrow emission optical lines. Only approximately 10 per cent of all quasars are radio loud (Kellermann *et al.*, 1989) exhibiting radio core and often extended radio emission.

Blazars (blazing quasi-stellar objects) include the so-called BL Lacertae objects (BL Lacs) and Optically Violent Variable quasars (OVV quasars), and are distinguished by

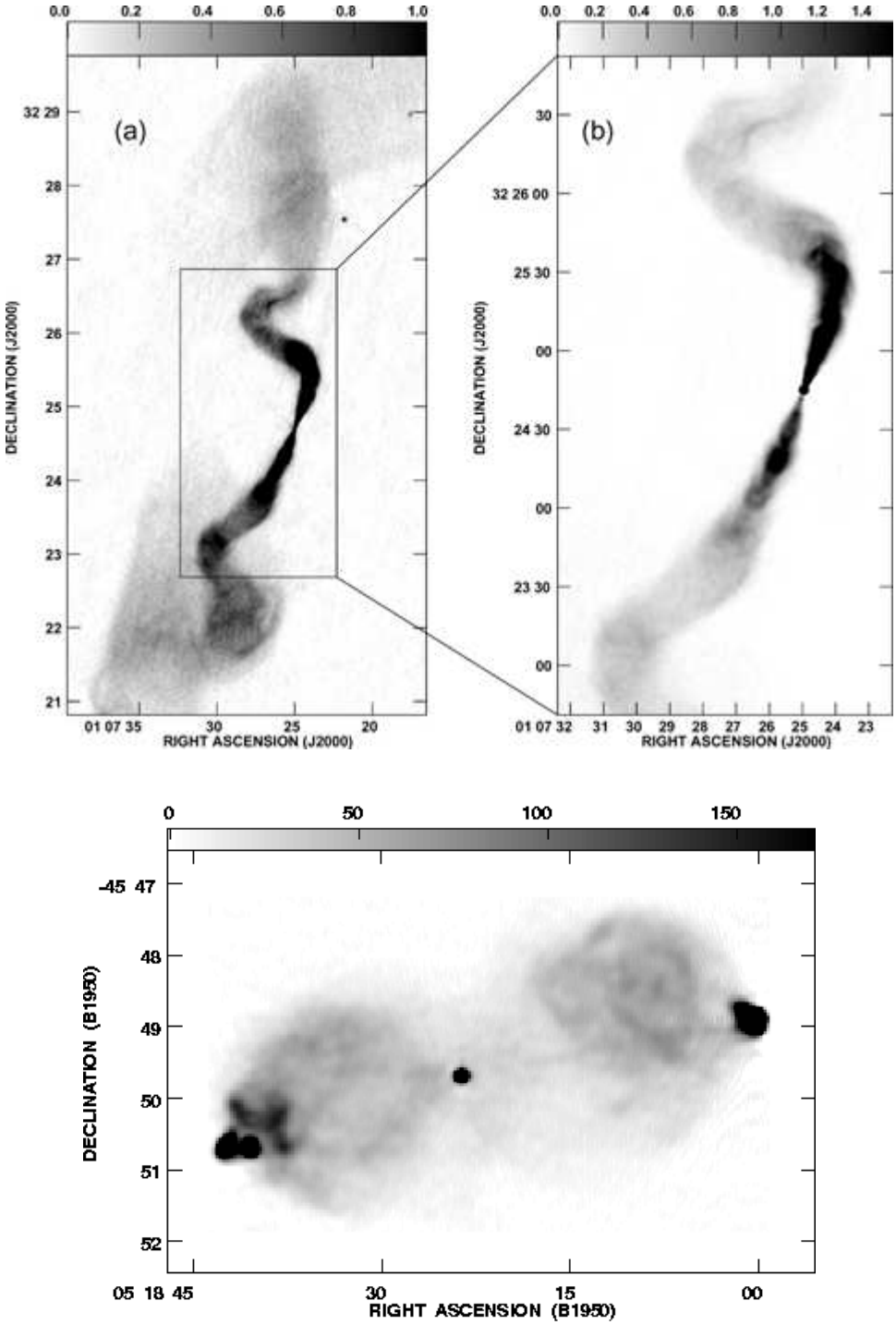

Figure 1.3: Grey scale total radio intensity maps of two radio galaxies with distinct morphologies. *Top:* 3C 31 FRI radio galaxy observed at 1.4 GHz shows well visible turbulent structure characteristic for this type of objects (Laing *et al.*, 2008). *Bottom:* Pictor A – an FRII radio galaxy with its symmetrical structure containing hotspots, radio lobes and faint one sided jet; observed at 1.4 GHz (Perley *et al.*, 1997). The top panels indicate the flux density variations in the images in Jy (*top*) and mJy (*bottom*).

rapidly variable and strongly polarised radio, optical and X-ray emission. The variable emission of blazars is thought to come from a relativistic jet oriented to the line of sight, hence often the apparent superluminal motion in the inner part of the jet is seen. When compared to quasars, blazars tend to have spectra dominated by the non-thermal continuum. For reviews see e.g. Angel and Stockman (1980), Fan and Xie (1996), Fossati *et al.* (1998), Fan *et al.* (2001).

Radio galaxies always manifest extended radio emission. Their observed radio structure depends on the interaction between the relativistic outflows of the active nucleus and the external medium. The large scale radio structure of radio galaxies and their classification is further discussed in §1.2.2. The optical hosts of radio galaxies are almost always massive ellipticals, although at least one exception has been found (Ledlow *et al.*, 1998). Radio galaxies may exhibit strong emission lines in their spectra, as well as be relatively featureless; some authors have argued that the existence of emission lines should be considered as the basis for further radio galaxy classification rather than their radio morphology, and this issue is discussed in §1.2.3.

1.2.2 Large Scale Radio Structures of AGN

Fanaroff and Riley (1974) divided the extragalactic large scale radio sources into two main classes, namely the low luminosity density FR I and more luminous FR II type. The division line was roughly set at $L_{178\mathrm{MHz}} \sim 2 \times 10^{25}$ W Hz^{-1} s^{-1}. However, it has been suggested since then (Owen and White, 1991), that the FR I/FR II break is a function of the optical luminosity density of the host galaxy; this has been further parametrised by Ledlow and Owen (1996) who showed that the break is rising with the optical luminosity density as $L_{\mathrm{R}} \propto L_{\mathrm{opt}}^{1.7}$.

It quickly became clear that sources of the two classes differ morphologically. FR IIs are limb-brightened, often symmetrical objects with well defined features such as jets, hot spots and radio lobes; they are often referred to as classical double radio sources. The relativistic outflows of FR IIs are tightly collimated and remarkably stable. They terminate in strong shocks, where the outflow particles may be re-accelerated, forming the so-called hot spots. The particles are then transported through the backflow filling in the cocoon, which in turn is formed by the expansion of jet through the external medium (the theory of relativistic jets is briefly reviewed in §2.1). In contrast, the outflows of FR I sources are poorly collimated, their decelerating jets start interacting with the external medium soon after their ejection. Unlike FR IIs, the vast majority of their radio emission is radiated close to their radio cores (which are believed to be at the base of the jets), hence they are often described as core-jet bright, edge-darkened objects. Examples of both classes are shown in radio maps of Figure 1.3. Interestingly, most quasars exhibit FR II morphology, while radio galaxies are found to be either FR I or FR IIs. The large scale radio structures of both morphologies may

extend up to Mpc scales, which is well beyond the optical extent of their host galaxies (e.g. 3C 236, which is one of the largest and most famous radio galaxies, extends to ~ 4.5 Mpc).

The emission mechanism for these radio structures is synchrotron radiation that originates from relativistic particles accelerating in a strong magnetic field (Rybicki and Lightman, 1979; Longair, 1992). The highly relativistic, shocked particles (typically assumed to be electron-positron dominated), composing the compact emission of radio core and jets, give rise to the spectrum predominantly at GHz frequencies as depicted in Figure 1.4, although the compact emission from relativistically beamed jets may be sometimes detectable also at MHz frequencies (e.g. 3C 345 and 3C 454.5, see BRW99). The radio lobes consist mostly of shocked jet material, freshly injected as well as older one, and are visible primarily at MHz radio frequencies.

1.2.3 Unification of Radio-loud AGN

Over the past three decades the orientation-based unification scheme has been the standard picture of the radio-loud AGNs. These unification models assume that different apparent classes of AGNs are in fact the same type of objects observed at different angles to the line of sight. The first idea that the orientation may play the role in AGN unification came from Orr and Browne (1982) who suggested that the core-dominated quasars were simply the lobe-dominated quasars viewed close to the line of sight. Further, Scheuer (1987) and Barthel (1989) reviewed the relativistic beaming model and proposed that the only difference between radio galaxies and quasars are their viewing angle, and often associated relativistic beaming. Based on this view, radio galaxies and radio-loud quasars of FR II morphology would belong to the same population of sources. Similar unification has been proposed for radio galaxies of FR I type and blazars, where the latter are the FR Is seen down the jet. Consult Antonucci (1993) and Urry and Padovani (1995) for reviews of these models, and e.g. Tadhunter (2008) for criticism of these views.

Although the orientation-based unification models suggest that radio galaxies of different Fanaroff-Riley morphology should be treated separately, the question of whether these morphologically different sources originate from the same parent population and are dependent on the environment they reside in, or whether they are intrinsically distinct, is still open (e.g. Baum *et al.*, 1992, 1995; Meier *et al.*, 1997; Gopal-Krishna and Wiita, 2000; Rawlings, 2002; Kaiser and Best, 2007; Kawakatu *et al.*, 2009; Wang *et al.*, 2011). In particular, Baum *et al.* (1992) in their interpretation of the radio galaxies' emission-line nebulae spectroscopy suggest that the angular momentum of the gas in the accretion disc of the AGN may be important in determining the radio morphology of the sources. According to their work FR Is are supposed to be fed at low accretion rate, and have presumably low spins, while FR IIs are expected to undergo higher accretion rates and their BH spins are supposed to be also higher (although the authors do admit that the spin suggestion is highly speculative, it would provide explanation for the differences in jet collimation and Mach num-

bers of the two classes; see Baum *et al.*, 1995). Similar interpretation is favoured by e.g. Rawlings (2002). However, such arguments lead to the conclusion that there should exist fundamental differences of the central engines of sources of the two morphological classes. Consequently, two classes have been introduced, namely the class of high-excitation galaxies (HEG) which includes the most powerful radio galaxies and quasars (nearly entirely of FR II morphology), and the low-excitation galaxy class (LEG) consisting of most FR I radio galaxies and low-luminosity FR II sources. As a counterargument to this reasoning Gopal-Krishna and Wiita (2000) present a sample of rare hybrid radio sources; HYMROS (HYbrid MOrphology Radio Sources) are radio sources with large scale structure which resembles both Fanaroff-Riley classes, that is they seem to be of FR I type on one side, and FR II on the opposite side. The existence of such sources supports the idea that the radio morphology depends on the jet interaction with the surrounding medium rather than intrinsic differences of the central engine. Also Kaiser and Best (2007) and Wang *et al.* (2011) present semi-analytical models that allow evolution of FR II objects into FR I type. On the other hand, it is noted that the model of Baum *et al.* (1995) allows for evolution of the central engine properties, that is the mass accretion rate may decline in time allowing FR II sources to evolve into FR I. Clearly, this issue is not yet resolved.

In this thesis I follow the orientation-based unification models assuming that the difference between radio galaxies and radio-loud quasars is only their viewing angle. Due to the availability of semi-analytic parametrisation of the jet modelling (see also §2.1), only FR II type sources are considered in this work. However, despite using the FR I/FR II distinction between radio sources rather than the LEG/HEG diagnostics, the question of and any evidence for LEG/HEG differentiation is tackled in my further analysis (Chapter 4).

1.3 Where the monsters live: the impact of the radio-loud AGN on the surrounding Universe

Radio galaxies and radio-loud quasars are believed to have had a significant impact on the evolving Universe and its large scale structure (e.g. Kronberg *et al.*, 2001; Gopal-Krishna and Wiita, 2001; Gopal-Krishna *et al.*, 2004; Silk, 2005). These radio sources are often found in galaxy groups and clusters (among others: Longair and Seldner, 1979; Hill and Lilly, 1991; Allington-Smith *et al.*, 1993; Deltorn *et al.*, 1997; Zirbel, 1997; Belsole *et al.*, 2007). Although, there is evidence that FR II sources at low redshifts seem to prefer lower density environments (poor clusters and groups of galaxies), while FR IIs at higher redshifts and the vast majority of FR Is are often found in clusters of galaxies, and high density environments (e.g. Zirbel, 1997). Since their jets inject a significant amount of energy into the surrounding medium, stored in the radio lobes, they can provide useful information in the study of the density and evolution of the intergalactic and intracluster medium. The jet activity is also believed to regulate the growth of massive galaxies through the compression

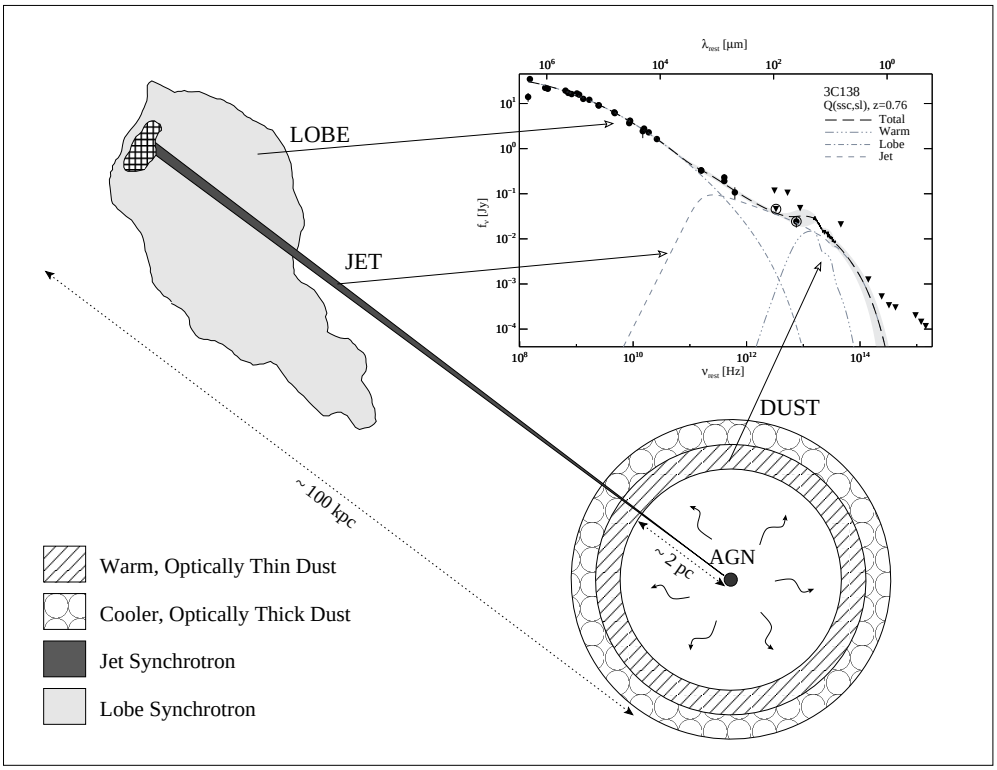

Figure 1.4: Radio-to-optical SED of 3C 138 radio galaxy. This example shows the physical origin that gives rise to the SED components. Low radio frequencies (MHz) unveil the synchrotron emission of the radio lobes, while radio jet starts contributing to radio luminosities at GHz frequencies. Although not indicated in the figure, the compact radio emission from hotspot and radio core contributes to the source luminosity density already at low GHz frequencies. The sketch is not to scale, here the dust shell is approximately $10^4\times$ its true size as compared to the length of the drawn jet. Credits: Cleary *et al.* (2007).

of the cold clouds of the ambient medium surrounding the outflow and thus triggering star formation either by the jet impact itself or by heating the intergalactic gas (e.g. Böhringer *et al.*, 1993; McNamara *et al.*, 2000; Rawlings and Jarvis, 2004; Scannapieco *et al.*, 2005; Croton *et al.*, 2006; Dopita *et al.*, 2007; Shabala *et al.*, 2011). Moreover, the powerful distant[2] radio galaxies and quasars allow us to trace the large scale structure of the early Universe (e.g. Miley *et al.*, 2004).

1.3.1 Clusters of galaxies

Clusters of galaxies are the largest gravitationally bound objects in the Universe. Their typical physical extent is of $1-10$ Mpc, and they contain masses of approximately 10^{15} $M_\odot$. They may contain hundreds of galaxies, although it has been loosely defined that agglomerations which contain no fewer than approximately 50 galaxies are to be classified as clusters

[2]The most distant quasar currently known (as of December 2011) resides at a redshift of $z = 7.085$ (Mortlock *et al.*, 2011).

of galaxies. Structures of smaller number of objects are classified as groups of galaxies; these do not have well defined centers[3] (cluster/group core), and are much smaller both in physical size ($1-2$ Mpc) and in mass ($10^{12}-10^{14}$ $M_{\odot}$) than galaxy clusters. Many galaxy clusters are bright X-ray sources with X-ray luminosities of $10^{43}-10^{45}$ erg s^{-1} (that is $10^{36}-10^{38}$ W). This X-ray emission has been found to be most consistent with thermal bremsstrahlung originating from hot gas. The gas, known as intracluster medium (ICM), is very hot ($10^{7}-10^{8}$ K), of rather low density (approximately $10^{-2}-10^{-4}$ atoms cm^{-3}), and consists of ionised hydrogen and helium enriched by heavy elements such as iron (see e.g. Tamura *et al.*, 2004, on the ICM metal abundances). For extensive reviews on galaxy clusters see e.g. Sarazin (1988) and Arnaud (2005).

Clusters of galaxies are assumed to be bound, self-gravitating systems. Based on this assumption already early estimations of masses of clusters (e.g. Zwicky, 1933; Smith, 1936) showed that their total masses are much greater than can be contributed by all of the galaxies in particular clusters; this is currently known as the missing mass problem. This discovery led to the hypothesis on the existence of 'dark matter' (Zwicky, 1933, 1937). In a typical galaxy cluster only approximately 15 per cent of the total mass is composed of the visible baryonic matter, while the remaining 85 per cent is believed to form the dark matter component. See e.g. Biviano and Salucci (2004) and Sand (2006) for reviews and discussions on this topic.

Giant elliptical cD galaxies are often found in the concentrated cores of galaxy clusters. These galaxies are the most luminous ones known, and are often inhabited by powerful radio sources (see e.g. Sarazin, 1988; Kormendy and Djorgovski, 1989). It has already been noted three decades ago (e.g. McHardy, 1979) that radio sources are often found in galaxy clusters and are located close to the cluster core (see also Hill and Lilly, 1991; Allington-Smith *et al.*, 1993; Ledlow and Owen, 1995; Deltorn *et al.*, 1997; Belsole *et al.*, 2007; Wing and Blanton, 2011).

1.3.2 AGN feedback

During the initial gravitational collapse that forms galaxies and galaxy clusters, the intracluster medium (intergalactic medium; thereafter IGM) is heated to high temperatures. The hot gas of the collapsing structures quickly loses its energy by the bremsstrahlung emission in X-rays; this cooling will be strongest in the densest regions. Once the material in the collapsing structure centre cools down, the pressure of the hot gas nearby will induce more material to flow inwards – this mechanism is referred to as the cooling flow. For comprehensive review on the physics of cooling flows see Fabian (1994). Surprisingly, however, it has been found that much less mass is actually being cooled that it is expected from the theoretical predictions; a term 'cooling flow problem' has been coined (e.g. Heckman *et al.*,

[3]Note, however, that this is not differentiating characteristics between groups and clusters of galaxies; galaxy clusters can be divided into regular (with well defined core and spherical symmetry, e.g. Coma Cluster) and irregular ones (e.g. Virgo Cluster).

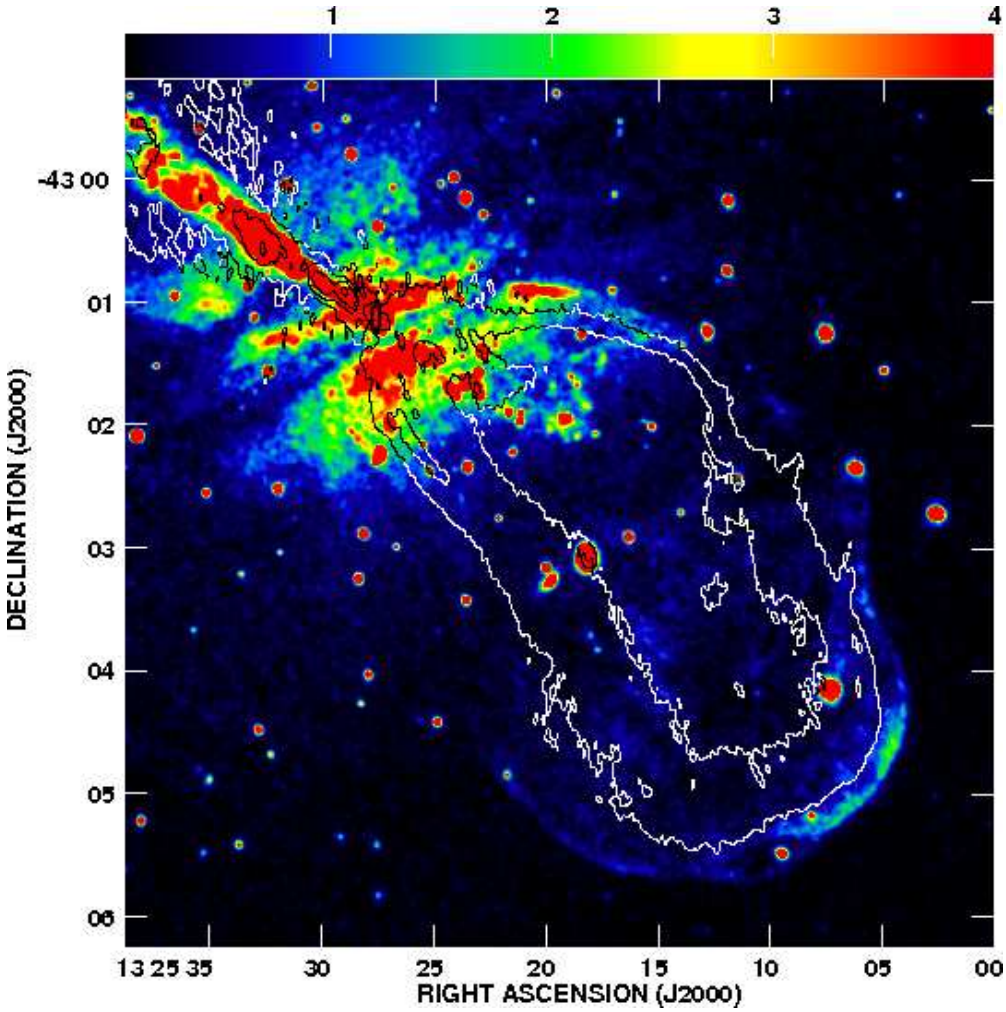

Figure 1.5: An example of shocked X-ray emission surrounding radio lobe of the Centaurus A, an FR I radio galaxy at $z = 0.0018$. Radio contours (1.4 GHz) are overlaid on the smoothed, colour coded (units of ACIS counts/pixel) X-ray *Chandra* data ($0.4 - 2.5$ keV). Credits: Croston *et al.* (2009).

1989; O'Dea *et al.*, 1994; Voit and Donahue, 1995; Edge and Frayer, 2003; Peterson *et al.*, 2003; Peterson and Fabian, 2006). The following mechanisms have been proposed as an additional source of heating of the cooling flows: AGN and supernova heating, thermal conduction, comic ray heating (see Peterson and Fabian, 2006, and references therein). The AGN feedback is presently considered to be the primary source of heating.

As previously mentioned, the outflows of the AGN inject a significant amount of energy into the surrounding medium. The interaction occurs between the expanding low density, high pressure radio lobes and denser ambient medium via the 'pdV' work done by the lobes. But even when the jet activity stops, the radio lobes start to expand buoyantly, and continue to interact with the ambient medium. The evidence confirming this view includes strong interaction of radio galaxies with surrounding environment (e.g. 3C 84: Böhringer

et al., 1993), radio bubbles, and X-ray shocks. The radio bubbles are 'holes' in the X-ray surface brightness, and studies have shown that they often coincide with radio lobes of radio galaxies (see McNamara and Nulsen, 2007, for review and references). The direct evidence for shocks in the hot phase (X-ray shocks) can be found around small scale radio lobes of nearby radio galaxies; examples include Centaurus A (Kraft *et al.*, 2003; Croston *et al.*, 2009, see Figure 1.5), NGC 3801 (Croston *et al.*, 2007), and Markarian 6 (Mingo *et al.*, 2011). Although more difficult to detect, evidence of shock heating has been also found in the case of FR II radio galaxies, e.g. 3C 444 (Croston *et al.*, 2011). However, AGN feedback is thought to be an intermittent process as many radio galaxies show signs of recurrent activity (e.g. Schoenmakers *et al.*, 2000a). The intergalactic and intracluster cold gas is directly connected to the accretion mechanism of the SMBH, and hence heating of the ICM (during the AGN activity, $t_{\rm on}$) most probably affects the accretion rate of the AGN central engine. Eventually, the accretion may shut off, and after some time ($t_{\rm off}$) may restart. Since each episode of the AGN activity will give rise to the overall feedback from the SMBH, estimation of the so-called duty cycles of AGNs (that is the ratio of the time spent in the active state to the time spent in the quiescent state, that is $t_{\rm on}/t_{\rm off}$) became of interest to many authors. For extensive reviews on the AGN feedback see e.g. McNamara and Nulsen (2007) and Gitti *et al.* (2012).

1.4 Extragalactic Radio Surveys

The interstellar medium (ISM), and particularly its cooler phases, consisting of neutral gas, molecular gas, and dust grains, is often a source of obscuration of radiation from astronomical objects. The obscuration by these particles, absorption and scattering, is inclined to be most severe at shorter wavelengths and particularly at ultraviolet part of the spectrum; the radiation is obscured by particles of sizes comparable to the considered (or shorter) wavelengths, and since typical dust grains are of 0.1μm in size (e.g. Weingartner and Draine, 2001; Zubko *et al.*, 2004), radio and infrared frequencies are the least affected (although at X-rays and gamma-rays the ISM starts to become again more transparent than at optical and ultraviolet wavelengths). Thus unobscured observations at radio wavelengths are very powerful in detecting high redshift astronomical objects, and are considered a perfect laboratory for cosmological studies.

One of the best known, as well as one of the first comprehensive catalogues of extragalactic radio sources, is the 3C catalogue (The Third Cambridge Catalogue of Radio Sources; Edge *et al.* 1959, see also Bennett 1962). Its 'revised revised' version (3CRR; Laing *et al.*, 1983) is formally a complete sample of extragalactic radio sources of the original survey, and is very commonly used in radio galaxy and quasar studies. The Radio Astronomy Observatory of the University of Cambridge provided a few more extragalactic radio catalogues at both low and high frequencies, for instance 6C measured at 151 MHz (The Sixth Cambridge Catalogue; Eales, 1985), and 9C at 15 GHz (The Ninth Cambridge

Catalogue; Waldram *et al.*, 2003), among others. As discussed by Condon (1999), the progress in electronics (and computing power) allowed us to employ the long known synthesis aperture techniques to a new, powerful level. Thus some of the new generation radio surveys came into existence, such as the still not yet complete FIRST survey (Faint Images of the Radio Sky at Twenty-centimetres; Becker *et al.*, 1995), NVSS (The NRAO VLA Sky Survey; Condon *et al.*, 1998) and WENSS (The Westerbork Northern Sky Survey; Rengelink *et al.*, 1997). Undeniably, all of the existing radio surveys contribute significantly to our knowledge of the radio Universe; their diverse frequencies at which the visibilities[4] are measured as well as angular resolutions do give a complementary insight into the radio sky.

However, one must remember that the longer the wavelength (λ) is, the lower the resolution ($\theta_{\rm res}$) becomes; the angular resolution may be balanced by increasing the size of the radio interferometer baseline ($D_{\rm baseline}$) since

$$\theta_{\rm res} \propto \frac{\lambda}{D_{\rm baseline}\sin(\Theta)}, \tag{1.2}$$

where Θ is the angle at which the source is observed and is measured from the baseline plane, $D_{\rm baseline}\sin(\Theta)$ may be referred to as the projected baseline. Yet the angular resolution cannot be increased infinitely, and some limitations exist. It is clear that the higher frequency surveys may reach better angular resolution (e.g. FIRST with $\theta_{\rm res} \sim 5$ arcsec) than the low frequency ones (e.g. WENSS with $\theta_{\rm res} \sim 54$ arcsec). One must bear in mind, however, that always both the longest interferometer baseline and the frequency are important for obtaining specific angular resolution. The high resolution of the FIRST survey is thanks to both of these parameters; for instance the NVSS survey measured at the same frequency as FIRST reaches only 45 arcsec in the angular resolution since its longest baselines are significantly shorter than those used for the FIRST survey. Another aspect that one must also consider is the effect commonly referred to as 'resolving out' the radio sources, especially the low luminosity sources of extended diffuse emission. Some explanation on the basics of the operation of radio interferometers is necessary at this point. The coordinate system of radio image is based on (u,v) coordinates, where the (u,v) plane represents the antennae spacings (baselines) tracing the radio source visibilities with respect to ω – the so-called phase tracking centre, and is measured in terms of wavelength (λ). The (u,v) plane is a Fourier transform of the 'true' sky which in turn is measured in (l,m) coordinates; the (l,m) plane is perpendicular to the phase tracking centre and is spatially described as direction cosines *l* and *m*, which are coordinates of source direction vector. The interferometer response to a radio source is derived from these position vectors. Therefore, it can be clearly seen that the response of an interferometer depends on the radio source's size and

[4]The *visibility* is the fundamental parameter of an interferometer and can be defined as a measure of coherence of the electric field. A radio interferometer measures discrete components of the spatial frequency spectrum of an object on the sky, and the 'visibility amplitude' is the maximum transmitted intensity (brightness) of the observed object.

its position; for extended sources the visibility amplitudes decrease with increasing baseline lengths, and for a radio source of angular size $\theta_{\rm size}$ interferometer antennae separated by baselines of $< (\lambda/\theta_{\rm size})$ only will contribute to the visibilities amplitude. This problem becomes significant at the longest baselines. For more detailed discussion on the radio interferometry techniques, especially regarding relationship between radio frequency, radio image resolution and interferometer baselines see Appendix C. For a comprehensive introduction to radio interferometry see e.g. Taylor *et al.* (1999) and Thompson *et al.* (2001).

Because of the reasons presented above there is a tight relationship between measuring total flux density of a radio source and settings of the interferometer with which observations are done; for that reason the FIRST and NVSS surveys are often used to complement each other, where the low resolution NVSS ($\theta_{\rm res} \sim 45$ arcsec) measures total radio flux density of the source, and FIRST provides detailed information on the radio source structure (which is important in the case of extended sources such as radio galaxies). Yet this is not all; the frequency of the radio observations also plays a crucial role. Measurements at low radio frequencies ($\nu < 500$ MHz) are, obviously, more sensitive to lower energy emission than observations at GHz frequencies and hence offer better detection of lower power, extended large scale radio structures. In addition, at high radio frequencies ($\nu > 1$ GHz) relativistic effects are more likely to be observed, and significantly more compact core-dominated radio sources are included. Hence, the 'old favourite', 3CRR, which is measured at 178 MHz, along with other catalogues such as 6C or 7C (The Seventh Cambridge Survey; McGilchrist *et al.*, 1990, both at 151 MHz), is often used in the studies of the radio galaxies and radio-loud quasars. See also detailed discussion in Blundell *et al.* (1999, hereafter BRW99) on this subject.

Although radio observations seem to be a perfect laboratory for studying both radio sources at cosmological distances and in population studies, one must bear in mind that these catalogues are not free from observational biases. Since radio luminosity density (L_ν) depends on the distance to the radiation source, that is

$$L_\nu = 4\pi d_{\rm L}^2 S_\nu, \tag{1.3}$$

where S_ν is radio source flux density measured at the radio frequency ν, and $d_{\rm L}$ is the luminosity distance (see Appendix C), at higher redshifts only the most powerful radio sources will be observed. This unavoidable Malmquist (1922) bias is referred to as the $L_\nu - z$ *degeneracy*, and is pictured in Chapter 3 (Fig. 3.1). The phrase 'complete, flux-limited radio sample' refers to surveys that contain all radio sources observed at a given sky area above the survey's flux limit, and hence they are considered to be complete despite the inclusion of the bias. Nonetheless, extra care must be taken while carrying out population studies.

To explore the population of low radio power high redshift radio galaxies and radio-loud quasars, deeper (more sensitive) radio observations than are currently available at MHz

frequencies, are needed. Two international projects that are of a particular importance are LOFAR (The LOw Frequency ARray; Lazio *et al.*, 1999), the first science of which is currently under its way, and SKA (Square Kilometre Array[5]) which is expected to be in operation in 2020. LOFAR will operate at radio frequencies of $30-240$ MHz with an angular resolution of the order of arcsec if observing with international baselines (baselines of ~ 1000 km). The estimated system sensitivity[6] of LOFAR array reaches 10 mJy at 30 MHz and 0.20 mJy at 200 MHz again using the longest international baselines. These characteristics are considerably improved as compared to the widely used 3CRR catalogue.

1.5 Previous Population Studies

The impact of radio galaxies and radio-loud quasars on their environments as well as their cosmological evolution has been addressed by many authors over the last few decades. The pioneering work on the evolution of these violent active galaxies, based purely on the observational data, was done, among others, by Oort *et al.* (1987), who for the first time broke the degeneracies between radio lobe luminosity density, redshift and linear size of the extragalactic radio source population, and found that generally the linear sizes of AGN radio lobes evolve with cosmic epoch as $D \propto (1+z)^n$, where $n \approx -3.3 \pm 0.5$. Similar results were obtained by, e.g., Singal (1988) and Kapahi (1989) who studied a variety of samples extending to $z \sim 1.8-2.9$ and both authors found $n \approx -3.0$. Moreover, in their work on high redshift quasars ($z > 1.5$) Barthel and Miley (1988) presented evidence that these powerful radio sources reflect a cosmic epoch dependent stage of the evolving large scale structures in their physical appearance. The interest in radio galaxy and quasar cosmological evolution lead to the work of Dunlop and Peacock (1990) who showed that the space densities of powerful radio galaxies were the largest in the so-called 'quasar era', i.e. between redshifts ~ 1.5 and 3 (see also Jackson and Wall, 1999). Through this discovery it became apparent that these radio sources carry important knowledge about the evolving Universe.

Because of the relatively simple structure of radio sources with FR II morphology (contrary to the turbulent nature of FR Is), attempts have been made to develop analytical models of their growth; the pioneering work of Scheuer (1974) and Blandford and Rees (1974), and further of Baldwin (1982) and Carvalho (1985) led eventually to the development of some sophisticated semi-analytical models of FR IIs' growth over the past 15 years (e.g. Kaiser and Alexander 1997, hereafter KA97; Kaiser *et al.* 1997, hereafter KDA97; BRW99). These models can predict source observables, that is radio lobe luminosity density and linear source size, from underlying physical properties such as jet kinetic luminosity (Q), source age (t), and the density of the intergalactic medium (ρ). This development has

[5] http://www.skatelescope.org

[6] The system sensitivity (system equivalent flux density, often referred to as SEFD) is the theoretical sensitivity that an interferometer can reach. Characteristics such as efficiency of the antennae, the collecting area as well as system noise are taken into account in the estimation of the system sensitivity.

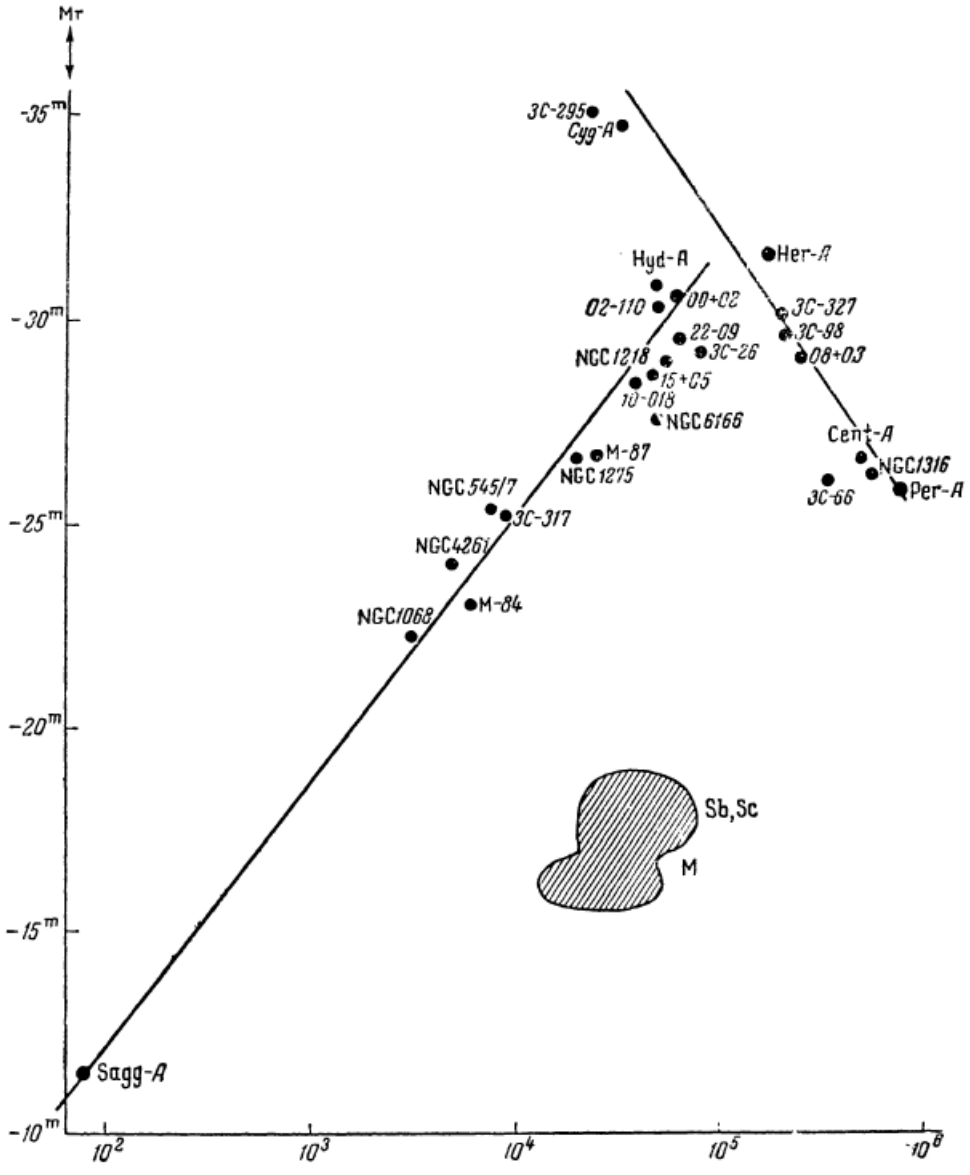

Figure 1.6: The reproduction of the original diagram of Shklovskii (1963), where *y*-axis represents the photographic absolute radio magnitude denoted as $M_{\rm r}$, and *x*-axis represents the source's linear dimensions denoted as $R_\bullet$ (for detailed explanation see the original paper). The author refers to the diagram as the 'absolute magnitude – linear dimensions' diagram for radio galaxies. Shklovskii (1963) defines two regions of the diagram that clearly stand out, namely the 'main sequence' (when the radio luminosity density increases), and the 'giant sequence' (for which the radio luminosity density decreases). The currently used $P_\nu - D$ diagrams in various radio galaxy and radio-loud quasar studies (§1.5) include only the giant sequence.

led to number of studies that investigated whole populations of these powerful sources and their evolution through exploration of their fundamental properties (Daly 1995; BRW99; Kaiser and Alexander 1999; Barai and Wiita 2006, 2007; Wang and Kaiser 2008). The basic methodology of these studies was to construct virtual populations of these sources choosing underlying properties for the population and running them through semi-analytical models to predict the distribution of source observables, the linear size and radio lobe luminosity density. The simulated populations were further compared to observed data from complete samples of radio sources.

However, those studies focused on the commonly used radio power – linear size ($P_\nu - D$) distribution diagram introduced by Shklovskii (1963; reproduced in Figure 1.6). The problem with such an analysis is that $P_\nu - D$ diagram is difficult to interpret in terms of other very commonly used techniques to study source populations such as the luminosity functions. Moreover, many studies, whether they were purely observational or based on the theoretical models of radio source growth, (e.g. Kapahi, 1989; Singal, 1993, BRW99) focused predominantly on the relationship between the observables and their trends with cosmological epochs. These observables are determined by the fundamental source properties, and hence they carry convolved effects of possible cosmological evolution of the underlying physical properties, as well as the influence of possible observational biases. There have been attempts to investigate the fundamental source parameter space and its redshift evolution (Kaiser and Alexander, 1999; Machalski *et al.*, 2004a; Wang and Kaiser, 2008), but sometimes strong assumptions have been adopted. For instance, assumptions on some of the intrinsic parameters of the relativistic jets, such as their particle content and the initial energy of the particles injected in the outflow, as I attempt to show in this thesis, may lead to different final results. Also, in the investigations of the redshift evolution of some of the radio source fundamental parameters (such as its age or ambient density in which the source expands), always one of these parameters was fixed when the other was explored. In Chapter 3 I show that such a procedure will lead to indirect assumptions on the final results.

1.6 The Holy Grail: Aims of this Work

Since the discovery of radio galaxies and quasars a number of 'big questions' have been posed, and their study over time has provided more questions than answers. These questions have changed depending on the decade and a good review highlighting these has been compiled by e.g. O'Dea (2002). Some of the important burning topics we face currently include detailed investigations of environments and length of the lifetimes of these powerful radio sources. The knowledge of the environments into which these radio sources expand is crucial in investigations of radio source propagation and, what follows, their morphology. Since radio galaxies have a significant and violent effect on their surroundings, these investigations would allow us to shed more light on the relation between radio source activity and the cooling flows in clusters of galaxies. Also, the estimation of the lifetimes of

these sources is of great importance as it will help one to measure for example the duty cycles of radio galaxies. Another question refers to the way the ages of radio galaxies can be measured, since commonly used methods disagree (e.g. synchrotron vs. dynamical age estimates). Radio galaxies and radio-loud quasars provide a unique opportunity for the exploration of the cosmological evolution of the large and small scale structures, hence the evolution of these sources, and investigation of their progenitors as well as relics seem to be of a great importance. Also, their activity in the observable bands (e.g. radio waves) as well as their effect on the environments in which they reside trace the activity of the central engine; exploration of these objects gives an opportunity of the investigation of the birth, death and evolution over the cosmic time of their activity and the supermassive black holes themselves.

In this project I develop a multidimensional Monte Carlo algorithm to generate virtual populations of FR II sources. Unlike previous studies (§1.5), I use distributions of radio lobe luminosity densities that can easily be transformed into radio luminosity functions, rather than the $P_\nu - D$ diagram, to compare the generated population and the observed data. Also, I attempt to set as few assumptions as possible on the underlying physical source properties to obtain more general results (although the resolution of these results are still restricted by computing time). The Monte Carlo simulation is repeated multiple times following grid minimisation that searches broad ranges of the possible underlying source properties, and which allows for generation of confidence intervals of the estimated parameters. Co-evolution of the physical source properties is also allowed. This will enable one to determine the dominant type of evolution, if any. Once the fundamental parameters of FR II radio galaxies and radio-loud quasars are estimated (that is their kinetic luminosities, ages, and environments) I investigate the impact of these sources on the evolving Universe through the significance of their AGN feedback. Ideally, one would like to uncover the information on the underlying parent populations (unbiased by the sensitivity of the instruments used by the surveys) of these radio galaxies and quasars, and I attempt to shed more light on this possibility. The study would be complete with the inclusion of the FR I radio sources, and this is discussed with the plans on the extension of this work in the conclusions of this thesis. Finally, one of the aims of this work has been to provide the community with a simple method which allows one to answer some of the above questions.

1.7 Synopsis

The multidimensional Monte Carlo simulation developed for this study is presented in *Chapter 2*. Statistical methods, such as the maximum likelihood method and the goodness-of-fit test, as well as techniques used to display results, that is the production of the confidence intervals, are discussed. I also present a brief introduction to the fundamentals of the jet physics, and the theoretical model considered in this project in particular (KA97, KDA97). An extensive overview of the assumptions and fitted intrinsic and extrinsic model

parameters is also given.

In *Chapter 3* I present and discuss the results obtained from the simulations based on the 3CRR and BRL radio catalogues. This part of the study focuses on some of the most powerful FR II type sources observed up to redshift $z = 2$. The evidence and the strength of the cosmological evolution of the intrinsic (e.g. kinetic luminosity, age) and extrinsic (e.g. density of source environment) parameters of these FR II sources is presented. Since the results may depend on the assumed secondary parameters, I discuss those and investigate how strong their influence might be. Based on these results I also discuss implications of the radio galaxy impact for the evolving Universe, and the AGN feedback in particular (*Chapter 6*). Similar analysis is further conducted on a low luminosity density, low redshift ($z < 0.2$) radio sample and is presented in *Chapter 4*. Since this sample (Best *et al.*, 2005; Best and Heckman, 2012) is constructed at 1.4 GHz, a detailed description of cross matching it with publicly available, low radio frequency radio surveys is presented. Further, the results of this chapter are compared to the results of the more powerful FR II sources of the 3CRR and BRL radio catalogues, and evidence for validity of the HEG/LEG classification of the large scale radio sources is discussed.

The much sought-after scaling relation between kinetic and radio lobe luminosity density of FR II sources is discussed in *Chapter 5*. Discussion on the scaling relation presented here is based on the theoretical model of KA97 and KDA97. The underlying physical parameters most strongly influencing the relation, for instance age of the source, jet composition etc, are discussed.

In *Chapter 7* conclusions drawn from this study, as well as newly posed questions are presented. I also discuss some possible directions for continuing and extending this work.

Finally, in *Appendix A* I present the maximum likelihood confidence intervals, and the respective best fitting parameter sets that maximise the likelihood, of the secondary assumptions that may influence the results (discussed in *Chapter 3*). *Appendix B* contains a list of multicomponent WENSS sources discussed in *Chapter 4*. And in *Appendices D* and *E* the fundamental formulae of the maximum likelihood estimator and adopted cosmology (respectively), which are widely used in this work, are presented.

The standard ΛCDM cosmology with $\Omega_{\rm M} = 0.3$, $\Omega_{\Lambda} = 0.7$ and the Hubble constant of $H_0 = 71$ km s^{-1} Mpc^{-1} is assumed throughout this thesis.

Things should be made as simple as possible, but not any simpler.

ALBERT EINSTEIN (1879 - 1955)

2

Application of Semi-Analytical Models of Radio Galaxy Evolution: the multidimensional Monte Carlo Simulations

---

Since the discovery of radio galaxies in the 1950s attempts have been made to formalise descriptions of the physical evolution which they undergo throughout their lifetimes. Given the cosmological distances at which these radio sources are often found, and their ability to trace the evolution of the expanding Universe, they are invaluable for cosmological studies. Consequently, the fundamental parameters characterising radio galaxies have been an objective in radio galaxy and quasar studies over the past few decades. In the following chapter I give a short overview of the existing theoretical models of radio galaxy growth and discuss the models' assumptions. Most importantly I outline the algorithm of the Monte Carlo simulations through which the underlying fundamental parameters of radio galaxies are explored in the further analysis of this dissertation. The content of this chapter has been submitted to the Monthly Notices of the Royal Astronomical Society (A.D. Kapińska, P. Uttley & C.R. Kaiser, 'Fundamental properties of Fanaroff-Riley II radio galaxies investigated via Monte Carlo simulations', MNRAS (2012) accepted, in press).

2.1 Theoretical models of radio galaxy and quasar time evolution

A basic picture of FR II type radio source growth, where the relativistic plasma is ejected in two opposite directions forming collimated outflows, is nowadays widely accepted. These outflows expand and interact with the surrounding medium until they terminate in strong shocks and create radio lobes where the excess transferred energy is stored. The idea first proposed by both Blandford and Rees (1974) and Scheuer (1974) has been developed, over the past 15 years, into a few more sophisticated models of the evolution of FR II sources. In particular, there are three models which have gained the most attention, KA97 (part 1) and subsequently KDA97 (part 2), BRW99, and Manolakou and Kirk (2002, hereafter MK02). The time evolution of FR I sources, on the other hand, has not been yet successfully developed into general models of source growth[1], although some attempts and considerations have been undertaken (e.g. Bicknell, 1994, 1995; Wang *et al.*, 2009; Luo and Sadler, 2010).

2.1.1 Relativistic jets

Many mechanisms have been proposed for production and collimation of astrophysical jets since their discovery, yet no final consensus has been reached. Here I will only outline the hypotheses put forward on the jet production and collimation problem, and also briefly discuss emission mechanisms of the large scale outflows and their structures. More detailed discussion on the theoretical model I will use in the further simulations of radio galaxies in this project is given in the two subsequent sections (§2.1.2 and §2.1.3), while the issue of the jet particle content will be discussed in the light of this project's results in §3.10.5 (but see also §2.3.6).

Formation of relativistic jets. The two crucial requirements while dealing with the jet production problem are the availability of the material that can be deposited into the outflows and the mechanism that will efficiently do this. The accreted material (material in the accretion disc, hot gas in the corona and/or thick torus) and the production of the jets are tightly linked. If the central source discards more material in the form of outflows than it is able to accrete, the jet will shut off, and restart only if enough material is accreted[2]. The purely dynamical models of the jet production include funnels (i.e. pre-existing channels) and nozzles in the clouds surrounding central BH, which are believed to be escape routes for the outflows. In particular the models predict that the jets are produced by the dynamical interaction between gas clouds and streams of gas in ion- or radiation-supported

[1] Some models of time evolution of the low luminosity radio galaxies, that is FR Is, do exist; however, they are not general enough to be used in a population study such as this one. These models are often developed as a case study for a few extensively observed FR I radio galaxies, and contain too many parameters that need to be constrained observationally.

[2] Examples of what is considered evidence for the intermittency of the outflows are discussed in §4.3.4.

thick discs or tori (e.g. Cassen and Pettibone, 1976; Paczyńsky and Wiita, 1980; Rees *et al.*, 1982; Begelman and Rees, 1984). Further, the so-called AGN winds may produce various types of outflows, but as shown through hydrodynamical simulations they are suspected not to be able to collimate the outflows (see Begelman *et al.*, 1984, and references therein). The currently favoured class of the jet production mechanisms are the ones which incorporate magneto-hydrodynamics (MHD), that is the strong influence from the magnetic field is recognised. In these mechanisms the outflows are considered to be produced by the AGN winds, where jets are composed of the extracted energy and excess angular momentum of the accreting matter (e.g. Lovelace, 1976; Blandford and Payne, 1982), may be produced by the BH rotational energy (e.g. Blandford and Znajek, 1977), or include both of these mechanisms (Meier *et al.* e.g. 1997; Meier e.g. 1999, but see also Ohsuga *et al.* 2005; Ohsuga and Mineshige 2007). Although the MHD simulations of the relativistic jet production are considered a good approximation, for the realistic representation of these mechanisms relativistic effects should be considered. The relativistic hydrodynamic mechanisms were investigated previously by e.g. Wilson (1972) and Martí and Müller (2003), but surprisingly full general-relativistic MHD has been considered only in the last decade (Koide *et al.*, 1998, 1999; Leismann *et al.*, 2005). Moreover, one of the important aspects of the jet production mechanisms is their ability to effectively collimate the outflow. Without adequate collimation the jet will not survive the interaction with ambient medium once it had travelled further away from the central engine. Aspects such as the jet pressure (e.g. FR Is usually have under-pressured jets[3], see e.g. Ferrari *et al.* 1995), the strength of the magnetic field, and the overall speed of the outflow are important, especially that the outflow must re-collimate once it travelled few parsecs (the reconfinement shock in Figure 2.1). Jets of FR Is are believed to be collimated to a smaller degree than those of FR IIs; the former sources will eventually develop instabilities and became turbulent flows. For more detailed discussion including concepts which are not considered here (e.g. the jet stability) see e.g. Blandford and Pringle (1976), Eilek and Caroff (1979), Bodo *et al.* (1990, 1996), see also Ferrari (1998) and Perucho (2011) for short reviews. For a good review on the nature of the extragalactic radio sources see early work of Begelman *et al.* (1984), and for a recent review specifically on the jet production mechanisms see e.g. Ferrari (1998), Meier (2001) and Meier *et al.* (2001).

Synchrotron radiation. The process responsible for the non-thermal radio emission observable in large scale extragalactic radio sources is predominantly synchrotron radiation – emission radiated by the relativistic charged particles spiralling in and accelerated by magnetic field[4]. Synchrotron radiation as the mechanism for producing emission from radio

[3]The minimum jet pressure can be found from the minimum energy requirements. I discuss the energy requirements later in this section.

[4]The continuum radio emission may be created by either thermal or non-thermal mechanisms. The thermal emission depends strongly on the temperature of the emitting object. The black body radiation is caused by

sources was first proposed in the 1950s by Alfvén and Herlofson (1950). The polarised optical emission of the M87 jet observed by Baade (1956), who followed the observations of the Crab Nebula polarised emission and conclusions on its synchrotron emission origin proposed by Oort and Walraven (1956), provided strong evidence for the earlier proposal (see also Burbidge, 1956). The current understanding of the radiation process assumes that the fields are purely magnetic and are assumed to be homogeneous. The total radiated power depends solely on the particles (their charge q, mass m and velocity v) and the strength of the magnetic field B. Specifically, the average radiated power per electron of the synchrotron emission is

$$P = \frac{4}{3c}\sigma_{\rm T}(\gamma v)^2 U_{\rm B}, \qquad \text{where} \quad U_{\rm B} = \frac{B^2}{8\pi}, \tag{2.1}$$

$\sigma_{\rm T}$ is the Thomson cross-section and γ denotes the Lorentz factor. Considering an ensemble of electrons that occupy volume V and which number density is described by $n(\gamma)$ given that their Lorentz factors are within γ and $\gamma + {\rm d}\gamma$, the total emitted synchrotron power per unit frequency is

$$P_\nu = \frac{1}{6\pi}\sigma_{\rm T} c U_{\rm B} \frac{\gamma^3}{\nu} n(\gamma) V. \tag{2.2}$$

In order to produce the observable synchrotron emission a minimum energy contained in the relativistic particles and the magnetic field is required. The minimum energy is often referred to as the 'equipartition energy', because the minimum occurs when the particle and the magnetic field energies ($U_{\rm par}$ and $U_{\rm B}$ respectively) are almost equal. That is

$$U_{\rm tot} = U_{\rm par} + U_{\rm B} \tag{2.3}$$

and it can be shown that the minimum occurs for

$$U_{\rm B} = \frac{3}{4} U_{\rm par}. \tag{2.4}$$

Many authors attempt to verify the minimum energy requirements from the large scale outflows and their imprint on the ambient medium (e.g. Burch, 1979; Alexander, 1987; Carilli *et al.*, 1991; Hardcastle *et al.*, 2002; Dunn and Fabian, 2004; O'Dea *et al.*, 2009, among others) since it will help to establish adequacy of the theory to the extragalactic large scale radio sources and/or any deviations. For detailed synchrotron theory see e.g. Rybicki & Lightman 1979, Longair 1994.

---

random motions of electrons. Further, the free-free emission (bremsstrahlung) created by colliding ions and electrons will contribute to the overall radio emission. The synchrotron radiation (magneto-bremsstrahlung) is referred to as non-thermal emission. The vast majority of the radio emission, especially at lower frequencies, comes from the synchrotron mechanism.

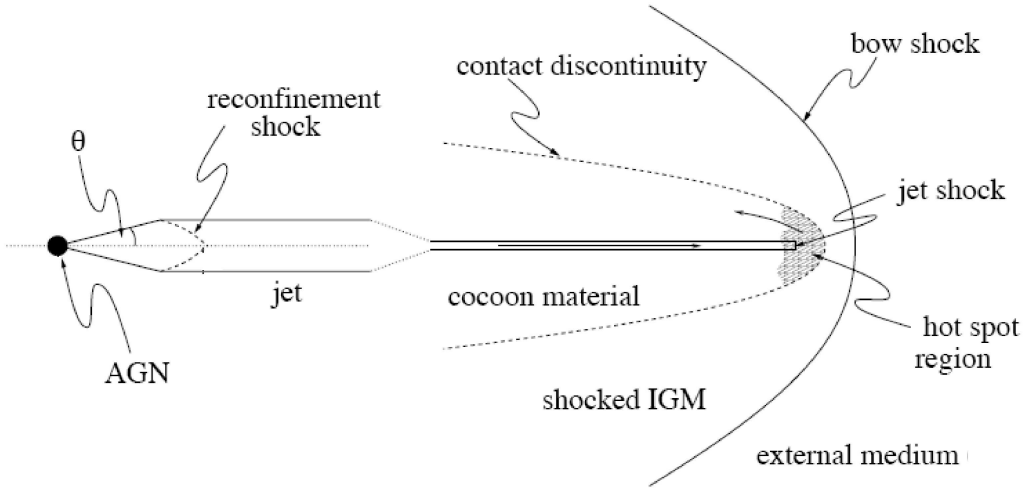

Figure 2.1: Sketch of FR II class radio source large scale structure elements. For explanation see §2.1.2. Credits: Kaiser and Alexander (1997).

2.1.2 Dynamical evolution of powerful extragalactic radio sources

In the following theoretical models of an FR II radio source growth (i.e. KA97/KDA97, BRW99 and MK02) only the large scale structure of the radio sources is considered. It is assumed that all of these sources produce well collimated outflows and further physics close to the BH is omitted. It is not my intent to compare the existing models, hence I will only briefly summarise the main features of the aforementioned semi-analytical approximations of the FR II radio source growth. The BRW99 and MK02 models follow the dynamical evolution of radio sources as described by KA97, which I will focus on in this work. For detailed discussion and derivation of the quoted equations the reader is referred to adequate models' original publications.

The following picture of the dynamical evolution of a relativistic jet is sketched in Figure 2.1. The outflow is ejected ballistically from the AGN and is initially characterised by a half-opening angle $\theta_{\rm jet}$. At some critical distance from the nucleus a reconfinement shock develops passing through which an initially ballistic jet transforms into an outflow which becomes pressure confined, that is the outflow is in pressure equilibrium with its immediate surroundings – the growing cocoon. At this point it is assumed that the jet radius is constant. The input rate of energy that is deposited into the source's cocoon is also constant; this input rate is referred to as the power of the jet or sometimes the jet kinetic luminosity, and is denoted as Q. Furthermore, the rest-mass transport rate in the jet ($\dot{M}_{\rm o}$), the bulk motion within the jet and so its velocity are also assumed to be constant. The environment into which the source expands is described by a density profile approximated here by the generalised King's (1972) profile

$$\rho_{\rm x} = \rho_{\rm o} \left(\frac{r}{a_{\rm o}} \right)^{-\beta} \text{ for } r > a_{\rm o}, \tag{2.5}$$

where r is the radial distance from the AGN core, and $\rho_{\rm o}$ is a constant central density within the core radius $a_{\rm o}$. The index β is usually constrained by the observations, although some restrictions may apply in the case of certain assumptions (e.g. the self-similarity assumption requires $\beta < 2$, see Falle, 1991). Note however, that the model depends on the combination of $(\rho_{\rm o} a_{\rm o}^{\beta})$ and not the parameters separately. The approximation is valid at distances of at least few core radii.

Given the characteristic quantities discussed above, that is Q, $\dot{M}_{\rm o}$ and $(\rho_{\rm o} a_{\rm o}^{\beta})$, one can define a characteristic length scale $D_{\rm o}$ (Falle, 1991)

$$D_{\rm o} = \left[\frac{(\rho_{\rm o} a_{\rm o}^{\beta})^2 Q}{\dot{M}_{\rm o}{}^3} \right]^{\frac{1}{2(\beta-2)}}. \tag{2.6}$$

Once the jet becomes significantly larger than this characteristic length scale, its flow no longer is dependent on the rest-mass transport rate $\dot{M}_{\rm o}$. Moreover, as Falle (1991) and KA97 show, the source expansion problem can be solved purely with a dimensional analysis where the source growth depends purely on the jet of the source with constant power (Q, hereafter referred to as the radio source's kinetic luminosity), its age (t) and the environment in which it self-similarly expands. The linear length of the radio lobe ($D_{\rm lobe}$) of the radio source is hence

$$D_{\rm lobe} = c_1 \left(\frac{Q}{\rho_{\rm o} a_{\rm o}^{\beta}} \right)^{\frac{1}{5-\beta}} t^{\frac{3}{5-\beta}}, \tag{2.7}$$

where the c_1 parameter depends solely on β, adiabatic indices of the radio lobe and the external medium ($\Gamma_{\rm l}$ and $\Gamma_{\rm x}$ respectively), and the source aspect ratio $R_{\rm T}$ (i.e. the ratio of the radio source length to its width, see §2.3.5), and is given by

$$c_1 = \left[\left(\frac{8 R_{\rm T}^4}{9\pi} \right) \frac{(\Gamma_{\rm x}+1)(\Gamma_{\rm l}-1)(5-\beta)^3}{9[\Gamma_{\rm l}+2R_{\rm T}(\Gamma_{\rm l}-1)]-4-\beta} \right]^{\frac{1}{5-\beta}}. \tag{2.8}$$

As the outflows drill their paths in the ambient medium they eventually terminate forming hot spots at the end of the jets. The hot spots, often referred to as the 'working surface', are situated at the 'head' of the strong shocks generated by the jets and are much larger than the cross section of the jet. Specifically, through the collision between the jet and the external medium two shocks form, one in each of the colliding medium. These are the bow shock, which propagates into the external medium, and an internal shock which propagates

into the cocoon. Additionally, the so-called contact discontinuity forms in between the two shocks (Figure 2.1). The dynamics of the bow shock is tightly linked to the mass of the shocked ambient medium. The contact discontinuity defines the cocoon of the radio source where the transported jet material and energy is stored. Specifically, the shocked jet material is diverted back towards the source's radio core filling in the cocoon (the process is often called a 'backflow'), the visible part of which is defined as the radio lobe. Although the shocked jet material is separated from the shocked ambient medium by the contact discontinuity, any mixing of the two materials may occur close to this border. KA97 assumes at this point that the pressure at the working surface ($p_{\rm hot\,spot}$) is completely balanced by the pressure of the surrounding shocked external medium ($p_{\rm bow\,shock}$), i.e. $p_{\rm hot\,spot} = p_{\rm bow\,shock}$. Based on the above scenario and the assumption that the relativistic particles of the outflow and the magnetic field pressure are balanced by the ram pressure of the IGM, the lobe pressure ($p_{\rm lobe}$) of a radio source at a given age t can be found with

$$p_{\rm lobe} \propto (\rho_{\rm o} a_{\rm o}^{\beta})^{1/3} Q^{2/3} D_{\rm lobe}^{(-4-\beta)/3}. \tag{2.9}$$

Note that the dependence on the age of the radio source is hidden in the expression on the linear size of the radio lobe $D_{\rm lobe}$. Also, it is important here to stress that the assumption on the jet being confined by the cocoon pressure implies that the jet pressure (after the reconfinement shock) equals $p_{\rm lobe}$. Furthermore, KA97 assume that any gradients in the lobe pressure are smoothed out; such an assumption does not apply only in the regions close to the working surface. For the full equation and its derivation see KA97 and Kaiser and Best (2007).

One of the important consequences of the KA97 model is the self-similarity of the radio source growth. The rate at which kinetic energy is transported into the bow shock in the KA97 model is

$$P_{\rm bow\,shock} = 0.5 \int_{A_{\rm bow\,shock}} \rho_{\rm x} v_{\rm bow\,shock}^{3} \, {\rm d}A_{\rm bow\,shock}, \tag{2.10}$$

where $A_{\rm bow\,shock}$ is the bow shock surface area, $v_{\rm bow\,shock}$ is the velocity perpendicular to it, and $\rho_{\rm x}$ is the gas density of the external medium as defined in Eqn. 2.5. Through the geometrical analysis KA97 shows that this can be expressed as

$$P_{\rm bow\,shock} \propto D_{\rm lobe}^{2-\beta} \left(\frac{{\rm d}D_{\rm lobe}}{{\rm d}t} \right)^{3}, \tag{2.11}$$

and is constant. Further, they also show that the volume of the radio source, assumed to be cylindrical, expands according to

$$V_{\rm lobe} \propto \left(\frac{D_{\rm lobe}}{a_{\rm o}} \right)^{3}. \tag{2.12}$$

Eqn. 2.11 and 2.12 indicate that both, the cocoon and the bow shock of the growing radio

source must expand self-similarly.

The BRW99 and MK02 models follow the formalism of KA97 for the dynamics of a growing radio source. The only difference lies in the interpretation of the hot spot and head region of the source structure; BRW99 (and so MK02 who follows formalism of BRW99) assume that hot spot region is not equivalent to the head region, the latter being much larger. Material transported by jets gets backflowed into the cocoon from the hot spot (where the particles may be re-accelerated) via the head of the jet. Also, they argue that radio sources do not expand self-similarly. Such an interpretation will influence prescriptions on the radio luminosity density evolution of the sources' lobes and is discussed in more detail in the next section (§2.1.3).

2.1.3 Luminosity density evolution of powerful extragalactic radio sources

The KDA97 formalism. To calculate the radio lobe luminosity density KDA97 assume that the radio lobe of a source is composed of small volume elements δV. Each of such volume elements depends on the particles' injection time $t_{\rm i}$. The internal energy (δU) of δV is expected to change as

$$\mathrm{d}(\delta U) = Q\mathrm{d}(\delta t_{\rm i}) - p_{\rm lobe}(t_{\rm i})\mathrm{d}(\delta V). \tag{2.13}$$

That is the internal energy of δV depends on the rate of the energy being deposited less the work done on the adiabatic expansion of the volume element. Further, KDA97 assume that the energy density of the particles is in equipartition with the magnetic field energy density (Eqn. 2.4). Given this, the volume elements are summed up and using Eqn. 2.2 for the total power of the synchrotron radiation KDA97 find the radio lobe luminosity density at a radio frequency ν (note that $L_\nu = 4\pi P_\nu$) of the radio source to be

$$L_\nu = f_{\rm L} Q p_{\rm lobe}^{(m+1)/4} t \int_{x_{\rm min}}^{1} C(x)\mathrm{d}x, \tag{2.14}$$

where m denotes the injection spectral index of the energy distribution of the relativistic particles (§2.3.4), the term $C(x)$, where $x = t_i/t$, depends on the energy losses of the relativistic plasma, and

$$f_{\rm L} = \left(\frac{\sigma_{\rm T} c}{\nu}\right) \frac{2(m+1)(2R_{\rm T})^{4(1-\Gamma_{\rm l})/\Gamma_{\rm l}} f_\gamma^{3-m} f_{\rm n}}{3(m+5)}. \tag{2.15}$$

The terms f_γ and $f_{\rm n}$ are normalisations of the Lorentz factor of the relativistic particles radiating at frequency ν in the evolving magnetic field and of the particle energy spectrum changes respectively. The energy losses depend on the time the particles have spent in the radio lobe. This means that the losses are not only depended on the age t of the radio

source, but also on the injection time of particles, given that $t_{\rm i} < t$. The following losses will affect the radio lobe luminosity density: adiabatic expansion, synchrotron and inverse Compton losses. The adiabatic energy losses occur due to the source expansion, while losses from the synchrotron emission and inverse Compton losses occur due to the (decreasing) magnetic field and the constant scattering of the cosmic microwave background (CMB) photons respectively. In particular, the synchrotron emission losses dominate mainly at the very early stages of the source's life when the magnetic field is the strongest. As the magnetic field decreases with the growth of the source, the inverse Compton losses will replace the synchrotron losses at the very late stages of the source life. The adiabatic losses affect the source evolution during its whole lifetime. Since these processes are incorporated into the model they allow to follow the source luminosity evolution more accurately.

In the derivation of Eqn. 2.14 it is assumed that the relativistic particles are initially accelerated at the time $t_{\rm i}$ and their energy distribution $n(\gamma_{\rm i})$ can be described by a power-law relation depending on their initial Lorentz factors $\gamma_{\rm i}$ (see also Eqn. 2.22). Furthermore, one cannot neglect the type of particles involved in the inflation of the cocoon. Synchrotron radiation requires charged particles; electrons are thought to be the typical constituent of the relativistic jets. However, to obtain neutrally charged flow some sort of positively charged particles must accompany electrons. Most commonly positrons or protons are invoked; however given fixed kinetic luminosity Q the choice of the positively charged particles in the flow will have profound influence on the resulting radio lobe luminosity density. This issue is further discussed in §2.3.6.

For the full derivation of the radio luminosity density equation see KDA97 and Kaiser and Best (2007, 2008). It is interesting to note here that the shocked jet material, which radio lobes are filled with, is still hot and relativistic as it may be re-accelerated in the hot spot region; the particles are believed to undergo the first-order Fermi process that accelerates them (Fermi, 1949). However, the surface brightness of the radio lobes may decay in the direction towards the radio core mainly due to adiabatic losses in the magnetic and particle energies, hence the visible radio lobes are much smaller than the expected cocoons. Nevertheless, the lower energy particles remain as heat in the cocoon for the lifetime of the radio source.

Modifications – the BRW99 and MK02 models. The BRW99 and MK02 models differ from KDA97 in their assumptions on the luminosity density evolution of the sources determined by the way the relativistic particles are injected from the jet to the radio lobe, and the particle transport. The original KDA97 model concludes that for the assumptions they adopt, the working surface, cocoon and bow shock of a source must expand self-similarly. This implies that the working surface grows proportionally to the size of the radio source. Note also that in the KDA97 model emission from hot spot is ignored, and a constant factor by which pressure in the cocoon differs from the pressure in the working surface is assumed.

BRW99 argue for the importance of the hot spot region pointing out the over-simplicity

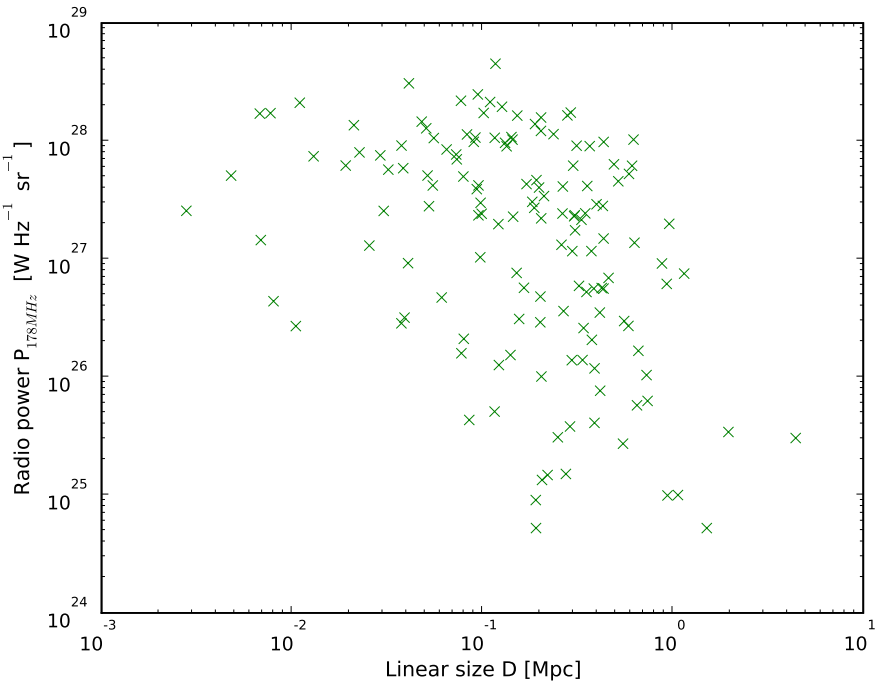

Figure 2.2: The $P_\nu - D$ diagram for the 3CRR sample (§3.2) of FR II radio galaxies and radio-loud quasars.

of the KA97/KDA97 model and its assumption of source self-similar expansion. They assume that hot spots do not grow self-similarly, and show that contribution of hot spot emission to the total radio luminosity density is, on average, approximately 0.04 per cent. The authors also argue that inverse Compton losses from the AGN's own radiation field cannot be neglected in the calculation of the total radio luminosity density. Given this, BRW99 follows the formalism of KDA97 but with two additional important modifications. Firstly, they assume that the injection index (that is the slope of the energy distribution of relativistic particles, see §2.3.4) is governed by the break frequencies of the energy distribution in the hot spots. Secondly, BRW99 assume that adiabatic expansion losses are controlled by the hot spot pressure which is *not* equivalent to the head region pressure.

Further, MK02 expands the KDA97 and BRW99 models incorporating details on the particle transport mechanisms. In particular, instead of assigning distribution to the particles which are deposited in the cocoon (which is the case in the KDA97 and BRW99 models), MK02 consider the actual first-order Fermi acceleration process occurring at the termination shock (the hot spot) that governs the particles' distribution. Further, they show that there must develop a re-acceleration process which occurs in the head region, after the particles pass through the termination shock. It is worth noting that assumptions of BRW99 and MK02 lead to much steeper evolutionary tracks of the sources in the radio power – linear size ($P_\nu - D$) plane as compared with the predictions of the KDA97 model.

More recently Barai and Wiita (2006, 2007) attempted to develop a more accurate model by testing and modifying the three leading theoretical models. They report that none of the existing models can give fully acceptable fits to all of the properties deduced from the radio surveys (especially the synchrotron spectral index α); however, according to their findings KA97/KDA97 give the best overall results as compared to the other two models. In this work the original KA97/KDA97 model is employed.

2.2 Monte Carlo Simulation Algorithm

In the traditional and most common way, the radio source evolution has been investigated through the $P_\nu - D$ diagram (Shklovskii, 1963, see also §1.5) presented in Figure 2.2 for the 3CRR sample (for the sample description see §3.2), which in recent studies has been extended into radio lobe spectral index (α) and redshift (z) parameter space. Here, an alternative approach is incorporated and instead of investigating $[P_\nu - D - z - \alpha]$ space radio luminosity functions (RLFs) are used in the analysis. An advantage of doing so is the direct link to the results of other source population studies which are most commonly expressed in terms of luminosity or mass functions. Due to degeneracy between the fundamental properties it is impossible to infer the source kinetic luminosity, the central ambient density and the source age directly from the observables of the radio lobe alone, and hence Monte Carlo simulations are necessary in order to generate simulated RLFs.

To construct a single virtual sample in total, $\sim$ few $\times 10^6$ virtual radio sources are generated. The subsequent prescription is followed.

1. For each source of the virtual sample I assign a set of physical parameters summarised in Table 2.1. Each of the parameters is either drawn from its respective distribution or is the same for each source; the details of these physical 'input' parameters are presented in §2.3.

2. Based on the theoretical model of KA97/KDA97 the source is evolved and its linear size D is calculated.

3. The linear size of the source is checked for its reliability, that is whether the source expansion exceeds an assumed fraction of the light speed (maximum allowed head advance speed, see §2.3.7). If it does, the source is rejected. Otherwise, the source is accepted and its linear size is corrected for the projection angle (§2.3.9).

4. The radio lobe luminosity density L_ν of the source at a frequency $\nu = 178$ MHz and its randomly generated redshift are calculated.

5. The radio luminosity density is subsequently randomised by adding a Gaussian variable of standard deviation $\Delta L_{\rm err} = 0.08 \times L_\nu$ to account for any instrumental/systematic errors. Moreover, since the source is evolved in its rest-frame, a correction of $(1+z)^\alpha$

transforming the calculated radio luminosity density to the common frequency must be included. The common frequency of 178 MHz is used. These corrections are discussed in detail in §2.3.4.

6. Steps 1 - 5 are repeated $\sim$ few $\times 10^6$ times.

7. The radio lobe luminosity density histograms for each redshift range and linear size bin are generated as discussed in §3.2. The binning of the virtual sample histograms matches exactly the one used for the real observed data sample. However, to ensure that the probability density functions of kinetic luminosities (Eqn. 2.19 and Eqn. 2.20) are represented by reasonable number of sources at the functions' exponentially falling ends, the virtual population is initially generated assuming that their kinetic luminosities are drawn from a uniform distribution, and later a weighting factor is applied to each source (see §2.3.1).

8. At this stage the histograms represent the total number of sources in the simulated sample since we have not determined yet the fluxes of the generated sources. In this sense, those are the 'true' numbers of the entire source population. However, to be able to compare the simulated sample to the observed data the selection effects arising from limited flux sensitivity must be taken into account, which is achieved by using radio luminosity functions. RLFs are an ideal tool when dealing with coupled selection effects such as limited sensitivity of radio surveys. They are defined as number density of sources per unit co-moving volume per unit luminosity. The initial histogram of the entire simulated population is therefore transformed into RLF ($\phi_{\mathrm{sim},i}$) by using the survey volume V_{survey},

$$\phi_{\mathrm{sim},i} = \frac{A}{4\pi}\frac{n_{L_i}}{V_{\mathrm{survey}}}, \tag{2.16}$$

where A is the area of the sky that the survey covers, and n_{L_i} represents the data counts in luminosity density bins L_i. Further, the RLF is transformed back into a histogram of number of expected sources for each linear size and luminosity density bin using V_{lim} – a maximum co-moving volume in which a source in a given luminosity density bin and with the flux limit of the survey would be included in the sample (Schmidt, 1968),

$$n_{L_i,S_{\mathrm{lim}}} = \frac{4\pi}{A}\phi_{\mathrm{sim},i}V_{\mathrm{lim}}. \tag{2.17}$$

The two transformations simplify to

$$n_{L_i,S_{\mathrm{lim}}} = n_{L_i}\frac{V_{\mathrm{lim}}}{V_{\mathrm{survey}}}. \tag{2.18}$$

Note that flux densities of the simulated radio galaxies ($S_{\mathrm{sim},i}$) are not examined directly, and hence no radio sources are rejected based on the limited sensitivity bias (i.e. requirement that $S_{\mathrm{sim},i} > S_{\mathrm{lim}}$). Instead, a correction factor ($V_{\mathrm{lim}}/V_{\mathrm{survey}}$), which indicates

the probability of radio source occurrence at a given flux limit, is employed. The effect of the limited flux sensitivity is an average for each considered bin. To ensure greater accuracy we perform the flux correction on much finer bin widths than those of the final histograms. In particular, in this step we use 20 times finer bins than used in the final histograms. These are later summed to match the initially constructed distributions.

9. So far, the number of progenitors becoming active and turning into FR II sources have not been discussed. To ensure a reasonably large statistical sample, the simulated sample is generated with a much larger number of virtual radio sources than the observed data sets contain. Instead of introducing a corresponding distribution function the full simulated sample is used. However, since both the simulated and observed samples must be of a similar size, that is of a similar number of sources considered, the data counts, which are found with Eqn. 2.18, need to be normalised in the virtual sample. I use the binned maximum likelihood method (MLM, see §2.4.1) together with Brent's method (Brent, 1973; Press *et al.*, 1992) to do so. The normalisation is set as a free parameter, but represents an average for the considered redshift range.

10. Finally, the goodness-of-fit test is performed. The statistics used, normalisation of the sample and the goodness-of-fit test are discussed in §2.4.

2.3 Monte Carlo Simulation Input Parameters

2.3.1 Kinetic Luminosity Distribution

The kinetic luminosity of each generated source is drawn randomly from a distribution function that acts as a probability density function. The form of the distribution function of sources' kinetic luminosities is not known, and various forms have been assumed in previous works ranging from a simple uniform distribution between minimum ($Q_{\rm min}$) and maximum ($Q_{\rm max}$) kinetic luminosity (e.g. Wang and Kaiser, 2008), through power-law scaling as Q^x (e.g. BRW99) to more complex functions as used by Willott et al. (2001, discussed below).

Two models for the initial distribution functions of the kinetic luminosities are considered. In Model S the kinetic luminosity distribution function is assumed to be modelled by the so-called Schechter function (Schechter, 1976) of a form

$$\psi(Q)\,{\rm d}Q = \psi^* \left(\frac{Q}{Q_{\rm B}}\right)^{-\alpha_{\rm s}} \exp\left(\frac{-Q}{Q_{\rm B}}\right)\,{\rm d}Q \qquad (2.19)$$

where the slope of the function for the kinetic luminosity values below the kinetic luminosity break ($Q_{\rm B}$) is described by the exponent $\alpha_{\rm s}$, and drops exponentially for the higher Q. ψ^* is a normalisation constant, which in our case is neglected at this stage as Eqn. 2.19 is used as a probability density function.

Model W follows Willott *et al.* (2001), who introduce a modified version of the above Schechter function of the form

$$\psi(Q)\,\mathrm{d}Q = \psi^* \left(\frac{Q}{Q_\mathrm{B}}\right)^{-\alpha_\mathrm{s}} \exp\left(\frac{-Q_\mathrm{B}}{Q}\right)\,\mathrm{d}Q, \tag{2.20}$$

and where the exponent α_s describes the function for kinetic luminosities higher than Q_B, while for lower kinetic luminosities the function drops exponentially, and ψ^* is used as in the Model S. In their original paper Willott *et al.* (2001) use a combination of Eqn. 2.19 and Eqn. 2.20 to describe the whole population that consists of high and low radio luminosity sources. Eqn. 2.20 was introduced to specifically model the high radio luminosity sub-population of radio sources. Since currently I do not consider FR I type sources in this study Eqn. 2.20 alone is used to describe the considered sub-population of powerful radio sources as opposed to the original method of Willott *et al.* (2001).

These functions and the effect the α_S parameter has on their shapes are plotted in Figure 2.3. Both functions describe the distribution of kinetic luminosities between Q_min and Q_max, which are set in such a way that contribution to the RLFs of sources with kinetic luminosities outside this range is negligible. To ensure these probability density functions are represented by reasonable number of sources, what will assure good statistics at the functions exponential ends, the kinetic luminosities are initially generated from a uniform distribution between Q_min and Q_max. Each of these kinetic luminosities is assigned a probability of its occurrence (a weighting factor) according to the considered probability function (Eqn. 2.19 and Eqn. 2.20). This weighting factor is applied to each source while constructing histograms at a later stage.

2.3.2 Ambient Density Distribution

The central density value (ρ_o) for each generated source is randomly drawn from a log-normal distribution with the mean value $\log_{10}(\rho_\mathrm{m})$ and standard deviation of $\sigma_{\log_{10}(\rho_o)} = 0.15$. The standard deviation is not introduced as a free parameter; however, it is tested how strong an effect it has on the results (see discussion in §3.10).

Since the type of the surrounding environment (clusters of galaxies or field galaxies) is tightly linked to the core radius of the source, these should never be discussed separately. Here one value of a_o is set for all the simulated sources (2 kpc). The choice of a_o may determine the most likely environments found in our simulation; this issue is discussed in detail in §3.7. The exponent β of the density profile (Eqn. 2.5) is randomly chosen from a uniform distribution between $\beta_\mathrm{min} = 1.2$ and $\beta_\mathrm{max} = 2.0$. Although many authors use a constant value of β (e.g. $\beta = 1.5$ is used by Daly 1995; BRW99; Kaiser and Alexander 1999; $\beta = 1.9$ and $\beta = 2.0$ by KDA97; Wang and Kaiser 2008), some observational evidence suggest that the parameter may vary between sources (e.g. Alshino et al. 2010).

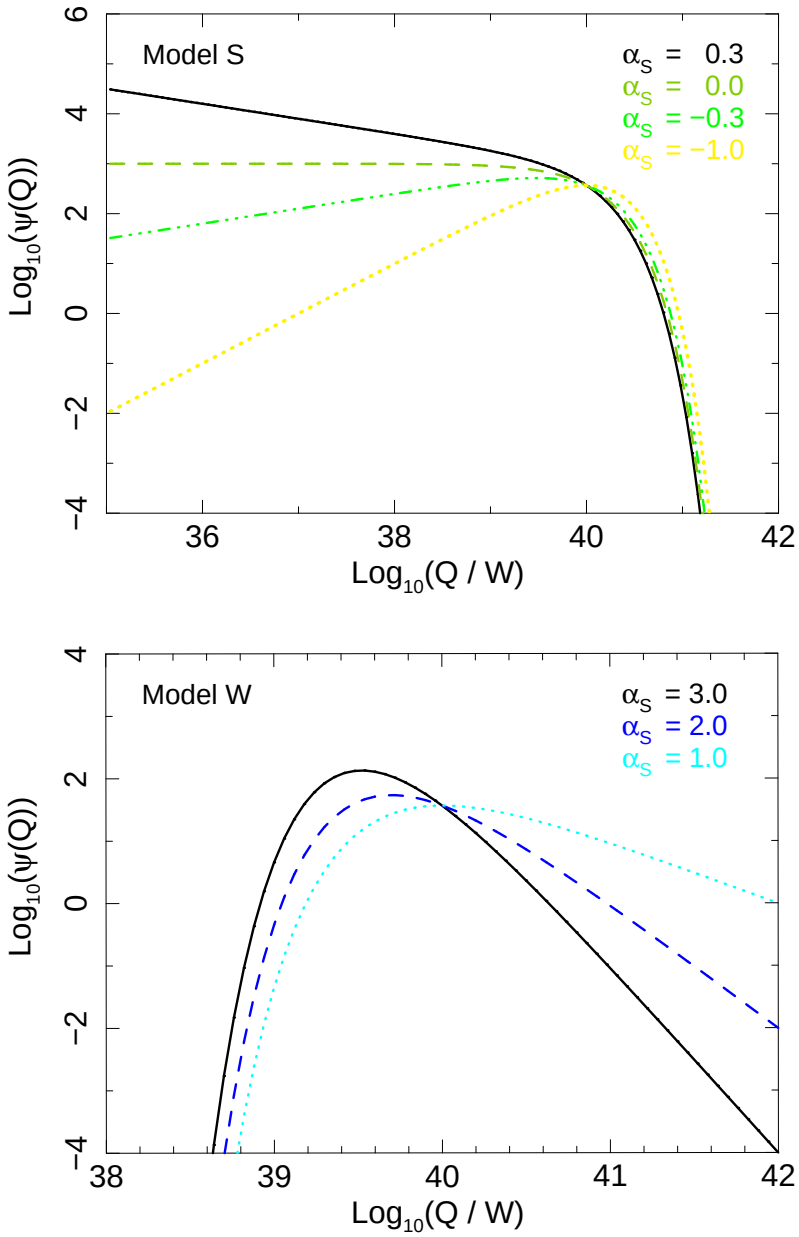

Figure 2.3: Examples of the Schechter function (*top*, model S) and its modification (*bottom*, model W). Both functions are plotted for $Q_B = 10^{40}$ W, and for normalisation which has been arbitrarily chosen to be $\psi^* = 10^3$ for model S and $\psi^* = 10^2$ for model W. The functions are plotted for a sample of different α_s parameter values as detailed in the plots. The change in the α_s parameter will change predominantly the slope of the function. In model S (*top*) the α_s parameter shapes the slope before Q_B, where for positive α_s the slope becomes negative (more low luminosity sources are included) and for negative α_s the slope becomes positive (i.e. less low luminosity sources are included). In model W (*bottom*) parameter α_s governs the shape of the post break part of the function. Here, the lower the value of α_s, the flatter the slope becomes allowing more high luminosity sources to be included. It is also worth noting that if α_s is the only parameter being changed, all plots (separately for each model) cross at the kinetic luminosity break value.

Table 2.1: Overview of a source physical parameters and default distributions from which they are drawn. Details on the assumed distribution or value of the respective parameters are discussed in sections as given in Column 4.

Parameter	Assumed distribution	Description	Discussed in
		PHYSICAL PARAMETERS	
z	distribution	source redshift	§2.3.10
Q	distribution	source jet power	§2.3.1
ρ_o	distribution	mean central density in which source expands	§2.3.2
a_o	value	core radius	§2.3.2
β	distribution	power law index of the radial density distribution	§2.3.2
t	distribution	source current age	§2.3.3
$t_{\rm max}$	distribution	source maximum age	§2.3.3
α	calculated value	radio spectral index	§2.3.4
m	distribution	power-law exponent of the relativistic particles' energy distribution	§2.3.4
$\gamma_{\rm min}$	value	minimum Lorentz factor of relativistic particles	§2.3.4
$\gamma_{\rm max}$	value	maximum Lorentz factor of relativistic particles	§2.3.4
$R_{\rm T}$	distribution	aspect ratio	§2.3.5
ϑ	distribution	projection angle	§2.3.9
$\Gamma_{\rm x}$	value	adiabatic index of the IGM	§2.3.8
$\Gamma_{\rm c}$	value	adiabatic index of the radio lobes	§2.3.8
$\Gamma_{\rm b}$	value	adiabatic index of the magnetic field energy density	§2.3.8
k	value	ratio of thermal to electron energy densities in the jet	§2.3.6
$v_{\rm max}$	value	maximum allowed head advance speed	§2.3.7
		DISTRIBUTIONS' PARAMETERS	
$Q_{\rm B}$	value	kinetic luminosity break	§2.3.1
$\alpha_{\rm s}$	value	exponent of the kinetic luminosity distribution	§2.3.1
$n_{\rm q}$	value	strength of the kinetic luminosity break redshift evolution	§3.4.2

continued on next page

Table 2.1: *Continued.*

Parameter	Assumed distribution	Description	Discussed in
$\rho_{\rm m}$	value	mean of log-normal distribution of radio sources' central densities	§2.3.2
σ_{ρ_o}	value	standard deviation of log-normal distribution of radio sources' central densities	§2.3.2
$n_{\rm r}$	value	strength of the central density redshift evolution	§3.4.2
$t_{\rm max_m}$	value	mean of log-normal distribution of radio sources' maximum ages	§2.3.3
$\sigma_{t_{\rm max}}$	value	standard deviation of log-normal distribution of radio sources' maximum ages	§2.3.3
$n_{\rm t}$	value	strength of the maximum source's lifetime redshift evolution	§3.4.2

2.3.3 Age distribution of the simulated sources

It is assumed that radio sources live up to a certain maximum age ($t_{\rm max}$) after which they instantly die. This may seem to be an oversimplification as any relic radio galaxies are going to be neglected; however, from previous work of KDA97 and BRW99 for instance, one can see that the luminosity tracks of radio sources steepen rapidly at the late stages of the source's life, quickly dropping below detectable flux levels.

Here the age of a source is randomly drawn from a uniform distribution between $t = 0$ and $t_{\rm max}$. The expectation that all radio sources have the same maximum age seems to be slightly unrealistic, hence a log-normal spread of the maximum ages around the mean $t_{\rm max_m}$, i.e. $\sigma_{\log_{10}({\rm t_{max}})} = 0.05$, is introduced. I also investigate the effect of the width of this distribution in §3.10.2.

2.3.4 Injection and radio spectral indices

The energy distribution of the relativistic particles initially follows a power-law relation with exponent m, the injection index,

$$N(E){\rm d}E \propto E^{-m}{\rm d}E, \tag{2.21}$$

which can be expressed in terms of the Lorentz factors γ of the particles, that is

$$n(\gamma)\mathrm{d}\gamma \propto \gamma^{-m}\mathrm{d}\gamma. \tag{2.22}$$

The exponent m assigned to a source is drawn from a uniform distribution with the minimum and maximum value allowed by the theoretical model of source growth used in this study, that is $m_{\mathrm{min}} = 2$ and $m_{\mathrm{max}} = 3$. However, theoretical studies of the particle acceleration in the relativistic shocks suggest a universal value ($m \sim 2.2-2.4$, e.g. Kirk *et al.*, 2000; Spitkovsky, 2008), while studies based on observations of gamma-ray burst afterglows favour a Gaussian distribution of this parameter (Curran *et al.*, 2010). Also, Machalski *et al.* (2007) conclude that the distribution of m is rather narrow with $m \in [2.0, 2.4]$ according to their modelling, and Meli and Mastichiadis (2008) report on good fits of the spectra by a power-law with index $m \cong 2.0-2.3$.

Moreover, the power-law of the relativistic electron energy distribution extends between γ_{min} and γ_{max}, i.e. between the Lorentz factors of the least and most energetic electrons of the outflow. I assume $\gamma_{\mathrm{min}} = 1$ and $\gamma_{\mathrm{max}} = 10^{10}$. KDA97 stresses that $\gamma_{\mathrm{min}} \ll \gamma_{\mathrm{max}}$. I decided to use much higher maximum Lorentz factor than KDA97 who used $\gamma_{\mathrm{max}} = 10^5$. Lorentz factors of $\gamma_{\mathrm{max}} \sim 10^5 - 10^6$ have also been measured by Meisenheimer *et al.* (1989) and Massaro and Ajello (2011), while BRW99 favour $\gamma_{\mathrm{max}} \cong 10^{14}$. I decided to use the intermediate value as a default one. Further, Blundell *et al.* (2006) report a new estimate for the low-energy cut-off of the energy distribution of relativistic electrons in FR II type sources. Based on the observations of Cygnus A they estimate a rather high value of $\gamma_{\mathrm{min}} = 10^4$. On the other hand, investigations of hot spots done by Meisenheimer *et al.* (1989) suggest that the minimum Lorentz factors, below which the synchrotron losses are unimportant, are typically $\gamma_{\mathrm{min}} \sim 10^2$, but may reach values of $1 - 10^4$. Values of 10^2 for the minimum energy cut-off are also supported by, for example, Barai and Wiita (2006) and Meli and Mastichiadis (2008). Since there is a large discrepancy, especially in the estimations of the Lorentz factors, the possible effects of these different assumptions on the simulated radio source populations are investigated in §3.10.4.

To find the radio spectral index α, a measure of the dependence of the source's flux density on the frequency, one needs at least two data points, that is two radio lobe luminosity densities of the same source measured at two different frequencies. A simple power-law is employed between $L_{\nu_{178}}$ and $L_{\nu_{\mathrm{x}}}$ to find α, which is finally used to correct the $L_{\nu_{178}}$ (see also Appendix E); the radio lobe luminosity density estimated with the model, $L_{\nu_{178}}$, is in the source rest-frame and one needs to convert it to the common frequency using $(1+z)^{\alpha}$. For consistency and to mimic behaviour of the 3CRR sample $\nu_{\mathrm{x}} = 750$ MHz is chosen (after Kaiser and Alexander, 1999). Note that BRW99, Jarvis and Rawlings (2000) and Jarvis *et al.* (2001) argue that this most commonly used relation (i.e. simple power-law) may be too simplistic, and instead, curved radio spectra should be considered. On the other hand, Bornancini *et al.* (2010) report that the radio spectrum of their sample is consistent with a single power law between 74 and 4850 MHz. See also §3.2 for more discussion on this

issue and a few examples.

2.3.5 Aspect ratio and self-similarity

One of the consequences of the KA97 dynamical model of the source expansion is its self-similar growth. Instead of measuring or introducing the jet opening angle, the aspect ratio ($R_{\rm T}$) is used. The aspect ratio is the ratio of a source length to its width. In the KA97 model $R_{\rm T}$ is linked to the jet opening angle ($\theta_{\rm jet}$) through $R_{\rm T} \propto 1/\theta_{\rm jet}$ based on the assumption that the radio lobe pressure is balanced by the external gas ram pressure. $R_{\rm T}$ stays constant through the source lifetime. The BRW99 model, on the other hand, assumes that $R_{\rm T}$ increases with the source growth, and their results suggest some dependence on the source kinetic luminosity and/or its age, while Machalski *et al.* (2004a,b) suggest that the self-similarity may not hold for old sources.

Mullin *et al.* (2008) present a detailed investigation of aspect ratios of 3C sources of $z < 1.0$. The observed $R_{\rm T}$ values are found to fall in a range of $1 < R_{\rm T} < 8$, with a median within $\langle R_{\rm T} \rangle \in 1.6 - 2.6$ (which depends on spectral class). Mullin et al. (2008) report that higher aspect ratios seem to occur for larger sources (> 100 kpc) which may suggest a non self-similar source growth, or a self-similar growth occurring only in the early stages of a source life. However, the aspect ratio has a predominant influence on the radio source linear size (hence its age). In particular, the smaller the aspect ratio gets, the wider the opening angle of the jet becomes, and thus a higher pressure of the radio lobe is needed to account for the faster sideways expansion of the lobe. This in turn will lead to smaller head advance speeds of the jet, as well as larger synchrotron losses, and will result in smaller linear sizes as compared to the sources with larger $R_{\rm T}$. This may be one of the reasons why larger sources seem to have larger aspect ratios. Similarly, BRW99 suggested that the aspect ratio might be higher for more powerful sources. However, one must notice that for a given age and environment of a radio source higher kinetic energy will lead to larger linear size, and, according to our argument above, larger aspect ratios may be expected.

Since the distribution of $R_{\rm T}$ is not yet well constrained; I decided to assume a uniform distribution of the aspect ratio with $8.0 > R_{\rm T} > 1.3$, which translates to the range of jet opening angles of $13.7^\circ < \theta_{\rm jet} < 63^\circ$ (values based on Leahy and Williams 1984; Daly 1995; Machalski *et al.* 2004a; Mullin *et al.* 2008), and to follow the original KDA97 model which implies self-similar growth of a radio source. A distribution of aspect ratios allows for a variation in growing rates of radio sources and hence is more realistic than a single value. In the application of the model in this study, the aspect ratio is used as the 'true' one which describes radio source real geometry (that is geometry unaffected by the projection effects). The projection angle correction is applied to the found linear size of the radio source, and not the aspect ratio (consult §2.3.9). For this reason, one must bear in mind that the ranges of the resulting final aspect ratios (that is affected by the projection effects) will differ slightly from the quoted here values.

2.3.6 Jet particle content

The ratio (k') of the energy densities of thermal particles to the energy densities of the electrons at the time they are injected into the cocoon is initially assumed to be $k' = 0$. Important to note is that this definition of k' differs slightly from typical assumptions (k) in such a way that relativistic and non-relativistic electrons are already included even if $k' = 0$ (this already implies that the typically assumed ratio is $k \neq 0$).

There is much debate on the particle content of the radio galaxy jets. Some argue that the FR II jets are lightweight (electron-positron dominated), while FR I jets are heavy, that is they may possess a significant proton content (e.g. Celotti and Fabian, 1993; Wardle *et al.*, 1998; Kino and Takahara, 2004; Dunn and Fabian, 2004; Croston *et al.*, 2005, 2008a). Moreover, Hardcastle and Croston (2010) based on the investigation of Cygnus A report that FR II radio galaxies may be more proton dominated ($k \sim 1-4$) if they reside in very rich environments. KDA97 showed that heavy FR II jets will require significantly higher jet powers to reproduce the same radio luminosity density as the electron-positron dominated jets, hence they concluded that k' must be close to 0. Initially, in my simulations I followed the conservative KDA97 assumption, but the effect of changing k' (to allow a proton content in the jets) on the whole population of simulated sources is investigated in §3.10.5.

2.3.7 Maximum head advance speeds

The head advance speed ($v_{\rm max}$) is the speed with which the jet propagates through the ambient medium. It is dependent on the density and pressure of the ambient medium, and the density and pressure of the outflow. As noted earlier the jet must be over-pressured with relation to its surroundings in order to drill its path through the ambient medium, hence the head advance speed will strongly depend on both density and pressure of the two components.

In the simulations it is at first assumed that $v_{\rm max}$ at the time of observation may not exceed $0.4c$, all sources that surpass this limit are rejected at the stage of generating the population. Such an upper limit is consistent with the speeds inferred from the synchrotron spectral ageing of high luminosity double radio sources (e.g. Liu *et al.*, 1992; Best *et al.*, 1995), and supported by the estimation of dynamical ages of FR II sources by Machalski *et al.* (2007) who report $v_{\rm max} \leq 0.3c$. However, there have been discussions on the possible overestimation of the lobe advance speed upper limits; results obtained through the analysis of lobe asymmetries and the steepening of radio spectra suggest that the head advance speeds do not exceed $0.15c$ (e.g. Arshakian and Longair, 2000), or even 0.05c (Scheuer, 1995). The effect of different assumptions of $v_{\rm max}$ on the results is discussed in §3.10.3.

2.3.8 Adiabatic indices of radio lobes, magnetic field, and external medium

After KA97/KDA97, the adiabatic indices of the radio lobes, magnetic fields and the external medium is assumed to be $\Gamma_{\rm l} = \Gamma_{\rm b} = 4/3$ and $\Gamma_{\rm x} = 5/3$ respectively, that is a non-relativistic equation of state for the closest external medium of the radio source, and relativistic particles inside the radio lobes is assumed.

2.3.9 Projection effects

The linear size calculated based on the randomly chosen and set physical parameters of each source in the generated population (see steps 2. and 3. in §2.2, and Appendix E) is the source true size, and is further randomly oriented in the sky as it is observed at some projection angle ϑ. It is assumed that the projection angle is distributed uniformly in $[1-\cos(\vartheta)]$ plane. Therefore, the size becomes $D_{\rm proj} = D_{\rm true}\sin(\vartheta)$. For simplicity I will refer to this projected size as D, and the true size is not considered from now on.

Also, note that Eqn. 2.5 is an approximation and is valid for distances r greater than few core radii. As argued by Alexander (2000, 2006), Eqn. 2.5 for the smallest radio sources should take a form of $\rho_x = \rho$ with $\beta = 0$, which represents a flat atmosphere in which the radio source expands. Hence sources of the projected linear sizes smaller than 10 kpc in the samples, either the simulated or the observed ones, are not considered. Radio sources affected by this limit are the so-called GHz-peaked spectrum (GPS) and compact steep spectrum (CSS) sources (their linear sizes reach $\sim 10-20$ kpc), which are believed to represent the youthful stages of the FR I and FR II populations (e.g. Carvalho, 1985; Mutel and Phillips, 1988; Fanti *et al.*, 1995), and/or are frustrated by their high density environments (e.g. Bicknell *et al.*, 1997; O'Dea, 1998).

2.3.10 Redshift distribution

It is assumed that sources are uniformly distributed in space, between minimum ($V_{\rm min}$) and maximum ($V_{\rm max}$) comoving volume depending on the considered redshift range. From this a radio source redshift (z) is found. Redshifts from $z = 0$ to $z = 2$ in steps of $\Delta z = 0.001$ are considered in this work. The evolution of source number density is not initially modelled in the construction of the simulated population; however a normalisation (scaling), which is a free parameter in each redshift range (step 9. in §2.2, §2.4.1), is applied before the maximum likelihood method and goodness-of-fit test are performed. Hence I obtain an average in radio source number density for each z bin considered.

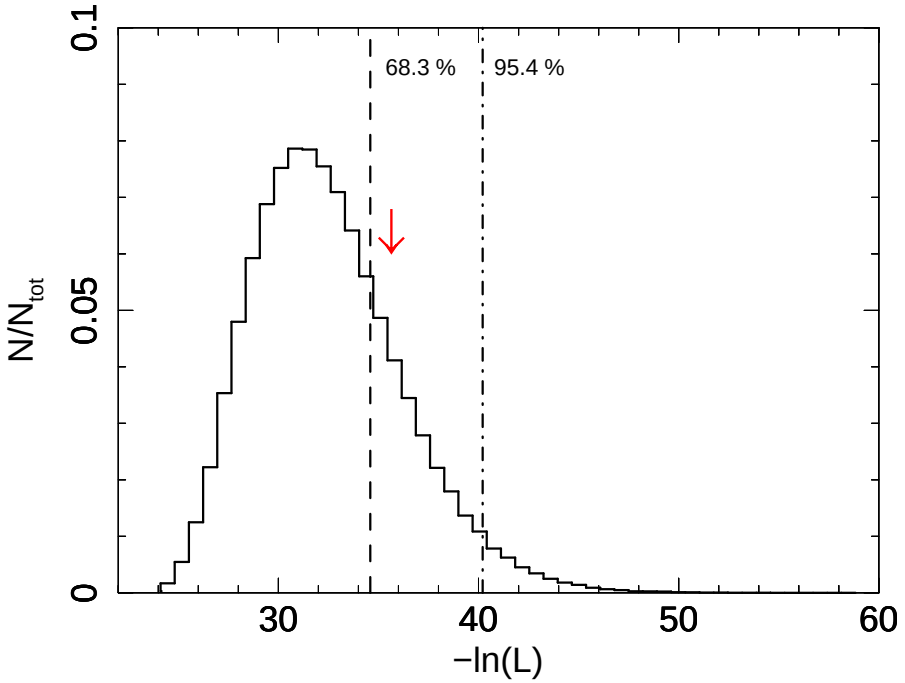

Figure 2.4: The goodness-of-fit test. The synthetic log-likelihood distribution of the 2×10^5 synthetic data sets generated from the model average histogram (consult §2.4 for term explanation). The red arrow indicates the position of the actual data set log-likelihood. The dashed line (black) marks the 68.3 per cent containment (from the minimum value of $-\ln(\mathcal{L})$, note that the distribution is one-sided), and the dot-dashed one (black) the 95.4 per cent containment. The histogram of the synthetic log-likelihood distribution of the lowest redshift data of Model S is shown. The data is consistent with the model at the 90 per cent confidence level ($p-$value = 0.234).

2.4 Confidence intervals and Goodness-of-Fit test

2.4.1 Binned Maximum Likelihood Method

In fitting the simulated to the observed samples, and in following statistical tests, I use the binned maximum likelihood method (MLM; e.g. Cash 1979). A log-likelihood is found in fitting each of the simulated samples to the observed data according to

$$\ln\mathcal{L} = \Sigma_{i=1}^{N}\left[x_i \ln\left(\frac{y_i}{n}\right) - \frac{y_i}{n} - \ln(x_i!)\right] \tag{2.23}$$

where N is the number of bins, each with an expected number of sources y_i and with the observed number of counts x_i, and n is the normalisation constant discussed in step 9. in §2.2. For the mathematical derivation of this equation and fundamentals of the maximum likelihood estimators the reader is referred to Appendix D.

2.4.2 Goodness-of-Fit

To perform the goodness-of-fit (GoF) test the Monte Carlo analysis is used. The final histogram of the simulated radio sources is in fact the mean of all possible realisations of the underlying 'true' population, which I refer to as the 'model average histogram'. The Monte Carlo procedure undertaken here is to randomise each bin of the model average histogram within the Poisson regime to obtain a 'synthetic data set', a single realisation of the 'true population'. Further, I apply the binned MLM method to find the log-likelihood between the newly created synthetic data set and the model average histogram. The procedure is repeated multiple times ($\sim 2\times10^5$) to obtain a distribution of the possible log-likelihoods of the true population, which I refer to as the 'synthetic log-likelihood distribution'. Finally, the log-likelihood of the observed data histogram is compared to the generated synthetic log-likelihood distribution. The 1σ level of consistency requires the actual data set log-likelihood to be placed within the 68.3 percentile of the log-likelihood distribution, i.e. between 0 and 68.3 per cent since the distribution is one-sided (Figure 2.4). The GoF test results are quoted in terms of $p-$value, which is the probability that the test statistic is at least as extreme as the one observed and assuming the null hypothesis is true. 1σ is equal to 0.317 in terms of $p-$value. The null hypothesis is rejected if the $p-$value is less than the significance level $\alpha_{\rm sig}$; a conservative value of $\alpha_{\rm sig}=0.1=10$ per cent is adopted. The choice of the number of synthetic histograms allows me to check the agreement up to 4σ level ($p-{\rm value}=2.3\times10^{-4}$). It is important to remember that the confidence levels obtained in such a way are nominal only as the synthetic log-likelihood distribution is not Gaussian here.

Although this technique tests whether a model fits data well, it is incapable of distinguishing the best-fitting models. To compare these best-fitting models one needs to perform the so-called likelihood ratio test the statistic of which is

$$d_{\rm LR}=-2\,[\,\log(\mathcal{L}(H_{\rm m0}))-\log(\mathcal{L}(H_{\rm m1}))\,] \tag{2.24}$$

and where $\mathcal{L}$ denotes log-likelihood, $H_{\rm m0}$ is the null model and $H_{\rm m1}$ an alternative one. The $p-$value of the $d_{\rm LR}$ statistics may be obtained to find which model should be preferred. However, the models must be nested and if this requirement is not fulfilled, the likelihood ratio test is invalid. For the models $H_{\rm m0}$ and $H_{\rm m1}$ to be nested it is necessary that $H_{\rm m1}$ contains the same parameters as $H_{\rm m0}$, and has at least one additional parameter.

2.4.3 Confidence intervals

The source physical parameters that are the main focus in this study are $t_{\rm max_m}$ (§2.3.3), $\rho_{\rm m}$ (§2.3.2), and $Q_{\rm B}$ and $\alpha_{\rm s}$ (§2.3.1). To obtain the confidence intervals of these parameters grid minimisation searching their broad ranges is performed (Table 3.2 and Table 4.3); I follow the method of Cash (1976). For each parameter set in the searched grid there is a

corresponding log-likelihood. From these, the global $\mathcal{L}_{\max}$ is found, indicating the best fit to the observed data (Eqn.2.23). Furthermore, as pointed out by Cash (1976), one may find the difference between $\mathcal{L}_{\max}$ and $\mathcal{L}$ for all the other sets of parameters in the evaluated grid, the so-called ΔC statistic, which is defined as

$$\Delta C = [-2\ln(\mathcal{L}_{\max}) + 2\ln(\mathcal{L})]. \tag{2.25}$$

$\mathcal{L}$ is the log-likelihood of the sub-grid, which is extracted from the global grid by setting each point of a parameter which we are focused on as non-varying and the corresponding set of log-likelihoods of these points are listed based on the all the other parameters that vary. The ΔC statistic is distributed as χ^2 with $n_{\mathcal{L}_{\max}} - n_{\mathcal{L}}$ degrees of freedom (dof), where $n_{\mathcal{L}_{\max}}$ denotes degrees of freedom associated with the global $\mathcal{L}_{\max}$ and $n_{\mathcal{L}}$ denotes the dof of restricted sub-grid (dof $= 2$ in all presented here plots). The confidence intervals are, therefore, defined such that contours encircle parameters for which their log-likelihood is above a certain value ($\mathcal{L} > \mathcal{L}_0$), and levels of χ^2 distribution may be used. Note that this may lead to disconnected regions in the case the likelihood function is highly irregular. For an in-depth description of constructing contour plots in cases such as this one the reader is referred to Lampton *et al.* (1976) and Cash (1979).

2.5 Markov chain Monte Carlo methods and the use of Bayesian evidence for model selection

Markov chain Monte Carlo. As it will be evident in Chapter 3, the likelihood distribution of the parameters being estimated here is highly irregular. In such cases, the well known optimisation techniques in function minimisation (maximisation), such as downhill simplex method (often referred to as amoeba method, e.g. Press *et al.* 1992) may fail by converging to non-stationary points (that is local minima/maxima). However, although not used here, a special class of Monte Carlo methods exists based on the so-called Markov chains, which may bring solution to such cases, especially regarding highly dimensional parameter spaces. Markov chains are mathematical systems in which a transition from one state to another occurs independently from the past sequence of the transitions. The Markov chain Monte Carlo (MCMC) methods require probability distributions of the searched parameters which are sampled instead of performing multi-dimensional grid minimisation on the full parameter set. In this sense the MCMC methods sample the *posterior* probability distribution of the searched parameters; in Bayesian statistics the posterior is the probability distribution assigned after the relevant evidence is obtained (see below). The specific MCMC algorithms search for regions of high probability of the parameter space avoiding low probability regions and thus being significantly faster than a standard grid search. The well known algorithms include Metropolis-Hastings algorithm, Gibbs sampling or slice sampling among others. The reader is referred to e.g. Neal (1993), MacKay (2003) and

Heavens (2009) for detailed discussions on the subject.

Bayesian evidence. One of the important questions one would like to answer concerns model selection. That is, ideally one would like to know which of the tested models, given the data, is preferred. In the frequentists approach, which I have been following in this work, the likelihood ratio test (§2.4.2) is the method which can be used to distinguish between the best-fitting models which are being tested. However, the requirement for the models to be nested is a great limitation of this method. One way around this is to use the Bayesian approach. In the mathematical formalism of Bayes' theorem the posterior probability for the searched parameter, $P_{\rm prob}(\theta|{\rm data})$, is given by

$$P_{\rm prob}(\theta|{\rm data}) = \frac{P_{\rm prob}({\rm data}|\theta)P_{\rm prob}(\theta)}{P_{\rm prob}({\rm data})}, \tag{2.26}$$

where θ is the adopted model (set of parameters to be estimated), $P_{\rm prob}({\rm data}|\theta)$ is the likelihood, $P_{\rm prob}(\theta)$ is the *prior* probability function, that is one's prior knowledge or belief about the parameters which are to be estimated, and $P_{\rm prob}({\rm data})$ is the Bayesian evidence. In the discrete case the Bayesian evidence is expressed as

$$P_{\rm prob}({\rm data}) = \sum_{i}^{k} P_{\rm prob}({\rm data}|\theta_i)P_{\rm prob}(\theta_i), \tag{2.27}$$

and one can use this to distinguish between models via the so-called Bayes factor. For two different models $H_{\rm m1}$ and $H_{\rm m2}$, which do need *not* to be nested and which are parametrised by parameter sets $\theta_{\rm m1} = (\theta_1, ..., \theta_k)$ and $\theta_{\rm m2} = (\theta_1, ..., \theta_n)$ respectively, the Bayes factor is defined as

$$K_{\rm stat} = \frac{P_{\rm prob}({\rm data}|H_{\rm m1})}{P_{\rm prob}({\rm data}|H_{\rm m2})} = \frac{\sum_i^k P_{\rm prob}({\rm data}|\theta_i, H_{\rm m1})P_{\rm prob}(\theta_i|H_{\rm m1})}{\sum_j^n P_{\rm prob}({\rm data}|\theta_j, H_{\rm m2})P_{\rm prob}(\theta_j|H_{\rm m2})}. \tag{2.28}$$

The higher the value of $K_{\rm stat}$ the stronger support for model $H_{\rm m1}$ develops. Consult e.g. Heavens (2009) and Feigelson and Jogesh Babu (2012) for more discussion on the subject. One must bear in mind, however, that, as phrased by Feigelson and Jogesh Babu (2012), while regarding Bayesian interference if '*the priors are not correct, the estimation process can lead to false conclusions*'.

My future plans on the simulation optimisation through expanding my current work into sketched here methods is further discussed in Chapter 7.

2.6 Summary

In the chapter I briefly discuss the fundamentals of the relativistic jets, and in particular I discuss one of the semi-analytical models of FR II radio galaxy time evolution developed by Kaiser and Alexander (1997) and Kaiser *et al.* (1997). Further, I describe the newly developed algorithm of multidimensional Monte Carlo simulation through which the fundamental parameters of radio galaxy populations can be explored. Unlike previous studies, the method compares radio luminosity functions found with both the observed and simulated data to explore the best-fitting sources' parameters. The method incorporates the maximum likelihood estimator to find the best-fitting parameters, and may be applied to small data sets (within Poisson regime). For further analysis the method for generating the confidence intervals of the estimated fundamental parameters, as developed by Cash (1979), is presented. The semi-analytical model's assumptions, such as the particle content of the relativistic jets or the particle energy distributions, as well as assumptions for the multidimensional Monte Carlo simulation, e.g. the distribution of kinetic luminosities or radio source lifetimes allowed, are extensively discussed.

The method presented in this chapter is applied to the observational data, flux-limited samples of radio galaxies and radio-loud quasars, and the analyses of the following best-fitting parameters are presented and discussed in Chapter 3 and Chapter 4.

Research is what I'm doing when I don't know what I'm doing.

WERNHER VON BRAUN (1912 – 1977)

3

Redshift Evolution of Powerful FR II Radio Galaxies and Radio-Loud Quasars

---

In the following chapter I present and discuss in detail the results on the fundamental properties of the most powerful FR II radio galaxies and radio-loud quasars and their evolution across cosmological epochs. The study is done through the application of the multidimensional Monte Carlo method presented in Chapter 2. I also discuss the possible influence some assumptions set in the semi-analytical models of radio source growth may have on the results. The content of this chapter has been submitted to the Monthly Notices of the Royal Astronomical Society (A.D. Kapińska, P. Uttley & C.R. Kaiser, 'Fundamental properties of Fanaroff-Riley II radio galaxies investigated via Monte Carlo simulations', MNRAS, submitted).

3.1 Objectives

I present and discuss results on the fundamental properties of the most powerful FR II radio galaxies and radio-loud quasars and their evolution across cosmological epochs. Some of the best known and most secure samples of radio galaxies and radio-loud quasars are considered here; these are one of the most powerful FR II radio sources and they extend to high redshifts. The study is done through the application of the newly developed multidimensional Monte Carlo method presented in Chapter 2. The use of such a secure, but of high flux limit, radio sample has both advantages and disadvantages. Firstly, since the sample has been used in many population studies it may provide a test for the newly developed method. Also, given that our analysis provides a significant improvement in exploring the fundamental properties of these extragalactic radio sources (cf. Chapter 1: §1.5) it may present our comprehension of these radio sources as well as the theoretical models used to model them in a new light. If a radio sample is very well known and thoroughly inspected it can be used as a secure representation of the whole source (sub)population. However, high flux limits mean that only the most powerful radio sources, especially at higher redshift, are included. This may limit what one can deduce from the results. Throughout this chapter I will highlight when this is the case. In addition, to complement this study, radio sample of lower flux limit is also investigated; this part of the study is presented in the next chapter (Chapter 4).

3.2 Observational data sets

Complete flux-limited radio samples which contain all extragalactic radio sources in a given sky area and above the sensitivity limit specified for each survey are used in this study. Currently, I concentrate only on sources of the FR II morphology due to the availability of semi-analytical models of their time evolution; however, the approach presented here may be extended to cover the whole radio source population once theoretical models for FR Is are developed. I use both radio galaxies and radio-loud quasars as it is assumed, following the unification models, that the only difference between these types of sources is their inclination angle (e.g. Barthel, 1989). Additionally, due to the sparse population of sources at high redshifts, and hence poor representation, I decided to limit the analysis to sources with redshifts up to $z = 2$. Due to the nature of the theoretical models that assume that most of the radio luminosity density comes from the radio lobes of the sources, one should use samples observed at low radio frequencies ($\sim$ few $\times$ 100 MHz) to avoid core radio emission that dominates at GHz frequencies. There are few commonly used low-frequency radio catalogues. Here, I present the work done with two such radio samples, namely the well known Third Cambridge Revised Revised Catalogue (Laing *et al.*, 1983, 3CRR), and the complete radio sample of Best *et al.* (1999, hereafter BRL).

The 3CRR radio sample is very shallow (its flux limit equals 10.9 Jy defined at 178 MHz),

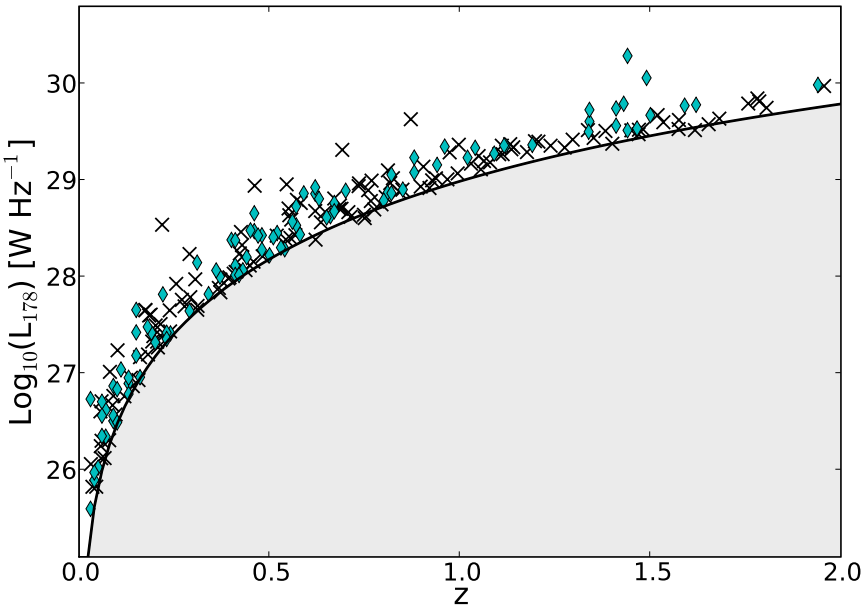

Figure 3.1: Radio lobe luminosity density vs redshift plane for the 3CRR (crosses) and BRL (diamonds) samples used in this work (sources of FR II morphology with flux densities above the limit $S = 10.9$ Jy at 178 MHz (solid line) and with $z < 2.0$ are shown). The shaded area shows the part of luminosity-redshift plane that is inaccessible due to the flux limit.

but covers a large area of the sky (4.23 sr); it contains some of the most powerful radio galaxies. To ensure the 3CRR catalogue of extragalactic radio sources to be as complete as possible, the 3CRR sample was based on the measurements from three catalogues (all composed at the observing frequency 178 MHz), namely the 3CR catalogue, the Fourth Cambridge catalogue (hereafter 4C, Pilkington and Scott, 1965; Gower *et al.*, 1967), and the pencil-beam survey catalogue (hereafter 4CT, Caswell and Crowther, 1969). 3CR, 4C and 4CT catalogue measurements were used for sources of linear sizes smaller than 10 arcmin. The beam size of the 3CR catalogue observations was approximately $13.6' \times 4.6^{\circ}$, of the 4C catalogue observations was $15' \times 5^{\circ}$, and $23' \times 23'$ of the 4CT catalogue observations. Further, the measurements of these three catalogues were supplemented by a separate observations of radio sources of large angular sizes, i.e. > 10 arcmin. For more details see Laing *et al.* (1983) and references therein. Total of 146 sources of FR II morphology are in the sample; however, 3C 231 (M82) is excluded in this study, as well as, following (Blundell *et al.*, 1999, hereafter BRW99), two additional sources, 3C 345 and 3C 454.5 (due to the Doppler boosting). Of the remaining sources 23 are of FR I type, and all are found at very low redshifts, not exceeding $z \approx 0.25$.

The BRL sample is defined at an observing frequency of 408 MHz with flux limit of

Table 3.1: Demography of the observational data from the 3CRR and BRL radio samples. Quoted numbers of sources valid after certain criteria are met ($S_{178MHz} > 10.9$ Jy, $D > 10$ kpc). FR I type sources are listed for reference only (for details see §3.2).

Redshift range (z)	No. of sources 3CRR FR I	3CRR FR II	BRL FR I	BRL FR II
$z_1 \in [0.0, 0.3]$	23	40	7	31
$z_2 \in (0.3, 0.8]$		45		35
$z_3 \in (0.8, 2.0]$		50		26

5 Jy. The sample has been created to complement other radio samples, and with the 3CRR catalogue it provides a coverage of the entire sky above -30° in declination. Its flux limit translates to ~ 9.7 Jy at 178 MHz assuming a typical radio spectral index $\alpha = 0.8$ and where the relation between the flux density of a source (S_ν) at a frequency ν, and its radio spectral index α, is defined as

$$S_\nu \propto \nu^{-\alpha}. \tag{3.1}$$

The sample is constructed based on the Molonglo Reference Catalogue (Large *et al.*, 1981). The beam size of the Molonglo telescope observations is in a range from $2.63' \times 2.87'$ arcmin for $\delta = -30^\circ$ to $2.63' \times 4.87'$ arcmin for $\delta = 18.5^\circ$. The BRL sample is 100 per cent spectroscopically complete (Best *et al.*, 2000, 2003). In total the BRL sample contains 178 sources of which 124 are of FR II morphology.

The two samples are analysed together and both are brought to the common observed frequency of 178 MHz. In the case of both samples the measured radio spectral index of each source is used. The spectral indices of the sources contained in the 3CRR sample is measured between 178 and 750 MHz, while in the BRL sample between 408 MHz and 1.4 GHz; the latter is extrapolated to 178 MHz based on the radio spectral index α_{408}^{1400}. It has been shown before that radio spectra of FR IIs may show curvature, where spectra steepening are observed at both very low and high radio frequencies (e.g. Laing and Peacock, 1980; Carilli *et al.*, 1991; Eilek and Arendt, 1996, among others). If the steepening is significant between the frequencies which I use here for spectral index estimation, the extrapolated flux densities of the BRL sample may be over or under estimated (depending on which frequency end the steepening is more severe). Carilli *et al.* (1991) report that for the most powerful FR IIs the steepening of the spectra may occur already at frequencies below 1 GHz; for Cygnus A they find that steepening occurs already at 750 MHz. However,

Cygnus A may be a somewhat special case. Laing and Peacock (1980) measured spectral curvature of a sample of FR IIs between 10 MHz−14.9 GHz, and they report that at the intermediate frequencies they considered, between 750 MHz and 5 GHz, a simple power-law relation holds, while the curvature of the spectra occurs at frequencies $\nu < 200$ MHz and $\nu > 5$ GHz. As pointed out by Blundell *et al.* (1998) the spectral curvature is a common but not universal characteristics; in the two examples shown by these authors 6C $0032+412$ radio source can easily be fitted with a power-law between 100 MHz and 10 GHz, while 6C $0032+412$ requires curved model to be fitted over the same frequency range. One of the issues one needs to consider at this point is what fraction of the BRL sources can be affected by such flux density extrapolation. Gopal-Krishna (1988), for instance, considers a sample of 102 extragalactic sources with flux densities measured at frequency range of 150 MHz−5 GHz, from which 32 (~ 30 per cent) required fitting a second order polynomial to their spectra. Given the above estimation, and the fact that (a) the spectral indices of the BRL radio sources are measured below 5 GHz, and (b) the frequency to which the flux densities of the BRL sources are extrapolated is not at the extreme low radio frequencies where sources may be self-absorbed to a significant degree, I assume that the curvature problem of the spectra is rather minor, but it is not non-existent and may influence the extrapolated flux densities to some degree.

The redshift distribution of all sources included in the analysis is presented in Figure 3.1. Further, the population is divided into size and luminosity density bins in given redshift ranges. Due to the number of available sources from the catalogues only three redshift ranges are considered,

$$z_1 \leq 0.3, \quad 0.3 < z_2 \leq 0.8 \quad \text{and} \quad 0.8 < z_3 \leq 2.0, \tag{3.2}$$

the borders of which are chosen to ensure similar source numbers per redshift bin. Incidentally, these redshift ranges span over similar relative light travel time intervals, i.e.

$$t_{\Delta z_1} = 3.370\,\mathrm{Gyr}, \quad t_{\Delta z_2} = 3.361\,\mathrm{Gyr} \quad \text{and} \quad t_{\Delta z_3} = 3.364\,\mathrm{Gyr}. \tag{3.3}$$

These subgroups of different redshifts are considered separately unless otherwise stated. Sources are grouped in size bins in the following manner:

in z_1 the size ranges are $10-245$ kpc, 245 kpc -1 Mpc and > 1 Mpc,

in z_2 the size ranges are $10-208$ kpc, 208 kpc -1 Mpc and > 1 Mpc, and

in z_3 they are $10-100$ kpc, 100 kpc -1 Mpc and > 1 Mpc.

The size ranges were chosen to contain similar number of sources in the case of the smallest and medium sized sources, while the last bin tracks giant radio galaxies more accurately (giant radio galaxies are defined as sources of total linear sizes of more than 1 Mpc). For each of these size bins a radio lobe luminosity density distribution is constructed. The distribution is constructed at an observing frequency of 178 MHz from $\log_{10}(L_{178MHz}) =$

22.0 to $\log_{10}(L_{178MHz}) = 35.0$ in steps of $\Delta\log_{10}(L_{178MHz}) = 0.5$. Such a division of the population allows one to track the relative number of the sources with a given size, and later to construct radio luminosity functions of the sources at the given redshift ranges and of the given sizes. The counts of sources used are summarised in Table 3.1, and their observed radio luminosity functions are presented in Figure 3.2.

As pointed out by BRW99 the use of only one radio sample in any population study may result in inevitable biases while interpreting results. This is due to the strong luminosity density – redshift ($L-z$) dependence (Fig. 3.1). It is important, therefore, to either include a few radio samples that will supplement each other in the luminosity density – redshift plane, or to be very cautious with interpreting results. For the extensive discussion on this and also frequency related issues the reader is referred to the original BRW99 paper. Commonly used catalogues include 6CE (Eales, 1985) and 7CRS (based on the Seventh Cambridge Redshift Survey Catalogue, McGilchrist *et al.*, 1990; Grimes *et al.*, 2004; Wang and Kaiser, 2008) besides 3CRR (e.g. BRW99, Willott *et al.*, 2001). The BRL sample has also been used along with the other three by Wang and Kaiser (2008). However, here, no attempt is made to reconstruct the previous population studies of the $[P-D-z]$ plane, but rather to analyse binned distributions of the sources, hence the presented work is based on only two samples. Because of considerably different flux limits of various samples other ones such as 7CRS will be analysed separately to 3CRR and BRL.

3.3 Radio Luminosity functions and fitted data counts

To obtain the confidence intervals of the fundamental parameters which are the main focus of this study, that is the maximum radio source lifetime $t_{\mathrm{max_m}}$, the central density in which the radio source expands ρ_{m}, and the kinetic luminosity break Q_{B} and the slope α_{s} which define the initial distribution of the kinetic luminosities, a grid minimisation was performed. The ranges of the parameters searched are given in Table 3.2. The semi-analytical models of the radio source growth, the Monte Carlo simulations, and the statistical methods used, are described in Chapter 2 of this thesis.

The best-fitting model histograms are presented in Figure 3.3 – Figure 3.5. The corresponding RLFs are shown in Figure 3.6 – Figure 3.8. The quoted uncertainties on the RLFs are the Poissonian errors only. The simulated RLFs appear to be consistent with the observed data. Moreover, it was possible to reconstruct the luminosity density distributions of the observed samples for their given linear size sub-samples as well as for the redshift ranges. The match in the linear size distribution is of particular interest, as it has been noted previously that not all previous work succeeded in reconstructing the linear size distributions and often too many large sources have been created (cf. Barai and Wiita, 2006, 2007). It may be possible that such an effect might not be due to the specific models used, but rather is due to restricting the model parameters, which in my case were kept free. I have not tested analytical models other than KA97/KDA97 in this work.

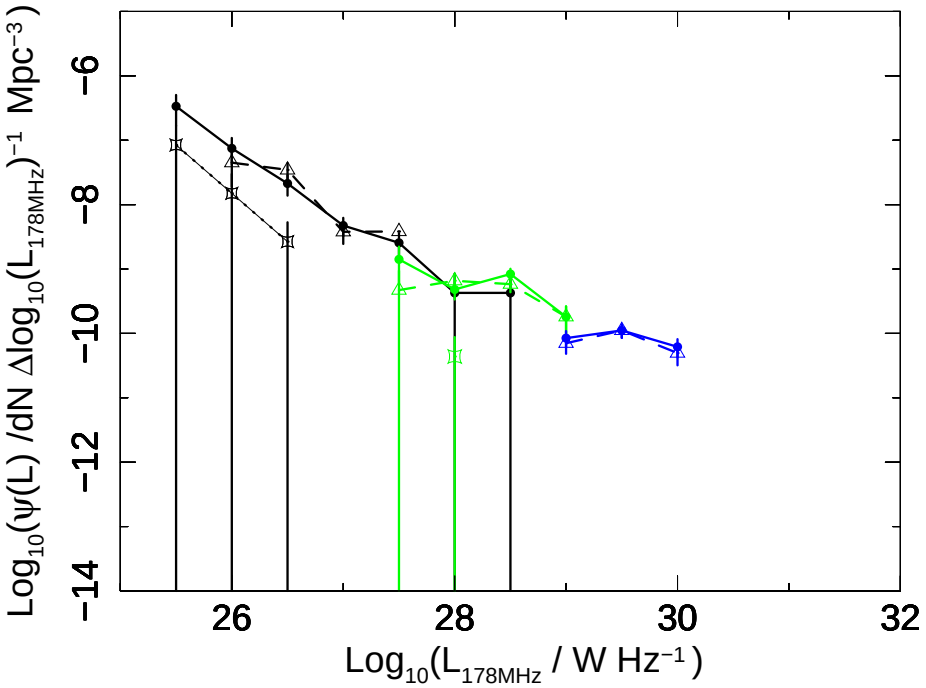

Figure 3.2: The observed radio luminosity functions of the analysed data (3CRR and BRL catalogues) for each of the considered redshift ranges, where z_1 is drawn in black, z_2 in blue, and z_3 in green. Each of the redshift bins is further divided in size bins, where solid lines correspond to smallest sources, dashed to medium size sources, and dotted to giant sources (see §3.2 for the exact values).

3.4 Evidence for the cosmological evolution of the intrinsic and extrinsic source parameters

In the simplest case that has been tested, it was assumed that the parameters which are the main focus (that is $t_{\mathrm{max_m}}, \rho_{\mathrm{m}}, Q_{\mathrm{B}}$ and α_{s}, see §2.3) do not evolve with redshift within each redshift bin. The redshift ranges are analysed independently, hence separate sets of best-fitting parameters for each redshift bin are found; if there is no redshift evolution of the intrinsic and extrinsic parameters, the results for each redshift range should not be significantly different. These are referred to as the independent-redshift fits and are presented in §3.4.1. Subsequently, the strength of the cosmological evolution of the source physical parameters has been investigated by allowing for continuous redshift evolution of $t_{\mathrm{max_m}}, \rho_{\mathrm{m}}$ and Q_{B} within each redshift bin, and fitting all the redshift bins simultaneously using the same parameters to describe the evolution. This latter case is referred to as the combined-redshift fits, and the results are presented in §3.4.2.

Table 3.2: Searched ranges and steps of the distribution parameters in the grid minimisation.

Parameter	Model	Searched range	Step	Unit
		INDEPENDENT-z		
$Q_{\rm B}$	S	$[\ 36.90,\ 44.10]$	0.15	$\log_{10}$(W)
$\alpha_{\rm s}$	S	$[-13.00,\ 1.70]$	0.1	
$Q_{\rm B}$	W	$[\ 35.60,\ 42.00]$	0.15	$\log_{10}$(W)
$\alpha_{\rm s}$	W	$[\ -0.45,\ 9.50]$	0.15	
ρ_o	S, W	$(-26.00, -16.80]$	0.2	$\log_{10}(\mathrm{kg\,m^{-3}})$
$t_{\rm max}$	S, W	$[\ 5.18,\ 10.00]$	0.15	$\log_{10}$(yr)
		COMBINED-z		
$Q_{\rm B}(z=0)$	S	$[\ 35.00,\ 40.70]$	0.3	$\log_{10}$(W)
$\alpha_{\rm s}$	S	$[\ -1.20,\ 1.60]$	0.2	
$Q_{\rm B}(z=0)$	W	$[\ 34.70,\ 39.50]$	0.3	$\log_{10}$(W)
$\alpha_{\rm s}$	W	$[\ 0.00,\ 4.00]$	0.2	
$n_{\rm q}$	S, W	$[\ 0.00,\ 12.00]$	0.5	
$\rho_o(z=0)$	S, W	$(-26.00, -19.40]$	0.3	$\log_{10}(\mathrm{kg\,m^{-3}})$
$n_{\rm r}$	S, W	$[\ 0.00,\ 12.00]$	0.5	
$t_{\rm max}(z=0)$	S, W	$[\ 6.58,\ 9.58]$	0.3	$\log_{10}$(yr)
$n_{\rm t}$	S, W	$[\ 0.50,\ -5.00]$	0.5	

3.4.1 Independent-z fits

The confidence intervals of the best-fitting parameters for the simple Model S in the respective redshift bins are shown in Figure 3.9 – Figure 3.12, and similarly for the Model W in Figure 3.13 – Figure 3.16. The best fits and the GoF test results are listed in Table 3.3, although it is once again stressed that the best-fitting parameters maximise the likelihood but are not the standard means of their respective distributions and the inspection of the associated confidence intervals is very important.

The following can be deduced from the results regarding both model S and model W (consult Figures 3.9 – 3.12):

(i) A very strong degeneracy occurs for $t_{\rm max_m}$ and $\rho_{\rm m}$, where for short lifetimes (10^7 yr) low gas density environments ($\sim 10^{-25}$ kg m^{-3}) are estimated, while for longest radio

sources' lifetimes (10^9 yr) very dense environments ($\sim 10^{-20}$ kg m^{-3}) are preferred.

(ii) Degeneracy occurs also between $Q_{\rm B}$ and $\rho_{\rm m}$, and between $Q_{\rm B}$ and $t_{\rm max_m}$. For higher kinetic luminosity breaks lower gas densities of sources' environments are preferred and the estimated sources' lifetimes are relatively short. For lowest $Q_{\rm B}$ dense sources' environments and long lifetimes are favoured.

(iii) The $\alpha_{\rm s}$ parameter is well defined at redshifts $z < 0.3$, but becomes highly uncertain at redshifts $z > 0.3$.

(iv) The confidence intervals span approximately $2-3$ orders of magnitude in kinetic luminosity break, $2-2.5$ orders of magnitude in the estimated maximum lifetimes of sources, and $5-6$ orders of magnitude in the possible gas density of the environments. This issue is further discussed below.

(v) The confidence intervals of joint probability between $Q_{\rm B}-\rho_{\rm m}$, $Q_{\rm B}-t_{\rm max_m}$ and $Q_{\rm B}-\alpha_{\rm s}$ shift towards higher $Q_{\rm B}$, denser $\rho_{\rm m}$, and shorter lifetimes with increasing redshift. However, one must be careful while considering this shift as an evidence for cosmological evolution of the investigated parameters as those intervals overlap. Interestingly, joint confidence intervals of $t_{\rm max_m}-\rho_{\rm m}$ for different redshift ranges do not overlap. This issue is discussed in detail below.

The confidence intervals span a wide range of the possible values for each of the parameters resulting in relatively large uncertainty in the best fit. One must bear in mind that these confidence intervals are based on the underlying five degrees of freedom allowed in the simulation, and any visible degeneracy or shift may be influenced by a change of other parameters. Indeed, some degeneracies are seen, especially strong in the case of the maximum source age and the corresponding central density, although the degeneracies seem to be also present for the $Q_{\rm B}-t_{\rm max_m}$ and $Q_{\rm B}-\rho_{\rm m}$ results. The degeneracy issue is discussed separately in §3.5.

The confidence intervals do not converge for the high kinetic luminosity break values ($> 10^{42}$ W) in the case of Model S, and for the low kinetic luminosity breaks ($< 10^{37}$ W) in the case of Model W. It is accompanied by negative slopes of approximately $0.5-1.5$ in both cases. At this stage the function becomes a power-law. Despite the fact that the kinetic luminosity break indicates values of $> 10^{42}$ W, the number density of jets with kinetic luminosities close to this break is so low that the actual $Q_{\rm max}$ contributing to the simulated population is $\sim 10^{41}$ W. Similarly, in the Model W the kinetic luminosity break shifts to very low values and only the high kinetic luminosity end of the distribution, which at this point is approximated by a power-law, contributes to the observed data counts. In previous studies, authors have assumed such power-law distributions. Assuming that

$$\psi(Q)\mathrm{d}Q = Q^{-x}\mathrm{d}Q, \tag{3.4}$$

slopes of $x = 2.6$ (BRW99), $x = 3.3$ and $x = 3.6$ (Barai and Wiita, 2006), $x = 1.6$ (Kaiser and Best, 2007), and $x \sim 0.9 - 1.3$ (Wang and Kaiser, 2008) have been found. Here, slopes of $x \sim 0.5 - 1.5$ (Model S and W) in the power-law extremum can be observed. It can be concluded here, therefore, that the hypothesis that kinetic luminosities follow an unbroken power-law distribution cannot be ruled out at a confidence level of more than 95.4 per cent.

To ease the investigation of the possible cosmological evolution of all the searched parameters Figure 3.12 and Figure 3.16 show super-imposed 90 per cent intervals of all redshifts. It is found that the kinetic luminosity break shifts to higher values for higher redshift ranges in the case of both Model S and Model W. Furthermore, both Figure 3.12 and Figure 3.16 clearly show that there is no common solution found for the maximum source age and the central density for all three redshift ranges. Consequently, the hypothesis that there is no evolution of $t_{\mathrm{max_m}}$ and ρ_{m} is ruled out with probability of > 99 per cent. One may notice, however, that it is possible to find Q_{B} to be constant for all redshifts (Model S only), but this would imply unrealistically strong evolution of ρ_{m}. To avoid such a strong evolution more than one parameter would have to undergo an evolution with redshift. As an additional test, I have attempted to fit the three redshift bins simultaneously with one set of parameters that would be valid for all redshift sub-samples. No satisfying results have been found for the latter test case, the consistency of the hypothesis with the data was ruled out at the nominal 5σ level.

3.4.2 Combined-z fits

It has been attempted to investigate the strength of the cosmological evolution of the intrinsic and extrinsic source parameters. The results of the independent-z fit suggest evolution of more than one parameter, and bearing in mind the possible degeneracies (see discussion in §3.5), it was attempted to restrict as few parameters as possible. A simultaneous evolution of the following parameters has been allowed: (i) the kinetic luminosity break was allowed to evolve with redshift as $Q_{\mathrm{B}}(z) = Q_{\mathrm{B}}(z=0)(1+z)^{n_{\mathrm{q}}}$, (ii) the central density of the environment as $\rho_{\mathrm{m}}(z) = \rho_{\mathrm{m}}(z=0)(1+z)^{n_{\mathrm{r}}}$, and (iii) the maximum age of the sources was assumed to undergo evolution according to $t_{\mathrm{max_m}}(z) = t_{\mathrm{max_m}}(z=0)(1+z)^{n_{\mathrm{t}}}$. However, due to limited computing time and power, I was forced to compromise on the resolution of the grid of the parameters searched over. For instance, the $n_{\mathrm{q}}, n_{\mathrm{r}}$ and n_{t} exponents were searched in steps of 0.5 only, and $Q_{\mathrm{B}}, \rho_{\mathrm{m}}$ and $t_{\mathrm{max_m}}$ in steps of 0.3 in a logarithmic scale.

The results are displayed in Figure 3.17 (Model S) and Figure 3.18 (Model W). The best agreement between the simulated populations and the observed samples is listed in Table 3.3.

[*Continued on page 90.*]

Table 3.3: The best-fitting parameters for the all tested cases of Model S and W for each redshift range. Due to occurring degeneracies (§5.3) one should always consult the corresponding confidence intervals (see Figure 6 – Figure 13). The following standard deviations of $\log_{10}(\rho_{\rm m})$ and $\log_{10}(\mathrm{t}_{\mathrm{max}_{\rm m}})$ log-normal distributions are used: $\log_{10}(\sigma_{\rho_{\rm o}}) = 0.15$ and $\log_{10}(\sigma_{\mathrm{t}_{\mathrm{max}}}) = 0.05$. 90 per cent uncertainties are quoted.

Model	z	$\log_{10}(Q_{\rm B}/{\rm W})$	$n_{\rm q}$	$\alpha_{\rm s}$	$\log_{10}(\rho_{\rm m}/{\rm kg\,m^{-3}})$	$n_{\rm r}$	$\log_{10}(t_{\mathrm{max}_{\rm m}}/{\rm yr})$	$n_{\rm t}$	$p-$value
Model S	z_1	$39.15^{+0.30}_{-0.30}$	–	$0.6^{+0.3}_{-0.6}$	$-23.4^{+0.6}_{-0.4}$	–	$7.23^{+0.30}_{-0.15}$	–	0.234
independent-z fits	z_2	$39.00^{+0.60}_{-0.45}$	–	$-0.9^{+1.3}_{-7.7}$	$-20.4^{+1.8}_{-2.0}$	–	$7.83^{+0.60}_{-0.75}$	–	0.639
	z_3	$39.90^{+0.60}_{-0.45}$	–	$-1.7^{+1.7}_{-8.3}$	$-20.0^{+2.0}_{-2.8}$	–	$7.13^{+0.60}_{-1.05}$	–	0.925
Model S combined-z fits	all	$38.0^{+(<0.3)\ddagger}_{-0.3}$	$10.5^{+(<0.5)\ddagger}_{-0.5}$	$0.6^{+(<0.2)\ddagger}_{-0.6}$	$-23.0^{+(<0.3)\ddagger}_{-(<0.3)\ddagger}$	$0.0^{+(<0.5)\ddagger}_{-(<0.5)\ddagger}$	$7.8^{+(<0.3)\ddagger}_{-(<0.3)\ddagger}$	$-4.0^{+(<0.5)\ddagger}_{-(<0.5)\ddagger}$	0.380
Model W	z_1	$38.25^{+0.45}_{-0.45}$	–	$1.80^{+0.75}_{-0.60}$	$-23.4^{+0.8}_{-1.0}$	–	$7.23^{+0.45}_{-0.45}$	–	0.251
independent-z fits	z_2	$40.60^{+0.30}_{-0.75}$	–	$7.30^{+5.60\dagger}_{-5.35}$	$-22.6^{+0.8}_{-0.8}$	–	$7.08^{+0.30}_{-0.30}$	–	0.674
	z_3	$41.35^{+0.45}_{-0.9}$	–	$3.50^{+7.40\dagger}_{-3.95\dagger}$	$-23.0^{+2.2}_{-0.4}$	–	$6.08^{+0.75}_{-0.15}$	–	0.885
Model W combined-z fits	all	$38.0^{+(<0.3)\ddagger}_{+(<0.3)\ddagger}$	$5.5^{+(<0.5)\ddagger}_{-0.5}$	$2.4^{+(<0.2)\ddagger}_{-0.6}$	$-24.2^{+(<0.3)\ddagger}_{-0.3}$	$10.5^{+(<0.5)\ddagger}_{-2.5}$	$7.5^{+(<0.3)\ddagger}_{-0.3}$	$-0.5^{+(<0.5)\ddagger}_{-0.5}$	0.557

Notes. The resolution of the results is $\Delta\log_{10}(\rho_{\rm m}) = 0.2$, $\Delta\log_{10}(\mathrm{Q_B}) = 0.15$, $\Delta\log_{10}(\mathrm{t_{max}}) = 0.15$, and $\Delta\alpha_{\rm s} = 0.1$ for the independent-z fits, and $\Delta\alpha_{\rm s} = 0.2$, $\Delta\log_{10}(\rho_{\rm m}) = \Delta\log_{10}(\mathrm{Q_B}) = \log_{10}(\mathrm{t_{max}}) = 0.3$, and $\Delta n_{\rm t} = \Delta n_{\rm r} = \Delta n_{\rm q} = 0.5$ for the combined-z fits.
† For errors which may be extending beyond the searched ranges (see Table 3) value up to the range border is quoted.
‡ If errors are smaller than their respective resolution, the value of $< \Delta$ is quoted.

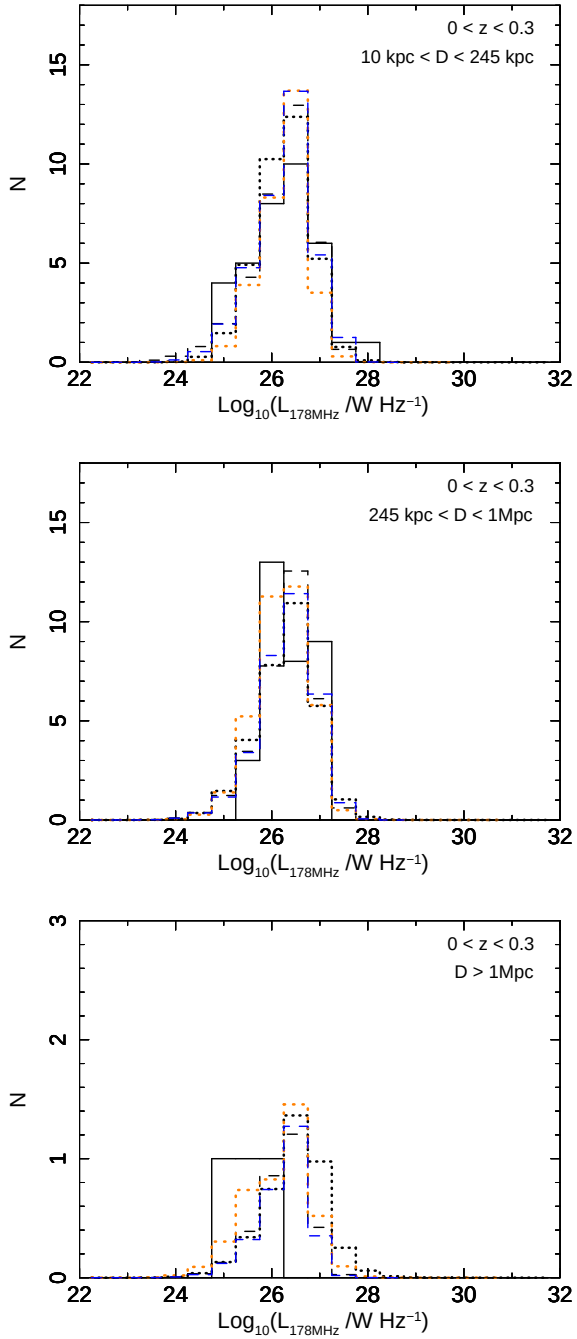

Figure 3.3: Histograms of the observed radio sample (black solid line) and simulated ones created with the best-fitting parameters of the independent-z fits of model S (black dashed line) and model W (black dotted line), and the combined-z fits of model S (blue dashed line) and model W (orange dotted line), in $z_1 < 0.3$. In each redshift range there are three separate size bins as described within the subplots (see also Figure 3.4 and Figure 3.5). Each redshift bin is simulated independently, while the FR IIs linear sizes within each redshift range are simulated simultaneously, that is a good fit to all linear sizes simultaneously at the same redshift is required. The simulated source populations created with the best-fitting parameters are consistent with the data at the 90 per cent confidence level based on the ΔC statistics (for exact $p-$values see Table 3.3).

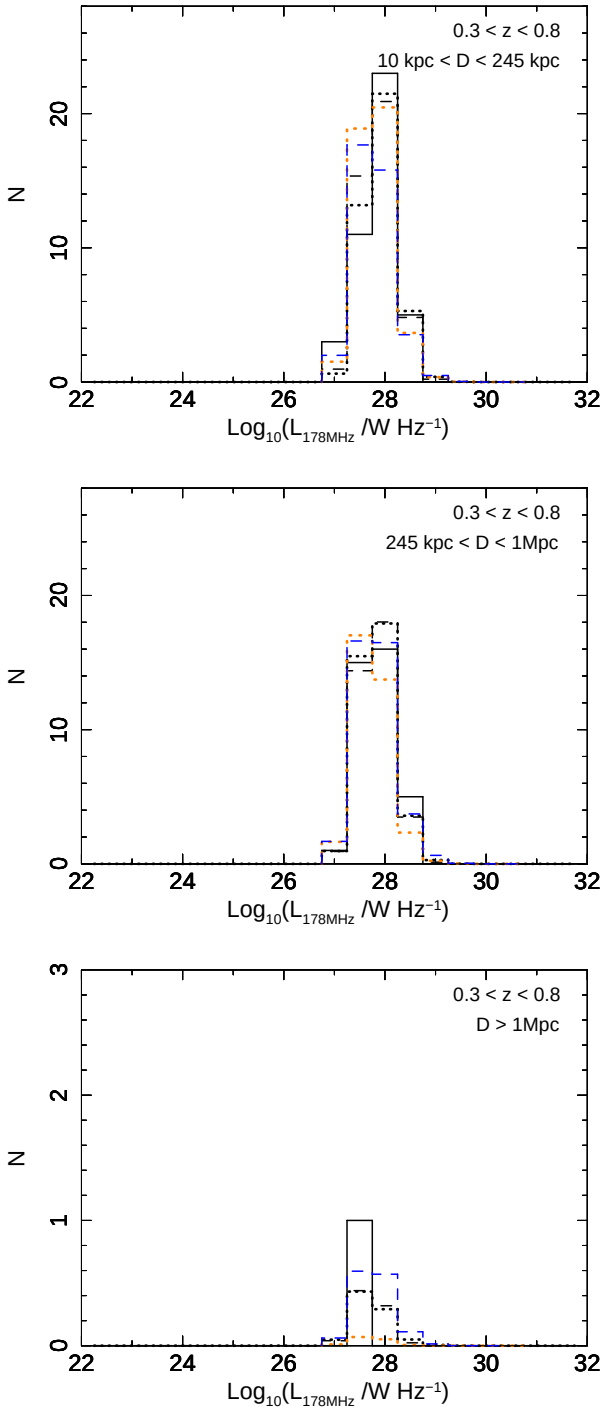

Figure 3.4: Same as Figure 3.3 but for the intermediate redshift range, $0.3 < z_2 < 0.8$.

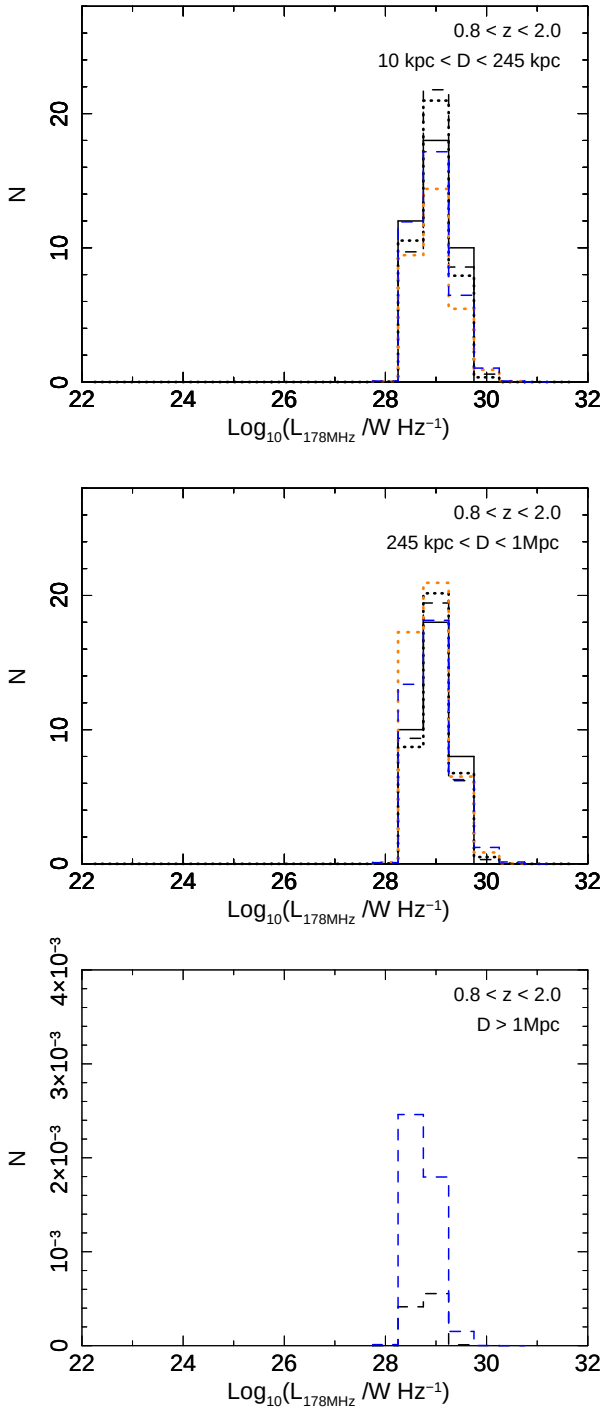

Figure 3.5: Same as Figure 3.3 but for the highest redshift range, $0.8 < z_3 < 2.0$.

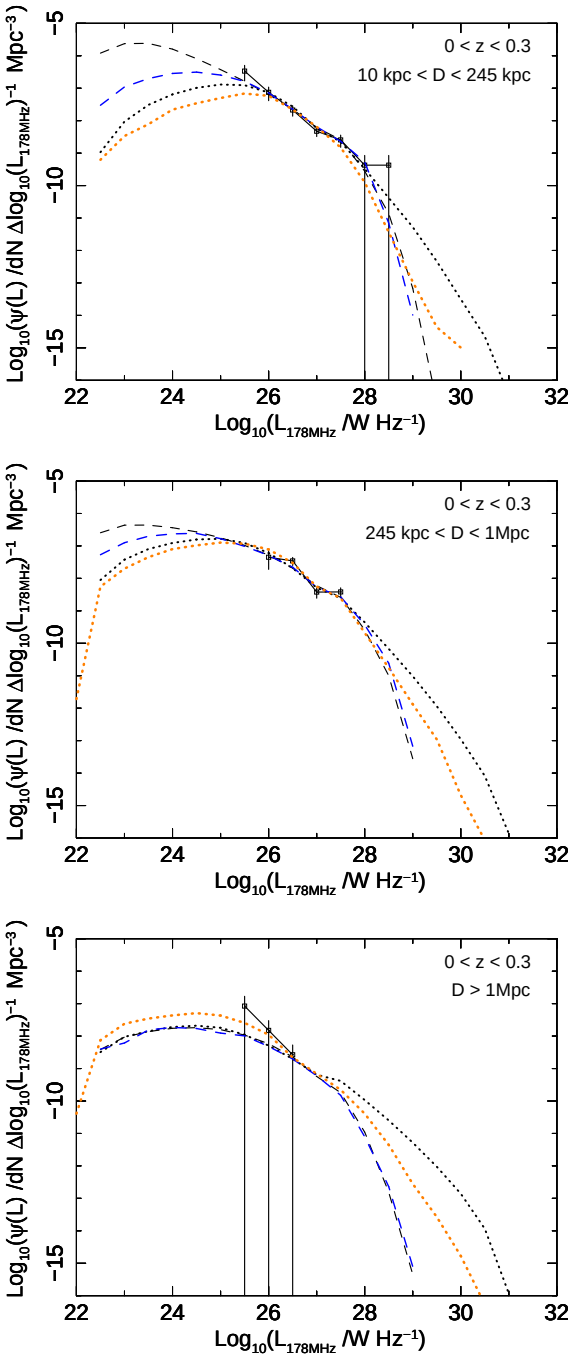

Figure 3.6: Radio luminosity functions of FR II type sources from 3CRR and BRL catalogues (solid) and the simulated populations generated with the best-fitting parameters for smallest redshift range ($z_1 < 0.3$) and for each model tested (independent-z fits of Model S drawn as black dashed line, independent-z fits of Model W as black dotted line, combined-z fits of model S as blue dashed line, and combined-z fits of model W as orange dotted line). Each redshift bin is simulated independently, while the FR IIs linear sizes within each redshift range are simulated simultaneously, that is a good fit to all linear sizes simultaneously at the same redshift is required. The simulated source populations created with the best-fitting parameters are consistent with the data at the 90 per cent confidence level based on ΔC statistics (for exact $p-$values see Table 3.3).

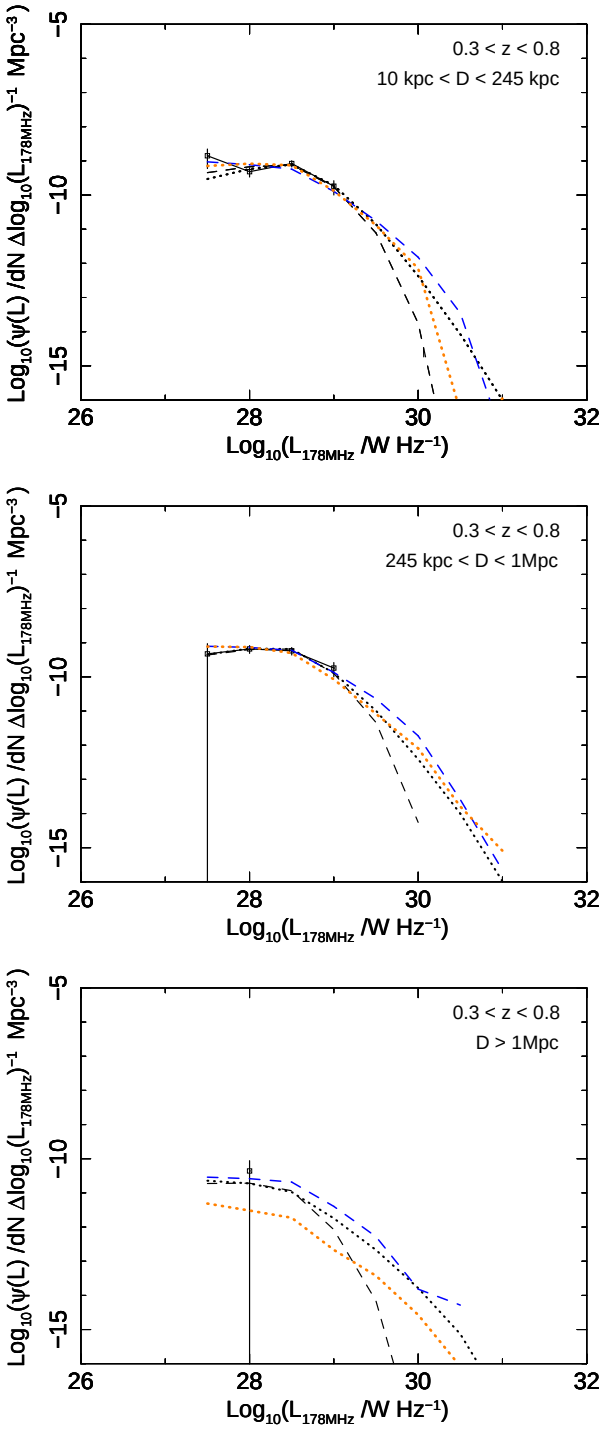

Figure 3.7: Same as Figure 3.6 but for the intermediate redshift range, $0.3 < z_2 < 0.8$.

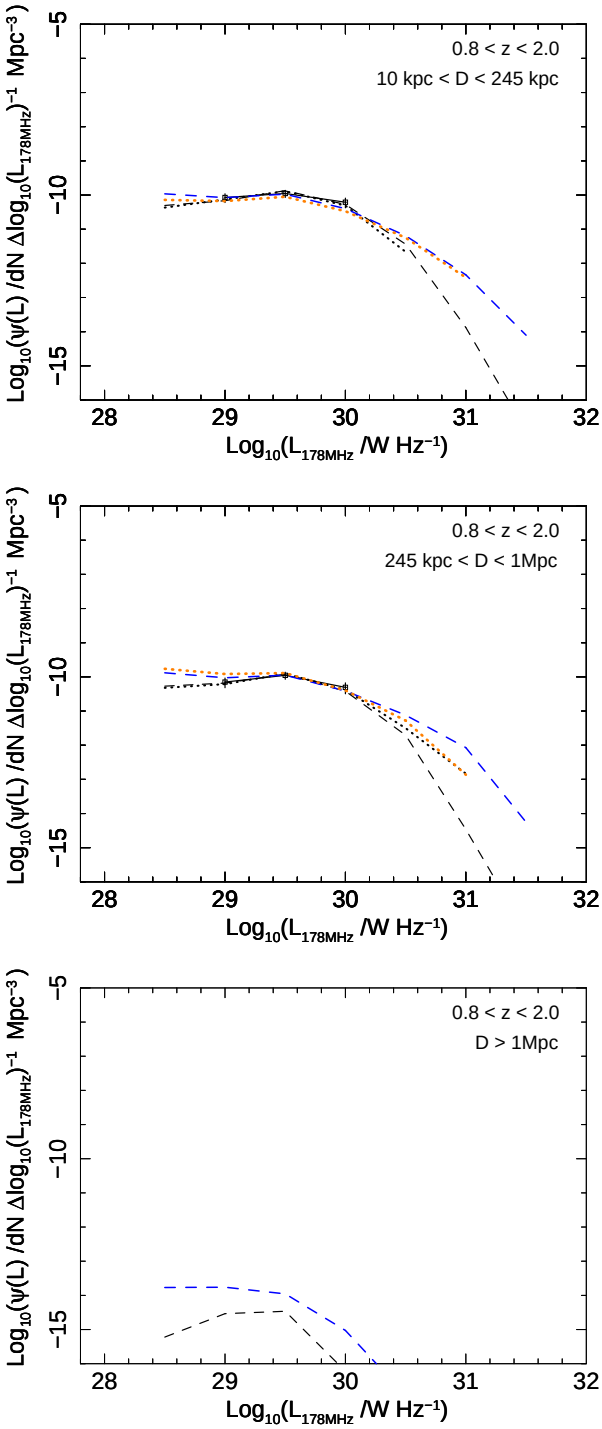

Figure 3.8: Same as Figure 3.6 but for the highest redshift range, $0.8 < z_3 < 2.0$.

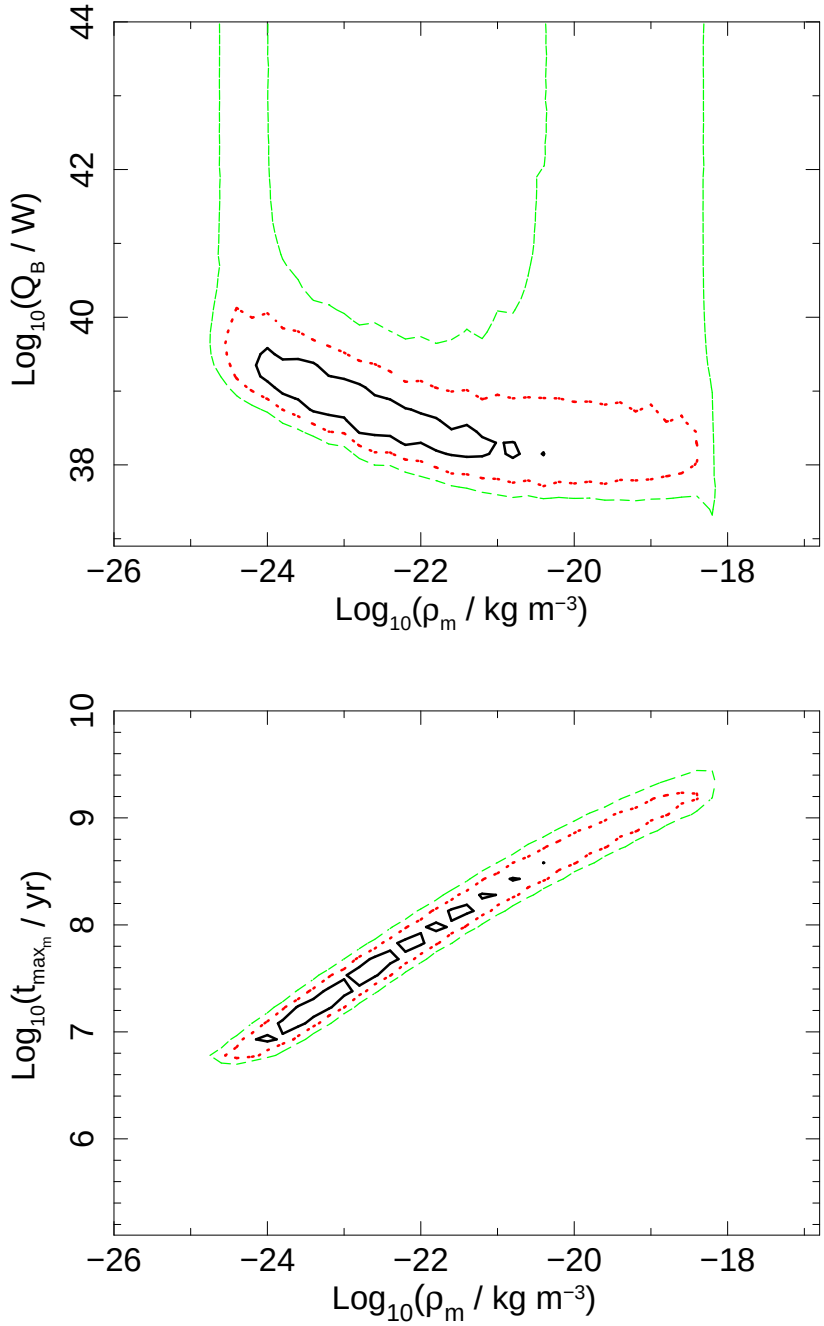

Figure 3.9: Joint confidence intervals for the independent-z fits of Model S in z_1 redshift range are shown ($z_1 \leq 0.3$). 68.3 per cent (solid, black), 95.4 per cent (dotted, red) and 99.7 per cent (dashed green) contours, based on ΔC statistics (see §2.4), are shown. The best-fitting parameters are consistent with the data at the 90 per cent confidence level ($p-\text{value} = 0.234$).

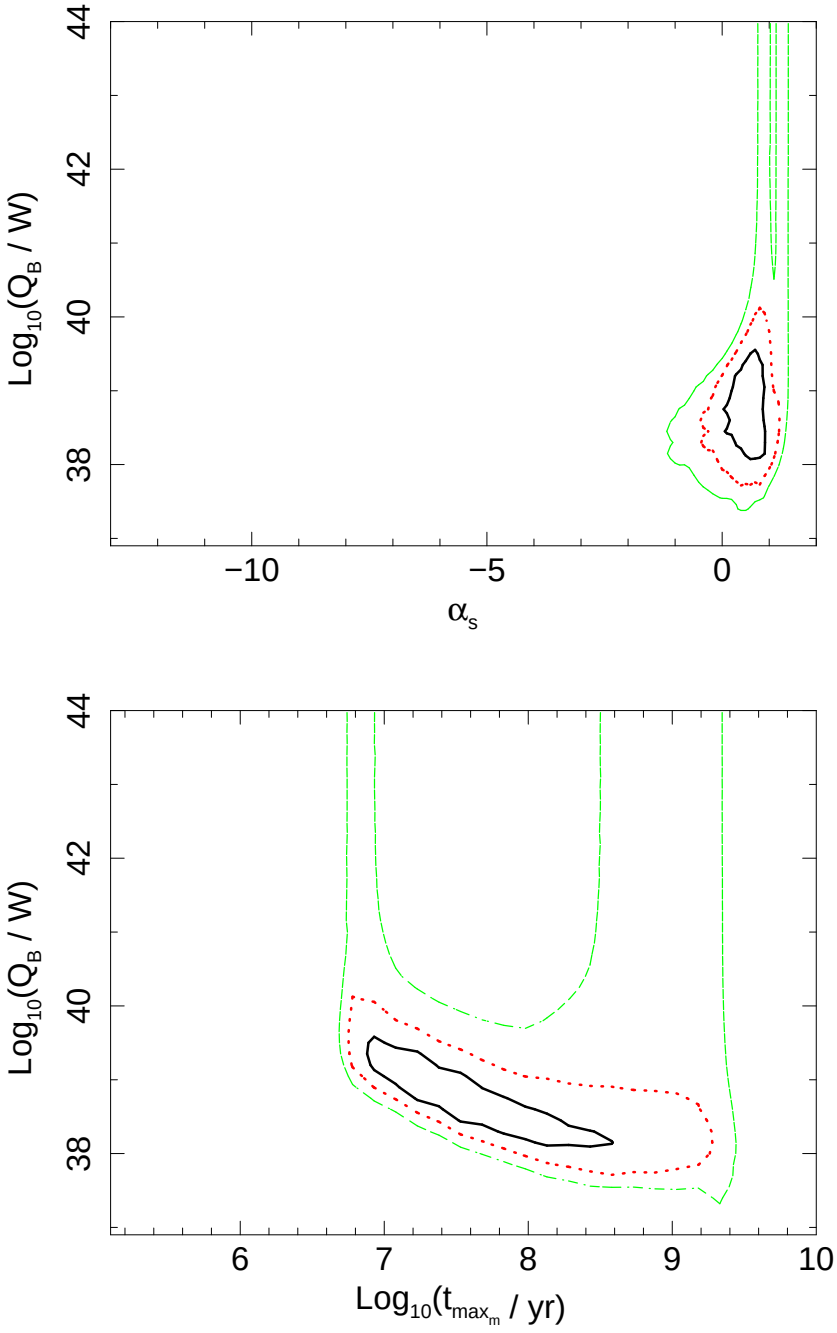

Figure 3.9: *Continued*.

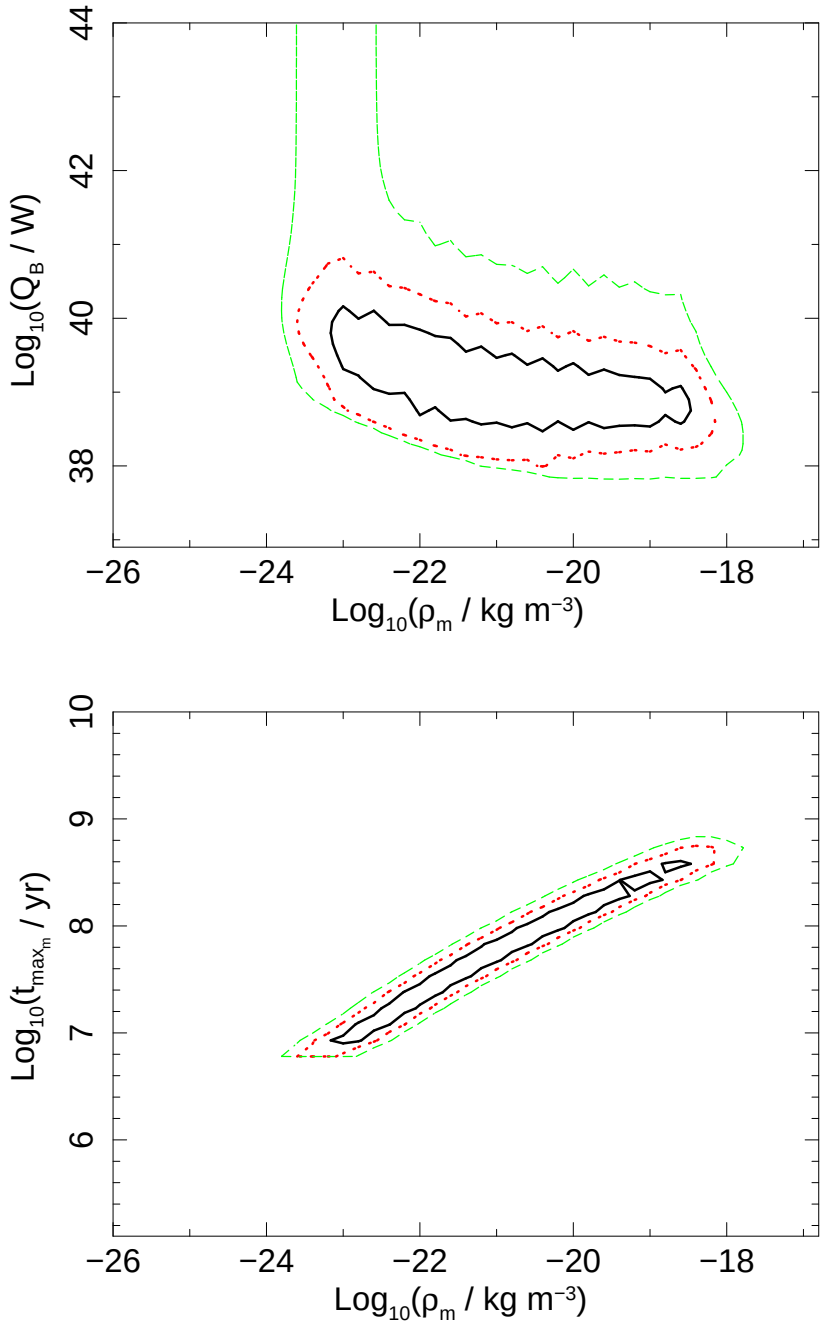

Figure 3.10: Joint confidence intervals for the independent-z fits of Model S in z_2 redshift range are shown ($0.3 < z_2 \leq 0.8$). 68.3 per cent (solid, black), 95.4 per cent (dotted, red) and 99.7 per cent (dashed green) contours, based on ΔC statistics (see §2.4), are shown. The best-fitting parameters are consistent with the data at the 90 per cent confidence level ($p-\text{value} = 0.639$).

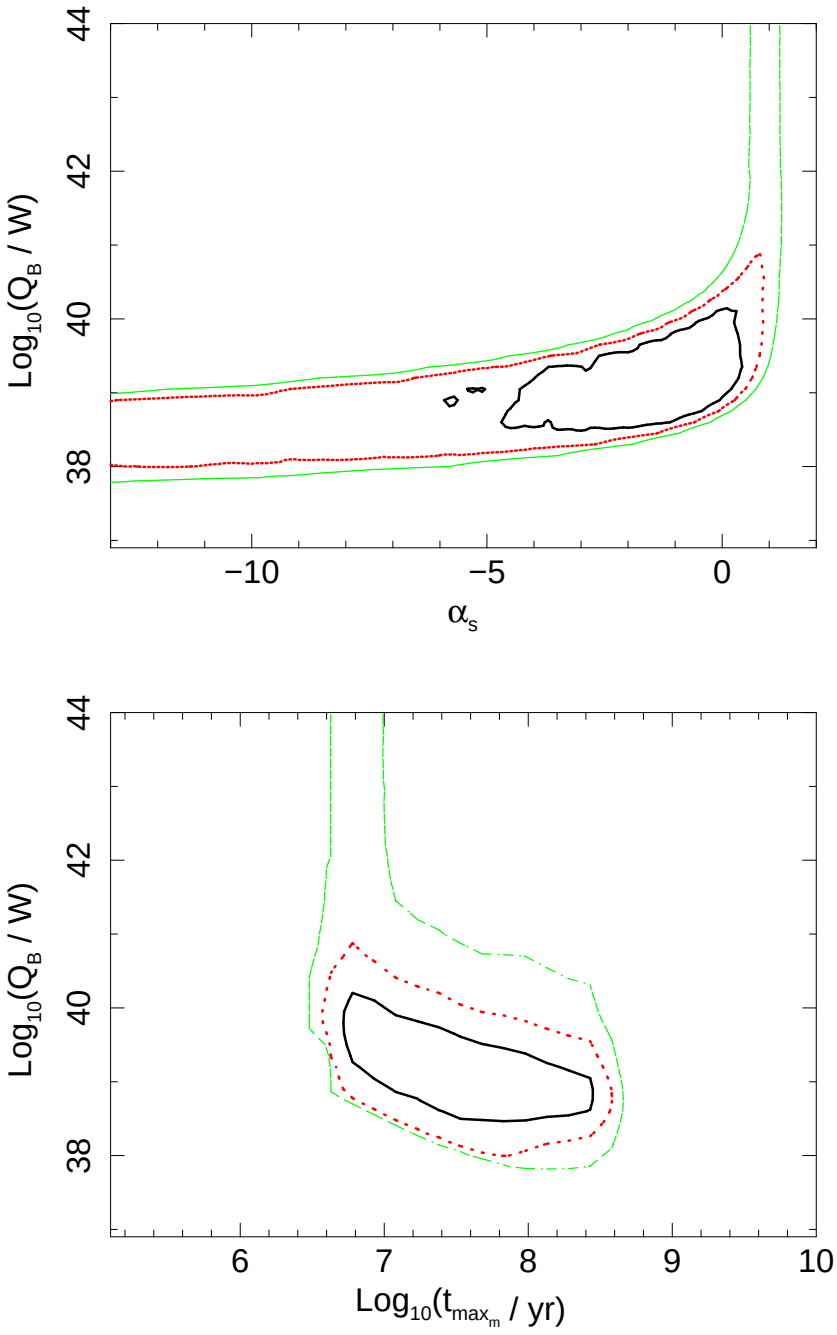

Figure 3.10: *Continued*.

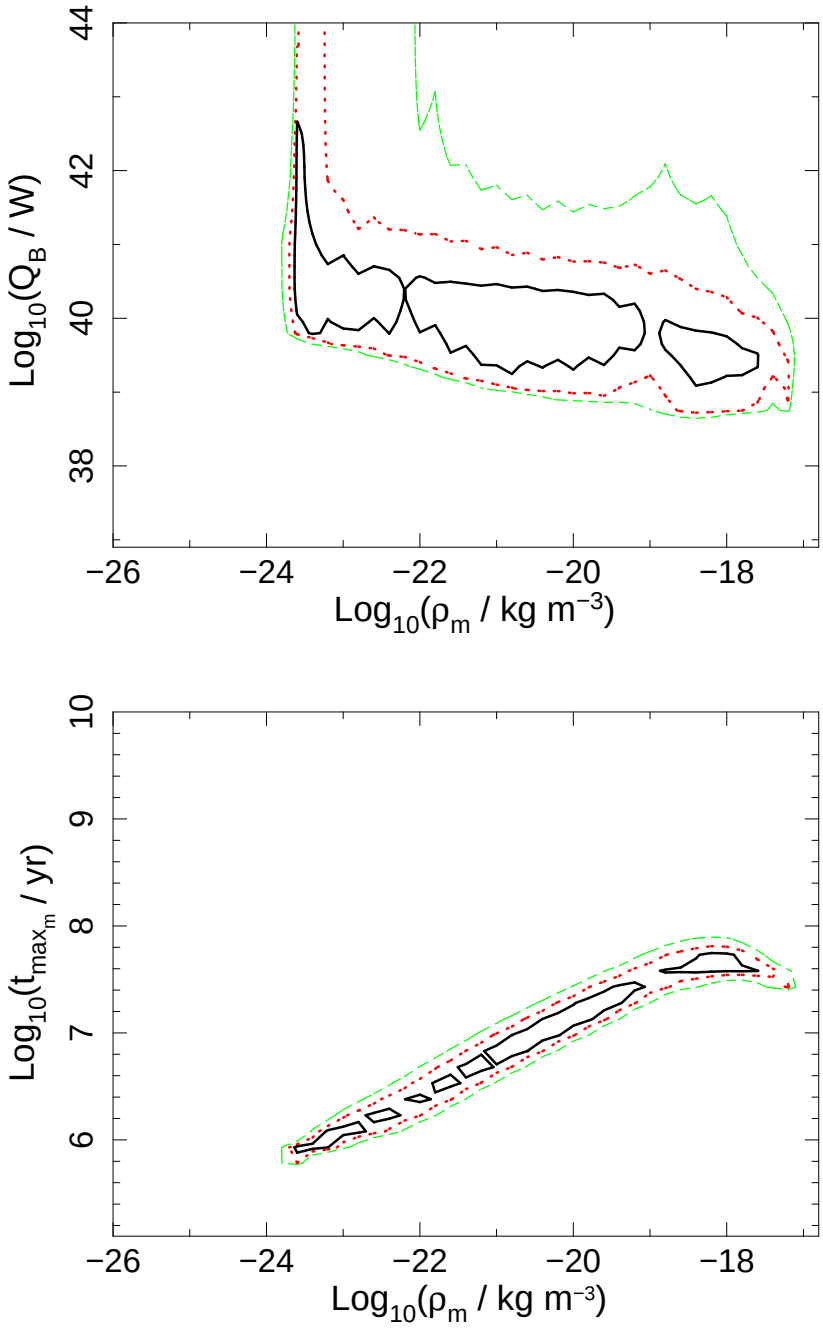

Figure 3.11: Joint confidence intervals for the independent-z fits of Model S in z_3 redshift range are shown ($0.8 < z_3 \leq 2.0$). 68.3 per cent (solid, black), 95.4 per cent (dotted, red) and 99.7 per cent (dashed green) contours, based on ΔC statistics (see §2.4), are shown. The best-fitting parameters are consistent with the data at the 90 per cent confidence level ($p-\text{value} = 0.925$).

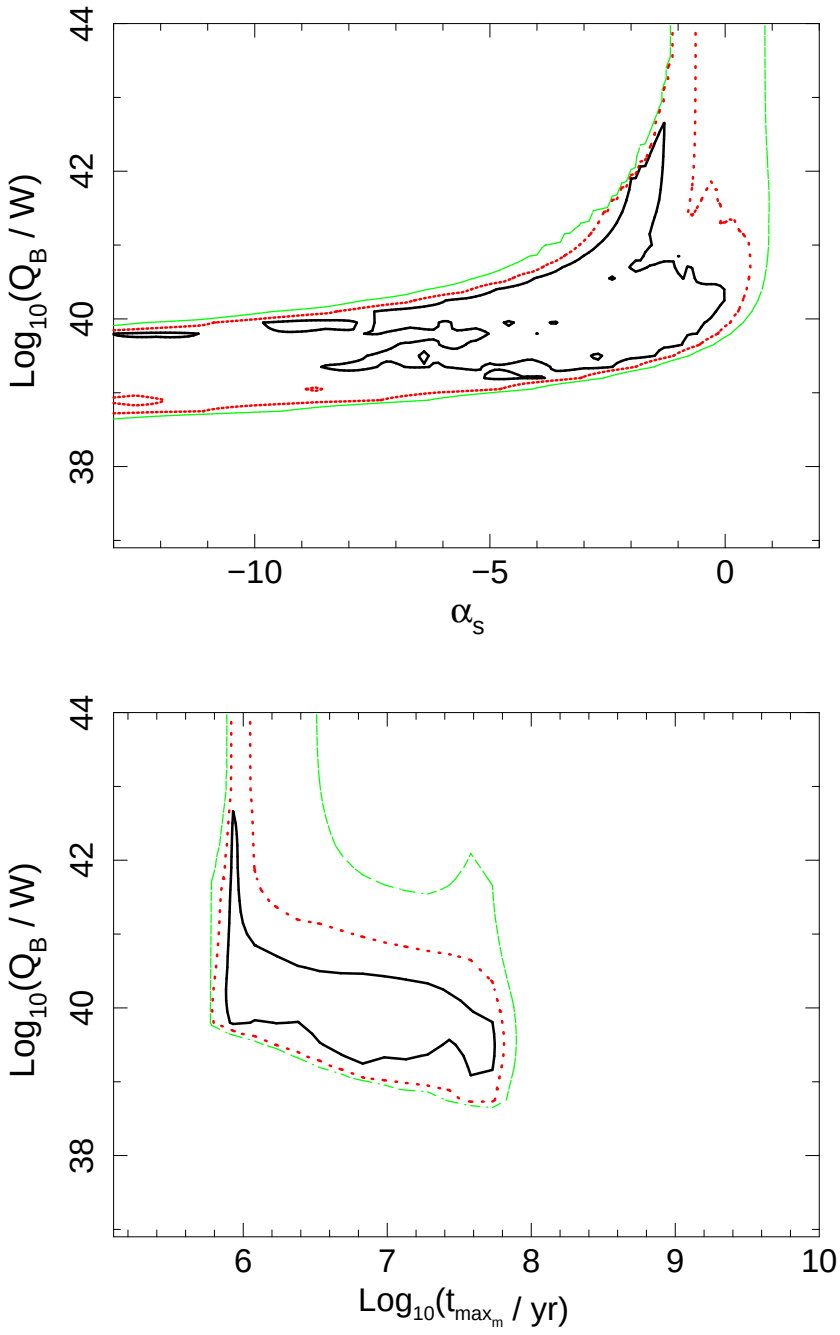

Figure 3.11: *Continued*.

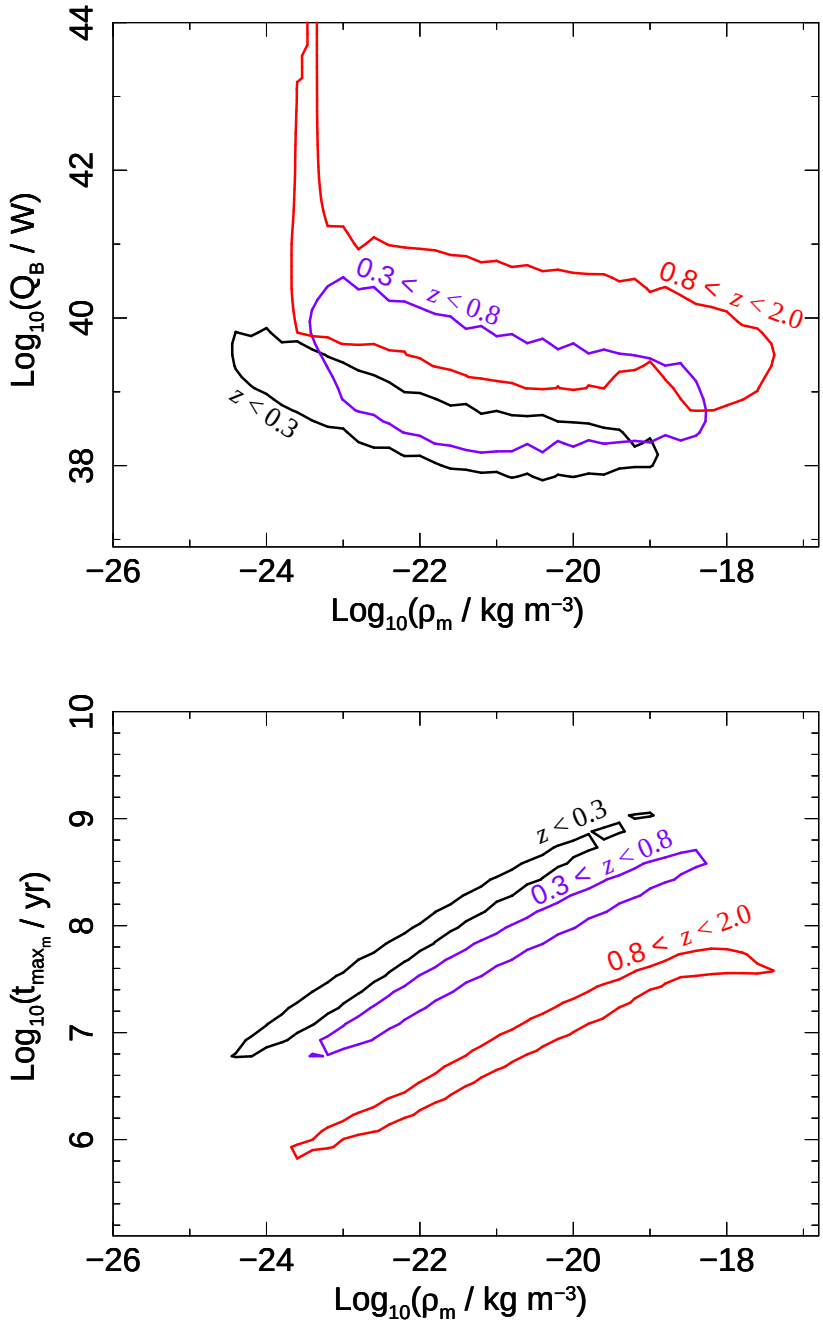

Figure 3.12: Overlaid 90 per cent confidence intervals based on ΔC statistics (§2.4) for the three redshift ranges considered (z_1 drawn in black, z_2 in blue, z_3 in red) of the independent-z fits of Model S.

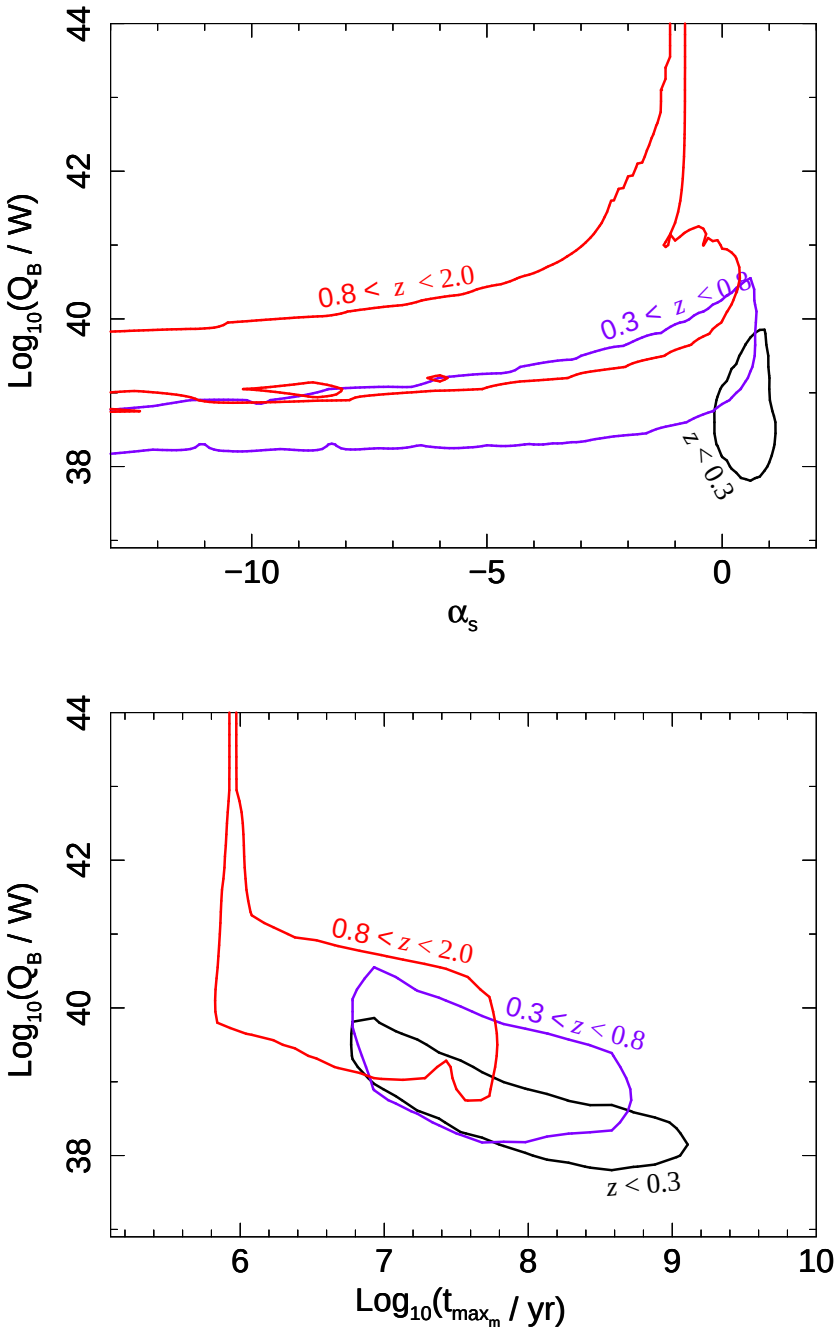

Figure 3.12: *Continued*.

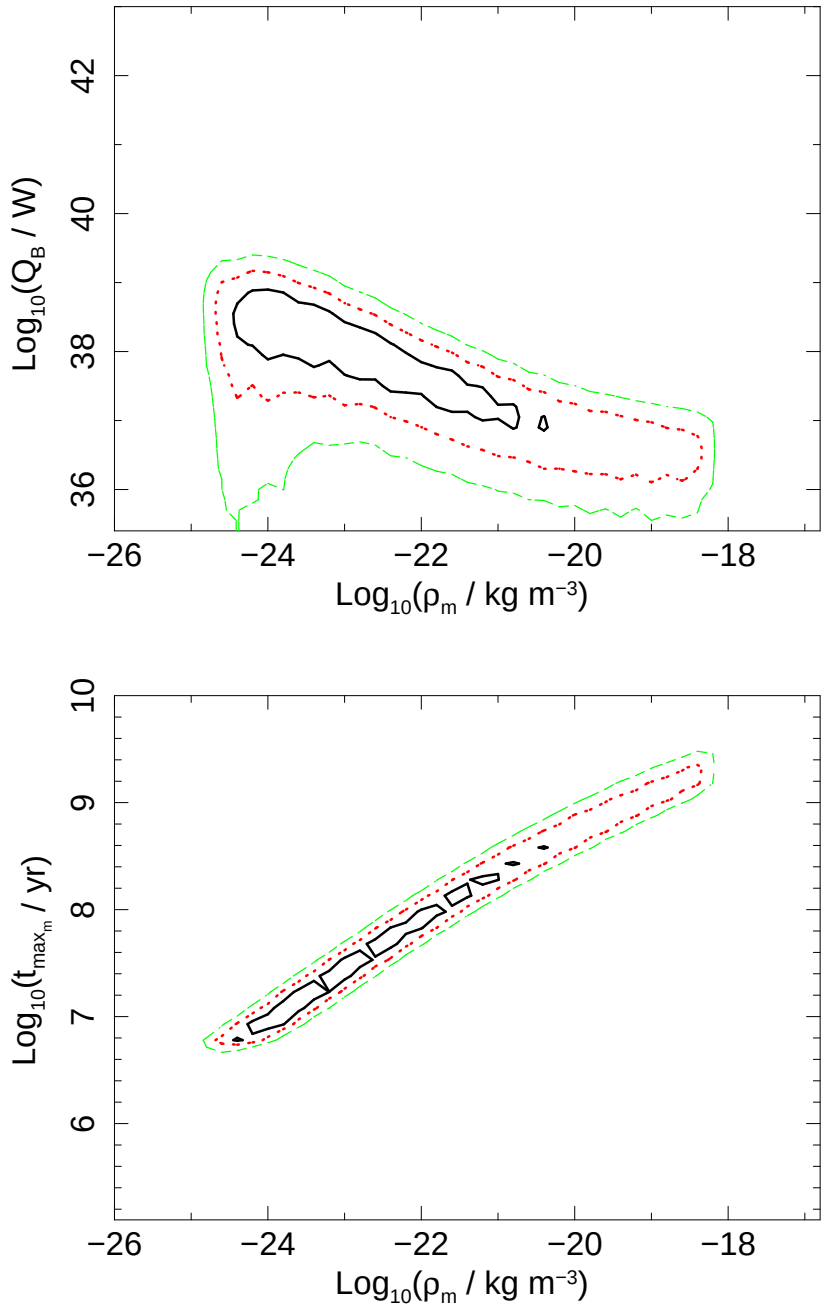

Figure 3.13: Joint confidence intervals for the independent-z fits of Model W in z_1 redshift range are shown ($z_3 \leq 0.3$). 68.3 per cent (solid, black), 95.4 per cent (dotted, red) and 99.7 per cent (dashed green) contours, based on ΔC statistics (see §2.4), are shown. The best-fitting parameters are consistent with the data at the 90 per cent level ($p-$value $= 0.251$).

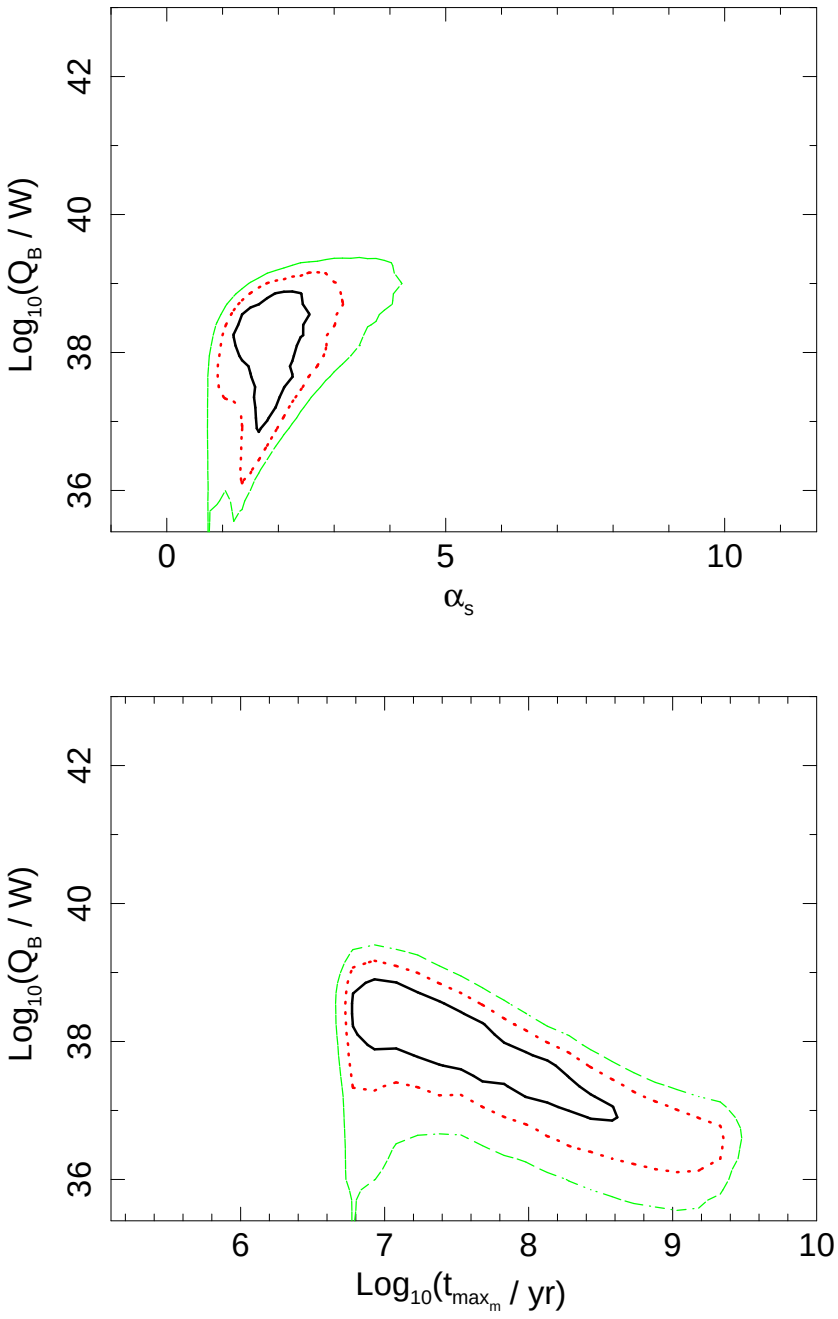

Figure 3.13: *Continued*.

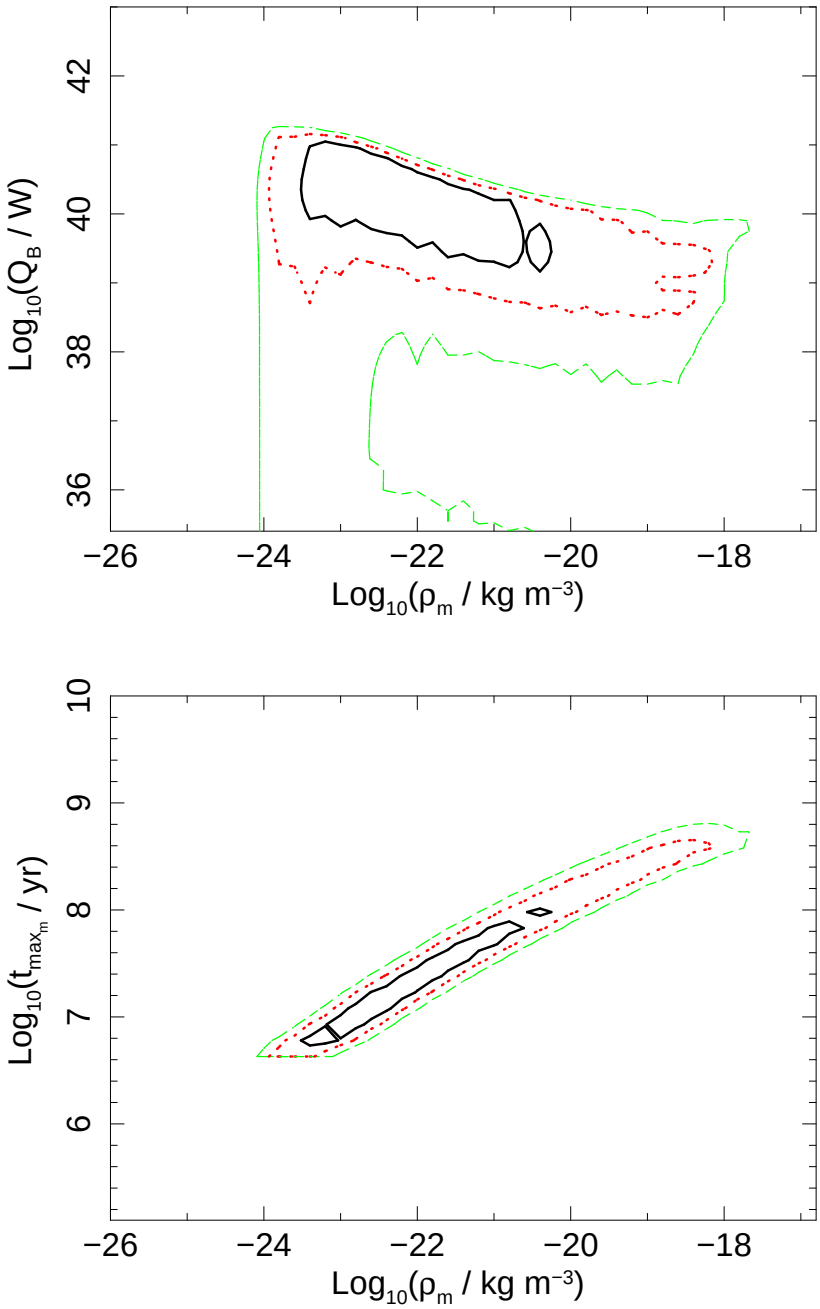

Figure 3.14: Joint confidence intervals for the independent-z fits of Model W in z_2 redshift range are shown ($0.3 < z_3 \leq 0.8$). 68.3 per cent (solid, black), 95.4 per cent (dotted, red) and 99.7 per cent (dashed green) contours, based on ΔC statistics (see §2.4), are shown. The best-fitting parameters are consistent with the data at the 90 per cent level ($p-\text{value} = 0.674$).

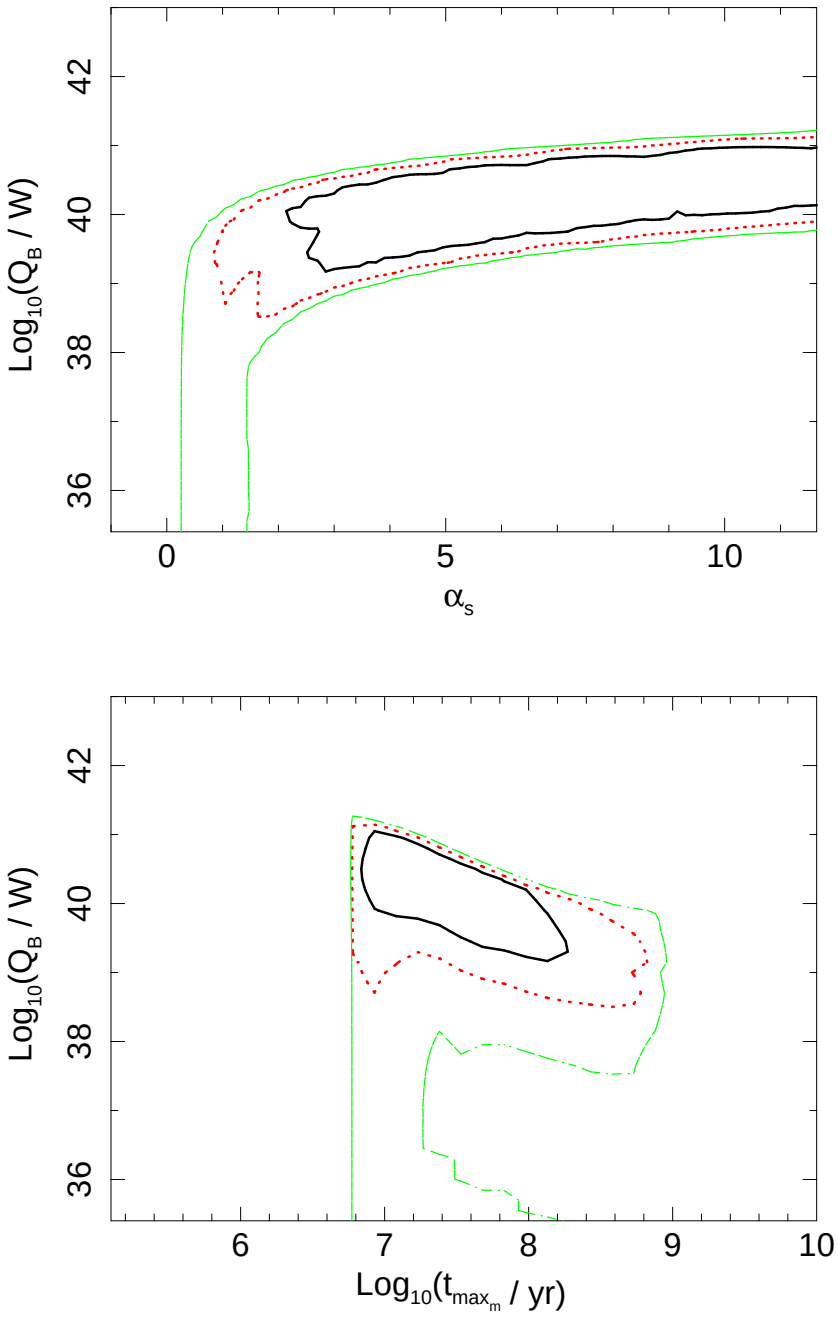

Figure 3.14: *Continued*.

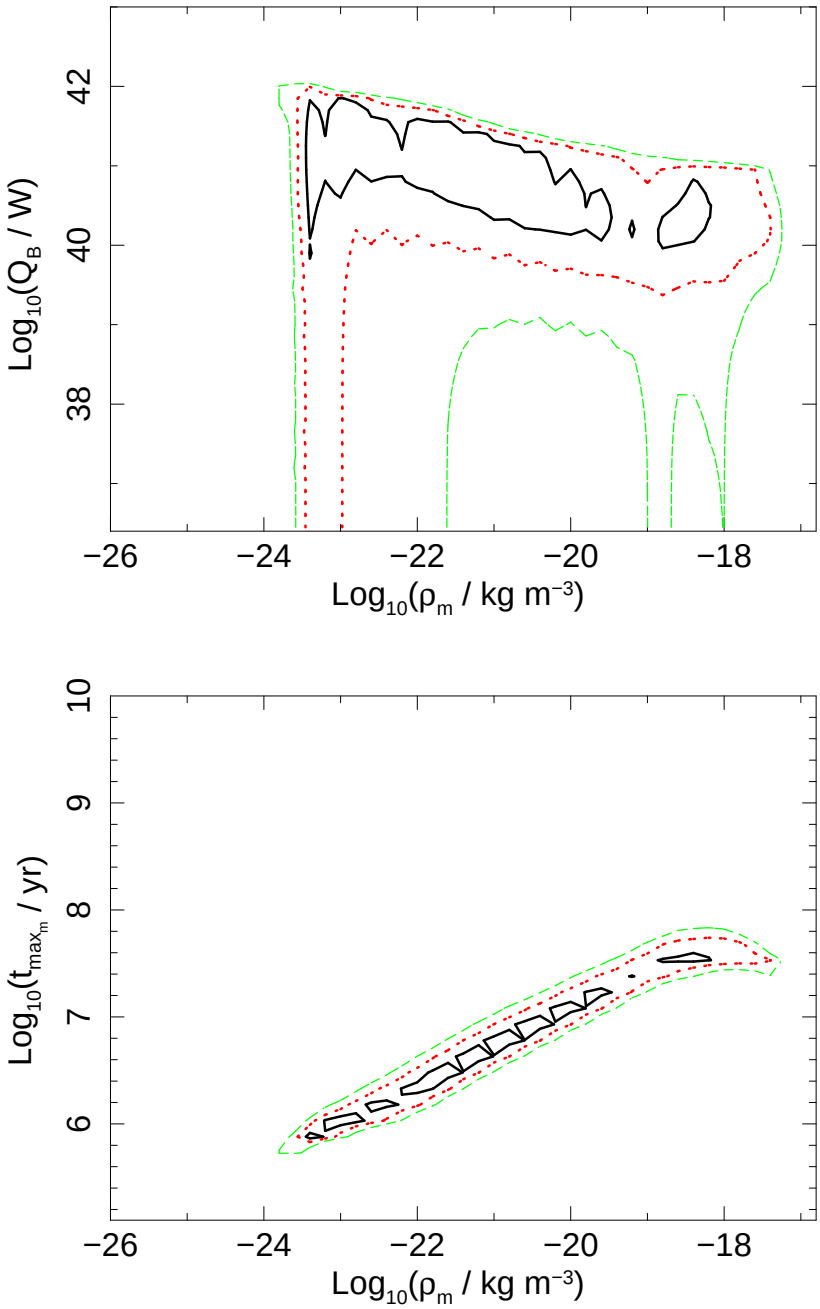

Figure 3.15: Joint confidence intervals for the independent-z fits of Model W in z_3 redshift range are shown ($0.8 < z_3 \leq 2.0$). 68.3 per cent (solid, black), 95.4 per cent (dotted, red) and 99.7 per cent (dashed green) contours, based on ΔC statistics (see §2.4), are shown. The best-fitting parameters are consistent with the data at the 90 per cent level ($p-\text{value} = 0.885$).

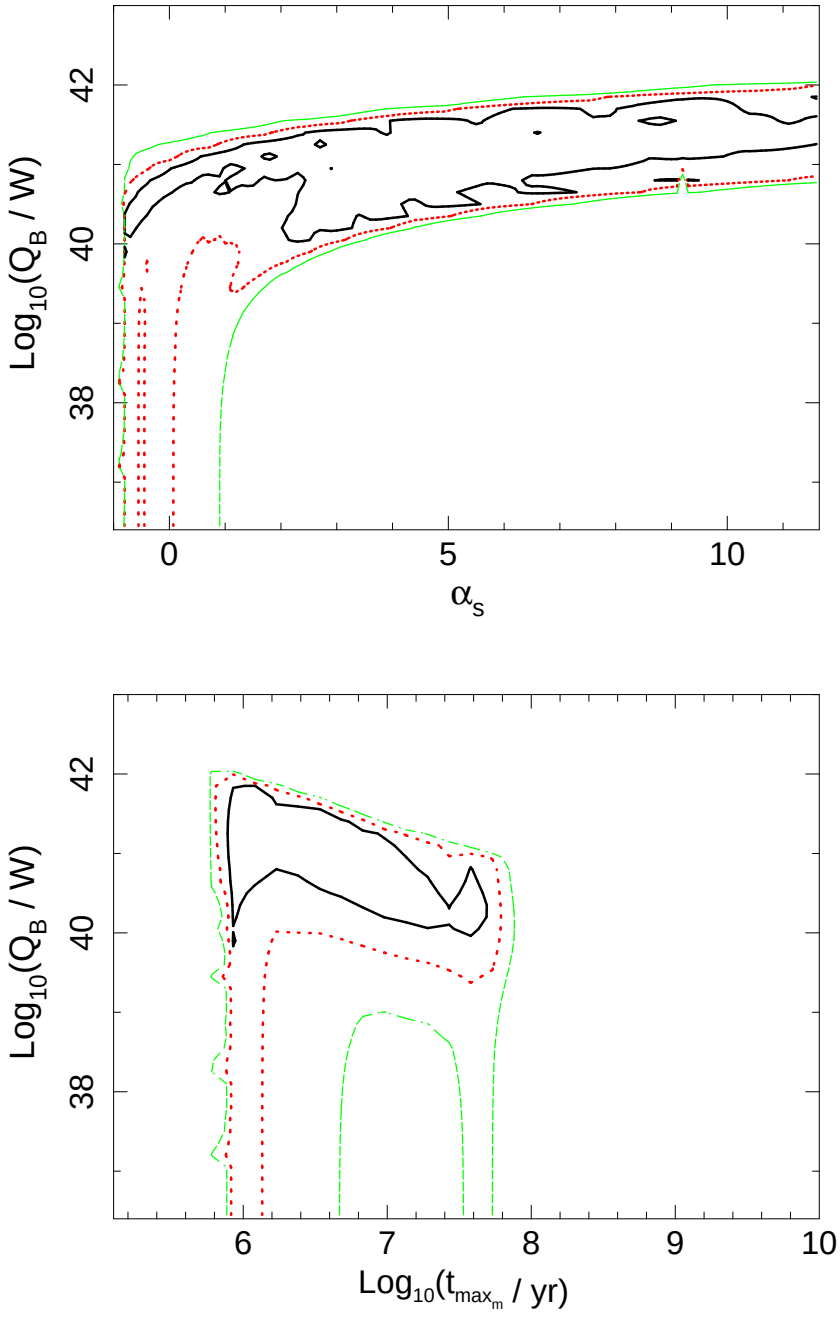

Figure 3.15: *Continued*.

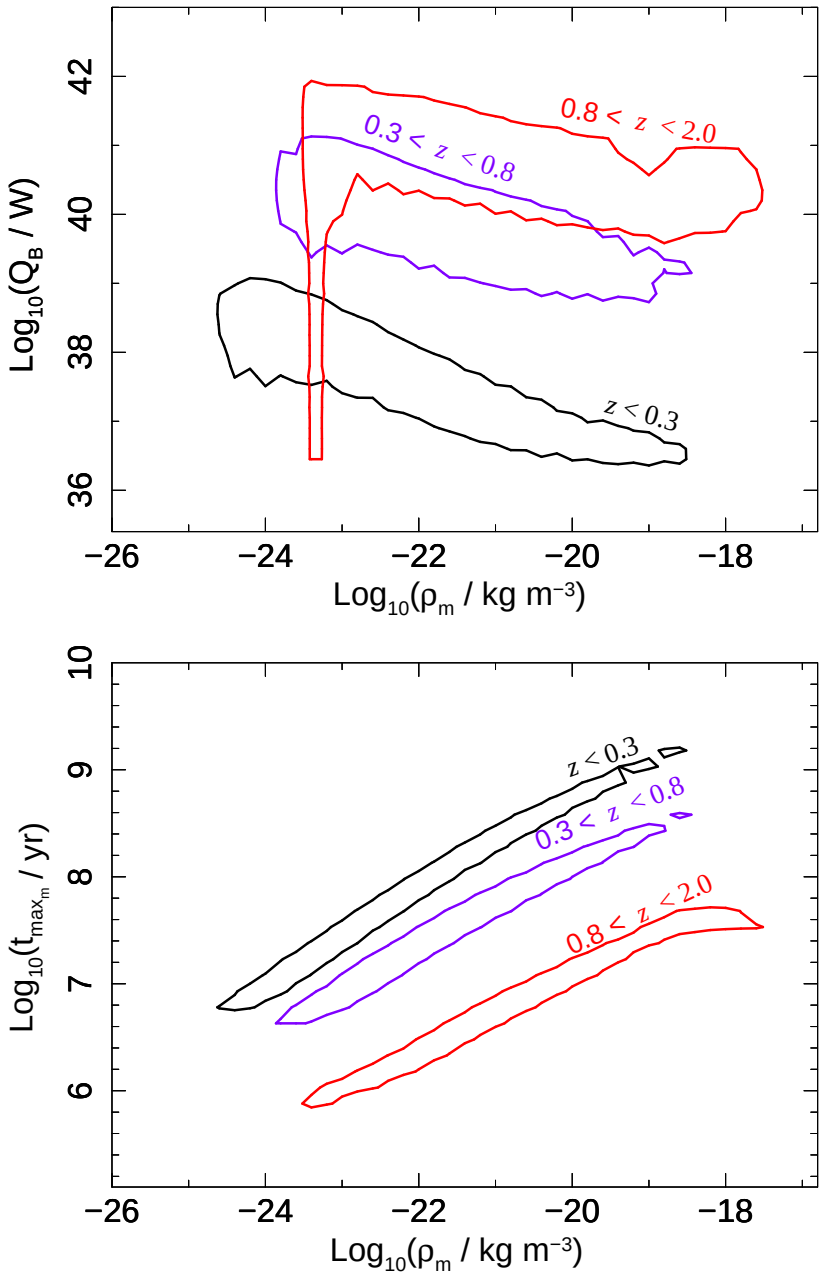

Figure 3.16: Overlaid 90 per cent confidence intervals based on ΔC statistics (§2.4) for the three redshift ranges considered (z_1 drawn in black, z_2 in blue, z_3 in red) of the independent-z fits of Model W.

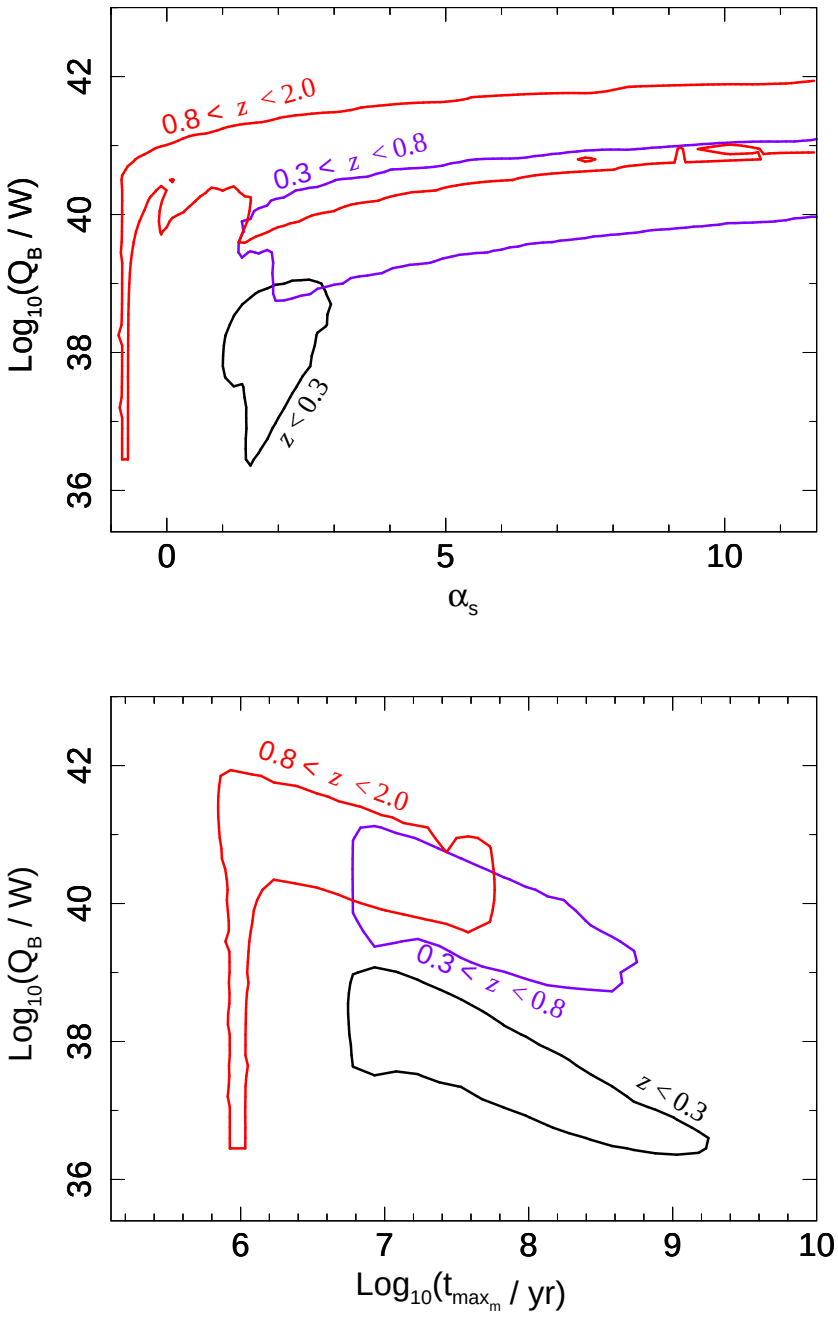

Figure 3.16: *Continued*.

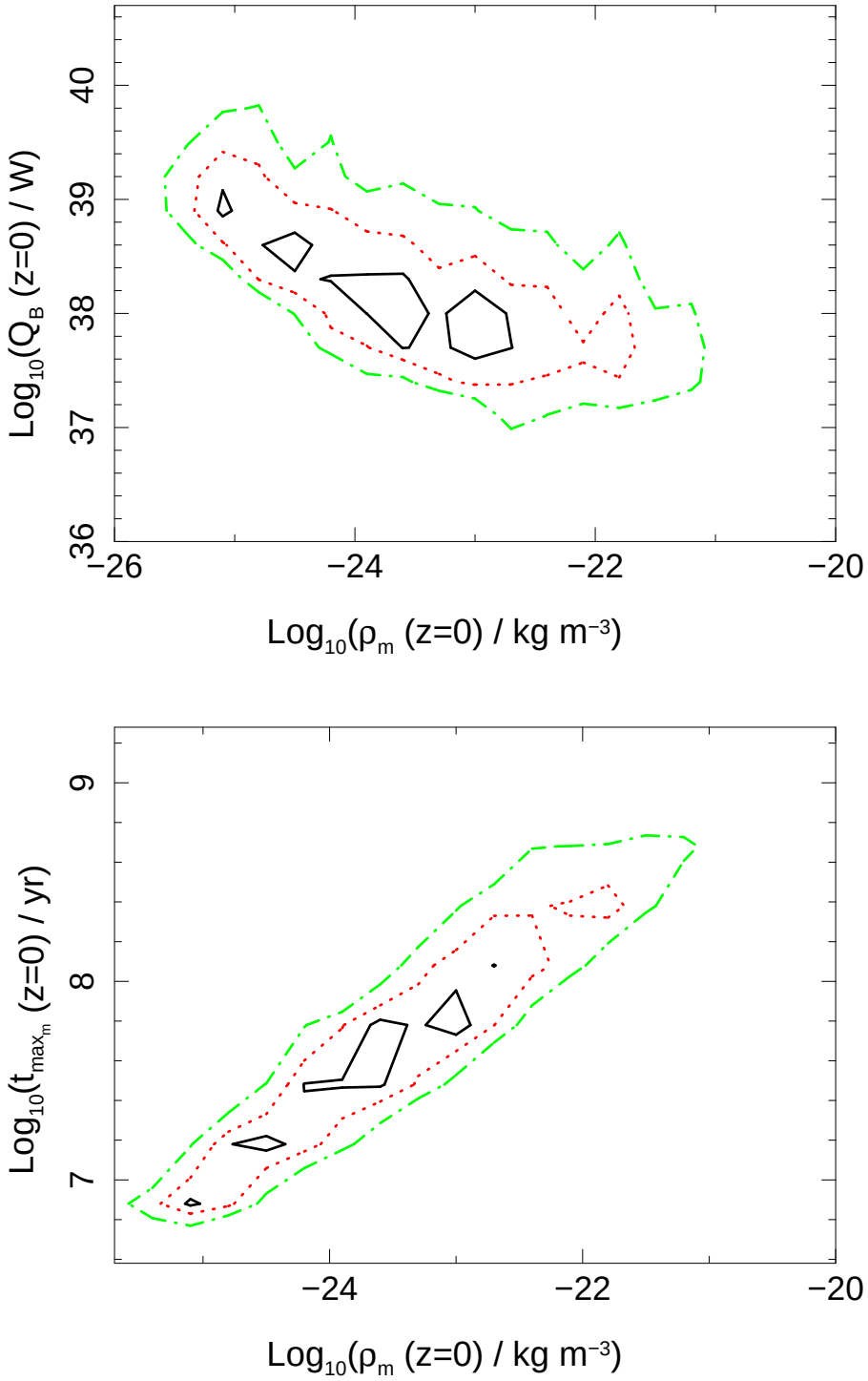

Figure 3.17: 68.3 per cent (solid, black), 95.4 per cent (dotted, red) and 99.7 per cent (dash-dotted, green) joint confidence intervals (based on ΔC statistics) of all the searched parameters of the combined-z fits of the Model S. Parameters $n_{\rm t}, n_{\rm q}$ and $n_{\rm r}$ quantify the strength of the redshift evolution of $t_{\rm max_m}(z=0), Q_{\rm B}(z=0)$ and $\rho_{\rm m}(z=0)$ respectively.

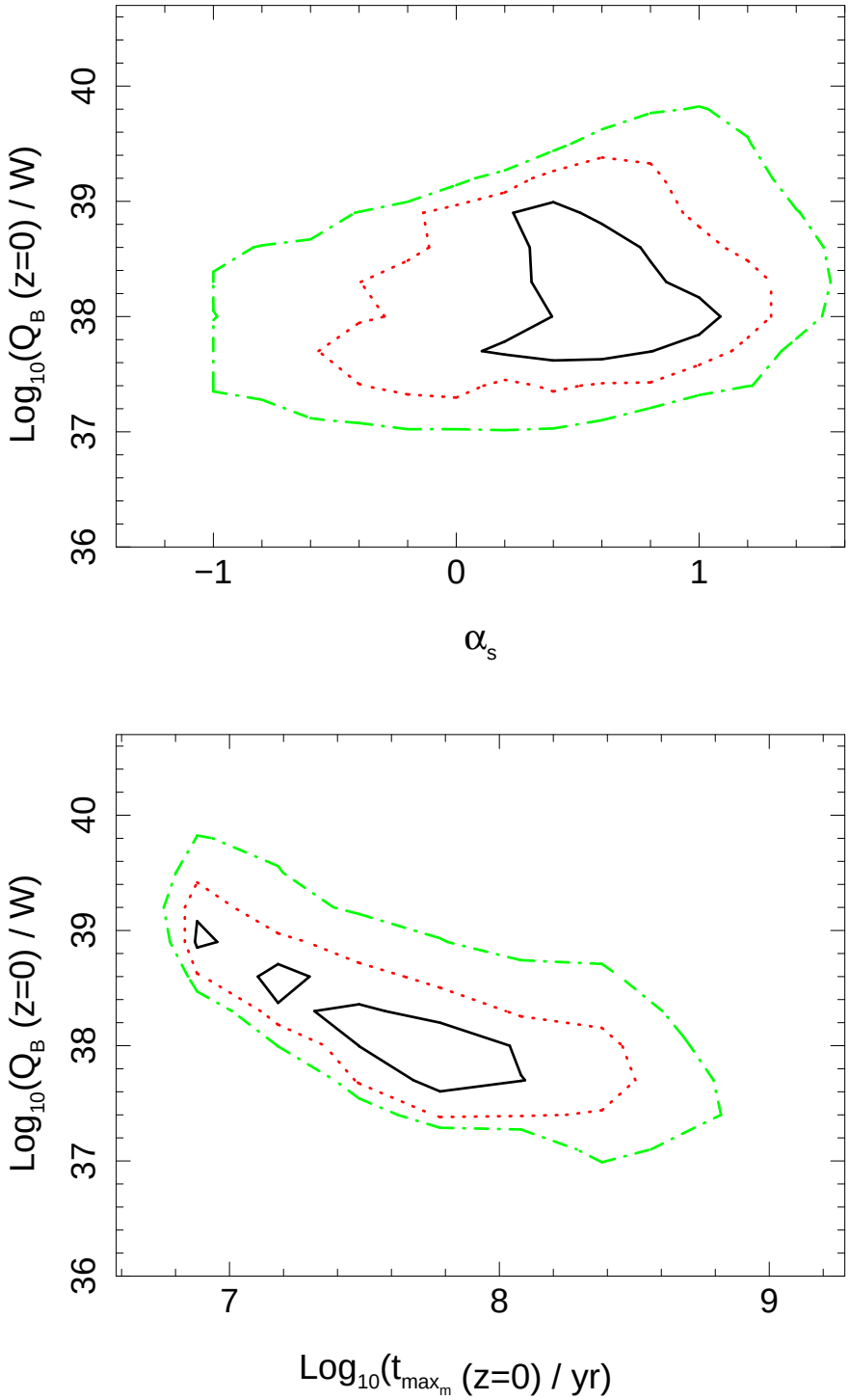

Figure 3.17: *Continued*.

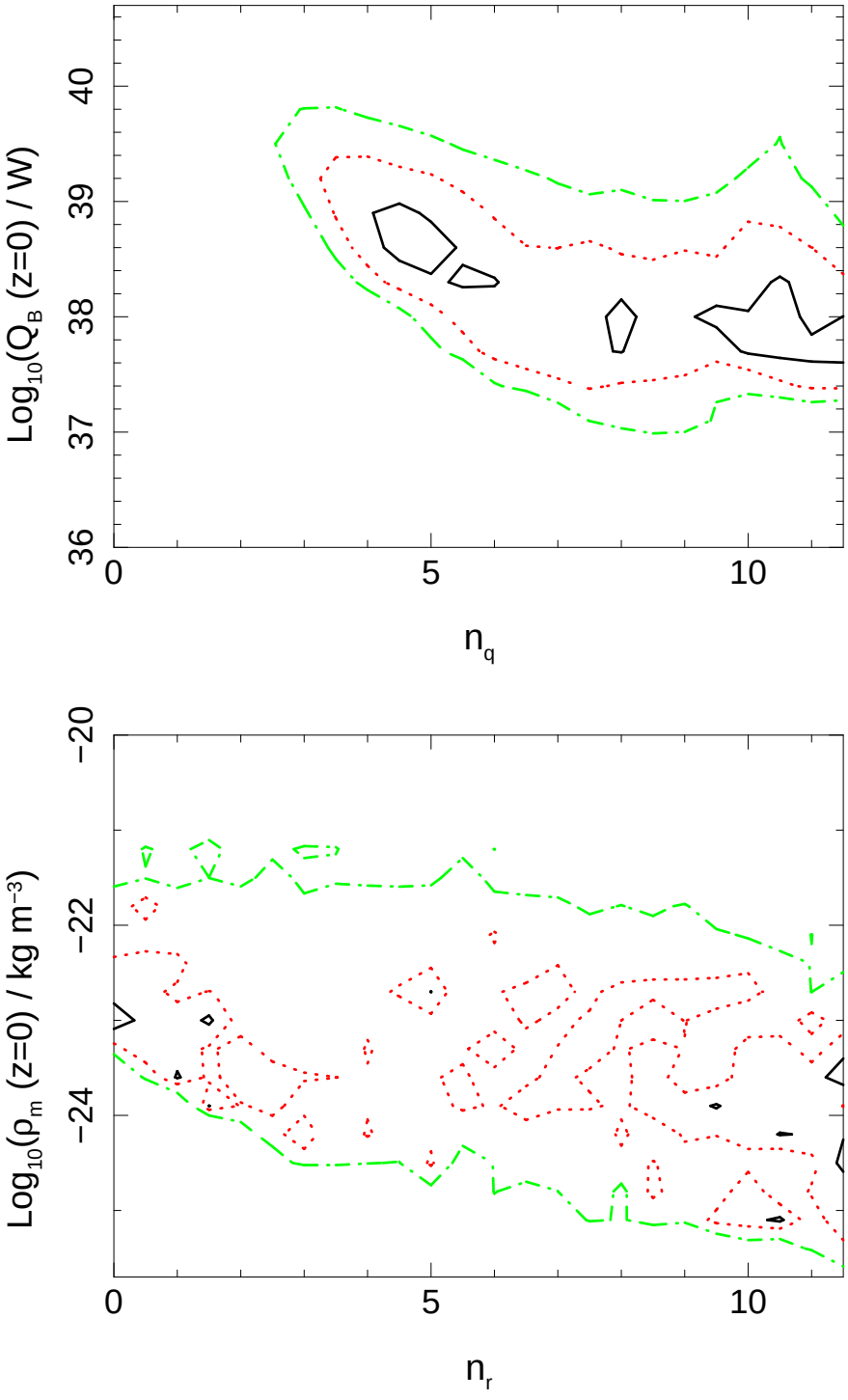

Figure 3.17: *Continued*.

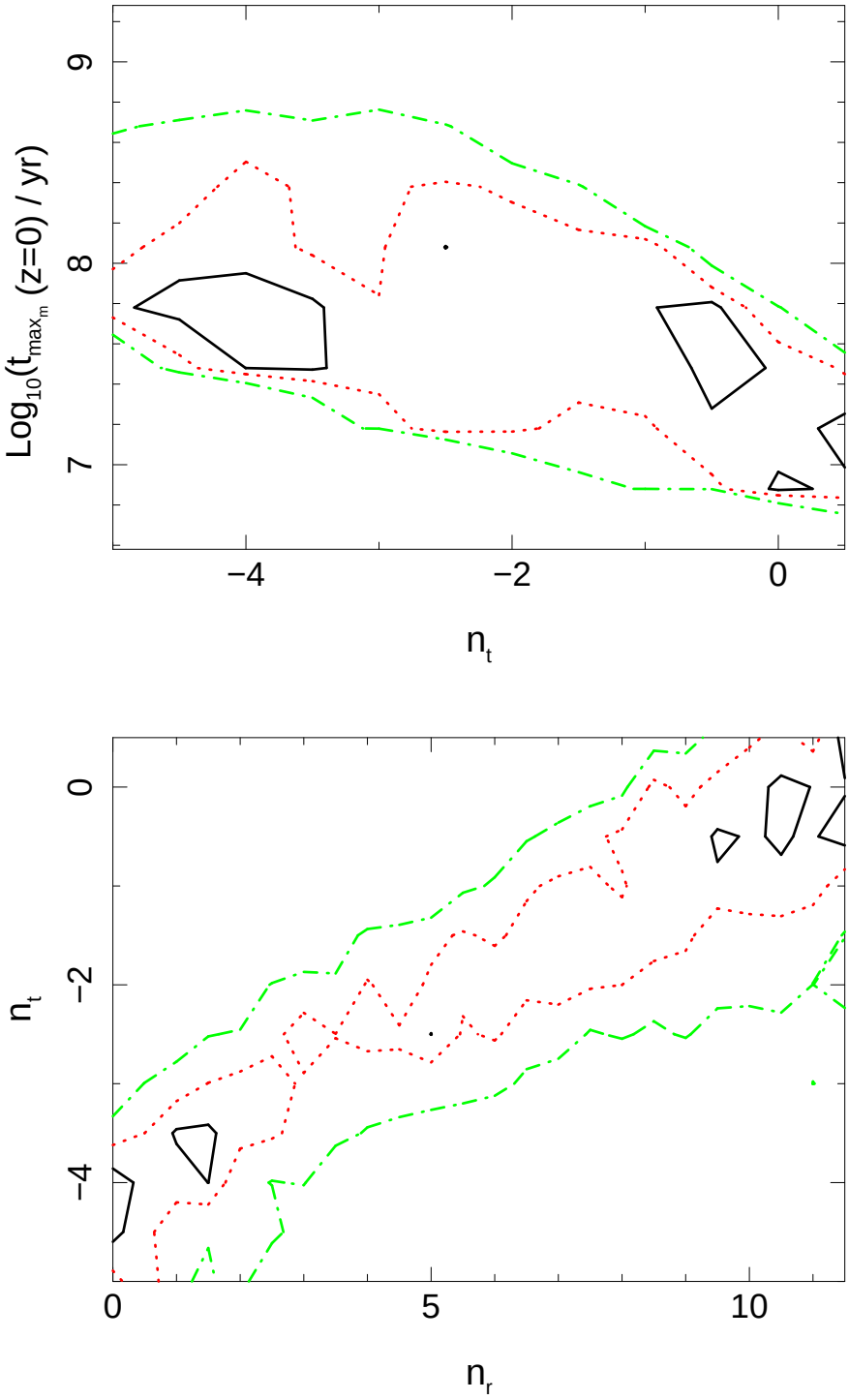

Figure 3.17: *Continued*.

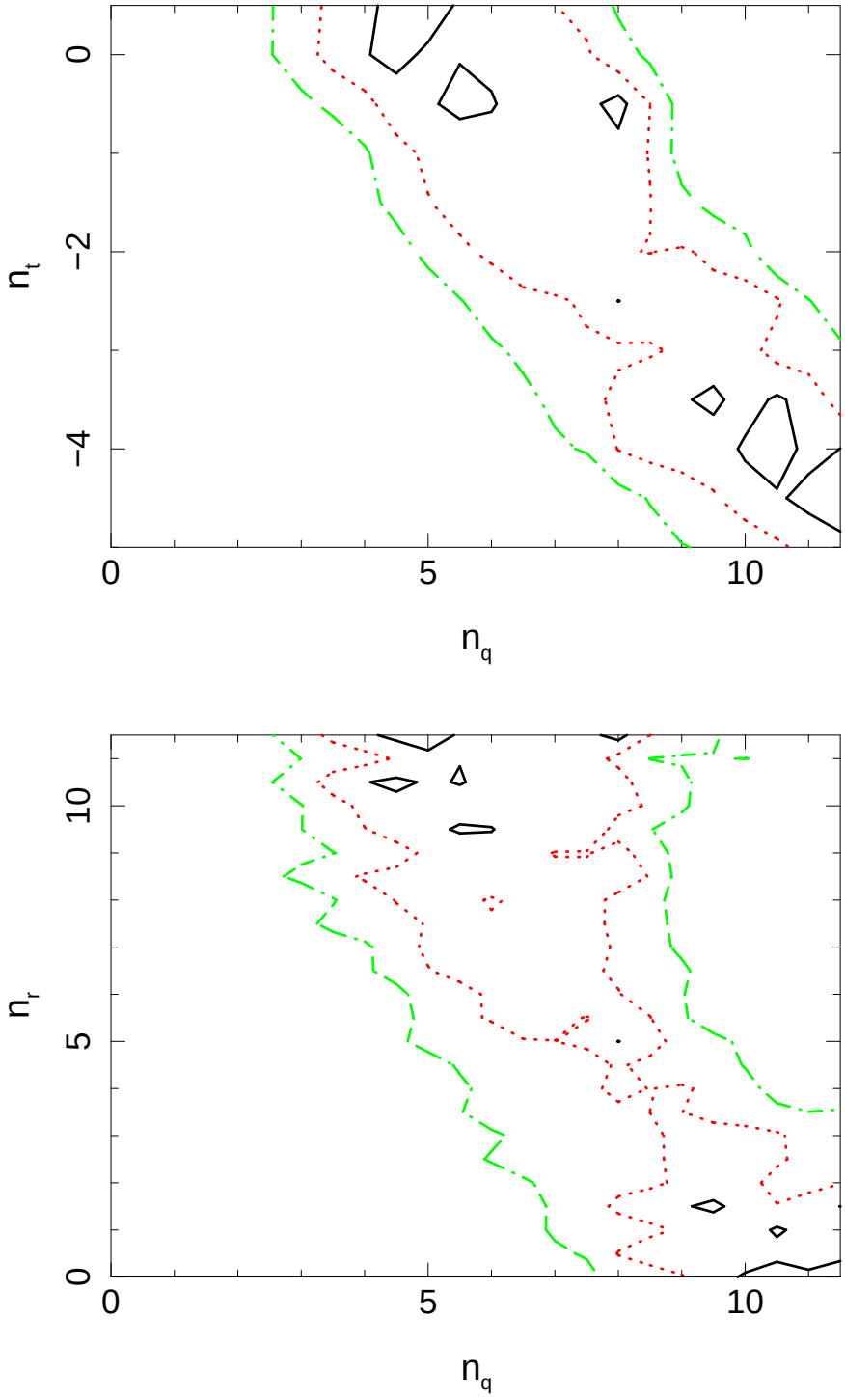

Figure 3.17: *Continued*.

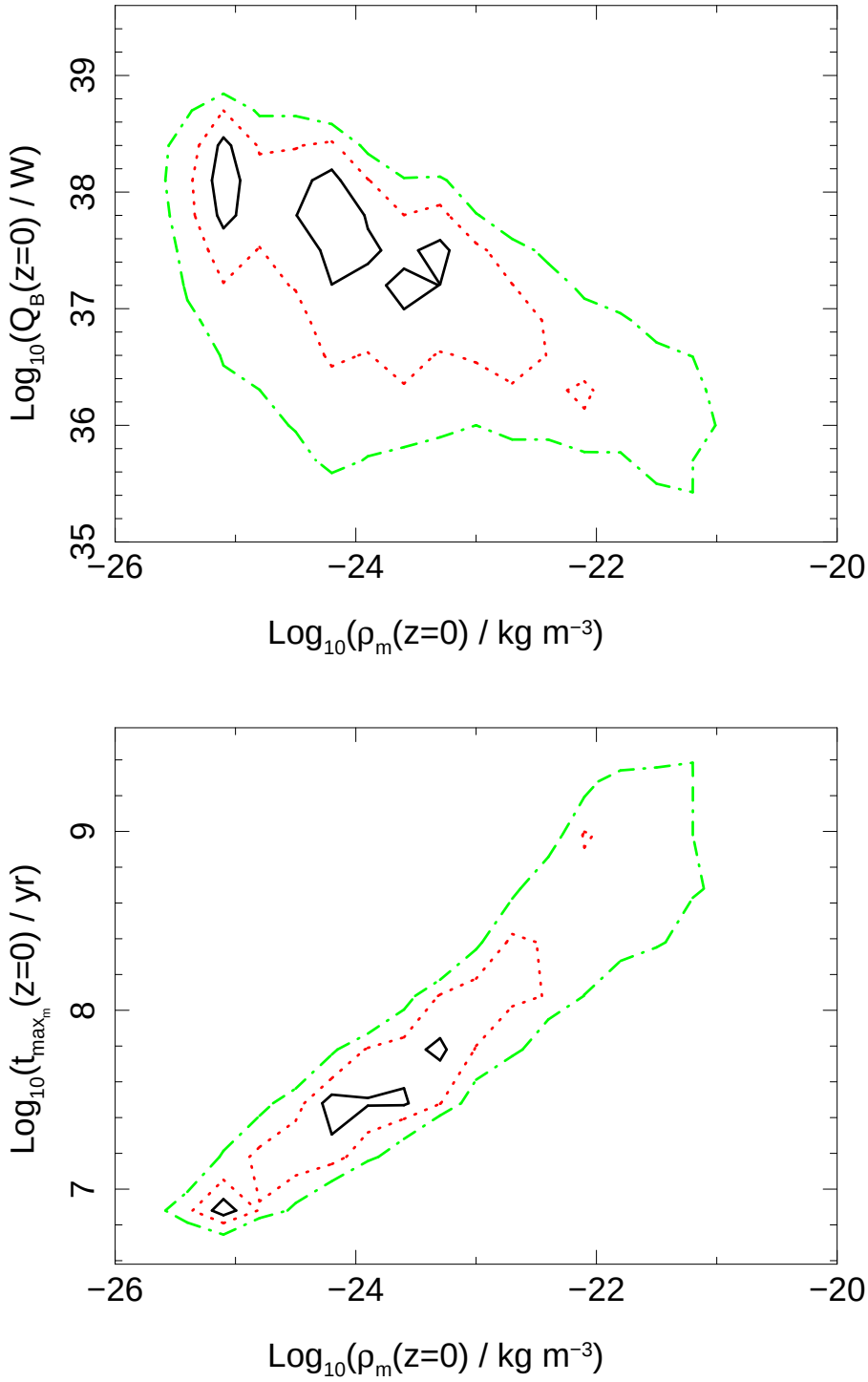

Figure 3.18: 68.3 per cent (solid, black), 95.4 per cent (dotted, red) and 99.7 per cent (dash-dotted, green) joint confidence intervals (based on ΔC statistics) of all the searched parameters of the combined-z fits of the Model W. Parameters $n_{\rm t}, n_{\rm q}$ and $n_{\rm r}$ quantify the strength of the redshift evolution of $t_{\max_{\rm m}}(z=0), Q_{\rm B}(z=0)$ and $\rho_{\rm m}(z=0)$ respectively.

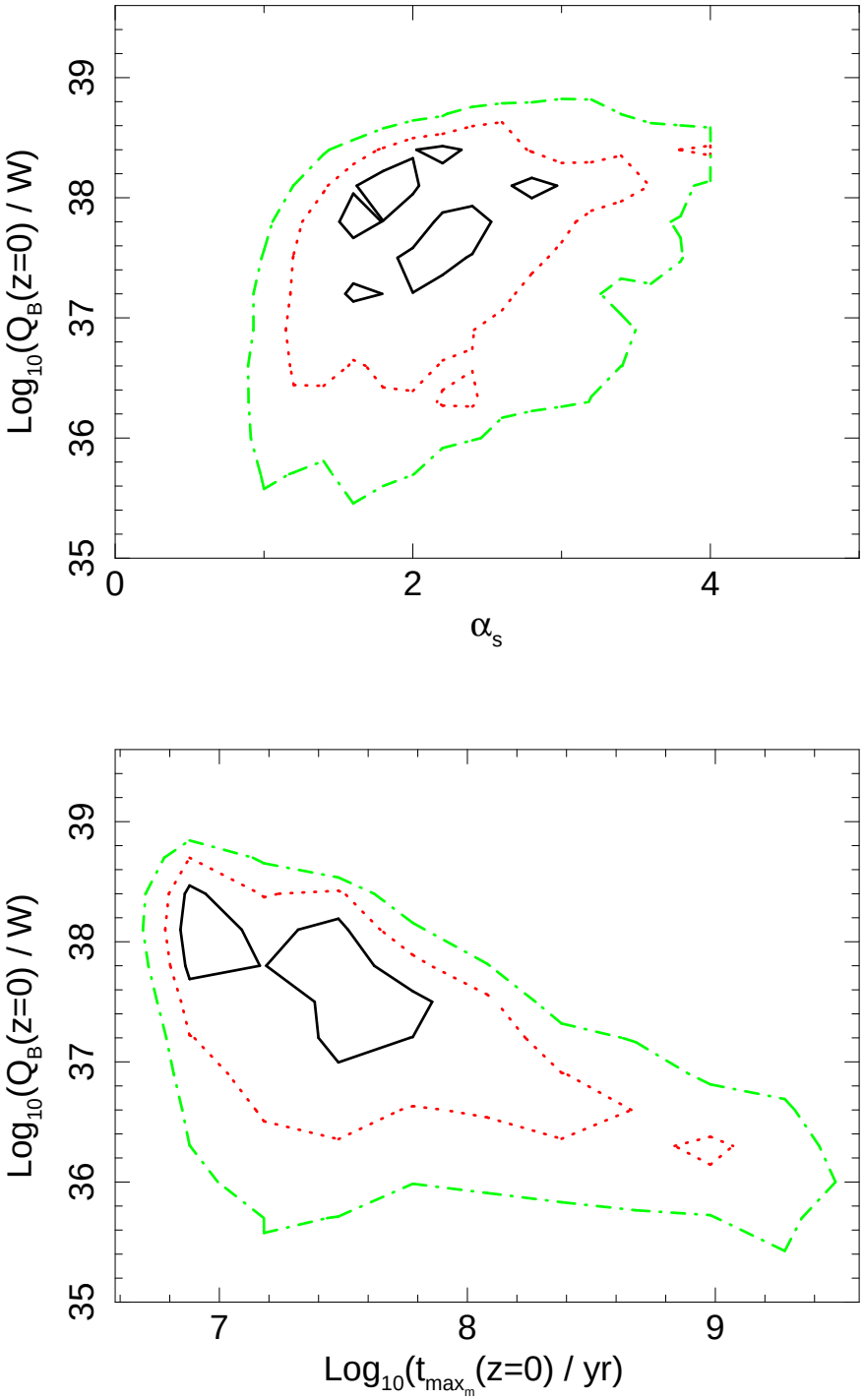

Figure 3.18: *Continued*.

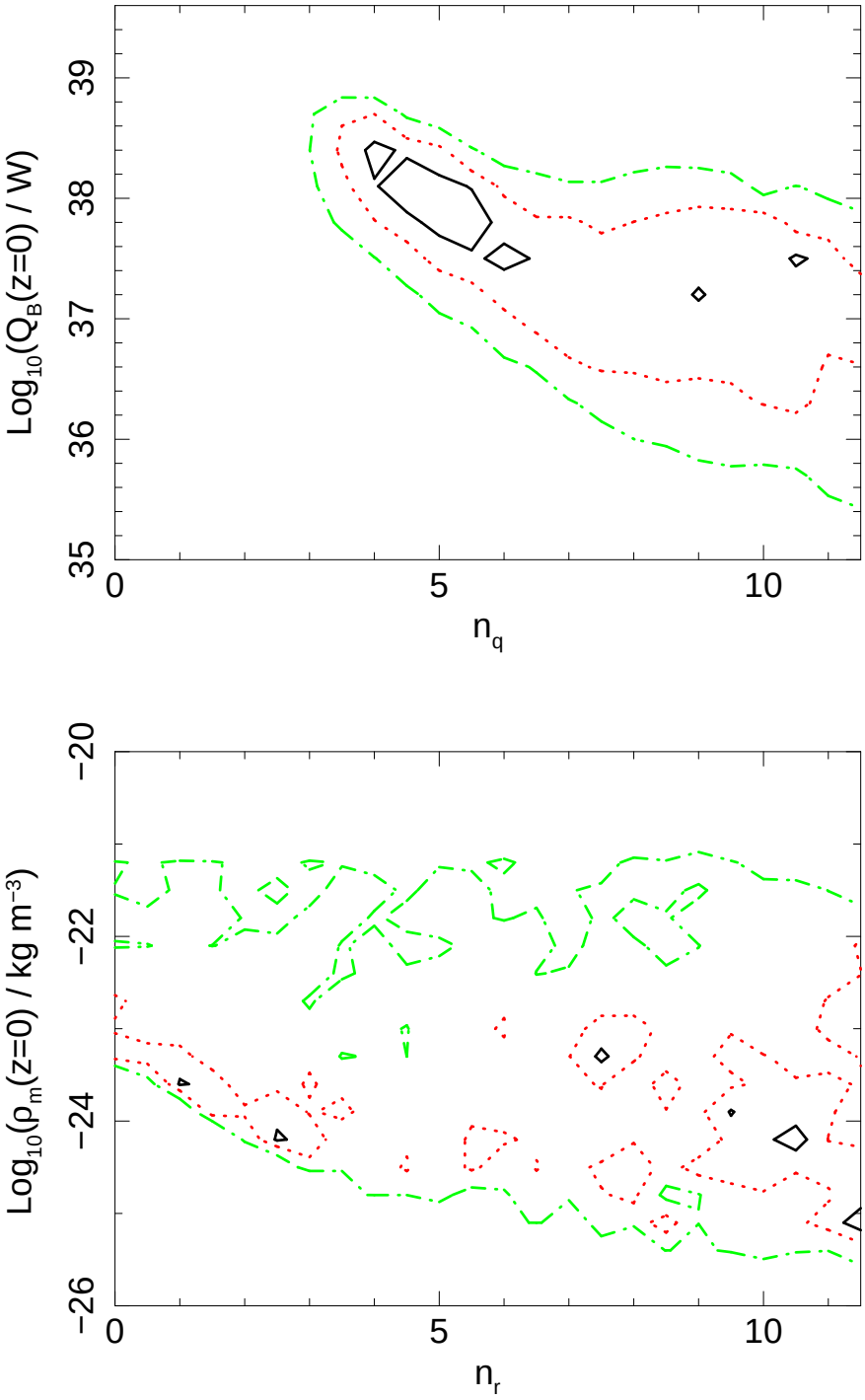

Figure 3.18: *Continued*.

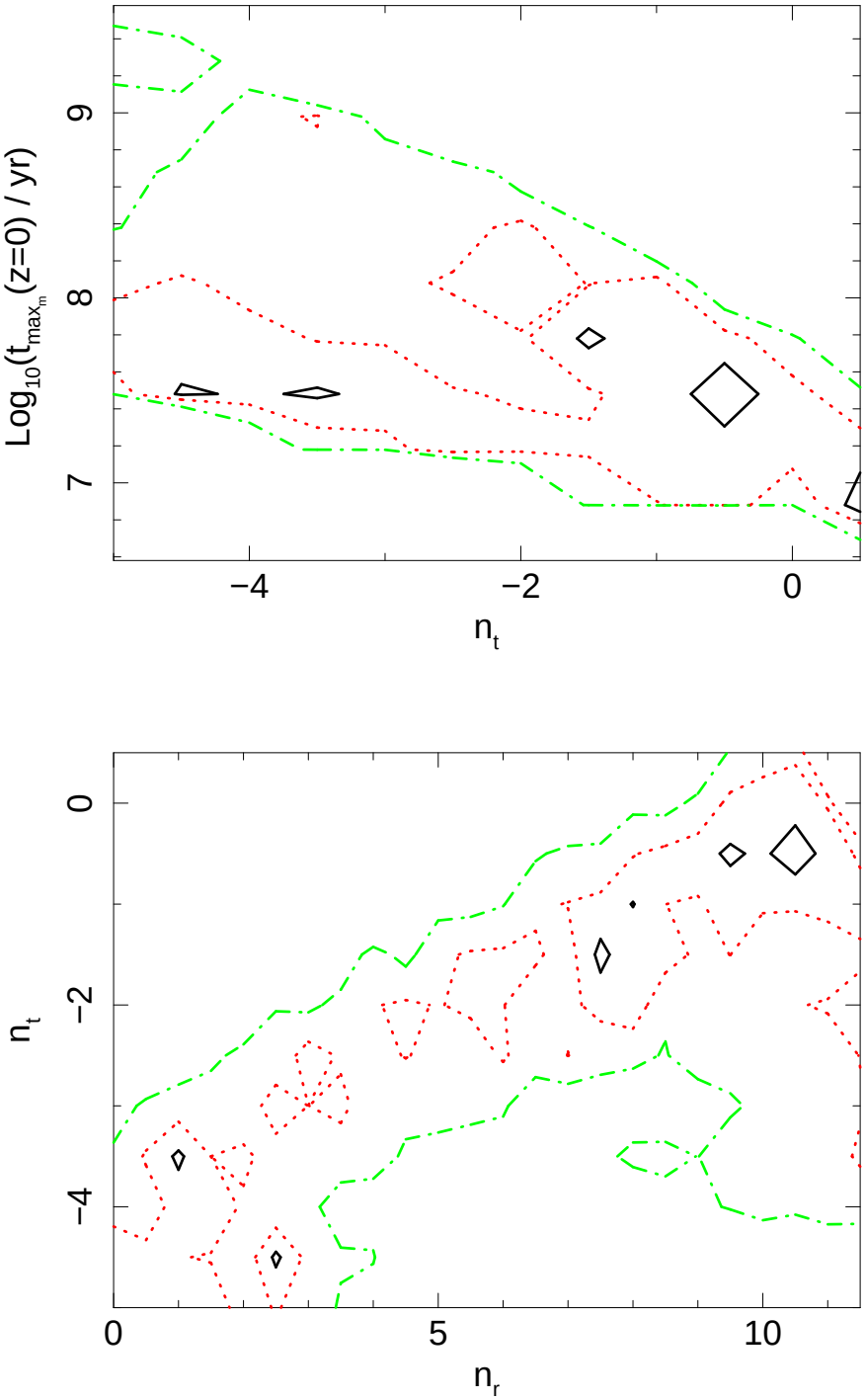

Figure 3.18: *Continued*.

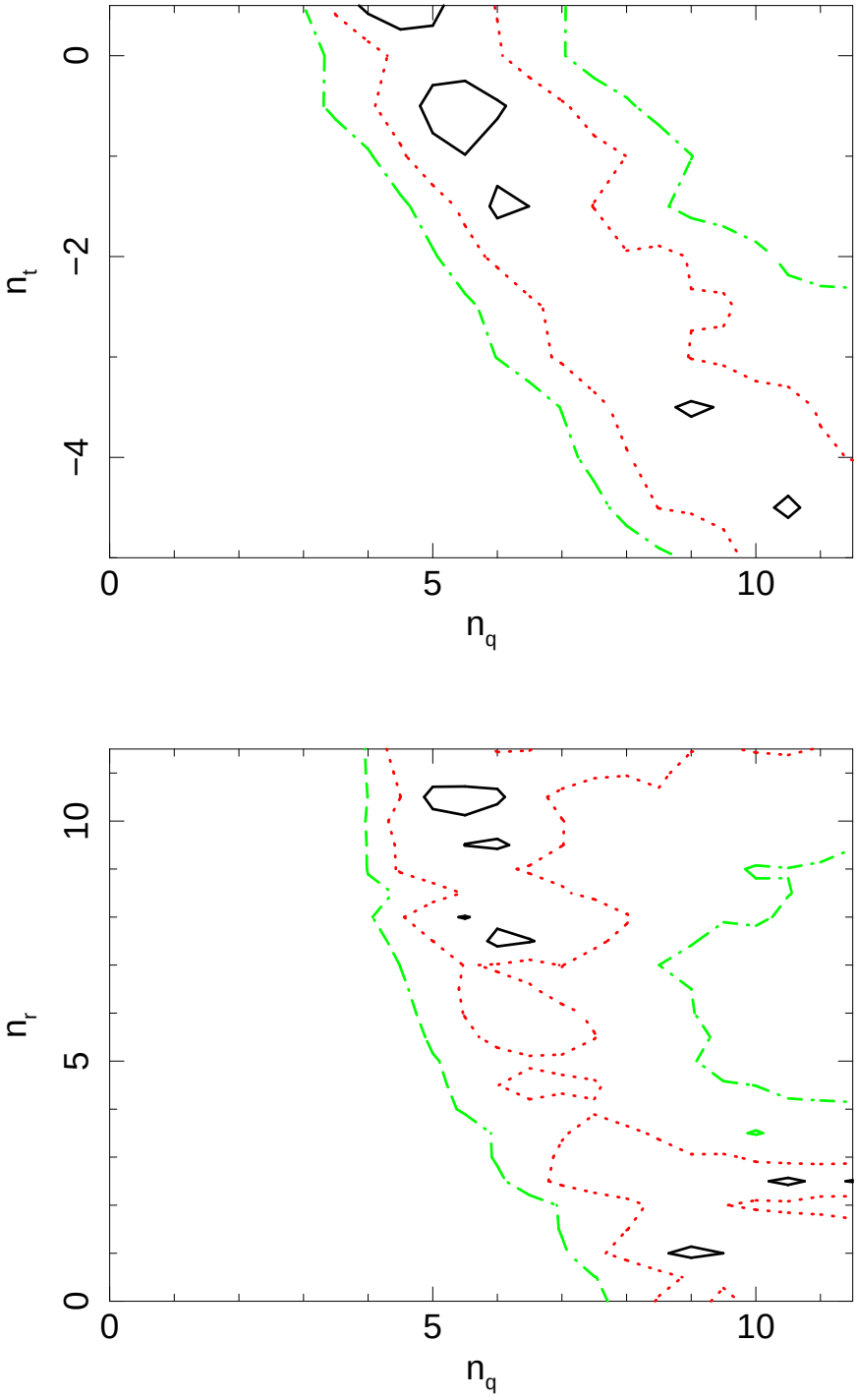

Figure 3.18: *Continued*.

The following can be deduced from the results regarding both model S and model W (consult Figures 3.17 – 3.18):

(i) As in the case of the independent-z fits, a degeneracy occurs between $Q_{\rm B}(z=0)-\rho_{\rm m}(z=0)$, between $Q_{\rm B}(z=0)-t_{\rm max_m}(z=0)$, and between $t_{\rm max_m}(z=0)-\rho_{\rm m}(z=0)$; however, here, in the combined-z fits these parameters are evaluated at redshift $z=0$. Similarly, for higher kinetic luminosity breaks lower gas densities of sources' environments are preferred and the estimated sources' lifetimes are relatively short. For lowest $Q_{\rm B}(z=0)$ dense environments and long lifetimes of the radio sources are favoured.

(ii) The $\alpha_{\rm s}$ parameter is well constrained, although the parameter is assumed to not evolve with redshift.

(iii) As in the case of the independent-z fits, the joint confidence intervals span approximately 3 orders of magnitude in kinetic luminosity break, $2-3$ orders of magnitude in the estimated maximum lifetimes of sources, and 5 orders of magnitude in the possible gas density of the environments.

(iv) If lower values (from within the confidence intervals) are assigned to the main parameters $(Q_{\rm B}(z=0),\rho_{\rm m}(z=0),t_{\rm max_m}(z=0))$ then their stronger cosmological evolution is required, whether positive (for $Q_{\rm B}(z=0)$ and $\rho_{\rm m}(z=0)$) or negative (for $t_{\rm max_m}(z=0)$). For instance, if kinetic luminosity break is taken to be $Q_{\rm B}(z=0)=10^{39}$ W its corresponding evolution with redshift is $(1+z)^4$, while if lower luminosity break value is considered, $Q_{\rm B}(z=0)=10^{36}$ W, then its redshift evolution is estimated to be much stronger, $(1+z)^{10}$.

(v) A strong degeneracy occurs between $n_{\rm q},n_{\rm r}$ and $n_{\rm t}$, and the parameters seem to compensate for each other; for high $n_{\rm t}$ values (strong lifetime evolution) high values of $n_{\rm q}$ and low values of $n_{\rm r}$ are favoured (that is strong kinetic luminosity break evolution, and weak gas density of the environments evolution are preferred). Such a strong degeneracy causes that the $n_{\rm q},n_{\rm r}$ and $n_{\rm t}$ parameters cannot be easily constrained, and additional constraints on the parameters are necessary. This is also discussed in §3.5.

(vi) An interesting result emerges for the kinetic luminosity break cosmological evolution, for which the trend with redshift seems to be unavoidable ($n_{\rm q}>3$). These results are discussed in detail in §3.8.

3.5 Central density – maximum age degeneracy

The degeneracy between central density and maximum age needs some extra attention as it seems to be often overlooked. The calculated radio lobe luminosity density of a radio source

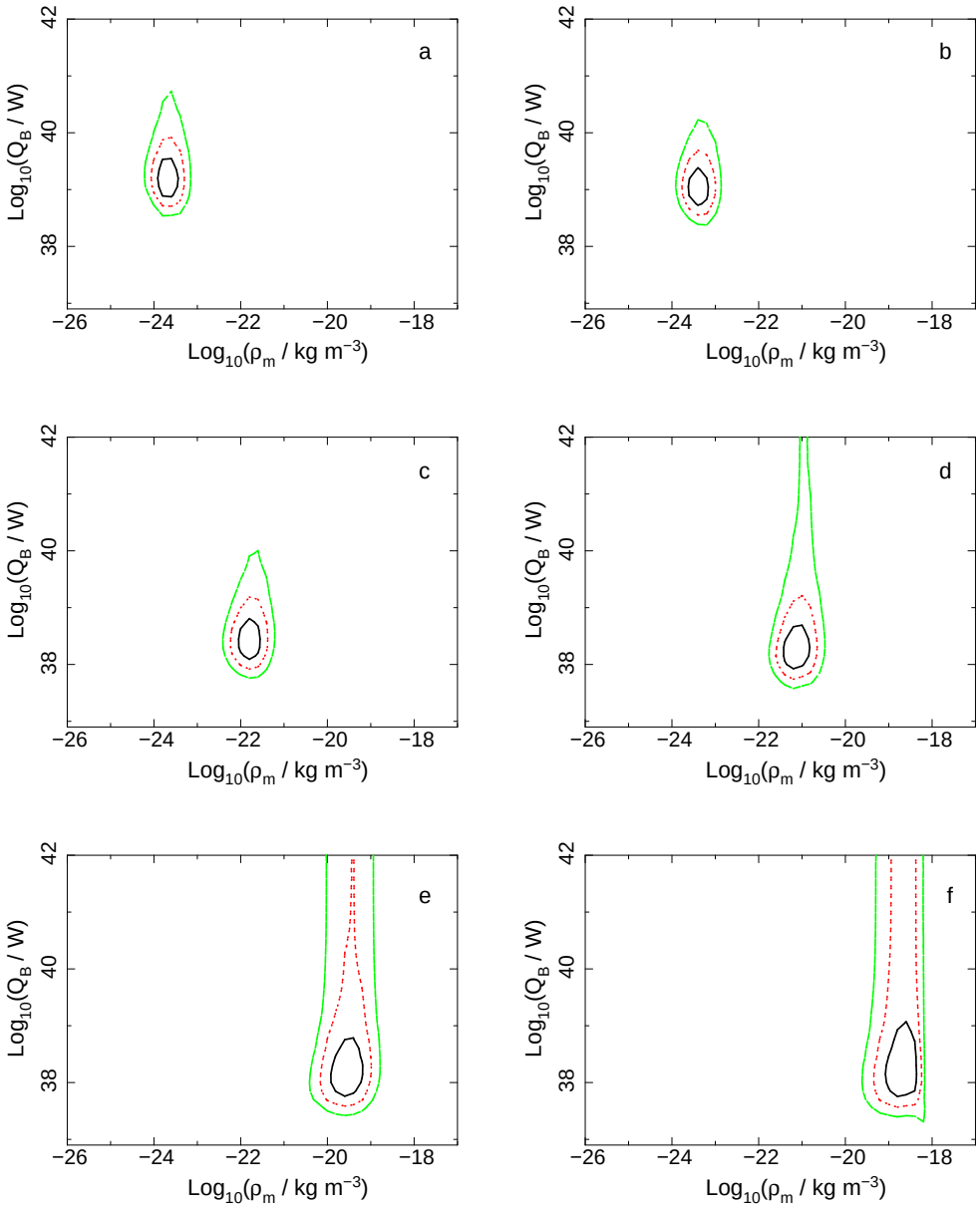

Figure 3.19: From top right: (a) the joint confidence intervals of the best-fitting $Q_{\rm B}$ and $\rho_{\rm m}$ for population of sources with fixed maximum lifetime of $t_{{\rm max}_{\rm m}} = 8.5 \times 10^6$ yr is presented, (b) with $t_{{\rm max}_{\rm m}} = 1.2 \times 10^7$ yr, (c) with $t_{{\rm max}_{\rm m}} = 6.8 \times 10^7$ yr, (d) with $t_{{\rm max}_{\rm m}} = 1.3 \times 10^8$ yr, (e) with $t_{{\rm max}_{\rm m}} = 5.4 \times 10^8$ yr, and (f) with the maximum source age of $t_{{\rm max}_{\rm m}} = 1.1 \times 10^9$ yr. In each case $t_{{\rm max}_{\rm m}}$ is drawn from log-normal distribution with $\sigma_{t_{{\rm max}_{\rm m}}} = 0.05$ (see §2.3.3). The independent-z fits of the Model S in the lowest redshift range ($z_1 \leq 0.3$) is presented. For each sub-plot the solid (black) line corresponds to 68.3 per cent of the best-fitting parameters for the particular choice of fixed $t_{{\rm max}_{\rm m}}$, the dotted (red) line corresponds to 95.4 per cent, and the dashed (green) contours contain 99.7 per cent of the best fits based on the ΔC statistics. It is clearly visible that the assumption on the maximum allowed age of the sources will strongly determine the density of the environment in which sources evolve (predominantly), as well as their jet powers (less strongly).

depends on its kinetic luminosity, central density and the age of the source. However, one must be aware that restricting one parameter will yield an adjustment in another. In particular, the maximum age of the sources and the central density in which sources evolve seem to be the most strongly correlated. From Eqn. 2.7 – 2.14 (see also Kaiser and Best, 2007, 2008) one can deduce that

$$L_\nu \propto Q^{\frac{12+2m-\beta(3+m)}{2(5-\beta)}} (\rho_o a_o^\beta)^{\frac{3+2m}{2(5-\beta)}} t^{\frac{6-4m-\beta(3+m)}{2(5-\beta)}} \int_{x_{\min}}^{1} C(x)\mathrm{d}x. \tag{3.5}$$

Assuming $m = 2.5$ and $\beta = 1.5$ (most commonly assumed values) and ignoring for a moment the energy losses term, one will see that

$$L_\nu \propto Q^{1.25} \rho_o^{1.15} t^{-1.75}. \tag{3.6}$$

Clearly, the radio lobe luminosity density, kinetic luminosity and all the other values are kept the same for a radio source, and a change is made only to its central density and the age, the two latter parameters will compensate for each other. For example, a change in the central density by a factor of 10 (reaching less dense environments) will yield a change in source age by a factor of 7 (implying younger ages) to maintain the same radio lobe and kinetic luminosities. Of course this is an approximation only as such a change will also yield changes in the source linear size and in the loss processes term $C(x)$ of Eqn. 2.14 (where $x = t_i/t$) since both depend on the stage of the source life. Note that Eqn. 3.6 cannot be used as an approximation for simple L_ν finding because the energy losses cannot be neglected. Eqn. 3.6 is used here solely for pictorial purposes.

One may also argue that the kinetic luminosity may compensate for the change of the source age instead of the ambient density (Eqn. 3.5). The presented results suggest that the $\rho_\mathrm{m} - t_{\max_\mathrm{m}}$ degeneracy is dominant. The effect of this degeneracy is seen in Figure 3.9 – Figure 3.16, and additionally in Figure 3.19 where results in the $Q_\mathrm{B} - \rho_\mathrm{m}$ plane for source populations of different assumed maximum ages are displayed.

3.6 The lifetimes of radio galaxies

The estimated maximum lifetimes of radio galaxies may seem to be rather low, especially given that sources of the observed ages of order of few $\times 10^8$ yr are known (e.g. $\sim 1.8 \times 10^8$ yr of B0319-454 reported by Saripalli *et al.* 1994, $\sim 1.4 \times 10^8$ yr in the case of B0313-683 reported by Schoenmakers *et al.* 1998). However, the presented here results are in agreement with other estimates of observed ages and total lifetimes of, specifically, 3CRR radio galaxies evaluated by either numerical simulations or multi-frequency radio observations (e.g. Alexander and Leahy, 1987; Machalski *et al.*, 2007; Wang and Kaiser, 2008; O'Dea *et al.*, 2009). Our results are also consistent with work of Bird *et al.* (2008)

based on an independent low redshift sample, who determined the maximum lifetime of the galaxies to be 1.5×10^7 yr. Further, the ages estimated by Machalski *et al.* (2004a) reach $1-2 \times 10^8$ yr, but only for giant radio sources, and for most normal radio galaxies they analysed, i.e. the ones with linear sizes smaller than 1 Mpc, ages few-10 times smaller were estimated. As a sanity check one can find that for the hardwired (in the simulations) maximum head advance speed of $0.4c$ a source of 1 Mpc in size may live for a maximum of 4×10^6 yr, while to increase the total lifetime to 1.6×10^8 yr, the source head advance speed would have to be of order of $0.01c$. Such a low head advance speed may be treated as a lower limit because the jet must be supersonic during the radio source lifetime to maintain the FR II morphology[1], and also classical double sources older than the inferred age are not observed. The model of Falle (1991) predicts that the source advance speed changes, i.e. decreases, with the age of the source. This would suggest that sources that initially have high maximum head advance speed, slow down as they get older and hence they reach older ages and smaller $v_{\rm max}$ are measured (e.g. Machalski *et al.*, 2007).

The radio samples which are currently been used contain the most powerful FR II radio galaxies and quasars, and the bias originating from the flux limit is particularly strong at high redshifts. This causes that only the youngest and most powerful sources are observed. Blundell and Rawlings (1999) suggested an explanation of the noticeable decrease with redshift in source lifetimes. The term 'Youth-Redshift degeneracy' has been coined to describe the effect. Due to the luminosity density – redshift degeneracy originating from the radio flux limits, at high redshifts one can observe only the most powerful objects. They seem to be also of smaller linear sizes as compared to the radio galaxies in the local Universe (Kapahi *et al.*, 1987; Barthel and Miley, 1988). The leading theoretical models of radio galaxy time evolution (e.g. KDA97, BRW99) predict a short initial phase of radio source growth where the radio lobe luminosity density increases (up to $\sim$few kpc), after which the radio lobe luminosity density decreases as the radio source ages and grows bigger (this behaviour is often depicted through the so-called evolutionary tracks, see e.g. KDA97). Therefore, to be able to reproduce linear sizes and radio lobe luminosities as observed at high redshifts, the radio galaxies must be younger than their low redshift equivalents. Based on the 3CRR and BRL samples the results indeed suggest a trend of the total radio source lifetimes decreasing with redshift. The best-fitting parameters found for the combined-z fits of the Models S and W indicate $n_{\rm t} \in [-3.5, -4.5]$, slightly stronger as compared to the results obtained by Wardle *et al.* (1998) who found $n_{\rm t} \cong -2.5$ and Wang and Kaiser (2008) who report $n_{\rm t} = -2.4$. However again, due to the degeneracy between $t_{\rm max_m}$ and $\rho_{\rm m}$ the strength of the possible evolution is not strongly constrained as it may be easily compensated by the redshift evolution of the central densities of the galaxy clusters or the kinetic luminosity break. Interestingly, a constant maximum lifetime for all redshifts is allowed, i.e. $n_{\rm t} \sim 0$, but this would require the cosmological evolution of $\rho_{\rm m}$ to be unfeasibly strong (see §3.7).

[1]The typical sound speed in a cluster medium is of order of $0.001-0.004c$ since the sound speed in the ICM must be similar to the velocity dispersion of the cluster (Fabian, 1994).

Unfortunately, at the current stage one is unable to verify whether the decrease in the maximum lifetimes of these radio sources is genuine, or whether this is just an observational bias due to the flux limit. Deeper high redshift radio samples are needed to resolve this issue.

3.7 Ambient gas densities

Some fraction (but note that not all) of the central gas densities estimated here are consistent with recent X-ray studies (e.g. Belsole *et al.*, 2007; Croston *et al.*, 2008b; Sanderson *et al.*, 2009). It can also be observed clearly that higher densities are favoured for earlier epochs. Redshift evolution of the source environments is expected, at least, due to the expansion of the Universe. Invoking textbook physics (see also Appendix E) it is known that

$$H^2(z) = H_0^2(\Omega_{\rm M}(1+z)^3 + \Omega_{\rm k}(1+z)^2 + \Omega_\Lambda), \tag{3.7}$$

where H is the Hubble parameter, H_0 is the Hubble constant, and the parameters $\Omega_{\rm M}$, Ω_Λ and $\Omega_{\rm k}$ define the matter density, the vacuum density and the spatial curvature respectively. From the above equation one can deduce that the critical density evolves ($\rho_{\rm c}$) with redshift as

$$\rho_{\rm c}(z) = \frac{3H_0^2}{8\pi G} \times [\Omega_{\rm M}(1+z)^3 + \Omega_\Lambda] \tag{3.8}$$

where G is the gravitational constant and assuming a flat Universe ($\Omega_{\rm k} = 0$). Since the radio galaxies are often found in clusters and galaxy groups, one may expect that their immediate environments will undergo similar evolution to the one predicted by models of cluster formation (see e.g. Arnaud, 2005, for a review and a discussion on the accordance between predictions from the theoretical models and the observational constraints on the evolution of clusters properties). Structure formation models predict that the mean dark matter density (the predominant constituent of galaxy clusters) scales as the critical density of the Universe, that is again $\rho_o(z) \propto \rho_{\rm c}(z) \propto H^2(z)$. The critical density will, therefore, change between redshifts $z_{\rm n2}$ and $z_{\rm n1}$ by a factor of $\rho_{\rm c}(z_{\rm n2})/\rho_{\rm c}(z_{\rm n1})$. If $z_{\rm n1} = 0$ and $z_{\rm n2} = 2$ then the density would be expected to be higher at $z_{\rm n2}$ by a factor of $z_{\rm n2}/z_{\rm n1} \cong 8.8$, equivalent to ~ 0.94 in logarithmic scale, and to the redshift dependence of approximately $(1+z)^2$. Similar trends have been recently found by Poggianti *et al.* (2010), and, as they point out, it can be also deduced from previous observational studies (e.g. Dressler, 1980; Dressler *et al.*, 1997). On the other hand, O'Dea *et al.* (2009) do not observe any density evolution up to $z \cong 0.5$. The best-fits for the combined-z fits of the tested models (Figure 3.17 and Figure 3.18) clearly show that $n_{\rm r}$ is degenerate and strongly dependent on $n_{\rm t}$ and $n_{\rm q}$; the value expected by the galaxy cluster cosmological evolution models and the effect of the

expanding Universe is possible for certain values of $n_{\rm t}$ and $n_{\rm q}$, but is not unique. Some may argue that environments of FR II sources may depend on the cosmological epoch. That is, beside the argument of the evolution following the expansion of the Universe, at low redshifts weak clusters and galaxy groups are favoured by FR II sources, while rich galaxy clusters are preferred at high redshifts (e.g. Deltorn *et al.*, 1997; Zirbel, 1997; Wold *et al.*, 2000). If this is the case the effect will be convolved in the $n_{\rm r}$ parameter resulting in evolution stronger than the expected $n_{\rm r} \sim 2.0-2.5$. The possible values of $n_{\rm r}$ and their consequences are discussed further in §3.8.

As it is shown in §3.10 the spread of the log-normal distribution of the density has a rather small effect on the results. This is highlighted by the fact that when a delta function is employed the final results are still in good agreement with the observed samples. It may be concluded therefore that at the current stage it is not possible to constrain the shape of the population ambient density distribution. Further, the mean central density value will depend on the assumed a_o and β, and hence if this study assumptions for these values are incorrect one may simply scale the fitted densities with the $(\rho_o a_o^{\beta})$ relation. It is currently assumed that there is no redshift evolution of the core radius or the density profile slope. If there is any intrinsic change this will be subsumed by the mean density value, possibly resulting in a stronger trend with redshift.

3.8 Kinetic luminosities of powerful FR II sources

The kinetic luminosity functions (KLFs) of the radio source populations generated with the best-fitting parameters for all redshift ranges and models are presented in Figure 3.20, while in Figure 3.21 the kinetic luminosity distributions and their corresponding underlying parent populations from which the observed samples originate are plotted for each redshift range, size bin and model. There are two main conclusions. Firstly, the higher the redshift the more powerful the jets are that are included; at $z < 0.3$ the highest Q are of order 10^{40} W (Model S), while in the highest redshift range, z_3, the most powerful sources seem to have jet luminosities reaching 10^{42} W (Figure 3.20). Secondly, the larger the radio sources are the more powerful AGN on average they host (Figure 3.21). The second effect seems to be much milder than the dependence on redshift, but it is present; a similar pattern has been already observed by Gopal-Krishna *et al.* (1989).

3.8.1 Differences between results of Model S and W

As can be seen from Figure 3.20 and Figure 3.21, although the parent populations of Model S and W are different, the predicted flux-limited samples of the two models are very similar. More interestingly, one would expect kinetic luminosities of sources of FR II type to be at least 10^{37} W. Indeed, although radio sources of kinetic luminosities of 10^{36} W are generated in the Monte Carlo simulation, these do not contribute to the observed populations. Some

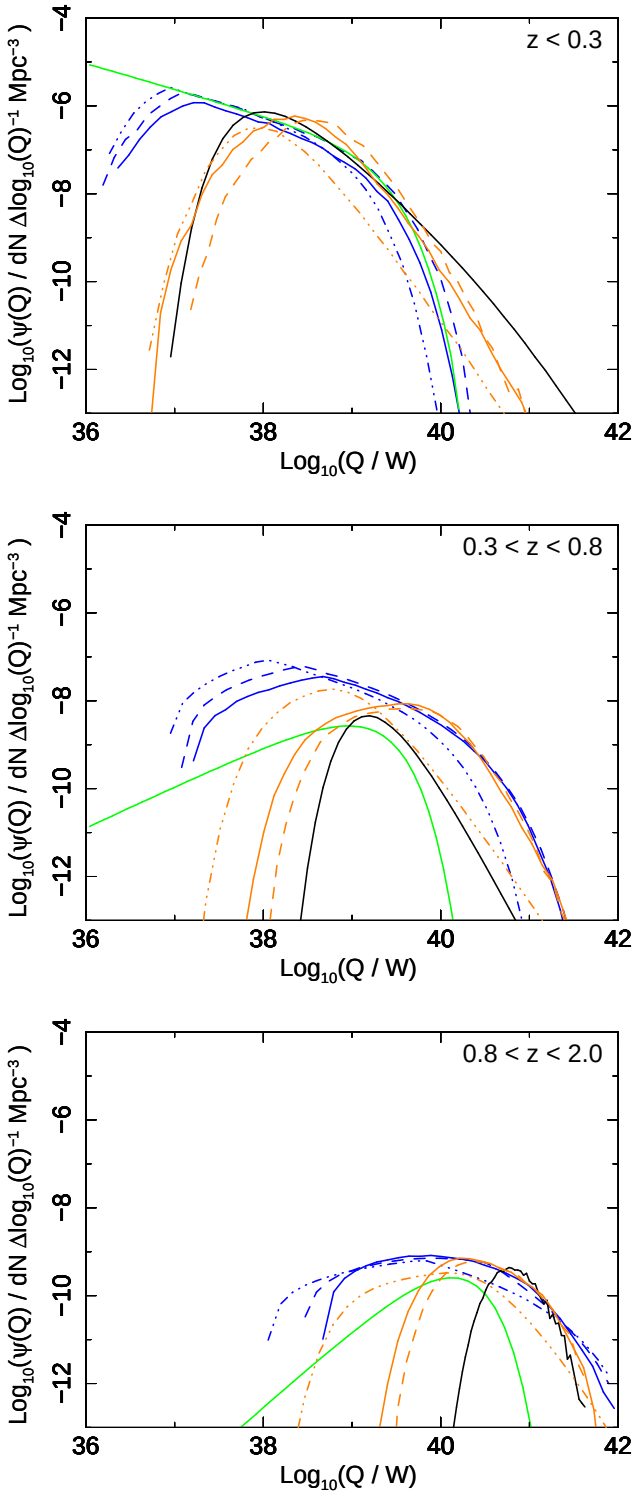

Figure 3.20: Kinetic luminosity functions generated with the best-fitting parameter sets of the independent-z fits of Model S (solid line, green) and Model W (solid line, black) for all redshift ranges, and combined-z fits of Model S (blue) and Model W (orange). The combined-z fits of Model S and Model W show their best fits (solid blue, solid orange respectively), and two restricted cases where $n_{\rm r}$ parameter is set to $n_{\rm r} = 2.5$ (dashed) and $n_{\rm r} = 4.0$ (dash-dot-dot-dotted).

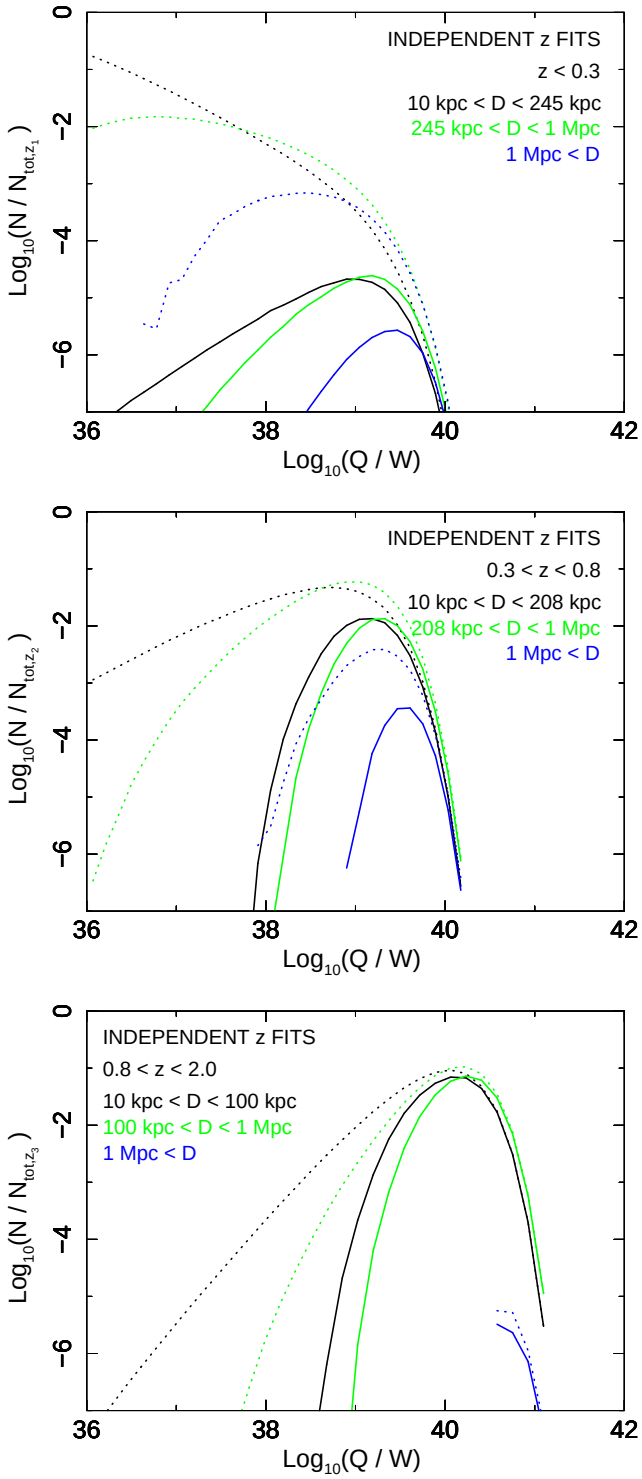

Figure 3.21: Functions showing kinetic luminosity distributions (normalised for each redshift range separately) of the observed, that is flux limited, sources (solid lines) and the corresponding underlying parent populations from which the observed samples originate (dotted lines). In each plot, for each redshift range and model considered, kinetic luminosity distributions for separate linear size bins (as used in fitting) are plotted. The exact radio galaxy linear sizes (D) falling into each size bin are detailed in corresponding panels. [*..continued on next page*]

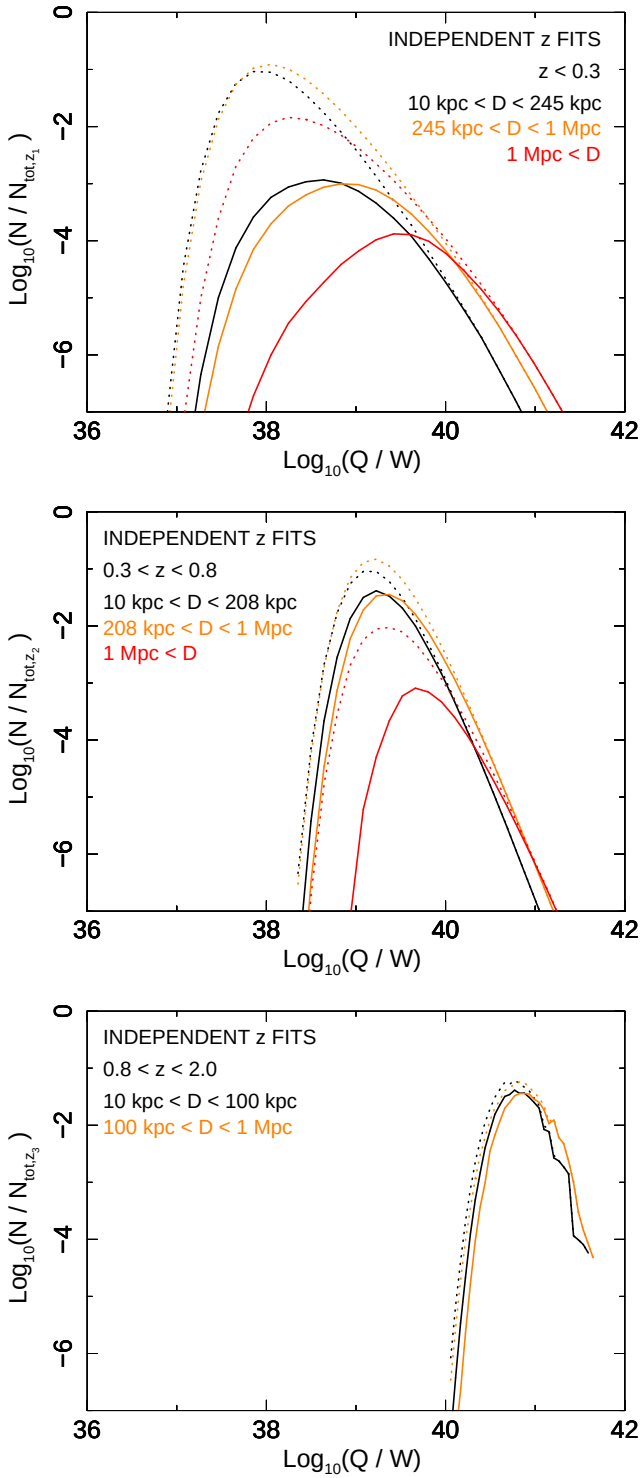

Figure 3.21: [*Continued*..] Colours denoting linear sizes of the radio galaxies are labelled. The distributions change for different redshifts as well as for different radio galaxy linear sizes, where larger radio sources on average seem to be also more powerful. Note that these distributions of parent populations depend strongly on the slope α_s which for $z > 0.3$ is associated large uncertainties. Here, for pictorial purposes, only the best-fits for each redshift range are presented.

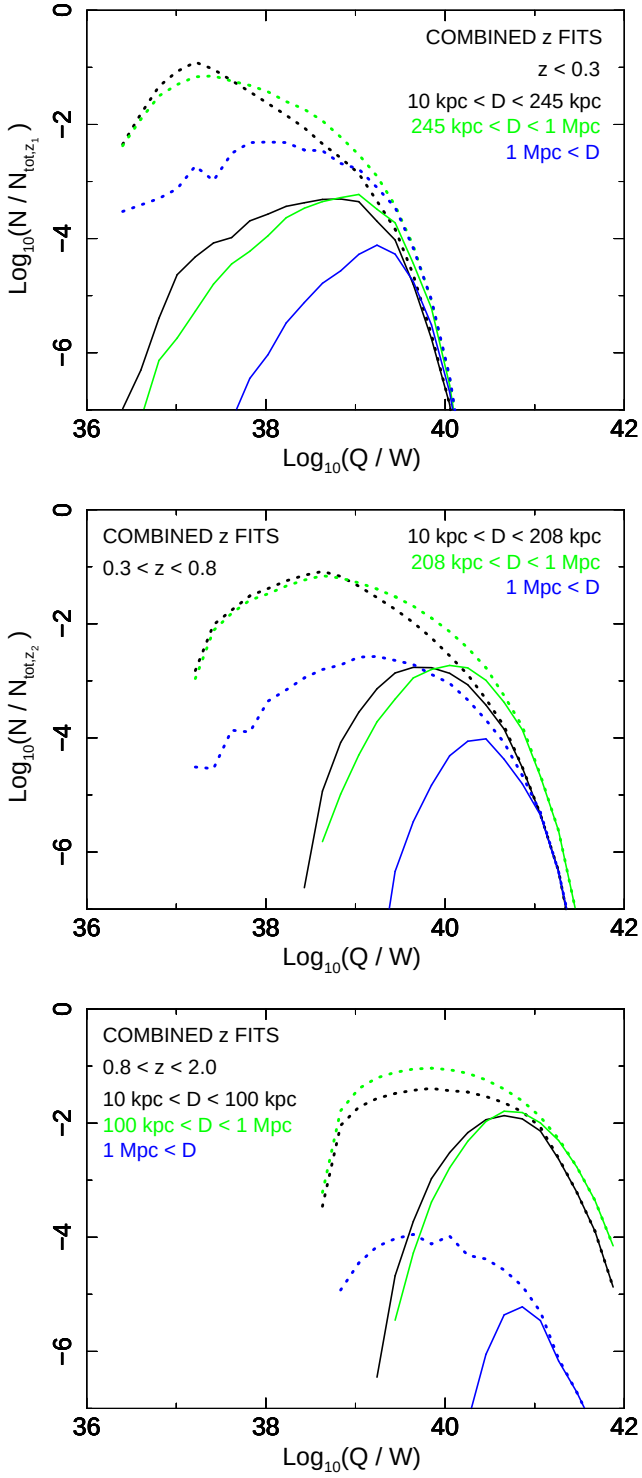

Figure 3.21: *Continued*.

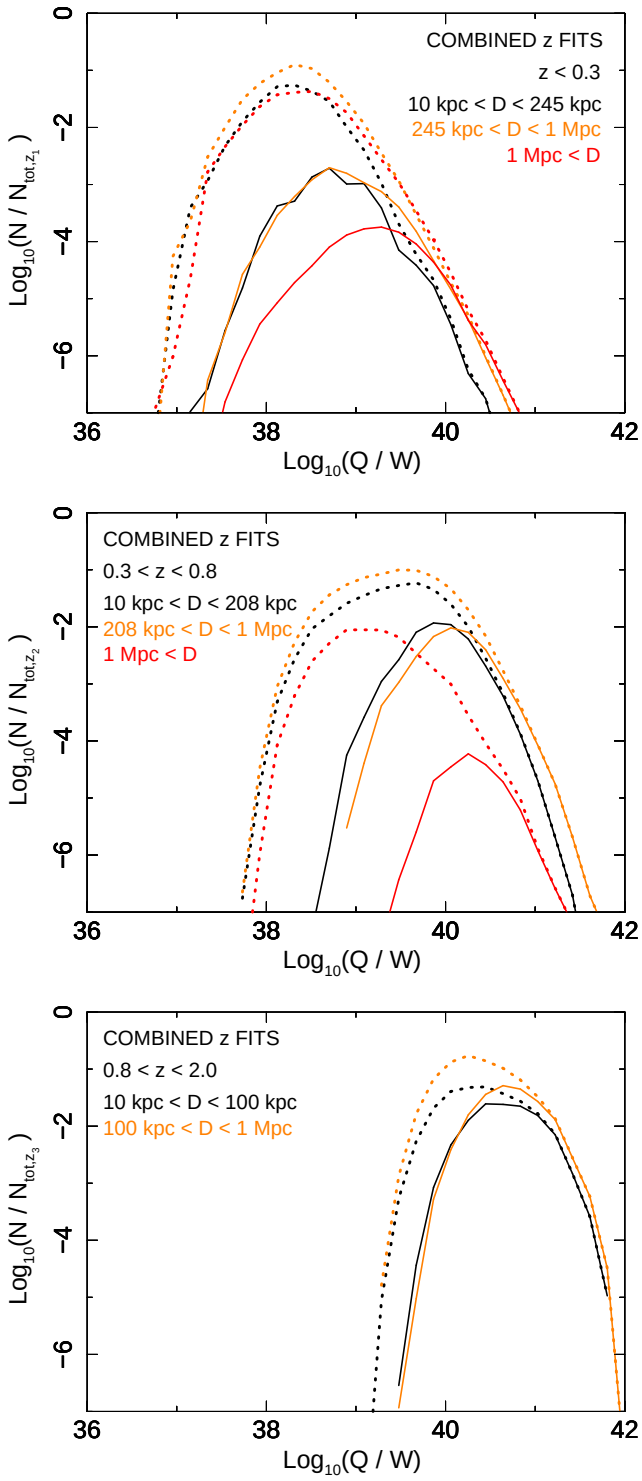

Figure 3.21: *Continued*.

Table 3.4: The best-fitting parameters for the independent-z fits of the model which uses bending power-law as the initial distribution of kinetic luminosities (§3.8.2) for each redshift range. Due to occurring degeneracies (§3.5) one should always consult the corresponding confidence intervals (see Figure 3.22). 90 per cent errors are quoted.

z	$\log_{10}(Q_{\rm B}/{\rm W})$	$\alpha_{\rm S}$	$\log_{10}(\rho_{\rm m}/{\rm kg\,m^{-3}})$	$\log_{10}(t_{\rm max_m}/{\rm yr})$	$p-$value
z_1	$38.70^{+0.45}_{-0.15}$	$0.2^{+0.6}_{-1.1}$	$-23.4^{+1.0}_{-0.4}$	$7.23^{+0.45}_{-0.15}$	0.223
z_2	$39.15^{+0.30}_{-0.15}$	$-0.4^{+0.9}_{-5.2\dagger}$	$-20.4^{+1.8}_{-1.2}$	$7.83^{+0.60}_{-0.45}$	0.787
z_3	$41.10^{+3.0\dagger}_{-0.15}$	$-2.5^{+2.0}_{-1.8}$	$-23.6^{+0.6}_{-(<0.2)\ddagger}$	$5.93^{+0.15}_{-(<0.15)\ddagger}$	0.784

Notes. The resolution of the results is $\Delta = 0.2$ for $\log_{10}(\rho_{\rm m})$, $\Delta = 0.15$ for $\log_{10}({\rm Q_B})$ and $\log_{10}({\rm t_{max}})$, and $\Delta = 0.1$ for $\alpha_{\rm s}$ for the simple cases, and $\Delta = 0.2$ for $\alpha_{\rm s}$, $\Delta = 0.3$ for $\log_{10}(\rho_{\rm m})$, $\log_{10}({\rm Q_B})$ and $\log_{10}({\rm t_{max}})$, $\Delta = 0.5$ for $n_{\rm t}$, $n_{\rm r}$ and $n_{\rm q}$ for the continuous evolution cases.
† For errors which may be extending beyond the searched ranges (see Table 3) value up to the range border is quoted.
‡ If errors are smaller than their respective resolution, the value of $< \Delta$ is quoted.

consideration is also needed of the lowest redshift bin best fits for Model W, where the kinetic luminosity break reaches somewhat low values and the slope is flatter compared to the other redshift ranges. The kinetic luminosity distribution function of Model W has been used by Willott *et al.* (2001) as their initial kinetic luminosity distribution function but for the most powerful sources only. In their work the population of radio galaxies and radio-loud quasars was divided based on the emission line characteristics rather, that is high- and low-excitation radio galaxies (HEG and LEG respectively as introduced in §1.2.3), than the historical FR I and FR II classes. HEG include powerful FR II and the most powerful FR I sources, while LEG include most FR Is and low-luminosity FR II objects. As mentioned before Model W may not be able to reproduce the faint end of the distribution. Contrary to Willott *et al.* (2001) low luminosity FR IIs are included in this study and perhaps this is the cause of the observed shift of $Q_{\rm B}$ and $\alpha_{\rm s}$.

3.8.2 Bending power-law as the initial distribution of kinetic luminosities

The thin, dotted lines in Figure 3.21 represent the possible parent populations generated according to the assumed distribution functions. The flux limit of the radio catalogues used is very high, and hence only the most powerful sources are observed; as estimated in performed here simulations their kinetic luminosities do not drop below $10^{37} - 10^{38}$ W. In such a strong flux limit regime either of the kinetic luminosity distribution functions

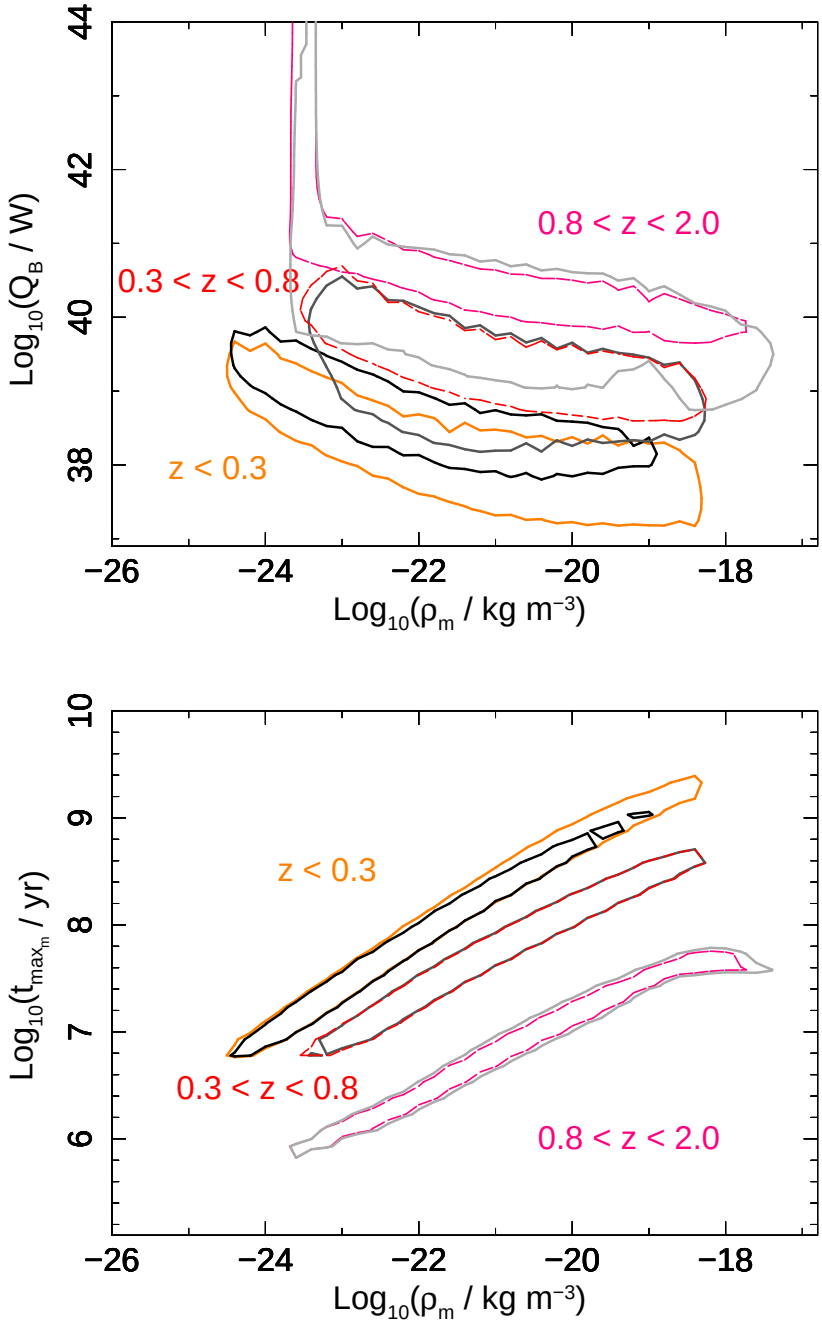

Figure 3.22: Joint 90 per cent confidence intervals for the independent-z fits of the bending power-law model (§3.8.2, orange for z_1, pink for z_2, red for z_3) and Model S (black for z_1, dark grey for z_2, light grey for z_3) for all redshift ranges are shown. Contours are based on ΔC statistics (see §2.4). The best-fitting parameters of the bending power-law model (Table 3.4) are consistent with the data at the 90 per cent level.

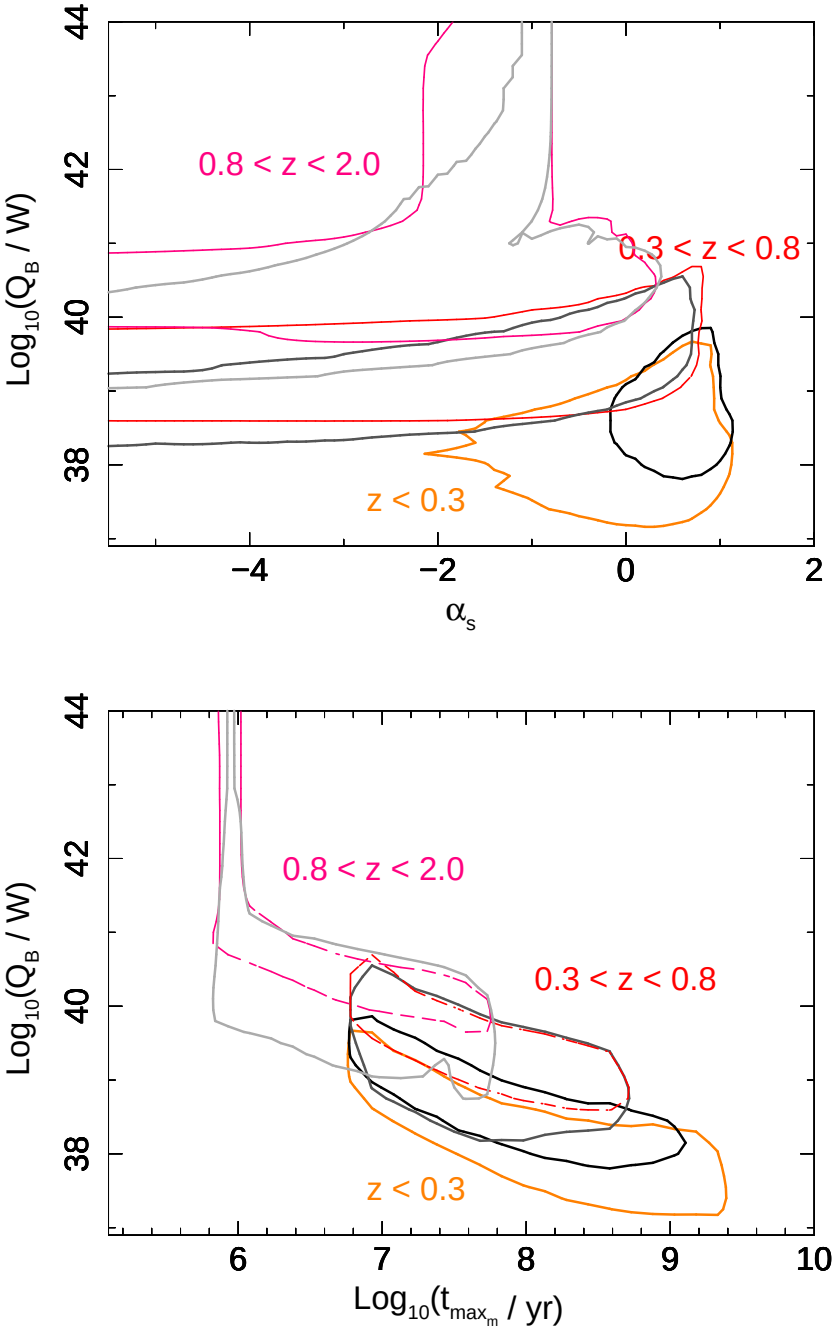

Figure 3.22: *Continued*.

(Models S and W) will shape the faint power end of the luminosity functions on the basis of a good fit to the high power end. However, with the lack of observed sources with $Q < 10^{38}$ W the faint end of the function is highly unconstrained especially at higher redshifts where, given currently used radio samples, only the most powerful sources are considered. To investigate this issue pre- and post- kinetic luminosity break slopes were attempted to be fitted separately. To do this the so-called curved power-law distribution has been tested

$$\psi(Q)\,\mathrm{d}Q = \psi^* \left[\left(\frac{Q}{Q_\mathrm{B}} \right)^{-\alpha_{s1}} + \left(\frac{Q}{Q_\mathrm{B}} \right)^{-\alpha_{s2}} \right] \mathrm{d}Q. \tag{3.9}$$

where α_{s1} describes the pre-break slope of the function, and α_{s2} the post-break slope. To avoid introducing more free parameters it has been decided to set the high power end of the kinetic luminosity distribution function to $\alpha_{s2} = 2.2$ (after the radiative luminosity functions of Hopkins *et al.*, 2007b), and allowed the pre-break slope to vary.

The results, while assuming the curved power-law as the initial distribution function of source kinetic luminosities, are in good agreement with those found with the Model S. The faint end of the kinetic luminosity function is well constrained in the lowest redshift range, but since now it is not dependent on the high power end of the function it becomes highly unconstrained at higher redshifts. It is necessary, therefore, to include lower luminosity radio samples in such an analysis to investigate the faint end of the kinetic luminosity functions. The best-fitting parameters found are listed in Table 3.4, and the confidence intervals are displayed in Figure 3.22.

3.8.3 Cosmic downsizing

The concept of cosmic downsizing, as an anti-correlation between the stellar mass of galaxies and the epoch of their formation, was introduced by Cowie *et al.* (1996). Since then, the term has been broadened to include the AGN evolution that has manifested similar anitihierarchical trends. The suggestion that the low-luminosity AGN X-ray luminosity functions seem to peak at lower redshifts than those of the luminous quasars (Ueda *et al.*, 2003; Hasinger *et al.*, 2005) has been interpreted as implying black hole anitihierarchical growth, and hence seems to be analogous to the star-forming galaxy downsizing (e.g. Merloni and Heinz, 2008). Furthermore, since the growth of the black hole and its kinetic luminosity may be linked, Merloni and Heinz (2008) and Cattaneo and Best (2009) suggested that the kinetic energy density of these active galaxies undergoes a similar cosmological evolution such that the most powerful jets are found at earlier epochs. Merloni and Heinz (2008) based their findings on the analysis of radio core kinetic luminosity functions, while Cattaneo and Best (2009) analysed imprints of the extended radio emission on the X-ray emitting plasma. It should not be surprising, therefore, if such an effect is seen in the presented here results. The results of the independent-z fits already suggest a

redshift evolution of the kinetic luminosity break. Moreover, the results of the combined-z fits of the fitted models confirm that this trend with redshift may be rather strong. Of course, the strength of this cosmological evolution depends on the assumed evolution of the sources' maximum lifetime and/or environment in which sources grow due to previously discussed degeneracies. One of the most plausible cases, where the galaxy cluster central environments evolve with the expanding Universe and according to the galaxy cluster evolutionary models, would require $n_{\rm r} \cong 2.0-2.5$, and this will lead to $n_{\rm q} = 9.5$ and $n_{\rm t} = -3.0$. Given that $Q_{\rm B}(z=0) \cong 2\times10^{38}$ W, such a strong redshift evolution would imply $Q_{\rm B}(z=2.0) \cong 6.8\times10^{42}$ W. This value is rather high, the highest kinetic luminosities of FR II radio sources estimated in other works are of order of 10^{41} W. Moreover, if one assumes that all these radio sources power their jets via accretion at their Eddington limits then the most powerful objects inferred here, at $z\sim2.0$, would host black holes of masses of $\sim5\times10^{11}$ M$_\odot$, while the most massive AGNs' black holes do not exceed $\sim10^{10}$ M$_\odot$ (e.g. McLure and Dunlop, 2004; Natarajan and Treister, 2009; Steinhardt and Elvis, 2010, 2011). Yet, equivalently to the independent-z fits, at these high redshifts the $Q_{\rm B}$ values are of such small number density that the highest kinetic luminosities that contribute to the population do not reach 10^{42} W (Figure 3.20).

Energy extraction from black hole spin is an attractive way to explain high jet luminosities and efficiencies (e.g. Penrose and Floyd, 1971; Blandford and Znajek, 1977; Rees *et al.*, 1982; Meier *et al.*, 1997; Meier, 1999). After Meier (2002) I denote

$$Q \propto j^2 B_{\rm pol}^2 (M_{\rm BH}/M_\odot)^2, \tag{3.10}$$

where j is the black hole spin and $B_{\rm pol}$ is the poloidal magnetic field. In such a case, for a given kinetic luminosity the higher the spin is, the less massive the black hole must be. However, one must bear in mind that the strength of the poloidal magnetic field will have a direct effect on the efficiency of the BH rotational energy extraction (for discussion on this issue see Meier, 2002). A combination of accretion and spin may play a significant role in producing the kinetic luminosities estimated here. However, the presented here results suggest that also environments and lifetimes of radio galaxies have a direct influence on the radio luminosity density of large scale structures of radio galaxies. It is worth considering, therefore, whether it is possible to reduce the redshift evolution in $Q_{\rm B}$ based on the interplay between the environments and radio galaxy lifetimes in the results. For instance, the $Q_{\rm B}$ cosmological evolution of $n_{\rm q} = 7.0$ will yield milder evolution of the radio source maximum lifetimes, $n_{\rm t} = -1.0$, and the trend with redshift of the galaxy cluster central densities can be as strong as $n_{\rm r} = 10.5$ (Model S) or even $n_{\rm r} = 11.5$ (Model W). With this pattern of cosmological evolution the kinetic luminosity break would reach $\sim1\times10^{41}$ W at $z=2.0$, which further implies maximum black hole masses of 10^{10} M$_\odot$ if the sources accrete close to their Eddington luminosity, and jets are predominantly accretion powered. However, this causes $n_{\rm r}$ to be unfeasibly strong. One may get more realistic results while assuming

$n_r = 4.0$, as then the results show that $n_q = 8.0$ and $n_t = -2.5$, which leads to $Q_B(z = 2.0) \cong 6.6 \times 10^{41}$ W, $t_{max_m}(z = 2.0) \cong 3.9 \times 10^6$ yr, and $\rho_m(z = 2.0) \cong 4 \times 10^{22}$ kg m^{-3} (Model S). The redshift evolution of the central densities may seem to be rather high, since at $n_r = 4.0$ it would exceed the effect from the Universe's expansion; however, as discussed in §3.7 such a strong evolution may be realistic if some intrinsic change in the environments, or other effect such as evolution of core radius, takes place. Alternatively, radio sources may be allowed to reach older ages than the ones found with the best-fitting parameters (but kept within the confidence intervals as found in this work). To lower the kinetic luminosities the sources would have to be younger or reside in higher density environments than the best-fitting parameters suggest, or undergo a combination of the two effects. For instance, if one attempts to match the kinetic luminosities and ages estimated by Rawlings and Saunders (1991) for 3CRR sources, the lifetimes would have to be allowed to reach 10^8 yr, and hence sources would have to reside in very high density environments. Finally, there is a possibility that, contrary to what has been assumed so far, the intrinsic source parameters are not independent. Scenarios where Q and t, and/or t and R_T are correlated are sometimes considered, but are beyond the scope of the current work.

It is necessary to point out that as the cosmological evolution of the source parameters is certainly real and is not an effect of an observational bias due to high flux limit of the observed samples, the location of the kinetic luminosity break can be only constrained in the highest redshift bin. From the results it seems that in the lower redshift bins the Q_B must be at the lower end of the luminosities that still contribute to reconstruction of the observed samples, but its exact location is uncertain (Figure 3.21). In addition, one may notice in Figure 3.21, that the independent-z fits predict lower number density of sources than the combined-z fits at intermediate and high redshifts. The reason for this behaviour lies in tying the α_s exponent of Eqn. 2.19 and Eqn. 2.20 in the case of the combined-z fits, where α_s is required to stay the same for all redshifts (unlike for the independent-z fits where the exponent may vary freely between redshift ranges). The best fits of both model S and W of the combined-z fits predict much flatter slopes of the kinetic luminosity distributions than the independent-z fits. This will cause the existence of low radio luminosity density sources that are not observed due to the high flux limit of the samples, but are unveiled in the KLFs. Both of these issues this may be verified with larger samples with lower flux limits than are currently being used in this study.

3.9 Constraints on AGN duty cycles

The black hole masses of massive elliptical galaxies, which are typical hosts of powerful radio galaxies, are known (e.g. Wolfe and Burbidge, 1970; Wu *et al.*, 2002; Dunlop *et al.*, 2003; Gadotti and Kauffmann, 2009). Hence, once number densities and kinetic luminosities of the sources have been estimated, one can set constraints on the AGN duty cycle which defines the fraction of black holes being active at a particular cosmological epoch.

The duty cycle, $\delta(M_{\rm BH},z)$, is defined as

$$\delta(M_{\rm BH},z) = \frac{\phi(M_{\rm activeBH},z)}{\phi(M_{\rm BH},z)}, \tag{3.11}$$

where $\phi(M_{\rm activeBH},z)$ is the space density of active AGN with mass M and at the redshift z, while $\phi(M_{\rm BH},z)$ analogously defines the space density of all AGN (see also Kelly *et al.*, 2010). Since in this work other types of radio-loud AGN are excluded, e.g. FR Is and blazars, I shall refer to the duty cycle of FR II radio galaxies only in this discussion; this will be denoted by $\delta_{\rm FRII}(M_{\rm BH},z)$.

A typical FR II source can be assumed to have a black hole mass of $\sim 10^9$ $M_\odot$, and initially it is assumed that there is no evolution in the BH masses with the cosmological epoch. If one assumes that these are the most typical sources during each epoch, then the typical kinetic luminosity of these black holes is around the value of $Q_{\rm B}$ of the considered cosmological epoch. For the lowest redshifts, with $Q_{\rm B} \simeq 10^{39}$ W, the space number density is approximately $\phi(M_{\rm activeBH},z_1) \sim 10^{-7}$ dN Mpc$^{-3}\Delta\log_{10}(Q)^{-1}$ (Figure 3.20); $\phi(M_{\rm activeBH},z)$ is found analogously for the other two redshift bins. These values are compared with the local black hole mass functions compiled by Shankar *et al.* (2009), which give approximately $\phi(M_{\rm BH}=10^9 M_\odot, z=0) = 10^{-4}$ dN Mpc$^{-3}\Delta\log_{10}(M_{\rm BH})^{-1}$. Assuming that, around 10^9 $M_\odot$, the average fractional accretion rate and efficiency of conversion to kinetic power are independent of black hole mass, we can infer that $\Delta\log_{10}(Q) = \Delta\log_{10}(M_{\rm BH})$. Then, neglecting redshift-evolution of the black hole mass function, duty cycles of $\delta_{\rm FRII}(M_{\rm BH},z_1) \sim 10^{-3}$, $\delta_{\rm FRII}(M_{\rm BH},z_2) \sim 10^{-4.5}$, and $\delta_{\rm FRII}(M_{\rm BH},z_3) \sim 10^{-5.5}$ are found. Although in the analysis ranges of redshifts are used, the measurement is instantaneous, and hence can be compared to other results for a single redshift; here the measurement will be an average for the redshifts within each range which is considered.

The estimated duty cycles can be compared with the maximum lifetimes of radio galaxies obtained from the fits to determine whether all or just a fraction of 10^9 $M_\odot$ black holes are likely to spend some time as a powerful FR II radio galaxy, where 'powerful' is defined to mean 'at the break luminosity', i.e. the most powerful 'typical' objects in the observed epochs. From the fits, it is found that the sources live for a maximum of approximately $10^{7.8}$ yr in the lowest redshift range, and since $\Delta z_1 = 10^{9.5}$ yr, then each radio galaxy is on for 1.6 per cent of this epoch, compared to a duty cycle of 0.1 per cent. If one assumes that an AGN goes though the FR II stage only once, if at all, during its lifetime, then around 10 per cent of 'typical' radio galaxy hosts are likely to spend time as a powerful FR II in the most recent epoch. Moreover, if it is assumed that these galaxies can go through their FR II episodes multiple times throughout this epoch, then the fraction will be even smaller. For the higher redshifts the inferred duty cycles are smaller as compared to the local Universe. From the fits, the radio sources at higher redshifts are found to live for a shorter time; the lifetimes of $10^{7.2}-10^{7.5}$ yr for redshift range z_2 and $10^{6.6}-10^{7.2}$ yr for z_3 are found, while

the time spanned by each epoch remains close to Δz_1. However, the reduction in lifetimes is not sufficient to explain the drop in duty cycle at high redshifts: the most powerful FR IIs become rarer, and a smaller fraction of potential FR II hosts spend time as powerful FR IIs (perhaps < 1 per cent for z_2, and < 0.1 per cent for z_3).

These apparent reductions in duty cycle may result from the assumption of no evolution in the number density of 10^9 $M_\odot$ black holes from the present epoch. In fact, based on the evolution of X-ray luminosity functions, Merloni and Heinz (2008, see also Natarajan and Treister 2009) estimate that the black hole number density of SMBHs declines from $\phi(M_{\rm BH} = 10^9 M_\odot, z = 0.3) \sim 10^{-4}$ to $\phi(M_{\rm BH} = 10^9 M_\odot, z = 2.0) \sim 10^{-5.8}$. This reduction in number density at higher redshifts could account for most of the apparent drop in duty cycle which can be inferred from the presented here fits. It is also important to note that since the break luminosity of the kinetic luminosity function increases by 2 decades from z_1 to z_3, the active fractions quoted here are tracing significantly different populations in terms of kinetic power, and if lower-power radio galaxies are included (e.g. the FR I population) the total duty cycle of radio-loud AGN may be much greater than the values given here.

It is interesting to compare these estimates of powerful radio galaxy duty cycles with estimates of AGN duty cycles based on radiative luminosity functions. In the higher redshift ranges, the duty cycle estimates given here are at least a decade lower than those inferred for 10^9 $M_\odot$ black holes by Shankar *et al.* (2009) and the lower bounds estimated by Kelly *et al.* (2010). This discrepancy may be understood in terms of the radio loud fraction of AGN, since for the high kinetic powers observed at higher redshifts, the accretion rates are expected to be large fractions of the Eddington rate and hence correspond to the underlying quasar population, which is known to be predominantly radio-quiet. Hence at these redshifts, the lower duty cycle inferred from kinetic luminosities may reflect the small fraction of high accretion-rate, radio-loud objects. However, at lower redshifts, the situation turns around, and the inferred here duty cycle for 10^9 $M_\odot$ may be up to a decade *larger* than that estimated from radiative luminosities by Shankar *et al.* (2009). This difference may reflect the evolution of the FR II kinetic break luminosity to lower values, which may correspond to a lower typical black hole mass at low redshifts than the 10^9 $M_\odot$ assumed here, for which the duty cycles predicted by Shankar *et al.* (2009) are higher. An alternative possibility is that the reduction in break luminosity corresponds to a change to a lower accretion rate (as a fraction of the Eddington rate), where a kinetically-dominated accretion mode dominates over radiatively efficient accretion (e.g. see Merloni and Heinz, 2008, and references therein).

3.10 Influence of the assumptions on the results

Although, one can easily estimate how strongly a given physical model assumption influences a single source, such predictions may not be trivial when considering the whole population of radio sources. Here, I discuss the possible influence of the model assumptions

introduced in §2.3 on the simulated source populations and the results. The corresponding confidence intervals for each case are plotted in the Appendix A.

3.10.1 Core radius and the shape of the central density distribution

The central density is tightly linked to the core radius a_o, and, it is stressed again, the parameter $(\rho_o a_o^{\beta})$ should not be considered separately in terms of ρ_o and a_o. In the current simulation the core radius is kept fixed at a value of 2 kpc, and the corresponding values of the mean central density are searched through. Any change to the value of a_o will affect the result of ρ_o only, where for lower values of the core radius the mean central density will compensate shifting towards higher values, and for larger a_o less dense environments will be preferred (assuming no change is made to β).

The initial log-normal distribution of central densities is assumed to be quite narrow, with $\sigma_{\log_{10}(\rho_o)} = 0.15$. It was tested how much the results will be affected if one allows a broader central density spread. As discussed in §3.5, the change in density will have very strong effect predominantly on the maximum allowed age of the sources. Moreover, since both radio luminosities and linear sizes depend on the density of the medium, allowing for larger standard deviation of the $\rho_{\rm m}$ distribution will affect the distributions of kinetic luminosities of the sources and their ages as these will have to compensate for the environment change to reproduce the observables (as compared to the initial narrow $\sigma_{\log_{10}(\rho_o)}$). Indeed, the results show that the kinetic luminosity break shifts to slightly lower values as the central density standard deviation gets broader. The mean central density and the maximum age of the source of the best fits seem to oscillate around similar values for the tested cases (see Figure A.3 and Figure A.4), where $\sigma_{\log_{10}(\rho_o)} = 0$ (delta function), $\sigma_{\log_{10}(\rho_o)} = 0.15$, $\sigma_{\log_{10}(\rho_o)} = 0.50$ and $\sigma_{\log_{10}(\rho_o)} = 0.75$ [in units of $\log_{10}(\rho_o)$]. However, a significant change for $\sigma_{\log_{10}(\rho_o)} = 1.00$ can be observed, when the confidence intervals of all parameters become more defined, in particular $Q_{\rm B}$ drops to values of 10^{38} W and the maximum age of the sources oscillates around $\sim 1 \times 10^8$ yr in the case of z_1, while for z_3 there are only very specific regions of the parameter space allowed. For best-fitting parameters consult Table A.2.

3.10.2 Distribution of the maximum source lifetimes

The initial log-normal distribution of the maximum source lifetimes is assumed to be very narrow, with $\sigma_{\log_{10}(t_{\rm max})} = 0.05$. It was tested, however, how much the results will be affected if one allows for greater variety in the maximum lifetimes within one population of the sources. The simulation has been re-run twice, with $\sigma_{\log_{10}(t_{\rm max})} = 0.3$, and with $\sigma_{\log_{10}(t_{\rm max})} = 0.6$. Similarly to the case of the standard deviation of the central density distribution, no significant changes in the confidence intervals of any of the searched parameters has been observed; however, in the case when $\sigma_{\log_{10}(t_{\rm max})} = 0.3$ for the lowest redshift range

the intervals seem to be slightly broader. The confidence intervals are presented in Figure A.11 and FigureA.12, and the best fitting parameters are listed in Table A.6.

3.10.3 Head advance speeds

Since there is much discussion on the value of maximum head advance speed of the FR II jets (see §2.3.7) the simulation was re-run with $v_{\rm max} = 0.05c$, $v_{\rm max} = 0.15c$, and further with $v_{\rm max} = 0.8c$, to investigate how strong an effect such an assumption may induce on the whole population. As seen in Figure A.1 and Figure A.2 the lower $v_{\rm max}$ allowed the more constrained confidence intervals become. Although there is no significant difference between the confidence intervals, stronger constraints, resulting from lower allowed $v_{\rm max}$ assumed, indicate that higher central densities, older source ages, and slightly less powerful sources (the latter seems to be the case only in the smallest redshift range) from the initial broad contours are indeed preferred.

Such results come from the fact that the energy density in the jet head (hot spot) is

$$u_{\rm HS} = \rho_{\rm x} v_{\rm adv}^2, \tag{3.12}$$

where $\rho_{\rm x}$ is the external medium, $v_{\rm adv}$ is the head advance speed, and

$$v_{\rm adv} = v_{\rm j}/[1 + (\rho_{\rm x}/\rho_{\rm j})^{1/2}] \tag{3.13}$$

with the jet speed $v_{\rm j}$ and jet density $\rho_{\rm j}$ (see Martí *et al.*, 1997, for a relativistic extension of this calculation which leads to very similar results). In the case of this speed being constant throughout a source life, this would imply that $v_{\rm adv} \propto \rho_{\rm x}^{-1/2}$ (see Scheuer, 1996). Thus, the smaller the head advance speed is, the higher the ambient density of the sources must become to reproduce their observed linear sizes and radio luminosities. If the external density changes then adjustment in the $t_{\rm max}$ and $Q_{\rm B}$ must develop to again ensure that the observed L_ν and D are reproduced. This is indeed what is observed.

Note, however, that since from the KA97 model it is known that the expansion speed decelerates with the source age, the maximum head advance speed that we refer here to is in fact the maximum expansion speed a source may have at the time of observation. Since there is a higher probability of observing an old source than a young one, these $v_{\rm max}$ may not be the highest possible expansion speeds during a source lifetime as at the earlier stages of the source life its early-$v_{\rm adv}$ (non observed) may be higher than the decelerated late-$v_{\rm adv}$ (observed, at the later stages of the source life). The latter, only, is compared to $v_{\rm max}$.

For the best-fitting parameters see Table A.1.

3.10.4 Energy distribution of the relativistic particles: the injection index and the Lorentz factors

Initially, a uniform distribution of $m \in [2,3]$ is assumed. However, the possible influence of the assumed m distribution on the results has been investigated, and the simulation has been re-run twice assuming that m is set to a single, universal value ($m = 2.3$), and further that m follows a Gaussian distribution with $m_{\rm mean} = 2.4$ and $\sigma_m = 0.3$ (refer to §2.3.4 for details). Note that this normal distribution is asymmetric here since it is not allowed to extend beyond the minimum and maximum m values. Curran *et al.* (2010) finds $m_{\rm mean} = 2.4$ and $\sigma_m = 0.6$; however, since m is restricted by its minimum and maximum allowed value in this study, such a distribution would be nearly uniform for $m_{\rm min} = 2$ and $m_{\rm max} = 3$. For this reason a smaller standard deviation of the distribution has been chosen in the tests. The confidence intervals are presented in Figure A.9 and Figure A.10, and the best-fitting parameters are listed in Table A.5. No difference between results found with either of the Gaussian, the uniform distributions or a single value of the injection index has been found. I conclude here, that most plausibly the currently used data and/or theoretical model are not sensitive enough to distinguish between the underlying distributions of m at this point.

Furthermore, since there has been discussion on the low-energy cut-off of the energy distribution of relativistic electrons present in the radio jet we tested the following cases to investigate the possible changes to the results:

(i) $\gamma_{\rm min} = 1$ and $\gamma_{\rm max} = 10^5$,

(ii) $\gamma_{\rm min} = 10^2$ and $\gamma_{\rm max} = 10^{10}$,

(iii) $\gamma_{\rm min} = 10^4$ and $\gamma_{\rm max} = 10^{10}$.

All of these were compared to our initially assumed case where $\gamma_{\rm min} = 1$ and $\gamma_{\rm max} = 10^{10}$. The confidence intervals are presented in Figure A.7 and Figure A.8, and the best-fitting parameters are listed in Table A.4. As expected, there is no difference between the initial assumptions and case (i), indicating that indeed the exact value of the maximum Lorentz factor is not crucial as long as $\gamma_{\rm min} \ll \gamma_{\rm max}$. In case (iii) a significant change of the kinetic luminosity break confidence intervals is observed, where for $\gamma_{\rm min} = 10^4$ the kinetic luminosity break is smaller by ~ 1.5 decades, as compared to the other cases. Such a drastic change in confidence intervals in case (ii) is not observed, despite $\gamma_{\rm min}$ being significantly larger than the initial case. Therefore it can be concluded that change in the minimum Lorentz factor for the whole source population will significantly affect their kinetic luminosities only.

$\gamma_{\rm min}$, $\gamma_{\rm max}$ and m directly influence the initial energy density distribution of the relativistic particles. The minimum Lorentz factor indicates how relativistic are the least energetic particles. The lower $\gamma_{\rm min}$ the more cold material is included. For cold plasma higher Q is required in order to obtain the observed radio luminosity density because a fraction of the kinetic luminosity will be lost for particle acceleration. However, if this material is not included, less power is required to reproduce the observed L, and hence significantly lower $Q_{\rm B}$ are observed in the results if $\gamma_{\rm min}$ is allowed to be as high as 10^4. The maximum Lorentz

factor characterises the cut-off at the high energy end of the particle distribution; particles can only be accelerated up to a certain frequency above which loss rates take over (see also Markoff *et al.*, 2001). The index *m* defines the slope of the energy density distribution, and hence determines the relative fraction of low and high energetic particles, where the flatter the distribution is the more energetic particles are included. Although the change of *m* may be significant for a single radio source, it does not seem to have a dramatic effect on the whole population of sources, and it is the low energy cut-off that influences the average properties of the population.

3.10.5 Jet particle content

As discussed in §2.3.6 there is much debate on the particle content of the radio jets. Initially, in the simulation the conservative KDA97 assumption ($k' = 0$) is followed, but to test the influence of this assumption on the whole population of sources three additional assumptions have been tested, that is it was assumed that the particle content of radio jet is drawn from a uniform distribution in a range $k' \in [0, 10]$, and further also $k' \in [0, 100]$. As an additional test the case when $k' = 100$ was also investigated. The confidence intervals are presented in Figure A.5 and Figure A.6, and for the best-fitting parameters consult Table A.3. A significant change in the fitted source parameters was observed only in the two latter cases. While assuming $k' \in [0, 100]$ (higher redshifts) or $k' = 100$ the best-fitting kinetic luminosity breaks shift significantly to higher values by ~ 1.5 decades. The other parameters do not seem to undergo any significant change.

Indeed, the addition of protons in the relativistic jets would require these particles, similarly to electrons, to be accelerated to the relativistic speeds. As already shown by e.g. Bell (1978), relativistic protons store much more energy than electrons typically do, and this in turn will give rise to the radio source kinetic luminosity. The argument may be turned around: to maintain the expected kinetic luminosity, the observed radio lobe luminosity density is much lower for proton dominated jets than for lightweight, electron-positron jets (see also KDA97). However, many authors favour proton-electron jets. Istomin and Sol (2011), for instance, draw a hypothesis that some low-luminosity AGN have proton dominated jets, which are supported by extracting energy from black hole spin. Sikora *et al.* (2005) report that jets of radio-loud quasars are also most likely heavy due to the positron-electron kinetic energy being too small to support energetics of radio lobes. However, Bicknell *et al.* (2001), extending the work of Celotti and Fabian (1993), show that in the case when jets are proton dominated the following criterion occurs: $\gamma_{\rm min} \cong 10^2$. This is not required by positron-electron jets, but the results are still consistent when such a value for $\gamma_{\rm min}$ is adopted (see §3.10.4). Indeed, if one considers the net effect of the two assumptions tested, that is the jet particle content and the minimum Lorentz factor, one will notice that their effects may cancel out. Setting $\gamma_{\rm min} \cong 10^2$ or more one ensures that only initially highly relativistic particles are included in the jet material and these are later being re-accelerated in the jet front;

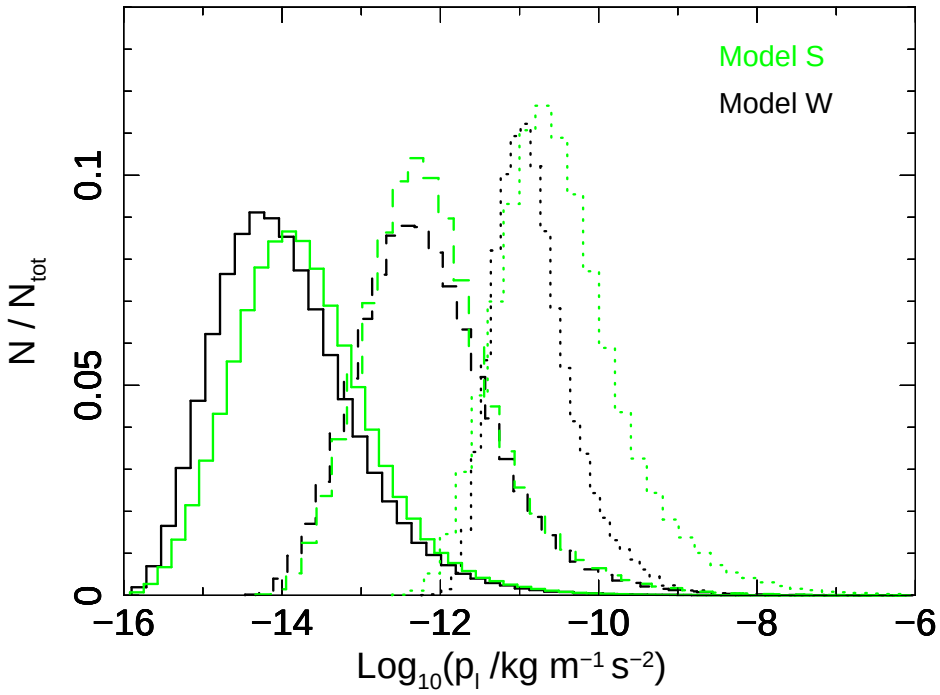

Figure 3.23: The predicted radio lobe pressures of the underlying parent populations, unaffected by the flux limit, of FR II radio sources generated with the best-fitting parameters (Table 3.3) of the independent-z fits of Model S (green) and Model W (black) for three redshift ranges, where z_1 (solid line), z_2 (dash-dotted line) and z_3 (dotted line). The minimum allowed kinetic luminosity set for each presented distribution is set to 10^{36} W.

it requires stronger momentum flux to affect the non-relativistic protons than relativistic ones, hence the change in kinetic luminosity in these two cases.

Based on the results I present here it is currently impossible to distinguish between purely electron-positron jets ($k' = 0$) and those that contain modest numbers of protons ($k' \in [0, 10]$). Very heavy FR II jets ($k' \sim 100$) consisting of an electron-proton plasma seem to be unlikely, unless the minimum Lorentz factor is set to large values ($\gamma_{\rm min} \cong 10^2 - 10^4$).

3.11 Distributions of parent population's measured properties

The content of this section is purely hypothetical due to both the unknown minimum kinetic luminosity of the FR II sources and the slope $\alpha_{\rm s}$ of the Schechter function (Eqn. 2.19) – quantities one is unable to set limits on with the radio catalogues used currently in this study. Nevertheless, the method presented in this work allows one to reproduce the possible parent populations of the analysed radio sources. The accuracy of these predictions depends on the number of radio samples of different flux limits and how well the faint end of the kinetic luminosity function is constrained.

As it is known, the distributions of the observed parameters (such as L_ν and D) vary with redshift; the radio lobe luminosity density and lobe pressure distributions shift towards higher values for higher redshifts, while distributions of the linear size tend to slightly shift towards smaller sizes at higher redshifts. This has been observed already by e.g. Kapahi (1989); Singal (1993), BRW99. Here, the predicted distributions of these parameters of the underlying parent populations (i.e. unaffected by the flux limit) are found to undergo a similar change with the cosmic epoch. Of course, one must expect that these parent distributions do depend on the allowed $Q_{\rm min}$ and the slope $\alpha_{\rm s}$, and since these have large uncertainties (especially $\alpha_{\rm s}$) the estimated parent populations must be taken with care. Radio luminosity density in particular will be dramatically affected by these two parameters, while linear sizes seem to undergo a smaller degree of change. Interestingly, the lobe pressure distributions do not seem to change with the different choices of the minimum allowed kinetic luminosity and $\alpha_{\rm s}$. Unfortunately, I am unable to estimate, with small uncertainties, the two parameters at this point of the study due to the choice of radio samples which are currently being used, and hence I will not discuss the highly uncertain radio lobe luminosities of parent populations.

In the case of the linear size of extended radio sources, one may not expect such a drastic change between observed and underlying distributions of the population because of the much smaller effect that the flux limit has on these. There are two linear size ranges of a particular interest. Since radio sources of linear sizes smaller than 10 kpc are not included in the fitting, it is worth checking how many of these are predicted in the parent populations. I find that for the best fitting parameters they make up not more than 5 per cent (Model S) or 2 per cent (Model W) of the whole parent population. Furthermore, one may consider the existence of old large sources which fall below the survey sensitivity. Given that the kinetic luminosity stays constant during a source lifetime, the source grows in size as it gets older, while its radio lobe luminosity density decreases. Eventually, the source drops beyond the flux limit of the survey, and hence is not detected by the radio survey. This would imply the existence of a sub-population of old low luminosity density objects which are present in the parent populations. Such populations are, however, not seen with either of the models considered in this study.

The KDA97 model employs the minimum energy relation of the relativistic particles and magnetic fields which are responsible for the synchrotron radiation. As provided in Eqn. 2.9 the radio lobe pressure can be inferred from the size and age of the source. The method presented here, given the semi-analytical model, can therefore constrain the most likely distributions of the radio lobe pressures of FR II sources (Figure 3.23). A strong trend with redshift is present, where the average lobe pressure $\hat{p}_{\rm l}$ in the local Universe of $\sim 3.4\times10^{-14}$ Pa drifts to $\hat{p}_{\rm l}\sim 5.1\times10^{-11}$ Pa for the redshifts $0.8<z<2.0$ of Model S, and similarly from $\hat{p}_{\rm l}\sim 2.1\times10^{-14}$ Pa in the local Universe to $\hat{p}_{\rm l}\sim 2.7\times10^{-12}$ Pa for the highest considered redshifts in the case of Model W. Both models predict similar results. Interestingly, even at this hypothetical stage these lobe pressure distributions agree with

previous numerical estimates (e.g. Wang and Kaiser, 2008) as well as values deduced from observations (e.g. O'Dea *et al.*, 2009).

As a final note, it is important to stress that beside the true, underlying parent populations, other predictions can be also made. By setting a desired flux limit to the parent population, one can produce catalogue predictions, which further can be tested against appropriate observed radio samples. The state-of-the-art LOw-Frequency ARray radio facility (LOFAR) is of a particular interest. Its large-scale deep extragalactic surveys will provide radio samples, with flux limits significantly lower than currently available catalogues, that predictions can be verified with. I will focus on this aspect in a future work.

3.12 Summary

Multidimensional Monte Carlo simulations are performed to investigate fundamental source parameters (such as kinetic luminosity, age and ambient density), and their possible trends with redshift of powerful radio galaxies and radio-loud quasars of FR II morphology based on the method presented in Chapter 2.

It has been found that:

(i) The total lifetimes of the radio galaxies are found to be few $\times 10^7$ yr at low redshift and decrease for earlier epochs. This is in agreement with independent studies on the 3CRR radio sources, but may be specific to these most powerful radio galaxies and quasars. With the current sample and its strong flux limit I and my collaborators are unable to draw final statements about the evolution of the lifetimes of the sources which is suggested by these current results.

(ii) The results suggest cosmological evolution of one or more source parameters. In particular the mean density of the immediate source environments (or the $\rho_o a_o^\beta$ parameter if one allows core radius or β to change with redshift) is found to undergo evolution with redshift; the hypothesis that there is no evolution is ruled out with probability of > 99 per cent.

(iii) The central density of the FR II environments is found to undergo redshift evolution of approximately $(1+z)^4$; evolution stronger than the one expected from the Universe expansion is possible if one considers additional effects from change of environment or core radius evolution.

(iv) The function describing the initial distribution of kinetic luminosities modelled by the Schechter function (or its modification) or smoothly broken power-law is favoured to simple power-law; however, the hypothesis of an unbroken power-law distribution cannot be ruled out at a confidence level of more than 95 per cent.

(v) The estimated kinetic luminosities are within $10^{38} - 10^{41}$ W for FR II type sources, which is consistent with previous studies. It is observed that the kinetic luminosities depend on the cosmological epoch and the linear size of the source, where larger in linear size as well as higher redshift sources are more powerful.

(vi) The FR IIs' kinetic luminosity function undergoes cosmological evolution of the break luminosities of at least $(1+z)^3$ and may be as strong as $(1+z)^{10}$. The uncertainty originates from the strong degeneracy between $Q_{\rm B}$, $t_{\rm max}$ and ρ_o. Evolution stronger than $(1+z)^9$ is rather unlikely since as the consequence the black hole masses of the most luminous FR II sources would have to be of $> 10^{11}$ $M_\odot$ assuming that there is no strong spin powering of the jets.

(vii) The results suggest that, at least at high redshifts, FR II sources most probably accrete at moderate/high Eddington ratios and the black hole spin may play a significant role in the jet production, as both effects seem to be necessary to explain the high estimated kinetic luminosities of FR II sources at higher z.

(viii) An attempt has been made to estimate the duty cycles of FR II radio galaxies at the break in the kinetic luminosity function, finding them to decrease with redshift from $\sim 10^{-3}$ for $z_1 \leq 0.3$, to $\sim 10^{-4.5}$ at $0.3 < z_3 \leq 0.8$, to $\sim 10^{-5.5}$ at $0.8 < z_3 \leq 2.0$. The decrease in duty cycle at higher redshifts may be explained by a combination of the reduction in the lifetime of FR II radio galaxies together with evolution in the number density of massive black holes. The shift in kinetic luminosity break to higher values also indicates an intrinsic change in the population of kinetic powers. Interestingly, at low redshifts the duty cycle of powerful FR IIs exceeds that estimated for 10^9 $M_\odot$ AGN based on radiative luminosities. This difference can be explained if the typical black hole mass of FR IIs shifts to lower masses at low z. Alternatively, the low-z FR II population may become dominated by a kinetically dominated, radiatively inefficient mode of accretion.

It is noted, however, that other theoretical models of radio galaxy time evolution, such as those of BRW99, MK02 (see §2.1.3 for a short discussion on main differences between the models), or the modified models of Barai and Wiita (2006, 2007), might yield somewhat different results.

Behind complexity, there is always simplicity to be revealed. Inside simplicity, there is always complexity to be discovered.

GANG YU

4

Low Radio Luminosity Density, Local Universe Sample of Radio Galaxies

---

It has been postulated that the low luminosity density FR II radio galaxies are distinct from their powerful equivalents, and thus the historical Fanaroff-Riley classification may be somewhat misleading. 3C extragalactic radio sources, which the study in Chapter 3 of this thesis was focused on, are some of the most powerful radio galaxies known and extend to high redshifts. But, the downside of catalogues such as 3C is their high flux limit which causes exclusion of any moderate and low power radio sources. The following chapter contains analysis of fundamental properties of a sample of low redshift and low radio luminosity density radio galaxies. The study is done via the method presented in Chapter 2 of this thesis, and a comparison with the results of the most powerful and high redshift radio galaxies, which were analysed in Chapter 3, is presented. In addition, the construction of the radio sample used in the Monte Carlo simulation is described. The content of this chapter is to be submitted to the Monthly Notices of the Royal Astronomical Society (A.D. Kapińska, P. Uttley, P.N. Best & T.J. Maccarone, 'Local low luminosity FR II radio galaxies: do they differ from their powerful cousins?', MNRAS, in prep.).

4.1 Objectives

It has been suggested that the low luminosity FR II radio galaxies may be distinct from their powerful cousins. 3CRR extragalactic radio sources, which the study in Chapter 3 of this thesis was focused on, are some of the most powerful radio galaxies known and extend to high redshifts. But, the downside of catalogues such as 3CRR is their high flux limit which causes exclusion of any moderate and low power radio sources. I have stressed before (cf. Chapter 3) the importance of including deeper data than catalogues such as 3CRR can provide for the investigations of the fundamental parameters of FR II sources. Here, I attempt to extend my work to include radio samples at vastly improved sensitivity as compared to the 3CRR/BRL sample. Two of such deep all sky radio surveys are the NRAO VLA[1] Sky Survey (NVSS; Condon *et al.*, 1998) and the VLA Faint Images of the Radio Sky at Twenty centimetres survey (FIRST; Becker *et al.*, 1995; White *et al.*, 1997), both of which are discussed in detail in §4.2. These are often matched to the Sloan Digital Sky Survey (SDSS; York *et al.*, 2000; Stoughton *et al.*, 2002) which provides the optical counterparts of the radio sources. Cross matching of the three surveys provides a unique opportunity for population studies; I will refer to the cross-matched sample based on the three surveys as the SDSS-FIRST-NVSS sample.

However, throughout this thesis I highlight the importance of using low radio frequencies while dealing with extended radio emission from radio lobes (see also BRW99). The theoretical models I consider assume that compact radio emission from hot spots and radio cores is negligible; this is often the case at $\sim$ few $\times$ 100 MHz, but is not necessarily true at GHz frequencies. Since both NVSS and FIRST were observed at 1.4 GHz, I do construct a new radio sample by cross matching the SDSS-FIRST-NVSS sample (compiled by Best *et al.*, 2005; Best and Heckman, 2012, see §4.2 for all details) with publicly available low frequency radio surveys (§4.2.3). This new sample of radio galaxies is further used in the Monte Carlo simulations to investigate their fundamental parameters, and comparison with the results of powerful radio galaxies and radio-loud quasars from Chapter 3 is performed.

4.2 Observational data sets

I use optically selected, flux-limited radio sample of extended radio sources created as described below. Currently, I concentrate only on sources of FR II morphology due to the availability of semi-analytical models of their time evolution.

[1]Very Large Array (VLA) radio interferometer is operated by the National Radio Astronomy Observatory (NRAO), see `http://www.vla.nrao.edu/`.

4.2.1 Radio galaxy sample from the Sloan Digital Sky Survey

4.2.1.1 Sample definition

Best et al. (2005) created a large sample of optically selected galaxies and their radio counterparts by cross-matching the SDSS survey with NVSS and FIRST. The current version of this catalogue uses the SDSS Data Release 7 (Best and Heckman, 2012). A sub-sample of the full Best et al. radio sample is used, which consists of 290 FR II type sources with declinations of $\delta > -10^\circ$ and with redshifts $0.03 < z \leq 0.2$. Although the full sample extends up to $z = 0.6$, I use the lower bound on the redshift due to possible bias that may be relevant in this study; at redshifts $0.3 < z < 0.6$ only red luminous galaxies are included, while at the lower redshifts the main galaxy survey spectroscopic sample (Strauss *et al.*, 2002) is used. If the type of the host galaxy determines the type of the radio source which resides in it, this would cause a significant bias in the analysis. There are no selection criteria on the host types of the SDSS sources up to approximately $z < 0.2$ apart from the radio cut-off of 40 mJy and optical cut-offs of $14.5 < r^* < 17.77$, where r^* is the optical r-band magnitude measured at the effective wavelength of 6165Å (see Fukugita *et al.*, 1996; Ivezić *et al.*, 2002; Graham *et al.*, 2005, for the definition of the system and discussion on the SDSS absolute calibration). In addition, although it is assumed, following the unification models, that the only difference between radio galaxies and radio-loud quasars is just their viewing angle (e.g. Barthel, 1989), objects classified as 'quasars' are excluded from the main SDSS galaxy catalogue, and so they are excluded from the Best et al. sample. Since there are very few such objects at these low redshifts (< 3 per cent at $z < 0.1$, see Best *et al.*, 2005), this should not introduce any significant bias in the analysis.

4.2.1.2 NVSS and FIRST radio surveys

The NVSS survey covers the entire sky north of $\delta = -40^\circ$ at 1.4 GHz. Resolution of the NVSS radio maps is approximately 45 arcsec, and the detection limit (the flux limit) is 2.5 mJy. The observations were performed with the VLA telescope in its D configuration, and thus the largest angular scale measured is of order of 15 arcmin[2].

The FIRST survey, at the current stage, covers declinations of $\delta > -10^\circ$ at 1.4 GHz and is still not yet a complete project. Resolution of the FIRST radio maps is ~ 5 arcsec, and the detection limit is 0.75 mJy. The observations were carried out with VLA in B configuration, and thus the largest angular scale that can be measured in the FIRST survey is approximately 2 arcmin.

An angular size of 2 arcmin corresponds to a linear size of approximately 390 kpc at redshift $z = 0.2$. Radio galaxies are often larger than this, and hence the FIRST survey should not be used for flux density measurements of the extended radio sources as simply

[2]Consult J.S. Ulvestad, R.A. Perley, & C.J. Chandler (eds), 'The Very Large Array Observational Summary', Jan 2009, `http://www.vla.nrao.edu/astro/guides/vlas/current/vlas.html`.

they will be resolved out (see Chapter 1: §1.4). The largest angular scale measured by the NVSS survey corresponds to a linear size of 2.93 Mpc; very few radio galaxies reach such enormous linear sizes, but some of such radio galaxies do exist (e.g. the well known 3C 236 with linear size ~ 4.5 Mpc: see §4.3.4 for references, and the recently discovered largest radio galaxy J1420-0545 which has a linear size of ~ 4.7 Mpc: Machalski *et al.* 2008, 2011). Although 3C 236 is in the Best et al. sample, its measurements are treated separately. Apart from 3C 236, the second largest FR II radio galaxy in the Best et al. FR II sub-sample at declinations $\delta \gtrsim +28.5^{\circ}$ and up to redshift $z = 0.2$ (see §4.3 for explanation) has an angular size of 5.5 arcmin. Therefore, the NVSS survey is considered perfect for the total flux density measurements as none of the radio sources are expected to be resolved out.

4.2.1.3 Radio morphological classification

The radio morphological classification has been performed by Prof. Philip N. Best (IfA, Royal Observatory, Edinburgh) through his automatic routine, and has been visually inspected by him, and also partly by myself (see also §4.3.2). The proper morphological classification of the radio sources has a profound influence on the accuracy of the radio sample and any further analysis. Due to the good angular resolution of the FIRST survey (~ 5 arcsec) a detailed investigation of the morphology of the extended radio sources can be done. The most important distinctions between FR I and FR II classes that are adopted in such sample classification are: (a) the vast majority of the radio emission from FR II sources comes from the outer regions of the radio structure, while for FR Is this emission is assumed to come from regions close to the radio core, (b) the extent of the FR II sources can be defined by measurements of their hot spots – these do not exist in FR I radio sources. The demography of the full radio galaxy sample, with classification based on the FR I / FR II morphology is given in Table 4.1.

4.2.2 Radio sample completeness

A complete flux-limited radio sample is usually defined as one which contains all extragalactic radio sources in a given sky area and above a sensitivity limit specified for a survey. The radio sample constructed by Best *et al.* (2005) and Best and Heckman (2012) is *not* a complete sample of all radio sources within the specified redshift range and the NVSS and FIRST sky area. This is due to three main reasons. Firstly, the sources are optically selected down to the magnitude of $r^* = 17.77$ and sources fainter than this are not included in the main galaxy sample[3]. Secondly, even within the accepted optical magnitude range, a galaxy may be missed by SDSS due to fibre-collision effects. This affects ~ 6 per cent of all galaxies, but is expected to be a random effect. Finally, a galaxy may be too bright for the SDSS spectroscopy and so, again, is likely to be missed. To minimise this last effect

[3]Fainter than this limit only luminous red galaxies are targeted as mentioned in §4.2.1.1.

Table 4.1: Demography of the radio galaxies in the Best et al. sample.

Redshift (z)	No. of sources (per cent)			
	FR I	FR II	hybrid	unclassifable
WENSS area				
$z \leq 0.2$	164 (55.6%)	118 (40.0%)	3 (1.0%)	10 (3.4%)
$z \leq 0.6$	259 (50.1%)	229 (44.3%)	10 (1.9%)	19 (3.7%)
Full sample				
$z \leq 0.2$	386 (54.1%)	290 (40.6%)	16 (2.2%)	22 (3.1%)
$z \leq 0.6$	620 (44.7%)	687 (49.6%)	37 (2.7%)	42 (3.0%)

the lower bounds on the redshift ($z \geq 0.03$) and the apparent optical magnitude ($r^* \geq 14.5$) are adopted by Best *et al.* (2005). The distributions of the radio lobe luminosity densities at 325 MHz of the sources, their apparent optical magnitudes and absolute magnitudes (for the Best et al. FR II sample matched with WENSS) are presented in Figure 4.11 – Figure 4.15. No apparent bias is visible. The absolute magnitudes of the FR IIs' host galaxies seem to be randomly distributed in the radio lobe luminosity density plane (Figure 4.13). One may notice that in the absolute – apparent optical magnitude plane (Figure 4.15) there is a suspiciously empty region for faint apparent and strong absolute magnitudes; clearly it is redshift dependent effect. This further corresponds to the bottom right corner of the radio lobe luminosity density – apparent optical magnitude plane (Figure 4.14, note that both quantities are redshift dependent).

4.2.3 Low radio frequency surveys

Due to the nature of the theoretical models of radio source growth which are used here and which assume that most of the radio luminosity density comes from the radio lobes of the sources, one should use samples observed at low radio frequencies ($\sim$ few $\times$ 100 MHz) to avoid compact radio emission that dominates at GHz frequencies. This flat spectrum compact radio emission has its origins in the synchrotron self-absorbed emission at the base of relativistic outflows, where Doppler boosting and/or deboosting effects may additionally become significant (but cf. Merloni and Heinz, 2007), and in the regions of hot spots where the jet terminates and particles are re-accelerated. Since the sample of Best et al. is constructed at 1.4 GHz (both NVSS and FIRST were observed at this frequency), it is attempted here to match it with publicly available low radio frequency catalogues, the VLA

Low-frequency Sky Survey[4] (VLSS; Cohen *et al.*, 2007) and the Westerbork Northern Sky Survey[5] (WENSS; Rengelink *et al.*, 1997).

VLSS (formerly 4MASS) is a relatively shallow (detection limit of 0.5 Jy) radio survey measured at 74 MHz. It covers the entire sky north of -30° in declination observed with an angular resolution of approximately 80 arcsec. The survey was performed with VLA in B configuration, and so the largest angular scale that can be detected is ~ 37 arcmin[6]. WENSS is a radio survey covering northern sky of declinations $\delta \gtrsim +28.5^{\circ}$. The survey is measured at 325 MHz with a detection limit of approximately 18 mJy and a resolution of $\sim 54 \times 54$ cosec(δ) arcsec. The survey was performed with the standard set-up of the Westerbork Synthesis Radio Telescope, which has the shortest baselines of 36 m $-$ 96 m. Therefore, the largest angular scales detected by WENSS are $\sim 1.5^{\circ}$ for the baselines of 36 m, and 33 arcmin for the baselines of 96 m. For the description of the mosaicing technique used for the WENSS survey, and the details on the choice of the shortest baselines, see Bremer (1994), and for discussion of the issue of the largest scale structures that can be measured by WENSS see e.g. Schnitzeler *et al.* (2007). Following the discussion in §4.2.1.2 on the largest angular sizes of the radio galaxies considered in this study, both VLSS and WENSS are considered to be adequate for the total flux density measurements of the extended structures of the radio sources, and none of the sources are expected to be resolved out.

4.3 Cross-matching of the samples

4.3.1 Matching procedure

The cross-matching procedure of the Best et al. FR II sub-sample with WENSS and (separately) with VLSS was performed as follows:

1. Best et al. FR II sources that lie outside the sky coverage of WENSS ($\delta \lesssim +28.5^{\circ}$) were excluded, which caused the sample size to decrease to 118 radio sources in this case. In the case of the cross-match with the VLSS survey no sources of the Best et al. FR II sub-sample were excluded.

2. An angular distance between two sources (d), from the Best et al. FR II sub-sample and either WENSS or VLSS, was found according to

[4] `http://lwa.nrl.navy.mil/VLSS/`

[5] `http://www.astron.nl/wow/`

[6] Consult J.S. Ulvestad, R.A. Perley, & C.J. Chandler (eds), 'The Very Large Array Observational Summary', Jan 2009, `http://www.vla.nrao.edu/astro/guides/vlas/current/vlas.html`.

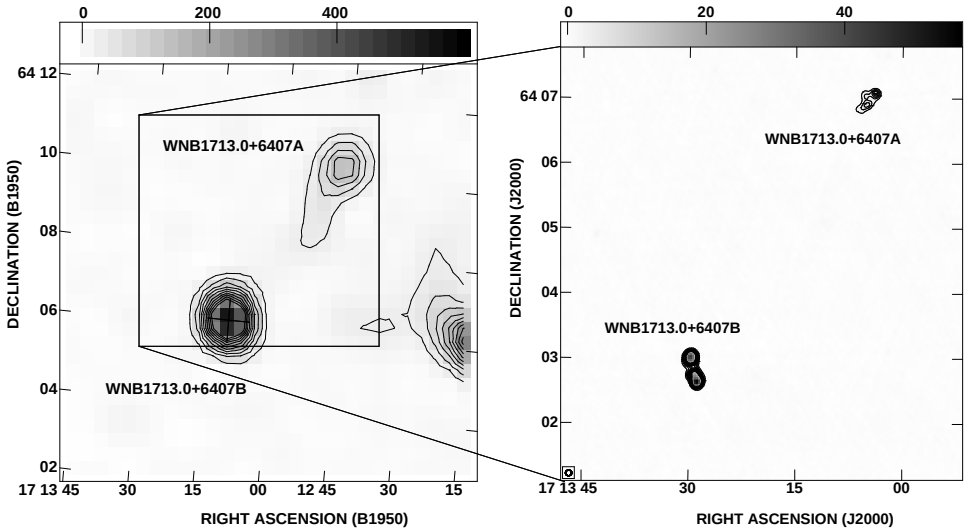

Figure 4.1: The image cutouts from the WENSS (327 MHz, $left$) and FIRST (1.4 GHz, *right*) surveys of a multicomponent WENSS source WNB1713.0+6407. In both panels the grey scale flux density is given in units of mJy/beam. $Left$: the contour levels are at 30 mJy/beam $\times(-10,-9,...,9,10)$, the peak flux density measured in the map is 599 mJy/beam, and the map resolution is 54×60 arcsec. The SDSS position of the source matched to the FIRST source is marked with a cross. *Right*: the contour levels are at 1.7 mJy/beam $\times(-10,-9,...,9,10)$, the peak flux density measured in the map is 57 mJy/beam, and the map resolution is 5.4×5.4 arcsec.

$$d = \arccos\left(\sin(\delta_1)\sin(\delta_2)+\cos(\delta_1)\cos(\delta_2)\cos(\alpha_1-\alpha_2)\right), \tag{4.1}$$

where δ_1,α_1 are the spherical coordinates of a source from one catalogue, and δ_2,α_2 of a source from the second catalogue.

3. A match was accepted only if the angular separation of the two sources was not more than the radio galaxy angular size as measured by Best et al. (2005) and Best and Heckman (2012), or the WENSS (or VLSS) beam size whichever was greater (a fixed value of 54 arcsec for the WENSS survey, and 80 arcsec for the VLSS survey was adopted). For radio sources of angular sizes smaller than the WENSS (or VLSS) beam size, I used the former in the counterpart search. Although WENSS is expected to have 1.5 arcsec positional accuracy (for strong sources only, and typically 5 arcsec for each field as declared by Rengelink et al. 1997), extra uncertainty comes from the case that one deals with extended emission here as opposed to point sources; therefore the regions' estimated maximum brightness at 325 MHz may not correspond to the same regions at 1.4 GHz at which the radio galaxy sizes are estimated. The same applies to the VLSS survey. In a procedure such as this one, typically a criterion of maximum angular separation of 3σ,

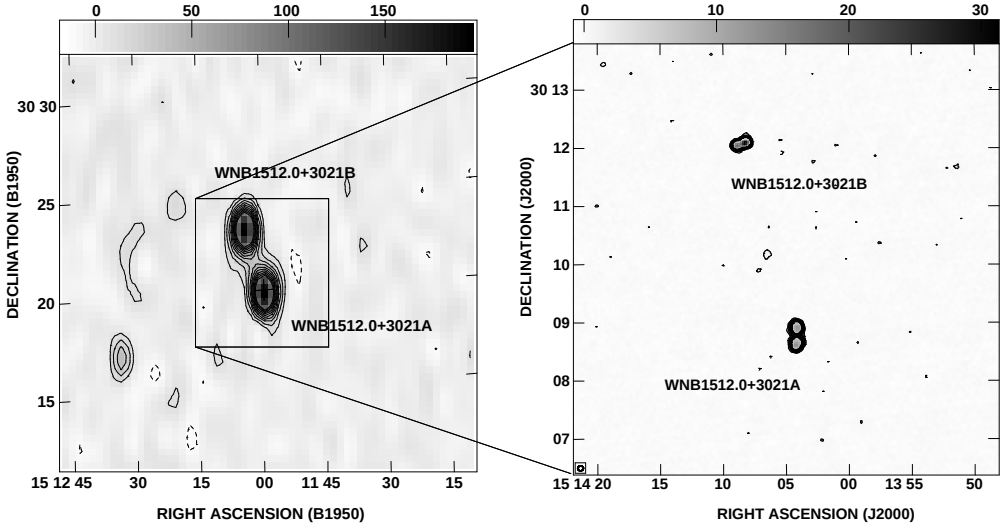

Figure 4.2: The image cutouts from the WENSS (609 MHz, *left*) and FIRST (1.4 GHz, *right*) surveys of a multicomponent WENSS source WNB1512.0+3021. In both panels the grey scale flux density is given in units of mJy/beam. *Left*: the contour levels are at 10 mJy/beam $\times(-10,-9,...,9,10)$, the peak flux density measured in the map is 194 mJy/beam, and the map resolution is 28×55 arcsec. The SDSS position of the source matched to the FIRST source is marked with a cross. *Right*: the contour levels are at 0.5 mJy/beam $\times(-10,-9,...,9,10)$, the peak flux density measured in the map is 31 mJy/beam, and the map resolution is 5.4×5.4 arcsec.

where σ is defined by the positional errors of two sources tested for a match, is used. This is indeed what had been initially performed. However, the radio source positions I am using to match with the low frequency radio catalogues originate from the SDSS survey, that is from the optical counterpart of the radio galaxy. Although this may be well matched to the FIRST observations if a source's core emission is present, at MHz frequencies these regions will coincide with the centres of the radio structures since the core compact emission is not expected to occur. For this reason, the offset may be of scales of arcmin (corresponding to radio galaxy linear sizes of kpc in scale) and multiple components are expected to be detected (see next step).

4. The WENSS survey has defined multicomponent sources, which is particularly relevant to my current study due to the type of the sources which are considered. I noticed, however, that in our procedure some of the radio sources were matched only to a subset of declared components in the WENSS catalogue. This issue required additional visual inspection, and is discussed in §4.3.2.

The matching procedure and its criteria for accepting a match were tested, and validated, with Monte-Carlo simulations. I constructed 1000 random catalogues of each the WENSS

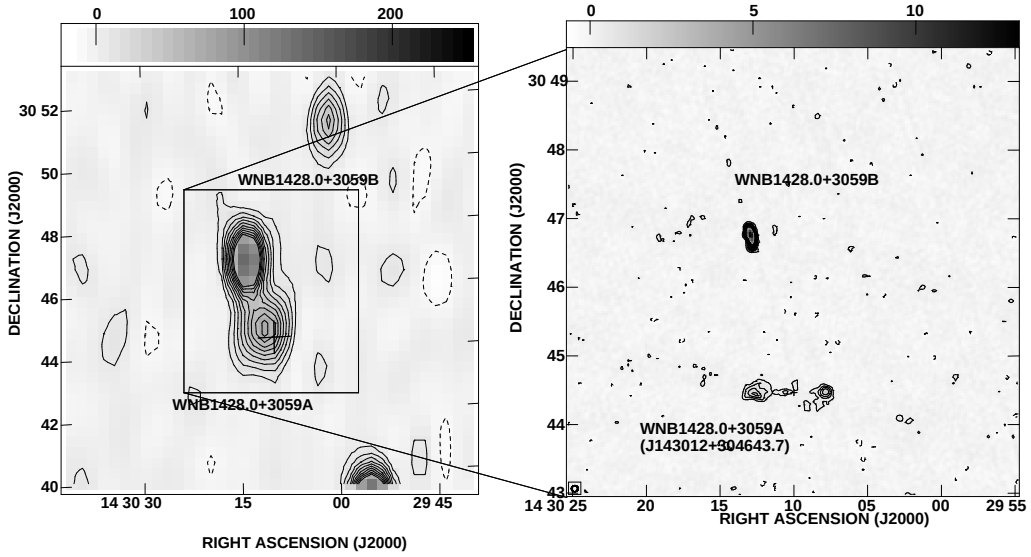

Figure 4.3: The image cutouts from the WENSS (609 MHz, $left$) and FIRST (1.4 GHz, *right*) surveys of a multicomponent WENSS source WNB1428.0+3059. In both panels the grey scale flux density is given in units of mJy/beam. $Left$: the contour levels are at 7.5 mJy/beam $\times(-10,-9,...,9,10)$, the peak flux density measured in the map is 251 mJy/beam, and the map resolution is 28×55 arcsec. The SDSS position of the source matched to the FIRST source is marked with a cross. *Right*: the contour levels are at 0.4 mJy/beam $\times(-10,-9,...,9,10)$, the peak flux density measured in the map is 13 mJy/beam, and the map resolution is 5.4×5.4 arcsec.

and VLSS catalogues over the same sky area as the respective catalogues, and attempted to match it to the Best et al. FR II sub-sample. For the VLSS mock survey on average only 2.6 sources were matched for a possible total of 290 sources (0.9 per cent) while using a criterion of the angular separation equal to the VLSS beam size only, and 3.3 sources (1.1 per cent) while using the actual radio galaxy angular size as described in step 3 above. For the WENSS mock survey on average 1.5 sources of a total of 118 sources (1.3 per cent) were matched if using the WENSS beam size only, and 3 sources (2.5 per cent) if again the actual angular size of the radio galaxy was used. These results confirm the reliability of our real catalogues' cross-match.

4.3.2 Additional visual inspection

The final cross-matched sample is presented in §4.3.3 and in Figure 4.6 – Figure 4.10. Investigation of the observables' distributions allow one to inspect the credibility of the final sample, and what follows, the credibility of the matching procedure. However, I noticed that in some cases not all components of the declared multicomponent sources from the WENSS catalogue were matched to the Best et al. FR II sub-sample. I investigated this issue in more

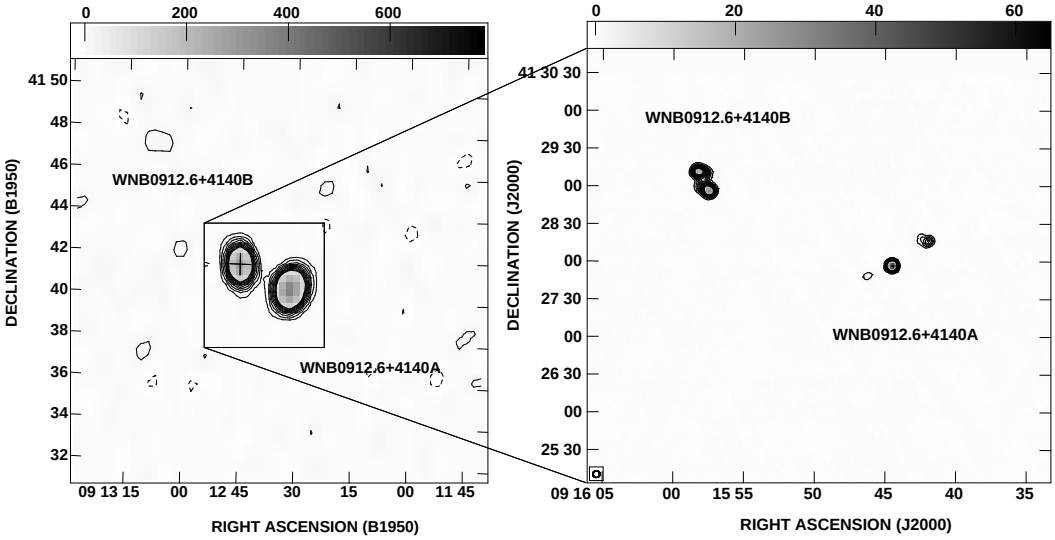

Figure 4.4: The image cutouts from the WENSS (327 MHz, $left$) and FIRST (1.4 GHz, *right*) surveys of a multicomponent WENSS source WNB0912.6+4140. In both panels the grey scale flux density is given in units of mJy/beam. $Left$: the contour levels are at 10 mJy/beam $\times(-10,-9,...,9,10)$, the peak flux density measured in the map is 778 mJy/beam, and the map resolution is 54×81 arcsec. The SDSS position of the source matched to the FIRST source is marked with a cross. *Right*: the contour levels are at 1.5 mJy/beam $\times(-10,-9,...,9,10)$, the peak flux density measured in the map is 64.7 mJy/beam, and the map resolution is 5.4×5.4 arcsec.

detail, and based on a sample of radio map comparison of the WENSS and FIRST surveys I discovered that many of the WENSS multicomponent sources are erroneously marked.

A sample of radio maps comparing the WENSS and FIRST observations is presented in Figure 4.1 – Figure 4.5. Due to the resolution of the FIRST radio maps being at least $10\times$ better than the WENSS observations at 325 MHz, the radio sources' morphology can be investigated in much more detail as compared to WENSS and NVSS. As can be seen in the provided here radio maps, some of the sources identified in WENSS to have multiple components (which may appear to be radio lobes) are further resolved into unconnected, often double radio sources by FIRST. Obviously, this is one of the shortcomings of automatic routines applied to large astronomical data, such as catalogues. The list of erroneously labelled sources in the WENSS catalogue is presented in Table B.1 (Appendix B). It is likely that additional such misidentifications are present in the WENSS catalogue among sources not matched to the SDSS-FIRST-NVSS sample considered here.

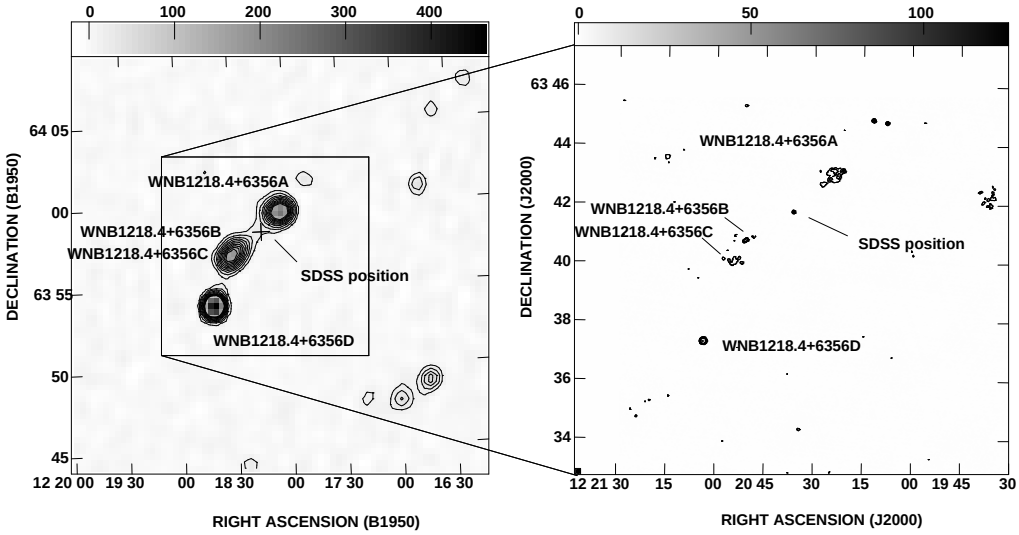

Figure 4.5: The image cutouts from the WENSS (327 MHz, $left$) and FIRST (1.4 GHz, *right*) surveys of a multicomponent WENSS source WNB1218.4+6356. In both panels the grey scale flux density is given in units of mJy/beam. $Left$: the contour levels are at 15 mJy/beam $\times(-10,-9,...,9,10)$, the peak flux density measured in the map is 461 mJy/beam, and the map resolution is 54×60 arcsec. The SDSS position of the source matched to the FIRST source is marked with a cross. *Right*: the contour levels are at 0.65 mJy/beam $\times(-10,-9,...,9,10)$, the peak flux density measured in the map is 124 mJy/beam, and the map resolution is 5.4×5.4 arcsec.

4.3.3 The final cross-matched sample

Although the Best et al. sample reaches the NVSS detection limit of 2.5 mJy, in the sub-sample of the extended radio sources which I focus on, the lowest integrated flux density of a source is 40 mJy. In the original sample of Best et al. (2005) the integrated flux limit of NVSS sources was set to 5 mJy, which is above the survey's completeness limit of 3.4 mJy of the survey[7]. However, at the faint flux densities the extended radio source morphological classification becomes ambiguous (P.N. Best, 2008, private communication). For the brighter flux densities the morphological classification of radio galaxies is considered secure, hence the NVSS flux limit of 40 mJy is introduced. Given that the WENSS survey contains sources detected down to ~ 18 mJy I expect to find matches for all sources, especially given that FR II sources are steep spectrum sources with a typical radio spectral index of $\alpha \approx 0.7-0.8$. For 118 sources from the Best et al. FR II sub-sample which are found at declinations of $\delta \gtrsim +28.5^{\circ}$ at 1.4 GHz all the sources with their WENSS counterparts are matched.

[7]The completeness limit of a survey is the flux density above which all radio sources are expected to be detected, and so it differs from the detection limit which is simply taken as 5σ the rms noise of the radio image. The completeness limit is often determined via simulations and statistical considerations.

A much worse situation arises in the case of the sample cross-match with the VLSS survey. The lowest integrated flux density of a source in the VLSS catalogue is 0.4 Jy, which indicates that sources with $\alpha_{1400}^{74} < 0.78$ will be missed due to the survey sensitivity. Such a difference in sensitivity of the two catalogues may lead to a significant bias in the cross-matched sample since even the steep spectrum sources, which are neither self-absorbed at low frequencies nor Doppler boosted at GHz frequencies, may undergo a selection. Indeed, although the Best et al. sample and the VLSS survey span similar areas of the sky, for 290 sources from the Best et al. FR II sub-sample only 134 VLSS sources were matched (46 per cent). For that reason I do not consider this survey further in this work.

The final observational data set is presented in Figure 4.17, and the demography of the sample is presented in Table 4.1. A total of 118 sources with linear sizes of more than 10 kpc are selected (none of the sources was excluded based on this criterion, but see also §4.3.4 for discussion on exclusion of an additional two sources). Since the flux limit is defined at 1.4 GHz, I decided to scale it to 325 MHz of the WENSS survey. Applying the simple power-law relation (Eqn. 3.1) and employing the typical radio spectral index of $\alpha = 0.7$, at 325 MHz I find flux limit of $S_{\rm lim,325MHz} = 110$ mJy. Once applied to the matched WENSS sample six further sources are excluded due to their radio flux densities at 325 MHz being less than adopted here $S_{\rm lim,325MHz}$. All of these sources have small physical sizes ($\lesssim$ 80kpc), and their 1.4 GHz radio flux densities are low, close to the introduced flux limit of 40 mJy ($\sim$ 45 mJy). It is possible that these sources were included in the 1.4 GHz sample due to some additional compact emission from the hot spots or/and compact radio cores. These excluded sources do not display any obvious difference in their redshift distribution as compared to the rest of the sample.

The sample is further divided into four linear size bins (Table 4.2). The size ranges were chosen to contain similar number of sources in the case of sources with linear sizes of < 1 Mpc, while the last size bin tracks giant radio galaxies more accurately (giant radio galaxies are defined as sources of total linear sizes of more than 1 Mpc). For each of these size bins a radio lobe luminosity density distribution is constructed. The distribution is constructed at an observing frequency of 325 MHz from $\log_{10}(L_{325MHz}) = 20.0$ to $\log_{10}(L_{325MHz}) = 27.0$ in steps of $\Delta\log_{10}(L_{325MHz}) = 0.5$. Such a division of the population allows one to track the relative number of the sources with a given size more accurately.

In Figure 4.6 the radio lobe luminosity density – redshift plane of the sources matched with the WENSS catalogue is displayed. 36 per cent of the matched sources (42 sources) have multicomponent matches which are considered as true multicomponent radio structures (see also §4.3.2). The radio lobe luminosity density – radio spectral index plane of the final sample is presented in Figure 4.7. To find radio spectral index a simple power-law scaling between 325 MHz and 1.4 GHz was used. The errors on the calculated radio spectral indices are propagated in quadrature, and a standard deviation is quoted for the average values of α. The average radio spectral index of all the matched sources is $\alpha_{1400}^{325} = 0.71 \pm 0.09$, where for the (true) multicomponent sources it is $\alpha_{1400}^{325} = 0.73 \pm 0.08$,

and for single matched sources is $\alpha_{1400}^{325} = 0.70 \pm 0.09$ (for all of these cases the average error on α of each radio source is ~ 0.003). Such values are expected for a population of steep spectrum sources such as FR II radio galaxies. It can be noticed from Figure 4.7, however, that lower luminosity density sources tend to have flatter radio spectral indices than the higher luminosity density ones. To investigate whether this is an observational bias (coming from the limited sensitivity for instance), the radio sources were grouped in redshift, flux density and linear size ranges (marked as different colours in Figure 4.7). The redshift and linear size do not seem to explain the visible tendency in the distribution. This indicates that the radio luminosity density dependence on the spectral index may be intrinsic. Indeed, while grouping the sources in flux density intervals it can be seen that the sources of higher flux density seem to have steeper radio spectra. Specifically, the average radio spectral index for the radio sources with flux densities of < 150 mJy is $\alpha_{1400}^{325} = 0.59$, while for those with flux densities of > 1.5 Jy the average radio spectral index is $\alpha_{1400}^{325} = 0.79$. Such a correlation between radio lobe luminosity density density and radio spectral index has been previously noted by e.g. BRW99. In particular, BRW99 postulate that the initial energy distribution of relativistic particles may steepen if the magnetic field in radio source's hot spots is particularly strong. The authors suggest that if the magnetic field in hot spots is stronger for powerful radio sources than it is for less powerful ones, then radio spectra will be steeper for the former ones. Nonetheless, even if the dependence is intrinsic it does not alter the completeness of the radio sample.

Finally, the radio lobe luminosity density – linear size plane, and also linear size and redshift and radio spectral index planes are plotted in Figure 4.8 – Figure 4.10. No obvious unexpected correlations, which would be a sign of a bias, seem to be present in the final cross-matched sample.

4.3.4 Excluded sources

Two radio galaxies were excluded from the final cross-matched sample based on other than a minimum linear size or flux limit criteria, namely 3C 236 and 4C 29.30.

3C 236 is one of the largest radio galaxies known in the Universe. Its linear size extends to ~ 4.5 Mpc. Although the source has been extensively studied (Willis *et al.*, 1974; Fomalont and Miley, 1975; Fomalont *et al.*, 1979; Schilizzi *et al.*, 1979; Barthel *et al.*, 1985; Mack *et al.*, 1997; Schilizzi *et al.*, 2001, among others) it is not as yet clear whether it has been undergoing interrupted (restarted) activity (e.g. O'Dea *et al.*, 2001; Tremblay *et al.*, 2010) which would classify it as a so-called double-double radio galaxy (DDRG; Schoenmakers *et al.*, 2000a, see also below), or whether its activity is continuous (Strom and Willis 1980, cf. Schilizzi *et al.* 2001). Nevertheless, even if the latter is the case, this radio source with its enormous physical size seems to act as an outlier (see e.g. Figure 4.8). The probability of detecting such a radio source will be further discussed in the light of the results in §4.4.

4C 29.30 (the FIRST source J0840+2949) at redshift $z = 0.0647$ and of the maximum

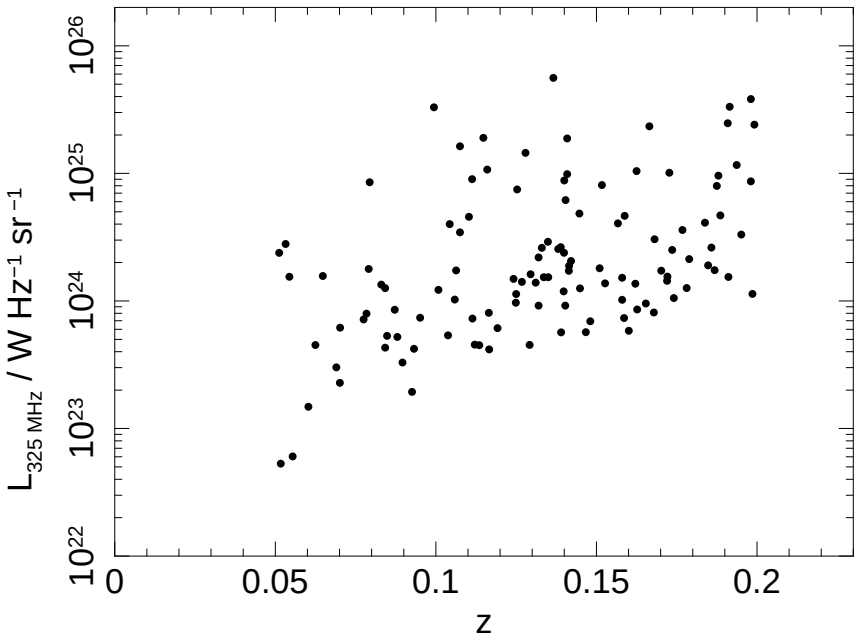

Figure 4.6: Radio lobe luminosity density – redshift plane of the matched Best et al. FR II sources with the WENSS survey.

linear size 640 kpc is a known DDRG (Jamrozy *et al.*, 2007).

Although their existence has been noted before (e.g. Bridle *et al.*, 1989; Clarke *et al.*, 1992), the double-double radio galaxies have been defined by Schoenmakers *et al.* (2000a). These peculiar radio sources are generally defined as extragalactic radio sources which consist of two (or more) radio sources with a common centre. The inner pair of radio structures are always classical, edge brightened radio lobes. Brocksopp *et al.* (2007) discovered the first known triple-double radio galaxy – a radio source that most probably carries evidence of three cycles of activity. Schoenmakers *et al.* (2000a) discuss three possible scenarios that may lead to such an observed radio morphology. These include the direction change in the jet outflow, the backflow instabilities, and the interrupted jet activity; the latter is argued to be the most likely scenario. As showed by Kaiser *et al.* (2000) and Brocksopp *et al.* (2011) the standard models of FR II growth can be applied to the outer 'old' lobes of DDRGs, although some modifications are required. The 'new' pair of radio lobes, however, are not well described by these theoretical models. Both of these authors used the KA97/KDA97 model in their analyses, which assumes that the relativistic outflow propagates through the under-pressured IGM/ICM. Obviously, such an assumption is not valid in the case of the inner, newly restarted jets which propagate through the old cocoon, that is through a much denser environment than the model predicts. Clarke and Burns (1991) present numerical simulations of restarting jets reporting that the restarted outflows are overdense as compared to the old material, and their advance speeds are also much higher than those of the

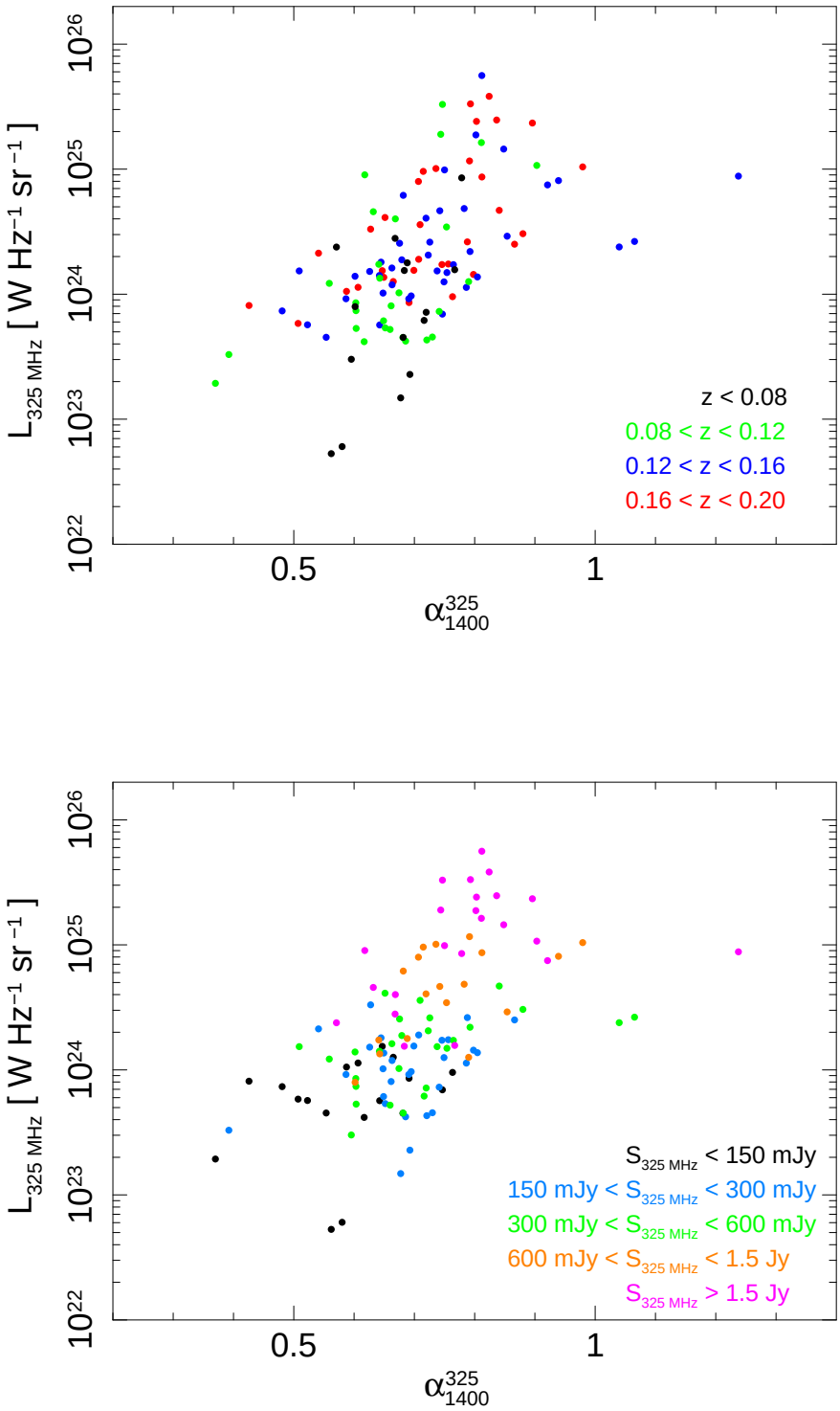

Figure 4.7: Radio lobe luminosity density – radio spectral index plane of the matched Best et al. FR II sources with the WENSS survey. In each plotted version of the figure the sample is divided into redshift (z), flux density at 325 MHz ($S_{325\mathrm{MHz}}$) or linear size (D) ranges as marked in the plots. [...*continued on next page*]

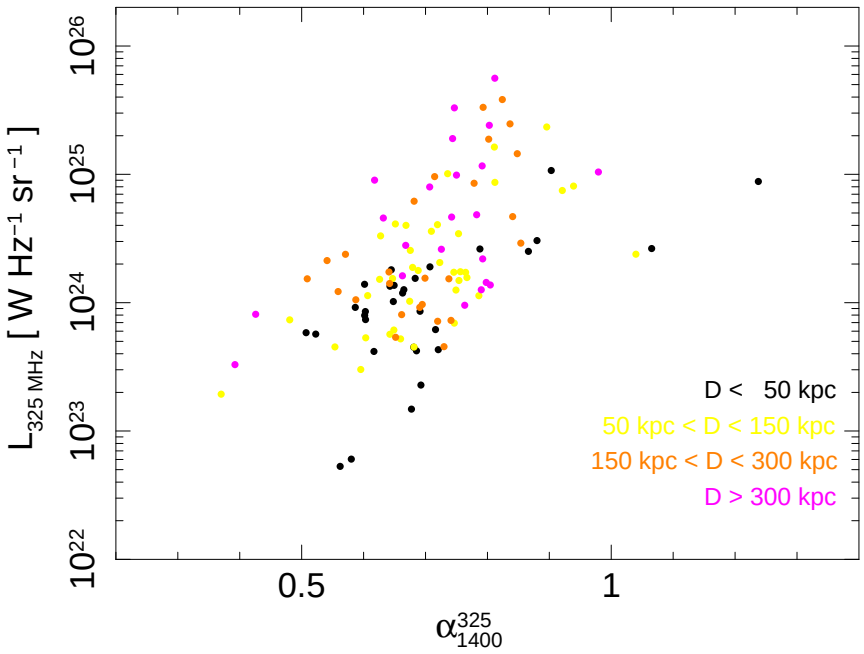

Figure 4.7: *Continued.*

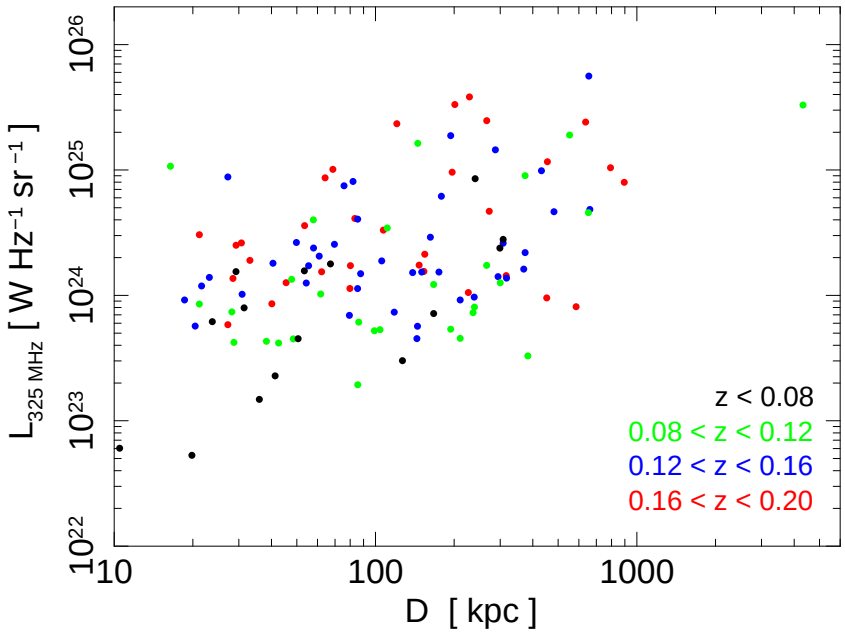

Figure 4.8: Radio lobe luminosity density – linear size of the matched Best et al. FR II sources with the WENSS survey. The sample is divided into redshift (z) ranges as marked in the plot.

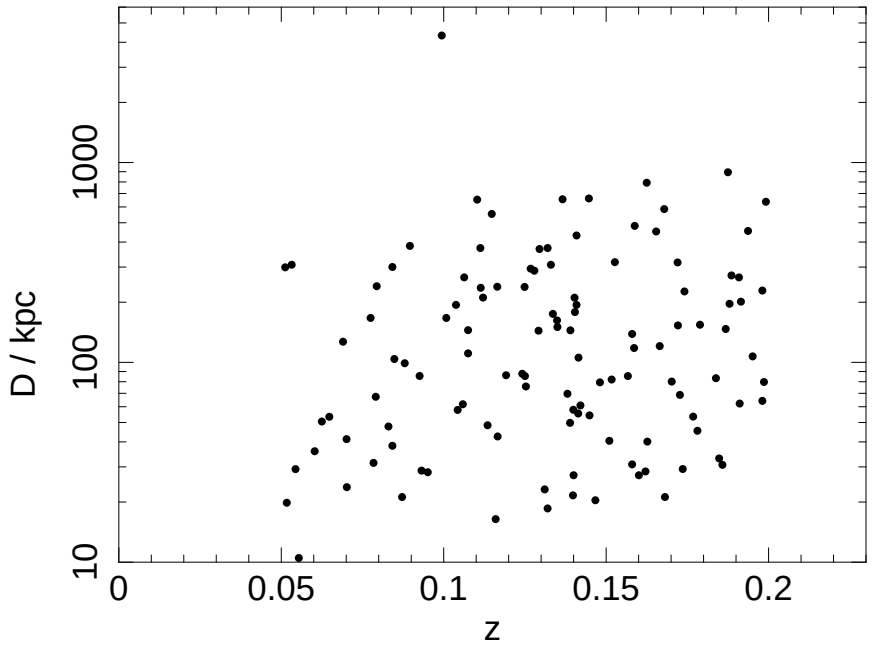

Figure 4.9: Linear size – redshift plane of the matched Best et al. FR II sources with the WENSS survey.

original jets.

DDRGs are rare radio sources; currently only $12-17$ sources are known (see Brocksopp *et al.*, 2011, and references therein). It has been suggested that DDRGs are a brief ($\sim 10^4$ yr), but expected evolutionary phase of the largest radio sources (Brocksopp *et al.*, 2011). Nevertheless, unless the original semi-analytical model of FR IIs' growth which are used here is appropriately modified, I am unable to model these sources, so I decided to exclude them from our radio samples.

4.3.5 Sources of particular interest

Apart from the two DDRGs discussed in §4.3.4 six so-called X-shaped (winged) radio sources (e.g. Ekers *et al.*, 1978; Leahy and Parma, 1992) are found in the sample. Up to 10 per cent of FR II radio galaxies are the X-shaped sources (e.g. Leahy and Parma, 1992). The following X-shaped RGs are found in our radio sample: the well known 3C 233.1, 4C+32.25 and 4C+48.29, and three confirmed candidates J1207+3352, J1444+4147 and J1455+3237 (Cheung, 2007; Cheung *et al.*, 2009). The origin of these sources has been discussed by, among others, Gopal-Krishna *et al.* (2003), Saripalli and Subrahmanyan (2009) and Gopal-Krishna *et al.* (2010), and it has been suggested that their morphology may originate due to the backflow (plasma flowing back from the source hot spots, see Gopal-Krishna *et al.* 2010 and references therein, and Hodges-Kluck and Reynolds 2011), or even may be the effect of the existence of twin SMBH in the AGN, and the effect of rapid jet reorientation (Gopal-Krishna *et al.* 2003; Mezcua *et al.* 2011; see also Gopal-Krishna *et al.* 2010

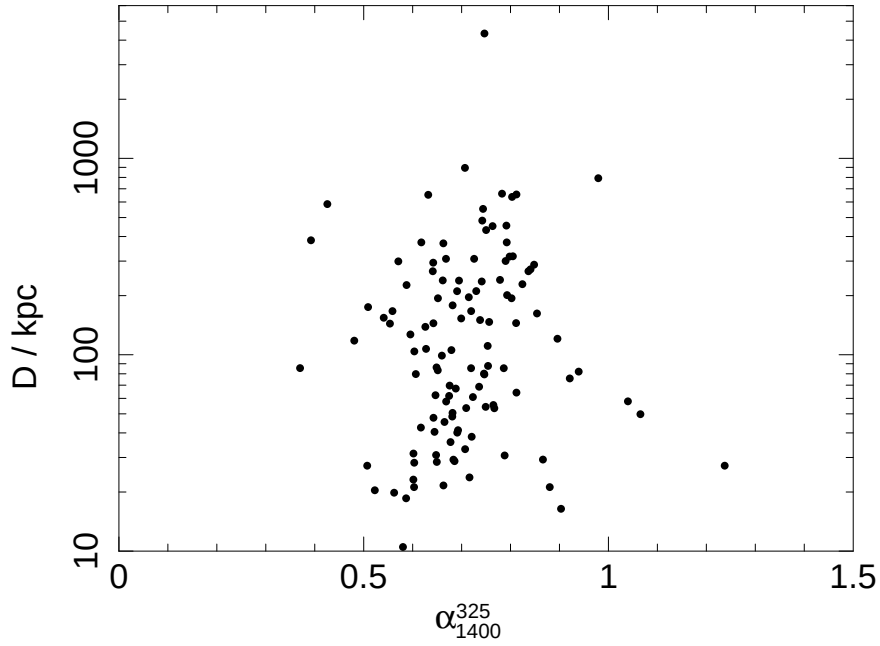

Figure 4.10: Linear size – radio spectral index plane of the matched Best et al. FR II sources with the WENSS survey.

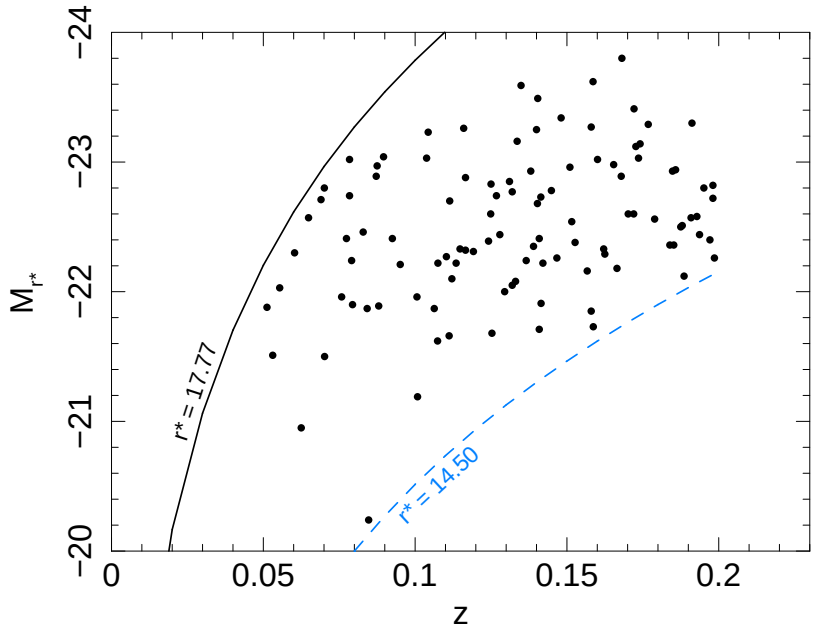

Figure 4.11: Redshift distribution of the absolute magnitudes of the matched Best et al. FR II sources (the M_{r^*} magnitudes obtained from P.N. Best, see also Best *et al.* 2005 and Best and Heckman 2012). The introduced apparent magnitude limits, where the lower limit $r* = 17.77$ (solid black) and upper limit $r* = 14.50$ (dashed blue), and their dependence on redshift are plotted and marked.

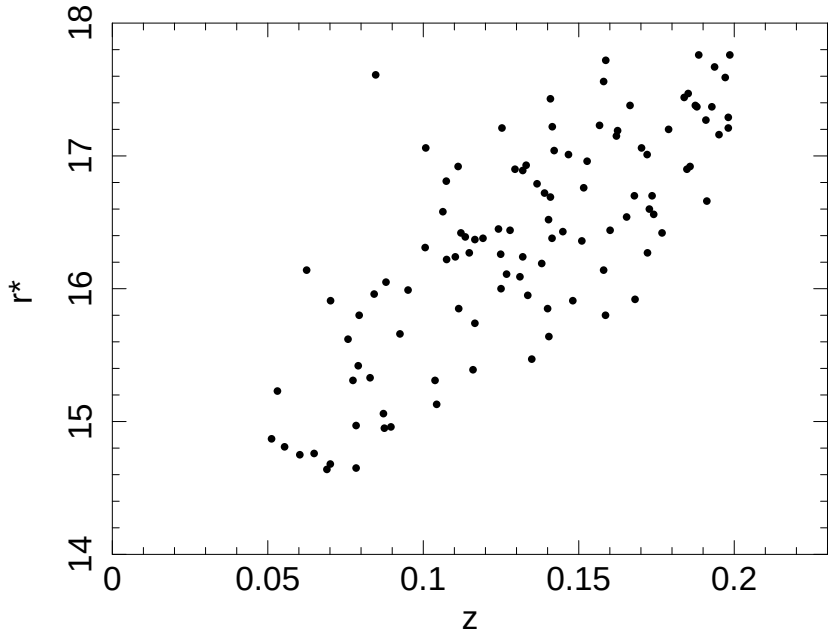

Figure 4.12: Redshift distribution of the apparent magnitudes of the matched Best et al. FR II sources (the r^* magnitudes obtained from P.N. Best, see also Best *et al.* 2005 and Best and Heckman 2012).

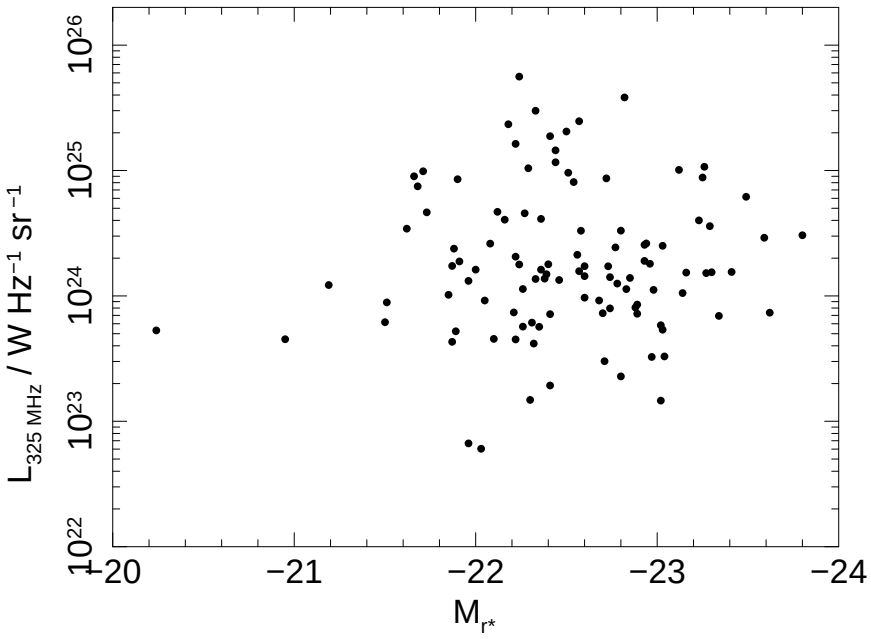

Figure 4.13: Radio lobe luminosity density of the Best et al. FR II sources matched with the WENSS survey and the absolute magnitudes of their host galaxies (the M_{r^*} magnitudes obtained from P.N. Best, see also Best *et al.* 2005 and Best and Heckman 2012).

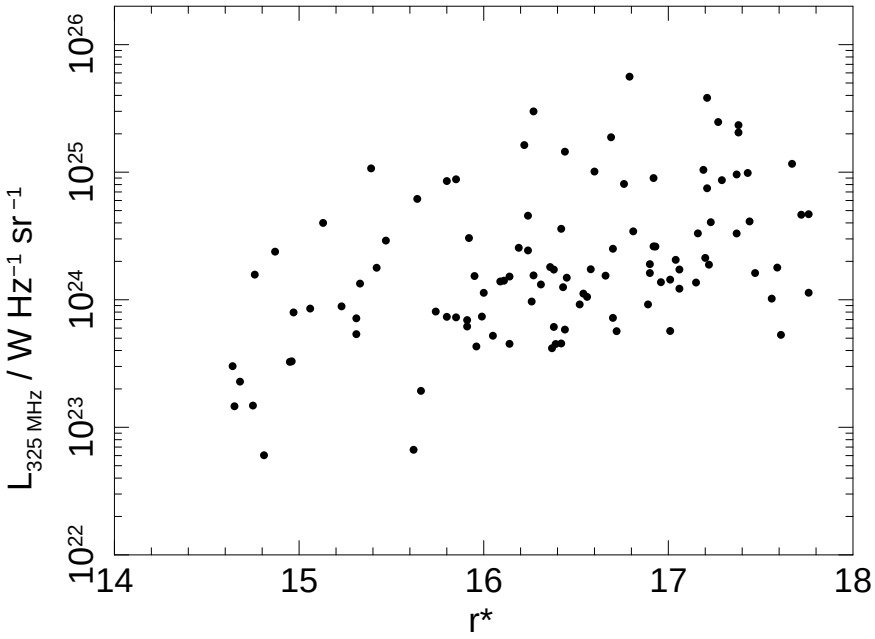

Figure 4.14: Radio lobe luminosity density of the Best et al. FR II sources matched with the WENSS survey and the apparent magnitudes of their host galaxies (the r^* magnitudes obtained from P.N. Best, see also Best *et al.* 2005 and Best and Heckman 2012).

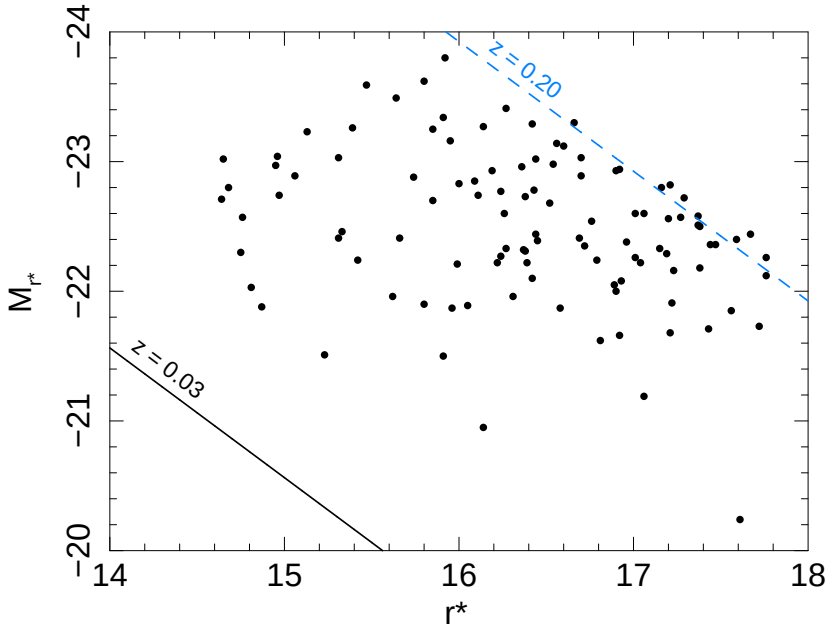

Figure 4.15: Absolute – apparent magnitude plane of the matched Best et al. FR II sources (magnitudes obtained from P.N. Best, see also Best *et al.* 2005 and Best and Heckman 2012). The relationship between the two magnitudes and redshift is plotted, where the solid line (black) represents the relation for redshift $z = 0.03$ and dashed (blue) represents the relation for $z = 0.20$.

for review). The former is currently the class of most popular models explaining X-shaped RGs. Nevertheless, none of these sources show signatures of restarted activity (i.e. none of them is a DDRG), so they are not excluded from the analysis.

4.4 Confidence intervals of the low luminosity radio galaxies' fundamental properties

To obtain the confidence intervals of the fundamental parameters which are the main focus of this study[8] a grid minimisation was performed. The ranges of the parameters searched are given in Table 4.3. The semi-analytical models of the radio source growth, the Monte Carlo simulations, and the statistical methods used, are described in Chapter 2 of this thesis. The influence of some of the radio source growth model assumptions are discussed in Chapter 3 (§3.10); in the study of the current low redshift, low radio luminosity sample of FR II sources the initial assumptions as described in Chapter 2 only are used (a summary is given in Table 4.4).

The best-fitting model histograms are presented in Figure 4.17 (for simulation run 1 only, consult Table 4.5). The best fitting parameters of the initial run 1 of the simulation are listed in Table 4.5. In the initial run of the simulation the same assumptions and their values have been adopted as in the case of the initial simulation runs of 3CRR/BRL samples of Chapter 3. As can be clearly seen, the GoF test results indicate that the probability that the investigated radio lobe luminosity density distribution originated from the parent population parametrised by the best fit parameters lies within 99.52 per cent of all possible realisations (see Chapter 2: §2.4.2 for detailed explanation of the GoF test). This means that the hypothesis that the observational radio sample originated from the found parent population should be rejected on the grounds of the adopted (rather conservative) level of significance ($\alpha_{\rm sig} = 0.1$, Chapter 2:§2.4.2). There are two possible reasons for such a result.

Figure 4.17 shows the radio lobe luminosity density distributions of the observed and simulated data (simulation run 1). As can be clearly seen the simulated data fail in the reconstruction of the radio lobe luminosity densities of the radio sources with the smallest linear sizes. The simulation was run with the initial assumptions which were defined in Chapter 2 (see also Table 4.4). The influence of these assumptions on the results has been discussed in §3.10. Although only a few of these assumptions seemed to have a profound influence on the confidence intervals of the powerful FR IIs analysed in Chapter 3 (e.g. the jet particle content, and the minimum Lorentz factor of the initial distribution of relativistic particles), it is possible that some of them may be more important for the population of low luminosity radio sources. In particular, the choice of maximum head advance speed may influence the sizes of radio galaxies. As discussed in §3.6 and §3.10.3 the lower $v_{\rm max}$ is

[8]The fundamental parameters are: the maximum radio source lifetime $t_{\rm max_m}$, the central density in which the radio source expands $\rho_{\rm m}$, and the kinetic luminosity break $Q_{\rm B}$ and the slope $\alpha_{\rm s}$ which define the initial distribution of the kinetic luminosities.

Table 4.2: Demography of the sample based on Best et al. FR II sub-sample matched with the WENSS survey. Redshifts covered: $z \leq 0.2$. In our analysis sources of linear sizes larger than 10 kpc only are considered.

Size range (D)	No. of FR II sources
excluded, $D < 10$ kpc	0
$D_1 \in [10, 62]$ kpc	36
$D_2 \in (62, 194]$ kpc	36
$D_3 \in (194, 1000]$ kpc	37
$D_4 > 1$ Mpc	0†

Notes. † A giant radio galaxy, 3C 236, has been additionally excluded from the sample, see text for details.

Table 4.3: Searched ranges and steps of the distribution parameters in the grid minimisation.

Parameter	Searched range	Step	Unit
$Q_{\rm B}$	$[35.0, 41.0]$	0.15	$\log_{10}$(W)
$\alpha_{\rm s}$	$[-4.0, 2.5]$	0.1	
$\rho_{\rm m}$	$(-26.0, -18.0]$	0.2	$\log_{10}(\mathrm{kg\,m^{-3}})$
$t_{\rm max_m}$	$[4.4, 10.2]$	0.15	$\log_{10}$(yr)

allowed, the older the radio sources may become. On the other hand, for a given lifetime the lower the head advance speed is set, the larger the radio source may grow. Moreover, other assumptions may also have stronger influence on the population of low luminosity sample than what was possible to verify with the powerful radio sources investigated in Chapter 3; the effect of adopting higher values of the minimum Lorentz factors for the initial relativistic particles and composition of the outflows are of particular interest here since these two quantities are not well constrained yet. Results of these tests are listed in Table 4.5. Based on the goodness-of-fit test no acceptable results are found for either the initial assumptions or their modifications.

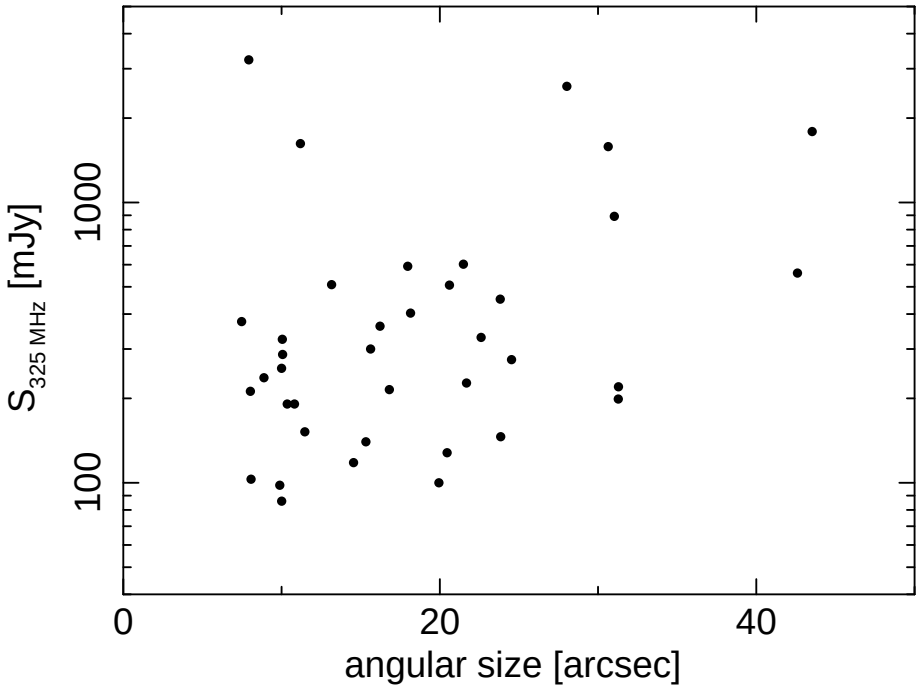

Figure 4.16: Distribution of flux densities and angular sizes of the problematic sources (that is when $D < 60$ kpc).

Therefore, the second possibility is that the radio sources are simply misclassified. To test this hypothesis I re-ran the Monte Carlo simulations on restricted versions of the initial radio sample. The following cases are investigated: (i) sources of linear sizes smaller than 60 kpc are excluded (33 sources), (ii) sources of small angular sizes are excluded (21 sources if the smallest angular size allowed is $\theta_{\rm size} = 20$ arcsec, 35 sources if $\theta_{\rm size} = 30$ arcsec, 45 sources if $\theta_{\rm size} = 35$ arcsec), and (iii) sources of flux densities fainter than 60 mJy at 1.4 GHz (which corresponds to 167 mJy at 325 MHz assuming typical spectral index of $\alpha = 0.7$) are excluded (20 sources). Results of these tests are listed in Table 4.5. Based on the goodness-of-fit test acceptable results are found only if sources of the smallest linear sizes ($D < 60$ kpc) are excluded from the sample. The fitted radio lobe luminosity densities of the observed and simulated distributions for this case are presented in Figure 4.17. This result suggests strongly that a significant fraction of the smallest radio sources in this sample may be misclassified FR Is; the lobed FR Is are most likely suspected which may resemble FR II especially at faint flux densities and/or small angular sizes (cf. e.g. Laing *et al.*, 2011). Distribution of flux densities and angular sizes of the problematic sources (that is when $D < 60$ kpc) are plotted in Figure 4.16. It is worrying, however, that restricting the sample in minimum allowed flux or radio source angular size does not lead to acceptable results as this suggests that the problem occurs at various fluxes and various angular sizes of the radio sources. The only solution to this problem at the current stage is to verify the original morphological classification of the initial SDSS-FIRST-NVSS radio sample.

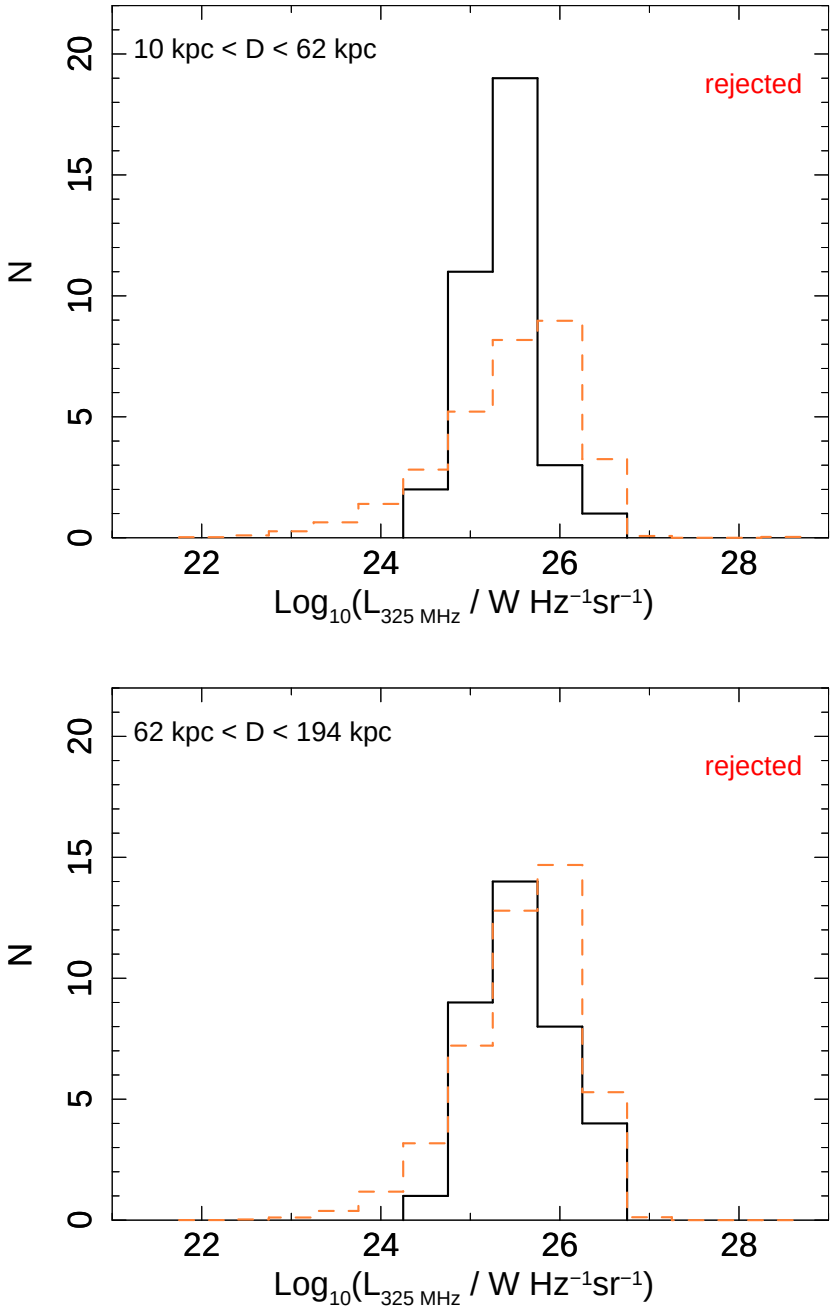

Figure 4.17: Histograms of the observed (black, solid) and simulated (orange, dashed) data, where *top* contains the smallest sources (10 kpc $< D \leq$ 62 kpc), and *bottom* contains sources of linear sizes within 62 kpc $< D \leq$ 194 kpc. [...*continued on next page*]

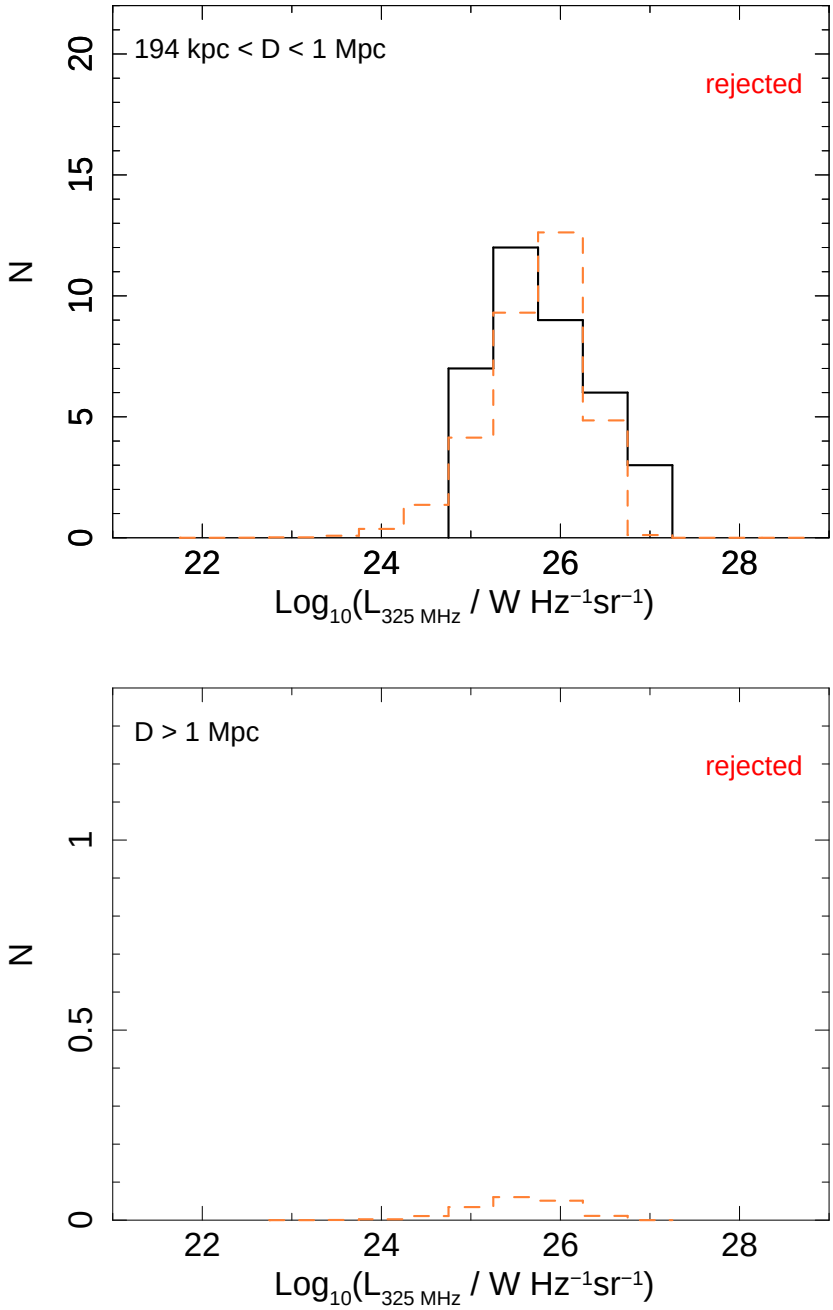

Figure 4.16: *Continued.* *Top* contains sources with 194 kpc $< D \leq$ 1.0 Mpc in linear extent, and *bottom* contains giant radio sources. Shown confidence intervals are for simulation run 1. These results are rejected based on the GoF results ($p-$value$= 0.0048$).

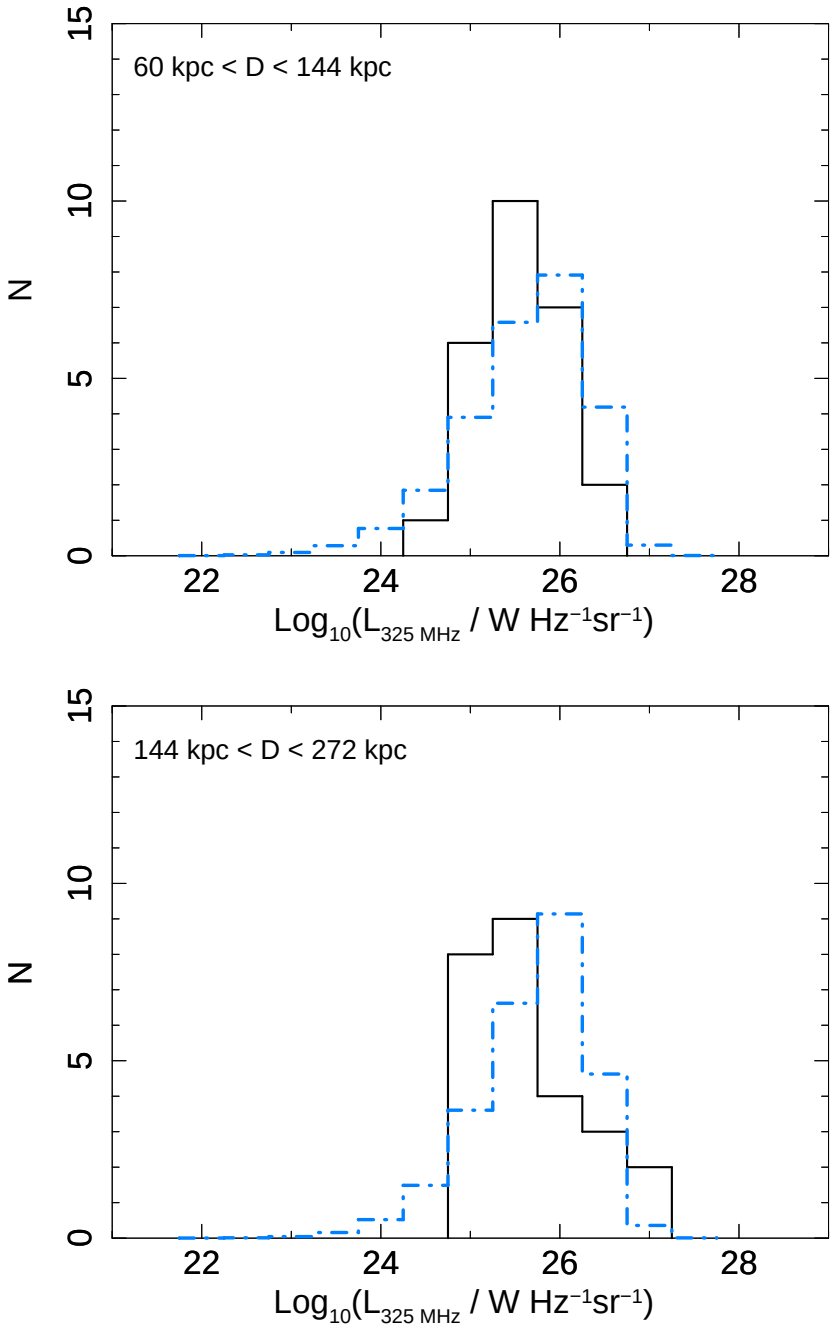

Figure 4.17: Histograms of the observed (black, solid) and simulated (blue, dash-dotted) data, where *top* contains the smallest sources (60 kpc $< D \leq$ 144 kpc), and *bottom* contains sources of linear sizes within 144 kpc $< D \leq$ 272 kpc. [...*continued on next page*]

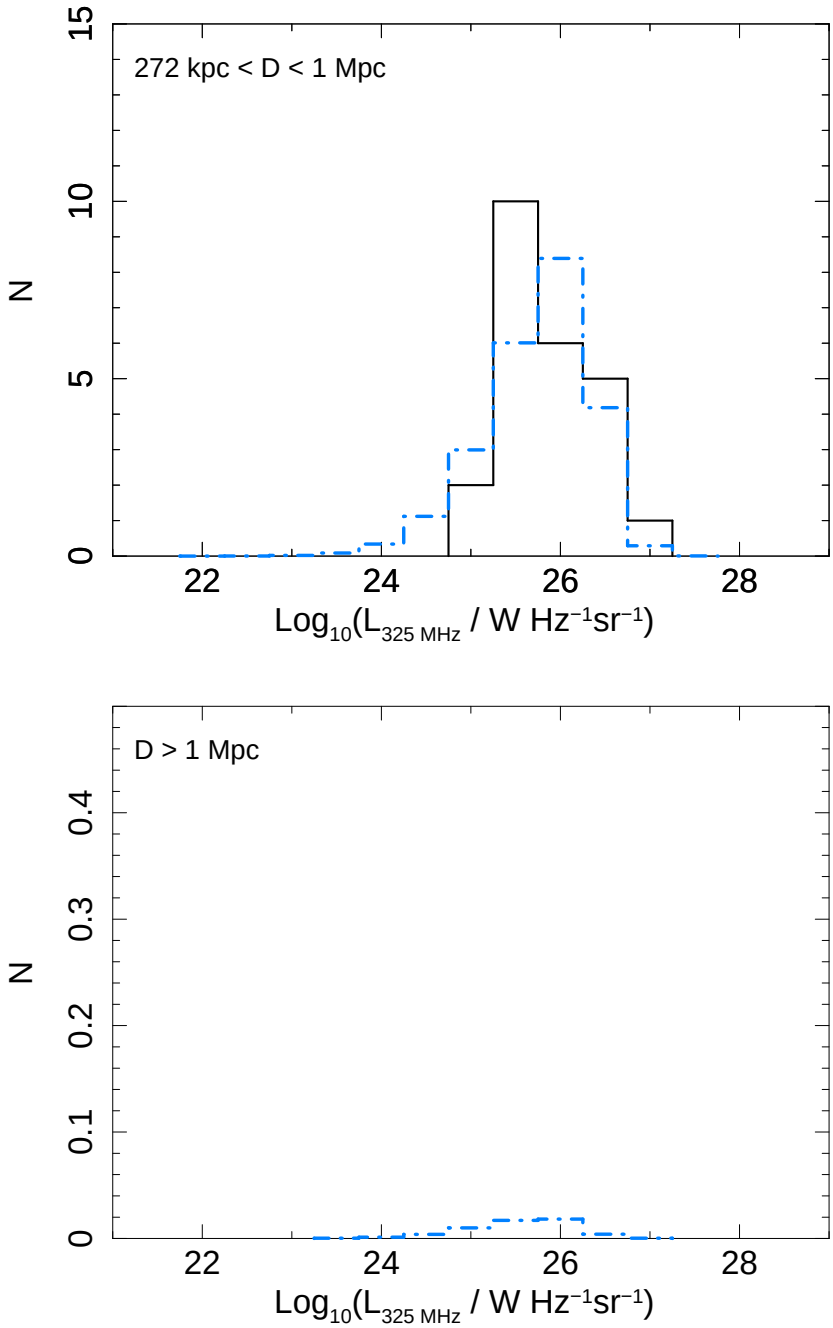

Figure 4.17: *Continued.* *Top* contains sources with 272 kpc $< D \leq$ 1.0 Mpc in linear extent, and *bottom* contains giant radio sources. Shown confidence intervals are for simulation run 12. The results are consistent with the data at the 90 per cent confidence level ($p-$value $= 0.310$).

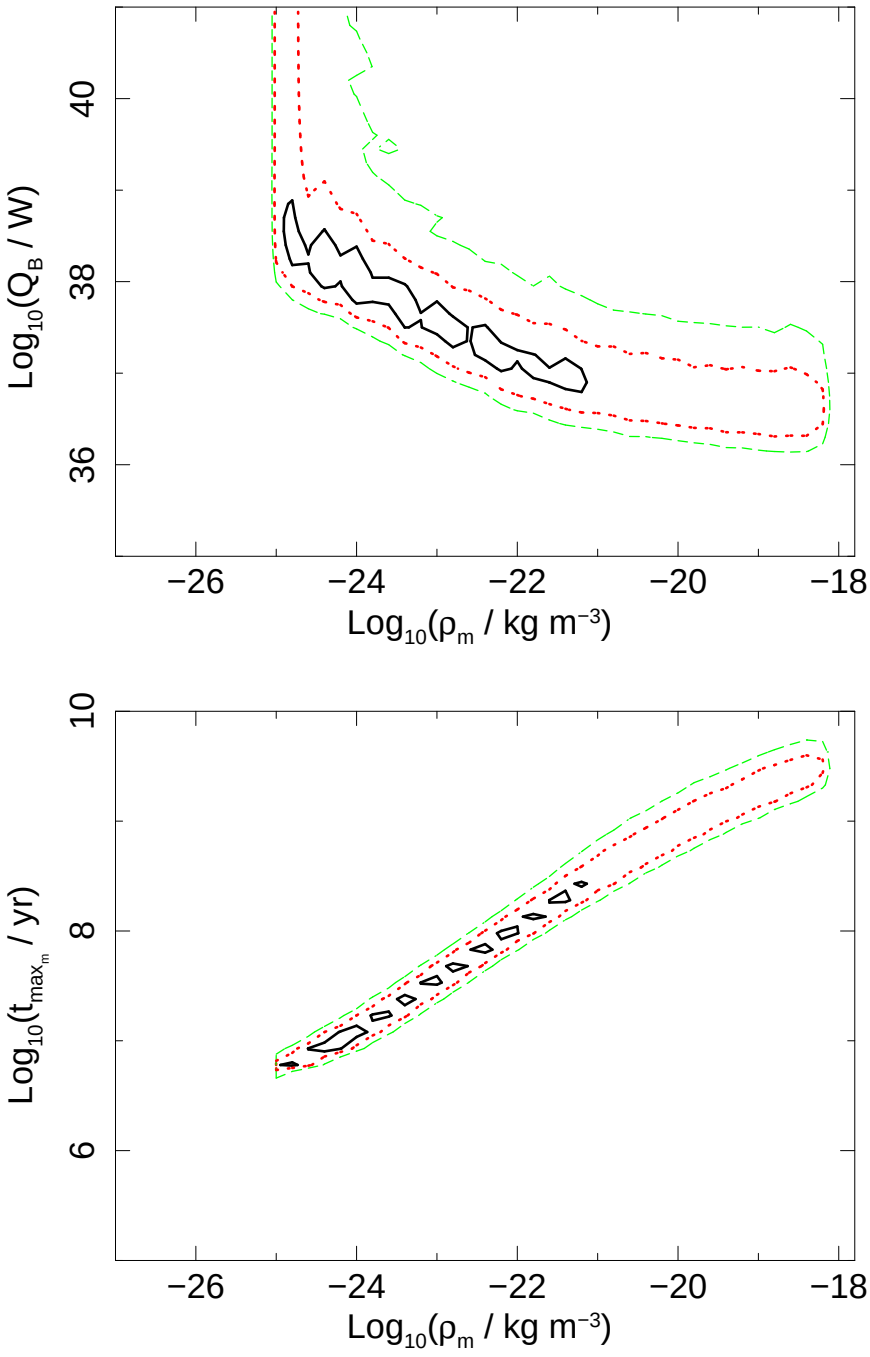

Figure 4.18: Joint confidence intervals for the simulation run 12 results ($z \leq 0.2$), where 68.3 per cent (solid, black), 95.4 per cent (dotted, red) and 99.7 per cent (dashed green) contours, based on ΔC statistics (see §2.4), are shown. The best-fitting parameters are consistent with the data at the 90 per cent confidence level ($p-\text{value} = 0.310$).

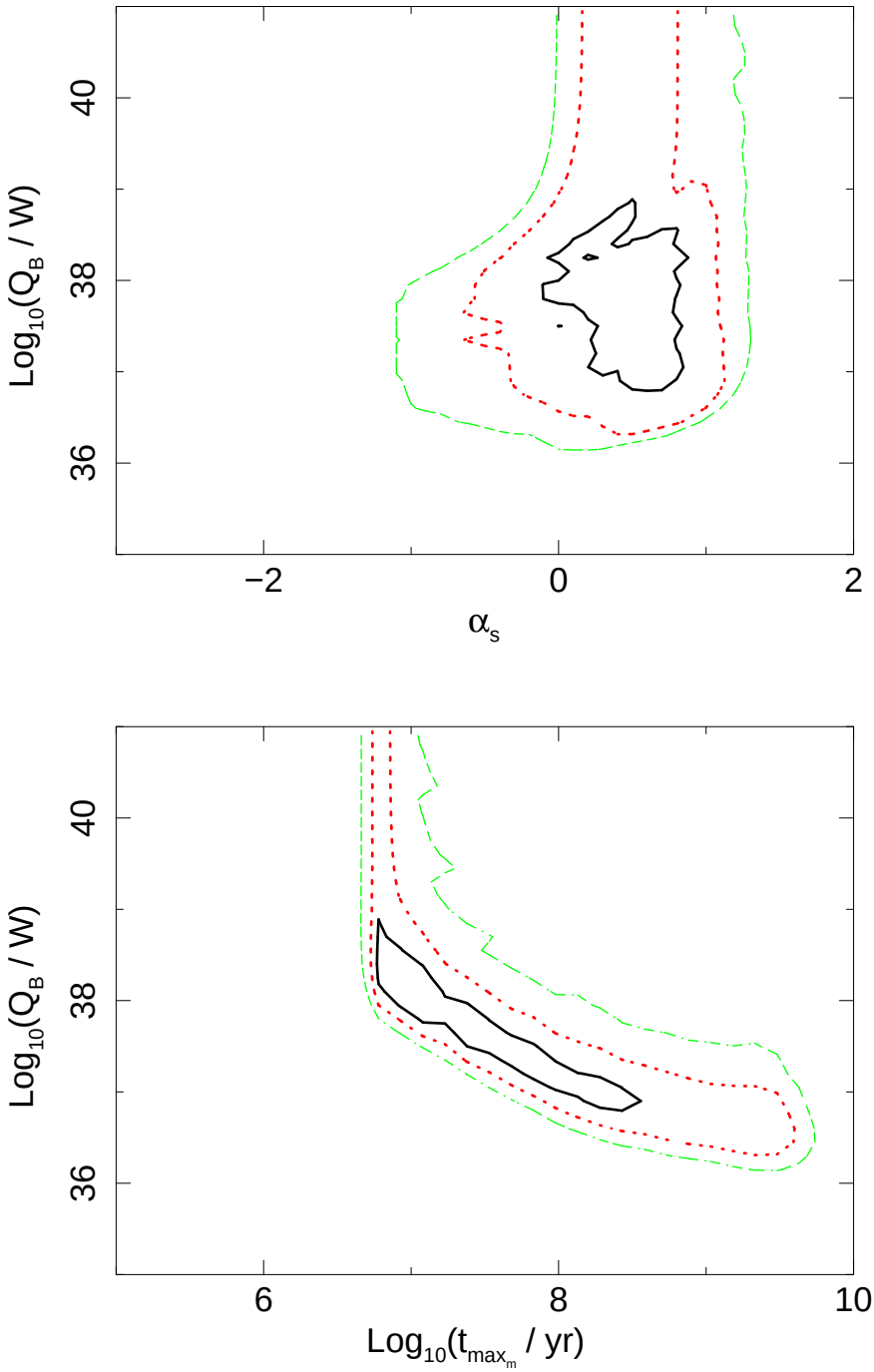

Figure 4.18: *Continued*.

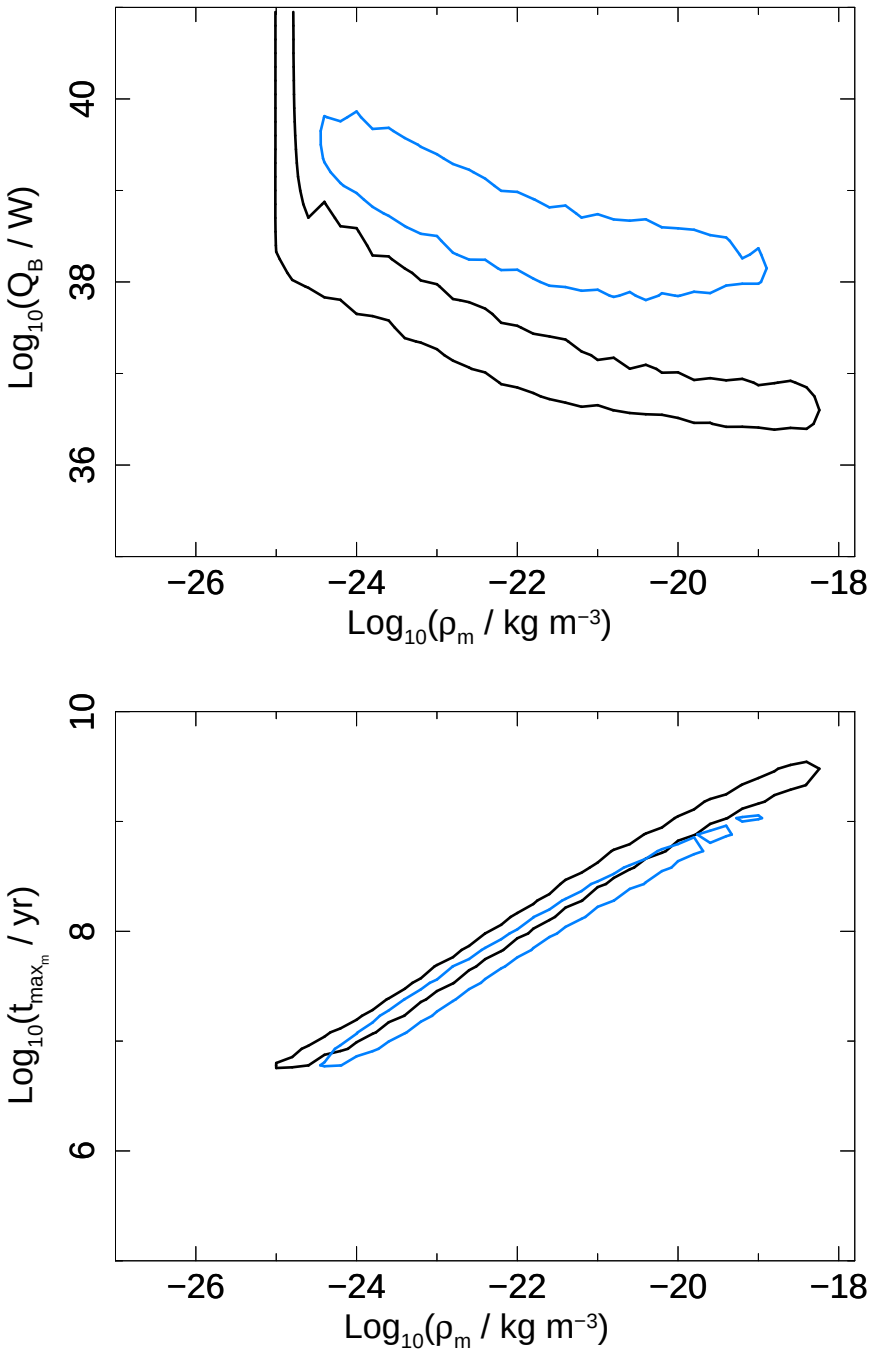

Figure 4.19: 90 per cent joint confidence intervals of the results found for simulation run 12 of the low luminosity sample considered in this chapter (black) and the results of the powerful FR IIs from Chapter 3 for redshifts $z < 0.3$ (blue). Confidence intervals are based on on ΔC statistics (see §2.4).

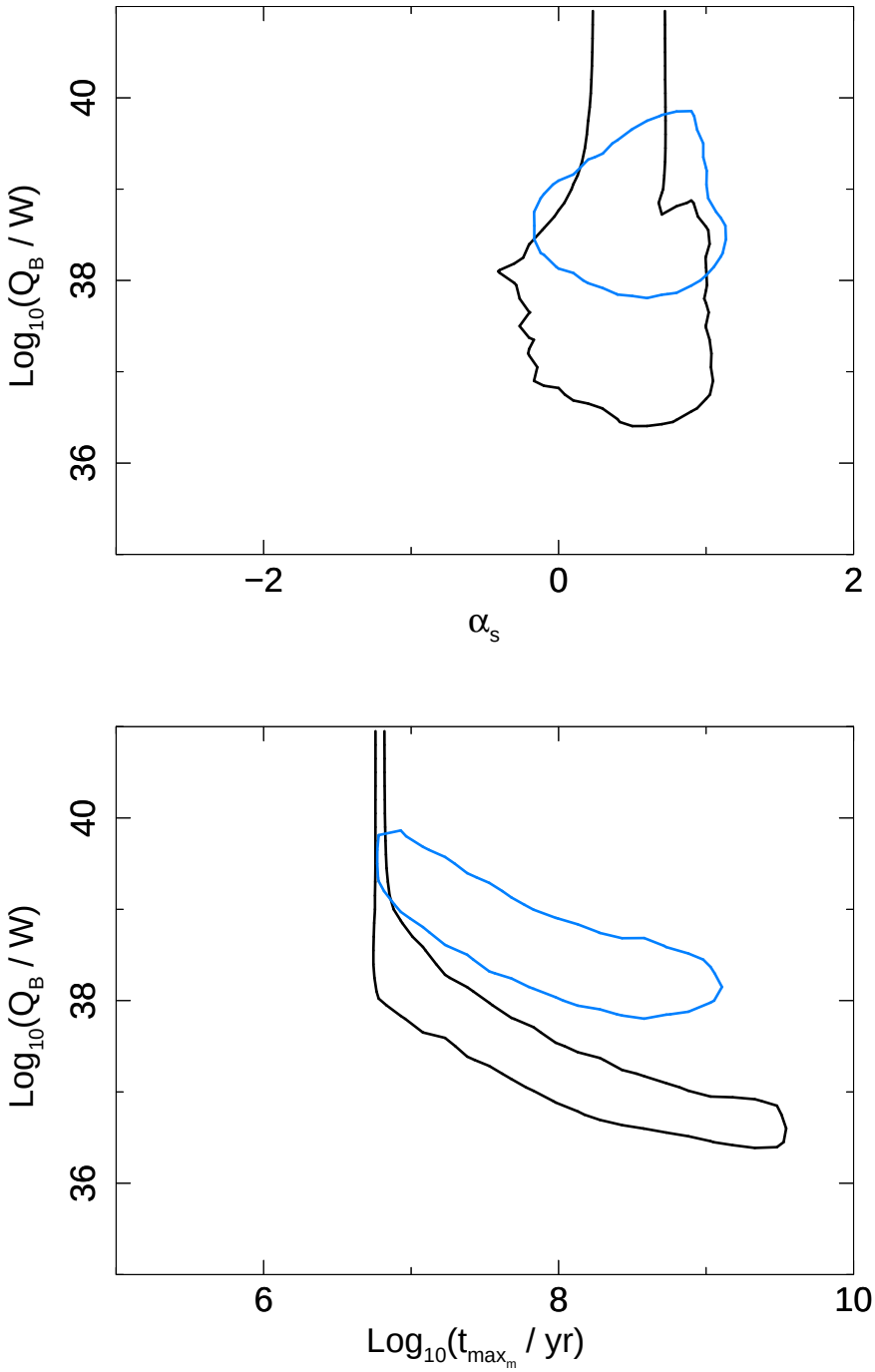

Figure 4.19: *Continued*.

Table 4.4: Summary of the initial assumptions for radio source physical parameters. For details on the parameters see Chapter 2.

Parameter	value	Assumed distribution	Units
		PHYSICAL PARAMETERS	
Q		Schechter function (Eqn. 2.19)	log(W)
$\rho_{\rm o}$		log-normal: mean $\rho_{\rm m}$, standard deviation $\sigma_{\rho_{\rm o}} = 0.15$	log(kg m^{-3})
t		uniform: $10^t \in [0, 10^{t_{\rm max}}]$	log(yr)
$t_{\rm max}$		log-normal: mean $t_{\rm max_m}$, standard deviation $\sigma_{t_{\rm max}} = 0.05$	log(yr)
$a_{\rm o}$	2.0		kpc
β		uniform: $\beta \in [1.2, 2.0]$	dimensionless
$R_{\rm T}$		uniform: $R_{\rm T} \in [1.3, 8.0]$	dimensionless
k'	0		dimensionless
$v_{\rm max}$	0.4c		light speed c
ϑ		uniform: $\vartheta \in (0, \{1-\cos(\vartheta)\}]$	dimensionless
m		uniform: $m \in [2, 3]$	dimensionless
$\gamma_{\rm min}$	1		dimensionless
$\gamma_{\rm max}$	10^{10}		dimensionless
$\Gamma_{\rm B}$	4/3		dimensionless
$\Gamma_{\rm l}$	4/3		dimensionless
$\Gamma_{\rm x}$	5/3		dimensionless

Table 4.5: The best-fitting parameters found for different model assumptions. See Table 4.4 for a list of initial assumptions. If any assumption differs from the initial ones, it is highlighted in Column 1. 90 per cent errors are quoted.

Simulation run	$\log_{10}(Q_{\rm B}/{\rm W})$	$\alpha_{\rm S}$	$\log_{10}(\rho_{\rm m}/{\rm kg\,m^{-3}})$	$\log_{10}(t_{\rm max_m}/{\rm yr})$	$p-$value
complete matched radio sample					
1) initial	$36.45^{+0.15}_{-0.15}$	$0.7^{+0.2}_{-0.2}$	$-18.6^{+0.2}_{-1.4}$	$9.33^{+0.15}_{-0.45}$	0.0048
2) $v_{\rm max}=0.15c$	$37.40^{+0.15}_{-0.15}$	$0.4^{+0.3}_{-0.4}$	$-23.0^{+0.4}_{-0.4}$	$7.53^{+0.15}_{-0.15}$	0.0043
3) $v_{\rm max}=0.15c$, $\gamma_{\rm min}=10^2$	$38.30^{+0.45}_{-0.30}$	$0.3^{+0.3}_{-0.4}$	$-25.0^{+0.2}_{-(<0.2)\dagger}$	$6.63^{+0.15}_{-(<0.15)\dagger}$	0.0019
4) $v_{\rm max}=0.15c$, $k'\in[0,100]$	$37.10^{+0.30}_{-0.30}$	$0.4^{+0.3}_{-0.8}$	$-20.0^{+1.2}_{-1.0}$	$8.58^{+0.45}_{-0.30}$	0.0164
5) $v_{\rm max}=0.15c$, $\gamma_{\rm min}=10^2$, $k'\in[0,100]$	$36.65^{+0.30}_{-0.30}$	$0.5^{+0.3}_{-0.7}$	$-18.6^{+(<0.2)\dagger}_{-1.6}$	$9.18^{+(<0.15)\dagger}_{-0.45}$	0.0133
6) $v_{\rm max}=0.15c$, $k'=1000$	$39.95^{+0.30}_{-0.15}$	$0.4^{+0.3}_{-0.3}$	$-22.8^{+0.4}_{-0.2}$	$6.78^{+0.15}_{-(<0.15)\dagger}$	0.0030
7) $v_{\rm max}=0.15c$, $\gamma_{\rm min}=2\times10^3$, $k'=1000$	$39.35^{+0.45}_{-0.15}$	$0.4^{+0.3}_{-0.3}$	$-23.8^{+(<0.2)\dagger}_{-(<0.4)\dagger}$	$6.78^{+(<0.15)\dagger}_{-(<0.15)\dagger}$	0.0057
8) $v_{\rm max}=0.01c$, $k'\in[0,100]$	$36.95^{+0.30}_{-0.30}$	$0.4^{+0.3}_{-0.9}$	$-19.0^{+0.2}_{-2.0}$	$8.88^{+0.15}_{-0.60}$	0.0129
minimum angular size ($\theta_{\rm size,min}$) limits					
9) $v_{\rm max}=0.15c$, $\theta_{\rm size,min}=20$ arcsec	$38.45^{+0.60}_{-0.30}$	$0.3^{+0.4}_{-0.4}$	$-24.8^{+0.4}_{-(<0.2)\dagger}$	$6.78^{+0.15}_{-(<0.15)\dagger}$	0.1120
10) $v_{\rm max}=0.15c$, $\theta_{\rm size,min}=30$ arcsec	$38.60^{+1.20}_{-0.15}$	$0.0^{+0.6}_{-0.2}$	$-25.0^{+0.4}_{-(<0.2)\dagger}$	$6.78^{+0.15}_{-(<0.15)\dagger}$	0.0919
11) $v_{\rm max}=0.15c$, $\theta_{\rm size,min}=35$ arcsec	$38.90^{+2.10\ddagger}_{-0.45}$	$-0.2^{+0.1}_{-0.3}$	$-25.2^{+(<0.2)\dagger}_{-(<0.4)\dagger}$	$6.78^{+(<0.15)\dagger}_{-(<0.15)\dagger}$	0.0583
minimum linear size limits					
12) $v_{\rm max}=0.15c$, $D>60$ kpc	$38.15^{+0.30}_{-0.30}$	$0.6^{+0.4}_{-0.7}$	$-24.4^{+0.4}_{-0.4}$	$7.08^{+0.15}_{-0.15}$	0.3082
minimum flux limits					
13) $v_{\rm max}=0.15c$, $S_{\rm 1.4GHz,lim}=60$ mJy	$38.15^{+0.15}_{-0.15}$	$0.2^{+0.3}_{-0.4}$	$-24.6^{+(<0.2)\dagger}_{-(<0.2)\dagger}$	$6.78^{+(<0.15)\dagger}_{-(<0.15)\dagger}$	0.0586

Notes. The resolution of the results is $\Delta\log_{10}(\rho_{\rm o})=0.2$, $\Delta\log_{10}({\rm Q_B})=0.15$, $\Delta\log_{10}({\rm t_{max}})=0.15$, and $\Delta\alpha_{\rm s}=0.1$.
† For errors which may be extending beyond the searched ranges (see Table 3.2) value up to the range border is quoted.
‡ If errors are smaller than their respective resolution, value of $<\Delta$ is quoted.

4.5 Are low luminosity density FR IIs different from their powerful cousins?

Furthermore, it is interesting to compare results of the two radio samples considered in this dissertation, that is the powerful FR II sources and lower luminosity FR II radio galaxies. In Figure 4.19 the confidence intervals of the lowest redshift range of the powerful FR IIs investigated in Chapter 3 are superimposed on the 90 per cent confidence intervals of the low luminosity sample. Interestingly, the only difference that can be deduced from these confidence intervals is the significant drop in the kinetic luminosity break, which indicates that the low radio lobe luminosity density sources are simply less powerful. The suggestion that low and high excitation sources are intrinsically different have been discussed in the light of FR I and FR II morphology distinction in §1.2.3 (Chapter 1). However, the LEG class includes both FR I radio galaxies and low luminosity density FR IIs (e.g. Laing *et al.*, 1994). Differences in accretion rates and BH spins between LEG and HEG classes have been suggested (e.g. Baum *et al.*, 1992, 1995; Ghisellini and Celotti, 2001; Lin *et al.*, 2010; Best and Heckman, 2012). Specifically, the LEG sources are believed to have lower accretion rates and perhaps also lower BH spins as compared to the HEG class sources. If the two radio samples of this study belong to different line excitation classes, then this would be reflected in the lower kinetic luminosity breaks allowed for the low luminosity sample. Also interestingly, the radio lobe luminosity densities of radio galaxies investigated in this chapter are typical of FR I sources. Figure 4.20 displays the radio lobe luminosity densities at 1.4 GHz of the sample versus the absolute optical magnitude of the radio galaxy hosts. The diagonal line marks the separation between FR I and FR II sources as proposed by Owen and Ledlow (1994) and Ledlow and Owen (1996), where FR II sources lie predominantly above the line and FR Is below. The fact that all of the sources from the low luminosity sample lie in the FR I region suggest that they may indeed be LEGs. *This result has to be taken with caution.* One cannot exclude the possibility that a fraction of these sources are in fact lobed FR Is which are misclassified as FR II radio galaxies. To resolve this issue the original morphological classification of the initial SDSS-FIRST-NVSS radio sample must be verified.

4.6 Summary

A new low frequency (325 MHz) sample of FR II radio galaxies is constructed based on the the cross match of the WENSS survey and the available 1.4 GHz optically selected SDSS-FIRST-NVSS sample of radio-loud AGN (Best and Heckman, 2012). The matching procedure is detailed and any possible observational biases are investigated. The resulting low frequency sample of radio galaxies is optically selected, hence it is not radio complete, but as it is argued the sample is free from any significant biases and can be used in popula-

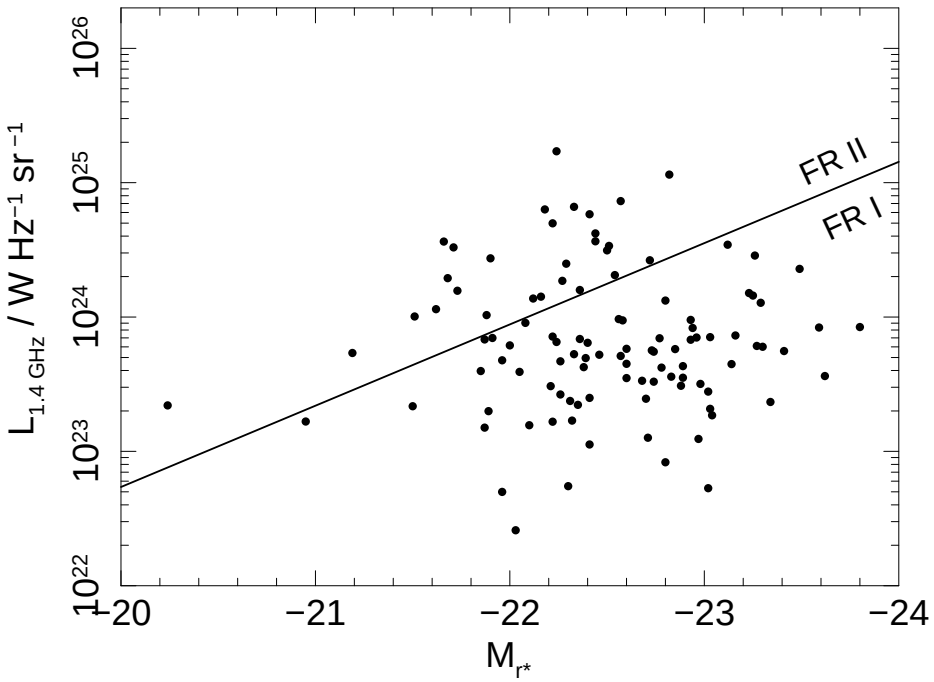

Figure 4.20: Radio lobe luminosity density at 1.4 GHz of the Best et al. FR II sources matched with the WENSS survey and the absolute magnitudes of their host galaxies (the M_r magnitudes obtained from P.N. Best, see also Best *et al.* 2005 and Best and Heckman 2012). The diagonal line was postulated by Owen and Ledlow (1994) to divide FR I and FR II populations.

tions study.

Multidimensional Monte Carlo simulations are further performed to investigate the intrinsic and extrinsic fundamental parameters of this low redshift low luminosity sample of radio galaxies. At first the initial assumptions for the Monte Carlo simulations and theoretical model parameters (as described in Chapter 2) only are adopted. Based on the goodness-of-fit test no acceptable results are found for either those initial assumptions or their modifications; the influence of the maximum allowed head advance speed, jet content and the minimum Lorentz factor of the initial distribution of the jet's relativistic particles has been tested. Acceptable results are found only if sources of the smallest linear sizes ($D < 60$ kpc) are excluded from the sample. This result suggests that the radio sample may be contaminated, and some FR I sources are misclassified as FR IIs. This may happen for lobed FR Is in particular. Although the sample is discussed in terms of its resemblance of radio sources of the LEG class, the morphological classification of the original SDSS-FIRST-NVSS radio sample needs to be verified before any conclusions can be drawn from this study.

University President: Why is it that you physicists always require so much expensive equipment? Now, the Department of Mathematics requires nothing but money for paper, pencils and erasers... and the Department of Philosophy is better still. It doesn't even ask for erasers.

ISAAC ASIMOV (1920 – 1992)

5

Kinetic Power – Radio Lobe Luminosity Density Scaling Relation

---

Kinetic – radio lobe luminosity scaling relation is of a particular interest to those who need a simple approximate method for estimating kinetic luminosities of radio galaxies. The method presented in Chapter 2 is difficult and numerically expensive, especially if to be used often for sources of various radio lobe luminosity densities. In this chapter I discuss the theoretical predictions for the scaling relation between the radio lobe luminosity density and kinetic luminosity. I compare these with estimates from X-ray cavities, and attempt to verify the reason for the observed scatter in the empirically obtained versions of the relation.

5.1 The Search for Scaling Relations

A few approaches have been developed for determining the kinetic luminosities of active galaxies. Such methods include the estimation of the mechanical work done on hot gas in clusters (e.g. Best *et al.*, 2006; Bîrzan *et al.*, 2008), and the analysis of the debeamed radio core emission in terms of the fundamental black hole plane (e.g. Heinz *et al.*, 2007; Merloni and Heinz, 2008; Körding *et al.*, 2008, see also Merloni *et al.* 2003 and Hopkins *et al.* 2007a on the fundamental BH plane). The first method is based on the fact that the expanding jet, and cocoon, of a radio source sweeps away the IGM/ICM gas encountered on its way. The effect of this expansion can be observed in X-rays where cavities and bubbles emptied from the hot gas are often present, and both strong and weak shocks around the cocoons emerge. The mechanical work done on the unshocked ICM can therefore be estimated, and under the assumption that only some fraction of the total kinetic luminosity of the radio source is spent on the 'pdV' work (that is work done against external pressure), the kinetic luminosity can be estimated. However, it needs to be stressed that the efficiency with which the outflows deposit the energy in the cocoons has to be assumed. Also recently, Binney *et al.* (2007) show, through their simulations, that the kinetic luminosities estimations based on the typically assumed values of the 'pdV' work efficiency may be strongly underestimated. The second method attempts to link the core radio emission which originates from the base of the jet with the kinetic luminosity, and thus investigates the jet radiative efficiency. The core radio luminosity is considered to be a good proxy for the kinetic luminosity of a radio source, but careful handling of possible (de)beaming effects must be considered. In addition, as discussed by e.g. Ghisellini *et al.* (1992), the assumption on the jet content will have a significant influence on these estimations. See Cattaneo and Best (2009) for a good review on this topic.

Here, I use the theoretical models based on radio emitting plasma stored in radio lobes of the radio source to find its kinetic luminosity; hence, this method is very similar to the one investigated by Willott *et al.* (1999). Contrary to previous methods I examine here the scaling relation between radio lobe and kinetic luminosities by looking into the theoretical model itself, and not the observed parameters of the populations. As I will show and discuss, any variation in the radio source's physical parameters, such as jet particle content or the relativistic particles minimum energy cut-off, will cause a spread in the $Q - L_\nu$ relation; this is indeed observed (e.g. Bîrzan *et al.*, 2008). Also, the uncertainty in the slope predictions of the relation will be influenced by the uncertainty in some of the assumptions, such as the age of radio sources or the gas density and its profile of the environments in which the sources reside for instance. Both of these issues are discussed in detail in §5.3. Also I discuss in detail the theoretical and observational investigations of Willott *et al.* (1999) in §5.3

Table 5.1: Overview of the fixed and investigated physical parameters. The quoted values of the investigated parameters refer to the 'standard' source (§5.2.1), and sections in which these parameters are explored are given (Column 4).

Parameter	Value	Unit	Reference
	FIXED PARAMETERS		
$\gamma_{\rm max}$	10^{10}	dimensionless	
$\Gamma_{\rm x}$	5/3	dimensionless	
$\Gamma_{\rm l}$	4/3	dimensionless	
$\Gamma_{\rm B}$	4/3	dimensionless	
	INVESTIGATED PARAMETERS		
t	10^{7}	yr	§5.2.2
ρ_o	10^{-22}	kg m^{-3}	§5.2.3
a_o	2	kpc	§5.2.3
β	1.5	dimensionless	§5.2.3
k'	0	dimensionless	§5.2.4
$\gamma_{\rm min}$	1	dimensionless	§5.2.5
m	2.2	dimensionless	§5.2.6
$R_{\rm T}$	2.0	dimensionless	§5.2.7

5.2 Predictions from the semi-analytical models

The original model of KA97/KDA97 of radio source time evolution is used. I assume that some of the radio source's physical parameters are fixed for all the cases considered in this section. The list of the fixed parameters and the values adopted are given in Table 5.1. In total eight physical parameters are investigated here for the strength of the effect they may have on the $Q - L_\nu$ scaling relation; these are: the radio source age (§5.2.2), the central density, the density profile slope and the radio core radius (§5.2.3), the jet particle content (§5.2.4), the relativistic particles' minimum energy cut-off (§5.2.5), the injection index (§5.2.6), and the radio source aspect ratio (§5.2.7). All of these parameters are listed in Table 5.1, and values adopted for these investigated parameters of a 'standard' source are given. The 'standard' source is assumed to be a typical radio galaxy to which all the investigations will be compared; the assumptions for the source and the resulting scaling relation are given in §5.2.2.

Throughout this chapter I will express the scaling relation in the following form

$$\log_{10}(Q) = \mathcal{A}\,\log_{10}\left(\frac{L_{178\mathrm{MHz}}}{10^{28}}\right) + \mathcal{N}, \tag{5.1}$$

where $\mathcal{A}$ will be referred to as a slope and $\mathcal{N}$ as a normalisation. The kinetic luminosity is expressed in units of W, and the radio lobe luminosity density in W Hz^{-1} (note also that $L_\nu = 4\pi P_\nu$). The units of radio lobe luminosity density as chosen so that it matches the form of scaling relation as reported by Willott *et al.* (1999). In the following investigations (§5.2.2 – §5.2.7) only one parameter is varied at a time. The cumulative effect of all factors is discussed in §5.2.8, and later in §5.3. The scaling relation is calculated numerically with Eqn. 2.14 (Chapter 2; see also Kaiser and Best, 2007, 2008, for the full set of equations).

5.2.1 A 'standard' source

I define the 'standard' source to take the following parameters: the age of the radio source is assumed to be 10^7 yr, and the source expands in an environment described by the central density of 10^{-22} kg m^{-3}, core radius of 2 kpc and the density profile slope of $\beta = 1.5$. The injection index of the initial population of relativistic electrons is assumed to be $m = 2.2$, the low energy cut off of the distribution is $\gamma_{\mathrm{min}} = 1$, and jet is assumed to be lightweight ($k' = 0$). Finally, the aspect ratio of the radio source is set to $R_\mathrm{T} = 2.0$. Given this the following scaling relation is found

$$\log_{10}(Q) = 0.909\,\log_{10}\left(\frac{L_{178\mathrm{MHz}}}{10^{28}}\right) + 38.84. \tag{5.2}$$

5.2.2 Effect of the source's age

The age of the source will have a significant effect on both, the slope and the normalisation of the relation, where the slope will become steeper and the normalisation lower for younger sources. In particular the following changes are observed

age of radio source (t)	$\mathcal{A}$	$\mathcal{N}$
10^5 yr	0.921	38.42
10^6 yr	0.915	38.64
10^7 yr	0.909	38.84
10^8 yr	0.906	39.06
10^9 yr	0.875	39.72
10^{10} yr	0.870	41.13
2.5×10^{10} yr	0.870	41.70

The radio lobe luminosity density of a radio source changes during its lifetime, where, for a given kinetic luminosity, there is a rapid but short increase in the radio lobe luminosity

density during the radio source's early life stages, after which the luminosity density consistently decreases. Hence the change in the relation for different assumed age of the source. Interestingly however, for the higher allowed ages (also unrealistic) the slope of the relation asymptotically reaches value $\mathcal{A} \sim 0.870$ which is very close to the relation slope derived by Willott *et al.* (1999).

5.2.3 Radio source's environment

All three parameters describing the density profile of the environments of the radio source will have an influence on both the slope and the normalisation of the scaling relation. The slope become steeper for higher central densities, steeper slopes of the density profile and larger radio cores, while the normalisation become lower for higher central densities, *flatter* slopes of the density profile and larger radio cores. The following changes are observed

central density (ρ_o)	$\mathcal{A}$	$\mathcal{N}$
10^{-21} kg m^{-3}	0.942	38.36
10^{-22} kg m^{-3}	0.909	38.84
10^{-23} kg m^{-3}	0.899	39.41
10^{-24} kg m^{-3}	0.898	41.03

density profile slope (β)	$\mathcal{A}$	$\mathcal{N}$
1.0	0.889	38.48
1.5	0.909	38.84
1.9	0.975	39.26
2.0	1.000	39.43

core radius (a_o)	$\mathcal{A}$	$\mathcal{N}$
2 kpc	0.909	38.84
10 kpc	0.943	38.32

The radio lobe luminosity density will depend strongly on the density of the environment in which the radio source expands. For a given kinetic luminosity denser environments will cause higher radio lobe luminosity densities. All three parameters, i.e. the central density, the gas density profile slope and the core radius, will have an effect on the relation. Note, however, that for $\beta = 2.0$ the model equations take a special form and the solution is self-similar on all length scales (consult Falle, 1991, and KA97).

5.2.4 Jet particle content

The choice of the particle content of the outflow seems to have a strong influence on the relation normalisation. In particular the following changes are observed

ratio (k')	$\mathcal{A}$	$\mathcal{N}$
0.0	0.909	38.84
1.0	0.909	39.11
10.0	0.909	39.77
100.0	0.910	40.67.

The addition of the thermal plasma to the jet would require these particles (protons) to be accelerated to the relativistic speeds the same way as the relativistic electrons are. As discussed in Chapter 3 (§ 3.10.5) protons store much more energy than electrons do, and because of this the kinetic luminosity would rise. Hence, the different assumed values of k' will only affect the normalisation of the relation.

5.2.5 Relativistic particles' minimum energy cut-off

The adopted minimum energy cut-off of the initial distribution of the relativistic particles in the outflow will induce an influence on the relation's normalisation only. The following changes are observed

minimum energy cut-off ($\gamma_{\rm min}$)	$\mathcal{A}$	$\mathcal{N}$
1.0	0.909	38.84
10^2	0.910	38.54
10^4	0.909	38.16.

The minimum Lorentz factor of this initial distribution indicates how relativistic are the least energetic particles that are forming the outflow. As discussed in Chapter 3 (§ 3.10.5), the lower the Lorentz factor is the more cold material is forming the jet. For a given radio lobe luminosity density the kinetic luminosity of a radio source must be higher if more cold plasma is present than in the case when this cold material is absent. For this reason the difference in scaling relation for different assumed values of $\gamma_{\rm min}$ will only be to the normalisation.

5.2.6 Injection index

The choice of slope of the initial distribution of the relativistic particles in the outflow seems to influences both the slope and the normalisation of the scaling relation. The following changes are observed

injection index (m)	$\mathcal{A}$	$\mathcal{N}$
2.0	0.916	38.94
2.5	0.899	39.22
3.0	0.885	40.20

The slope of the initial distribution of the relativistic particles is tightly linked to the minimum energy cut-off of this distribution. In particular, the steeper the slope is the more low energy particles are included in the outflow (unless $\gamma_{\rm min}$ is altered alongside). As pointed out in previous section, if more low energetic material composes the outflow the kinetic luminosity will rise. This is indeed what is observed here in the scaling relation.

5.2.7 Aspect ratio

The aspect ratio of a radio source seems to influence both the slope and the normalisation of the scaling relation. The following changes are observed

aspect ratio ($R_{\rm T}$)	$\mathcal{A}$	$\mathcal{N}$
1.3	0.916	38.57
2.0	0.909	38.84
4.0	0.901	39.29
8.0	0.898	39.78

It has been argued that higher aspect ratio are measured predominantly for older radio sources (see §2.3.5) and some correlation between age of radio source and its $R_{\rm T}$ value may hold. However, Gaibler *et al.* (2009) discuss that due to spherical expansion (where $R_{\rm T} \sim 1$) young, and so small, radio sources may have lower aspect ratios. The authors argue that there is a strong dependence of $R_{\rm T}$ on the cocoon and its balance with the external medium; if radio source reaches pressure equilibrium with the ambient medium the sideways expansion of the cocoon stops. This would cause the scaling relation for higher aspect ratios to change similarly as in the case of changing the age of the source. One must also remember that these parameters change throughout the radio source's life, and there will be a variation of these parameters (both aspect ratio and age) within one population of observed radio sources.

5.2.8 Combined effect of the significant factors

Although each of the predicted versions of the scaling relation depends only on the change of one parameter at the time, two conclusions can be drawn immediately. Firstly, the slope $\mathcal{A}$ of the scaling relation vary only slightly between each investigated case and is relatively steep. Secondly, the normalisation $\mathcal{N}$ vary significantly implying change of a few orders of magnitude between different cases. Furthermore, some of the parameters, such as the jet particle content and the minimum energy cut-off of the jet relativistic particles are expected to be similar for all radio sources of the same kind (here, for instance, for FR II radio galaxies, but these parameters may be different for FR Is). While other parameters, such as age of the radio source, ambient medium or aspect ratio do change from source to source. Note also, that these some of these parameters may be also dependent on the cosmological epoch (cf. Chapter 3). For this reason if the relation is attempted to be measured for a

sample of sources then the resulting steepness of the slope will be different; the slope may become flatter. The variation in the parameters will also introduce scatter to such a simple relation.

5.3 Comparison with existing empirical estimates

Below I outline three commonly used scaling relations, one based on a theoretical model by Willott *et al.* (1999), and two based on estimations of work done on the environment by radio lobes of sources by Best *et al.* (2006, 2007) and Bîrzan *et al.* (2008).

Willott *et al.* (1999) determined the scaling relation via theoretical consideration of the minimum energy density requirements for the radio lobe material. The authors find the following relation

$$Q = 3 \times 10^{38} f^{3/2} \left(\frac{L_{151\mathrm{MHz}}}{10^{28}} \right)^{6/7}, \tag{5.3}$$

where f represents non-negligible but unconstrained factors. Willott *et al.* (1999) stress the importance of jet particle content as one of the 'most uncertain values', but volume filling factor, the minimum Lorentz factor of the relativistic jet particles and deviations from minimum energy conditions are of an importance. The authors estimate that these factors range between $1 < f \leq 20$. This scaling relation represented in the form of Eqn. 5.1 and scaled to the radio frequency of 178 MHz (via a simple power-law and assuming radio spectral index of $\alpha = 0.7$) takes the following form

$$\log_{10}(Q) = 0.86 \log_{10} \left(\frac{L_{178\mathrm{MHz}}}{10^{28}} \right) + 38.80 + 1.5 \log_{10}(f). \tag{5.4}$$

The factor f term will vary from 0 to 1.95 for the suggested f ranges. The slope of Eqn. 5.4 is barely flatter than the estimates I presented in §5.2. Although both theoretical models, that is KA97/KDA97 which I use here and BRW99 used by Willott *et al.* (1999), assume energy equipartition of the emitting plasma of the radio lobes, these models do differ in some on the assumptions the relativistic particles are injected into radio lobes which will alter the radio luminosity density predictions between the models (see also Chapter 2: §2.1.3). Therefore, the similarity in the scaling relation estimated of these two separate theoretical models is of some importance and suggests that these predictions are most probably not too model dependent. To allow easy comparison between theoretical predictions as investigated by me in this thesis and by Willott *et al.* (1999), I set assumptions adopted by the latter authors and I attempt to reproduce their predictions with the KA97/KDA97 model. In particular the following values for the source parameters have been adopted: $\beta = 1.5$, $R_{\mathrm{T}} = 5.0$, $m = 2.0$, $t_{max} = 10^7$ yr, $\rho_o = 2.8 \times 10^{-22}$ kg m^{-3}, and finally for $f = 0$: $k' = 0$ and $\gamma_{\mathrm{min}} = 2$ and for $f = 20$: $k' = 20$ and $\gamma_{\mathrm{min}} = 2$. The results of this test are displayed in Figure 5.1. Note, that the scaling relation is calculated numerically here, and so deviations from the simple power-

law relation between Q and L_ν may occur (this can be observed in Figure 5.1). For $f = 20$ the agreements between models is striking. However, there is a systematic offset between the two models' predictions for $f = 0$. The difference originates in the definition of the k' ratio. In the KA97/KDA97 the ratio is defined as ratio of the energy density of electrons to the energy density of thermal particles, while typically (and also adopted by Willott *et al.* 1999) the ratio is defined as ratio k of the energy densities of relativistic to non-relativistic particles. Since in the KA97/KDA97 definition the non-relativistic electrons are included even if $k' = 0$, then it follows that $k' \neq k$, and if $k' = 0$ then $k \neq 0$.

The kinetic – radio lobe luminosity scaling relation has been also investigated by many authors who attempted to determine the relationship through the observations of X-ray cavities. Since those cavities are the result from the AGN jets drilling through the ICM and the expanding radio cocoons formed by the jets, they are considered to provide information on the AGN's engine that powers the jets. The method requires measurements of the work done on the environment to displace the ambient IGM and ICM gas by expanding jets via 'pdV' estimates, where p is the pressure of the ambient gas and V is volume of the cavity. Under the assumption that the cavity enthalpy (free energy) is given by $\left(\frac{\Gamma_{\rm cav}}{\Gamma_{\rm cav}-1}\right) pdV$ (e.g. Gitti *et al.*, 2012, and references therein), then the internal energy of the radio lobes is $\sim 4p$dV (since for non-relativistic plasma $\Gamma_{\rm cav} = 4/3$). Assuming that $50-70$ per cent of the total kinetic luminosity is spent on the 'pdV' work (see also Gaibler *et al.*, 2009), Q can be estimated. Incorporating this method Best *et al.* (2006) finds

$$Q = 3.0(\pm 0.2) \times 10^{37} \left(\frac{L_{\rm 1.4GHz}}{10^{25}}\right)^{0.40\pm0.13}, \tag{5.5}$$

which, if again represented in the form of Eqn.5.1, will take the following form

$$\log_{10}(Q) = 0.40(\pm 0.13)\, \log_{10}\left(\frac{L_{\rm 178MHz}}{10^{28}}\right) + 37.43(\pm 0.03). \tag{5.6}$$

While Bîrzan *et al.* (2008) estimates

$$\log_{10}(Q) = 0.62(\pm 0.08)\, \log_{10}\left(\frac{L_{\rm 327MHz}}{10^{24}}\right) + 8.11(\pm 0.17), \tag{5.7}$$

which is

$$\log_{10}(Q) = 0.62(\pm 0.08)\, \log_{10}\left(\frac{L_{\rm 178MHz}}{10^{28}}\right) + 38.48(\pm 0.17). \tag{5.8}$$

when transformed to the form of Eqn.5.1.

It can immediately be seen that the estimates from the X-ray cavities have much flatter slopes than the theoretical predictions from the minimum energy requirements. Predictions from both methods are plotted in Figure 5.1 so that they can be confronted with the theoretical investigations of mine and with those of Willott *et al.* (1999).

Neither of these methods is free from criticism. The methods involving measurements of cavities 'pdV' work are known for being greatly dependent on the cavity X-ray obser-

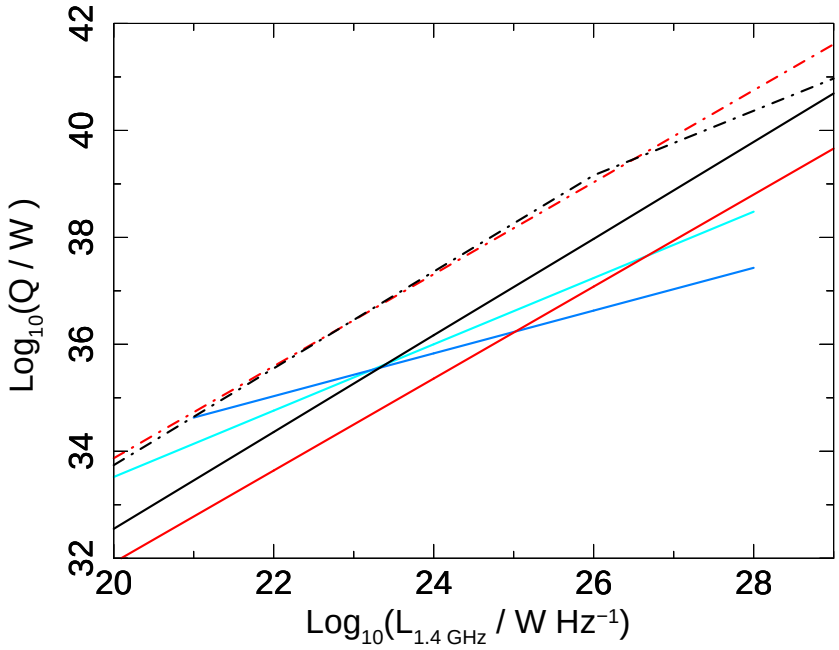

Figure 5.1: Kinetic power – radio luminosity density scaling relation as predicted by Willott *et al.* (1999), where cases for $f = 0$ (red, solid) and $f = 20$ (red, dash-dotted) are plotted, and two relations based on the observations of X-ray cavities, by Best *et al.* (2006) (cyan, solid) and by Bîrzan *et al.* (2008) (blue, solid). To allow easy comparison between theoretical predictions as investigated by me in this thesis and by Willott *et al.* (1999), I set assumptions adopted by the latter authors to my predictions on the scaling relation, where assumptions equivalent to setting $f = 0$ (black, solid) and $f = 20$ (black, dash-dotted) are adopted (see text for more details).

vations which may lead to discrepant results, as well as it has been suggested that due to its variability the 'pdV' estimator may not be robust enough for the energy measurements (see Gitti *et al.*, 2012, and references therein). For a list of potential problems with the cavity estimations of kinetic luminosity see O'Sullivan *et al.* (2011). Furthermore, although a vast majority of authors assume that the cavity enthalpy is of order of $\sim 4p\mathrm{d}V$, it has been suggested that this value is highly underestimated (see Binney *et al.*, 2007). Here, I also see that the KA97/KDA97 model predicts the efficiency with which the jets deposit material in radio cocoon to be of order of few – 20 per cent[1]. It is also very important to bear in mind that the radio emission of these radio sources at 1.4 GHz may be contaminated by compact core, jet and sometimes hot spot emission which will enhance radio luminosity density and may introduce deviations on the Q estimations. This effect may significantly influence the scaling relation by Best *et al.* (2006). It worth noting that the slope of the relation reported by Bîrzan *et al.* (2008) flattens to $\mathcal{A} = 0.35 \pm 0.07$ if measured at 1.4 GHz.

[1]Although not presented in this thesis, this work is planned to be expanded in my future work (see also Chapter 7).

Furthermore, an important difference between the X-ray cavity and the theoretical predictions from the minimum energy requirements is the fact that in those two methods different sources have been considered. In particular, I as well as Willott *et al.* (1999) consider FR II radio sources which can be modelled assuming near equipartition energy conditions in their radio cocoons. On the contrary, the X-ray cavity methods consider mainly FR I radio sources. This has also been noted recently by O'Sullivan *et al.* (2011). Results of Chapter 4 of this thesis strongly suggest that FR I radio sources cannot be, even approximately, modelled with the evolutionary models developed for FR IIs. FR Is are often referred to as low luminosity radio sources. It is plausible that apart from lower kinetic luminosity as compared with FR IIs, FR I may also show significantly different dependence between Q and radio lobe luminosity density, which may be reflected in the steepness of the relation slope. It will be of a great importance to attempt to carry similar theoretical investigations for FR I radio sources to shed more light on this issue.

5.4 Summary

I revisit the KA97/KDA97 theoretical model to investigate the radio lobe – kinetic luminosity scaling relation. Through numerical exploration of the nonlinear model equations I find that the scaling relation is influenced mainly by the radio source age, aspect ratio, the injection index of the relativistic particles' initial distribution, and the radio source environment density and its profile. I contrast these results to the observationally found radio lobe – kinetic luminosity scaling relations reported in the literature. I discuss the possible origin of the differences between the scaling relations estimated through observations of X-ray cavities associated with radio galaxies and those estimated via theoretical models. A detailed comparison between my theoretical predictions based on the KA97/KDA97 model and the theoretical predictions of Willott *et al.* (1999) is presented.

The aim of science is not the things themselves, as the dogmatists in their simplicity imagine, but the relation between things.

HENRI POINCARÉ (1854 – 1912)

6

Implications of Radio Galaxy Impact for the Evolving Universe

---

Radio galaxies and quasars are among the largest and most powerful single objects known and are believed to have had significant impact on the evolving Universe and its large scale structure. Their jets inject a significant amount of energy into the surrounding medium, hence they can provide useful information in the study of the density and evolution of the intergalactic and intracluster medium. The jet activity is also believed to regulate the growth of massive galaxies via the AGN feedback. In this chapter I present analysis of the energetics of radio sources following the results obtained in Chapter 3. I investigate the total injected power by populations of radio galaxies and radio-loud quasars at various cosmological epochs. The results are discussed in the scope of the significance of the AGN kinetic feedback. The content of this chapter is to be submitted to the Monthly Notices of the Royal Astronomical Society (A.D. Kapińska & P. Uttley, 'On the implications of radio galaxy impact for the evolving Universe', MNRAS, in prep.).

6.1 Clusters of galaxies and cooling flows

The following section is based on the review on galaxy clusters by Sarazin (1988), the review on cooling flows by Fabian (1994) and the review on evolution of galaxy clusters by Voit (2005), to which the reader is referred for relevant references and derivations of the quoted equations.

In a simple picture a cooling flow forms in massive systems (galaxies or galaxy clusters) when after the initial gravitational collapse of the system some fraction of the gas cooled slowly (slower than gas which formed stars) and created a hot 'quasi-hydrostatic' atmosphere. This gas can be directly observed in X-rays, and under the assumption that the clusters are virialised systems and that the hydrostatic equilibrium holds, the temperature of this hot gas is estimated to be $10^6 - 10^8$ K. In particular, the following relation applies

$$k_{\rm B} T_{\rm vir} = \frac{\mu m_{\rm p} G M_{R_{\rm vir}}}{2 R_{\rm vir}}, \tag{6.1}$$

where $T_{\rm vir}$ is virial temperature of the hot gas of mass $M_{R_{\rm vir}}$ encompassed in the sphere of a virial radius $R_{\rm vir}$, $k_{\rm B}$ is the Boltzmann constant and μ is the molecular weight of the gas particles. In the original models of the cooling flows (see Cowie and Binney, 1977; Fabian and Nulsen, 1977; Mathews and Bregman, 1978) this hot gas has been assumed to be homogeneous with well defined density and temperature at each radius. The density of the gas is expected to decrease radially as defined by the generalised King's profile (Chapter 2: Eqn. 2.5, re-written below), which is often referred to as the $\beta - model$,

$$\rho_{\rm x} = \rho_{\rm o} \left(\frac{r}{a_{\rm o}} \right)^{-\beta} \text{ for } r > a_{\rm o}, \tag{6.2}$$

where again r is the radial distance from the AGN core, and $\rho_{\rm o}$ is a constant central density within the core radius $a_{\rm o}$. Since the gas is densest in the central regions of the system it cools there fastest. The cooling region of the system is defined by the so-called cooling radius, $r_{\rm cool}$, which is usually taken as a radius at which the cooling time is equal to look-back time at redshift $z = 1.0$ (i.e. $\sim 8 \times 10^9$ yr). Furthermore, clusters of galaxies are gravitationally bound systems; hence, due to the gravitational potential the weight of the gas which lies in the system's outer regions will cause a slow inflow of this hotter gas towards the cluster's centre where the faster cooling gas resides. Given the quasi-hydrostatic equilibrium of the clusters and assuming spherical symmetry the following applies

$$\frac{\mathrm{d}\ \ln(\rho)}{\mathrm{d}\ \ln(\mathrm{r})} + \frac{\mathrm{d}\ \ln(\mathrm{T})}{\mathrm{d}\ \ln(\mathrm{r})} = -2 \frac{k_{\rm B} T_{\rm vir}}{T}, \tag{6.3}$$

where r is the radius from the cluster's core, which means that the densest central regions of clusters have low X-ray temperature, while the significantly lower density clusters' outskirts are composed of much hotter plasma. Such well defined systems are particularly attractive for cosmological studies of structure formation.

6.1.1 Non-gravitational heating

However, as discussed in §1.3.2 in Chapter 1, it was soon discovered that the theoretical predictions for the cooling of galaxy clusters over-predict the cooling rates (the so-called *overcooling* or *cooling flow problem*); if only the gravitational heating is included in the models, too many baryons cool to form stars and galaxies become too luminous, while the intracluster gas is heated to the virial temperature (Eqn. 6.1). The gravitational heating is caused by the gas that passes through the cluster's accretion shocks while entering the system. The absence of cold gas at temperatures of < 1 keV (as observed by e.g. Peterson *et al.*, 2001) points to the currently broadly accepted view that there must occur some additional source of heating (see e.g. Peterson *et al.*, 2001; Fabian *et al.*, 2001; Kaastra *et al.*, 2004, and references therein). Mechanisms that have been proposed to explain this cooling flow problem include supernovae and AGN feedback (e.g. Ponman *et al.*, 1999; Brüggen and Kaiser, 2001; Domainko *et al.*, 2004; Omma *et al.*, 2004; McNamara *et al.*, 2005; Nulsen *et al.*, 2005; McNamara and Nulsen, 2007), sub-cluster merging (e.g. Markevitch and Vikhlinin, 2001), thermal conduction (e.g. Rosner and Tucker, 1989; Fabian *et al.*, 2002; Voigt *et al.*, 2002) and thermal cooling (e.g. Voit and Bryan, 2001) among others; these mechanisms are often referred to as non-gravitational heating. It has been suggested that all of these mechanisms contribute to the problem as none of them seem to be powerful enough to tune the clusters cooling flows by themselves (see McNamara and Nulsen, 2007, for a review). This is due to the fact that any effective heating mechanism, which would be able to stop or delay the cluster cooling flows, requires energies of $0.5 - 3$ keV; this issue has been discussed both analytically and numerically by many authors (e.g. Wu *et al.*, 2001; Tozzi and Norman, 2001; Bialek *et al.*, 2001; Voit *et al.*, 2002; Borgani *et al.*, 2002; Magliocchetti and Brüggen, 2007; Sijacki *et al.*, 2007; McNamara and Nulsen, 2007).

Here, I will focus on the AGN feedback only, and on the impact of FR II radio galaxies in particular. The main effects the AGN exert on its surrounding include removing cold low entropy gas from the centres of clusters and groups to the outskirts of these structures; this process will also cause dimming of the cluster's X-ray luminosity while its temperature being kept roughly constant. Through the work done on the environment by the AGN jets, excess energy is transferred to the ambient gas, this will cause increase in the ambient temperature as well as in the cluster gas entropy.

6.1.2 Intracluster gas entropy

On the macroscopic level the gas entropy measures the enthalpy of a system (the free energy) and the system's change in temperature, while on a microscopic level the gas entropy is defined as a measure of the number of microstates of this system (both in units of J K^{-1}). This quantity has attracted considerable attention due to its essential importance; entropy traces the thermodynamical history of the intracluster gas, and as phrased by Voit (2005) *'the gas density profile and temperature profile of the intracluster medium (...) are just man-*

ifestations of its entropy distribution'. In classical thermodynamics entropy per particle (S) is given by

$$S = Nk_{\rm B}[\ln(\mathrm{K}^{2/3}) + \mathrm{const}], \tag{6.4}$$

where N is the number of particles, and K is the entropy index defined as

$$K \equiv p\rho^{-5/3} = \frac{k_{\rm B}T}{\mu m_{\rm p}}\rho^{-2/3}. \tag{6.5}$$

The term p denotes the gas pressure and is given by $p = \rho k_{\rm B}T/(\mu m_{\rm p})$. See for instance Kaiser and Binney (2004), Voit (2005) and Gitti *et al.* (2012) for derivation and discussion. However, in the galaxy cluster community a variant of the entropy index is used and referred to as 'entropy', namely

$$K_{\rm ent} = k_{\rm B}Tn_{\rm p}^{-2/3} \tag{6.6}$$

measured in units of keV cm^2. I will follow the popular convention and discuss the 'entropy' as defined in Eqn. 6.6.

The measurements of entropy are particularly important in the discussions of the galaxy clusters' scaling relations; to be able to reproduce the structure formation of the expanding Universe one needs to understand both the observable signatures of the ICM and the physics governing the baryons during formation of galaxies. It soon became clear that idealised models are not consistent with observations. In the presence of gravitational processes only acting on the ICM (§6.1.1), the temperature and gas density structures of galaxy clusters obey self-similar scaling predictions (e.g. Kaiser, 1986). Typically an *overdensity* (Δ_ρ) parameter is introduced, which is the ratio of the dark matter halo of the system ($\rho_{\rm DM}$) to the critical density at the cluster's redshift z, $\rho_{\rm crit}(z)$, namely $\Delta_\rho = \rho_{\rm DM}/\rho_{\rm crit}(z)$. The critical density of the expanding Universe is defined as $\rho_{\rm crit}(z) = 3H(z)^2/8\pi G$ (see also discussion in Chapter 3: §3.7 and Appendix E). It is also assumed that the baryonic matter distribution traces the distribution of dark matter[1], that is $\rho \propto \rho_{\rm DM} \propto \rho_{\rm crit}(z)$. All galaxy clusters are expected to hold the same properties when expressed (and scaled) via Δ_ρ, if of course clusters do evolve in the self-similar fashion. Any significant observed deviations from the self-similar predictions point towards the non negligible involvement of processes in addition to gravity. Indeed, similarity-breaking has been observed (e.g. Markevitch, 1998; Arnaud and Evrard, 1999; Ettori *et al.*, 2004; Maughan *et al.*, 2006). To explain these observational results, models that invoke a non-gravitationally preheated intergalactic medium have been proposed (e.g. Kaiser, 1991). The similarity-breaking is also considered as strong evidence for episodic non-gravitational heating by supernovae and AGN (e.g. Cavaliere *et al.*, 1999; Wu *et al.*, 2001; Tozzi and Norman, 2001; Bialek *et al.*, 2001; Voit *et al.*, 2002; Borgani

[1]This assumption is valid only if gravitational (shock) heating is the sole process contributing to the entropy of the system (see e.g. Arnaud and Evrard, 1999, and references therein).

Table 6.1: List of defining parameters for the radio source populations as discussed in §6.2.2. The following parameter sets were used to represent a typical radio galaxy for their respective data sets. For details see §6.2.2 and §6.3.

Data set	$Q_{\rm B}(z=0)$ [log(W)]	$n_{\rm q}$	$\alpha_{\rm S}$	$\rho_{\rm m}(z=0)$ [log(kg m^{-3})]	$n_{\rm r}$	$t_{\rm max_m}(z=0)$ [log(yr)]	$n_{\rm t}$
1*a*	38.0	8.0	0.6	−23.3	4.0	7.8	−2.5
1*b*	38.0	10.5	0.6	−23.0	0	7.8	−4.0
2	39.2	10.5	0.4	−25.1	4.0	6.9	0
3	37.4	8.0	0.6	−21.5	5.5	8.7	−3.0

et al., 2002) and radiative cooling (e.g. Voit and Bryan, 2001; Wu and Xue, 2002). The relativistic outflows of AGNs can reach Mpc scales, and despite their radio activity being significantly shorter than the lifetime of galaxy clusters they reside in, radio galaxies are powerful enough to alter the overall ICM properties, including the gas entropy.

6.2 Methods

The method presented in Chapter 2 allows one to narrow down the possible ranges of the fundamental parameters of radio sources, yet degeneracy persists. Based on the results of Chapter 3, I investigate here other physical parameters, especially the ones which are relevant in terms of the scale of the radio source impact on its immediate environments, and which can be derived from the intrinsic and extrinsic fundamental parameters.

6.2.1 Source energetics

The total injected power by a radio galaxy over its lifetime equals $\int_0^{t_{\rm max}} Q\ {\rm d}t$. Since in the KA97/KDA97 model, which is used throughout this thesis, the kinetic luminosity of a radio source is assumed to be constant over the radio source's life, the total power of the radio source is simply $Q\,t_{\rm max}$. Neither of these quantities can be measured directly. In this work both Q and $t_{\rm max}$ have been estimated via Monte Carlo simulations which attempt to fit radio luminosity functions of observed radio source populations to the simulated ones (for the method and results see Chapters 2 and 3 respectively). This total power is used by radio source, via its relativistic outflows, to (a) drill jets' paths through the ambient medium which will (b) displace the cold ambient medium gas and push it to the outer regions of the clusters and (c) inflate these radio lobes with the transported relativistic jet material. It

is known that the kinetic luminosities of radio galaxies, especially those of the FR II type, may be enormous ($\sim 10^{40}$ W) and that the radio structures of these sources may reach Mpc scales (this has also been presented and discussed in Chapter 3 of this dissertation), it is likely therefore that these radio sources induce significant effects on the environments in which they reside. Here, I investigate the total injected power of FR II radio galaxies, and attempt to examine the resulting heating rate and entropy change of the ambient gas. Most importantly, however, one of the questions one may raise here is whether the effects of the radio source populations on their immediate environments are robust despite the wide range of allowed parameter sets (which are due to occurring degeneracies, see Chapter 3, and particularly §3.5), or whether constraints from X-ray observations of galaxy clusters can provide us with diagnostics that will break the degeneracy between the fundamental radio source parameters.

6.2.2 Tested data sets

The data sets considered here are: the best fit reported in Chapter 3 (data set 1*b*), one of the best fits discussed alongside it (data set 1*a*), and two randomly picked sets of best fitting parameters which are at the extremities of the 90 per cent confidence intervals (Chapter 3: Figure 3.17, data sets 2 and 3). Particularly, the two latter cases were specified to lie at each end of the 90 per cent confidence intervals of the ($Q_{\rm B} - \rho_{\rm m}$), ($Q_{\rm B} - t_{\rm max_m}$) and ($t_{\rm max_m} - \rho_{\rm m}$) plots of Figure 3.17, so that the cases where populations with (2) high kinetic luminosity break, low central density, short maximum source lifetime, and (3) low kinetic luminosity break, high central density, long maximum source lifetime can be tested and compared to the best fits. The parameters of the tested data sets are listed in Table 6.1. The total injected power of a typical source of the kinetic luminosity which equals $Q_{\rm B}$ is calculated for each data set and for four redshift slices, i.e. $z \in (0.1, 0.5, 1.0, 1.5)$. These break luminosities are typical luminosities of radio sources in the respective populations, and hence only these are discussed in the simplified picture presented here. It is also assumed that radio sources at the break kinetic luminosity have maximum lifetimes and external gas densities typical for the population; these are also listed in Table 6.1. For consistency with the previous calculations of this thesis the core radius is assumed to be $a_o = 2$ kpc, while slope parameter of the density profile is taken to be $\beta = 1.5$ (it is assumed that the gas density profile follows the relation given in Eqn. 6.2, see also Chapter 2: Eqn. 2.5).

6.3 Total injected power by Fanaroff-Riley II radio galaxies

The total injected power per baryon ($Q\ t_{\rm max}/{\rm baryon}$) has been calculated for a typical radio source of each data set, that is assuming the kinetic luminosity of the radio source is represented by $Q_{\rm B}$. Since the best fitting ambient density and volume of the radio source are known, and the density profile is given by Eqn. 6.2, the baryon number density can

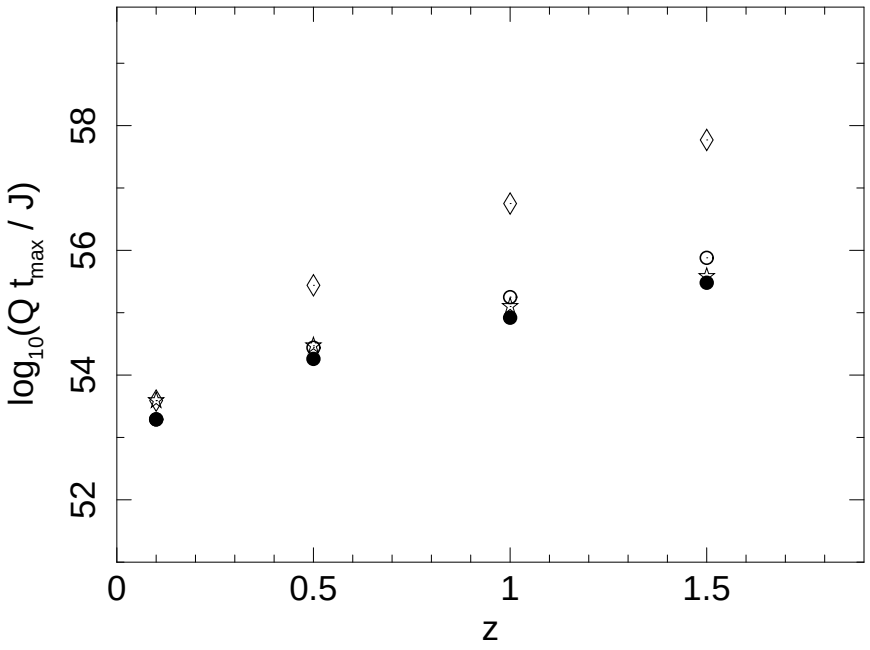

Figure 6.1: The total power of FR II radio galaxies produced during their lifetimes. Each data point marker refers to different data set considered, where (i) data set 1*a* (filled circles) represents the case when the gas density redshift evolution is set to $n_{\rm r} = 4.0$ (Chapter 3: §3.8), (ii) data set 1*b* (open circles) is the best fit, (iii) data set 2 (diamonds) represents the case with high kinetic luminosity break, low central density and short maximum source lifetime, and (iv) data set 3 (stars) represents the case with low kinetic luminosity break, high central density, long maximum source lifetime. All data sets are within 90 per cent confidence intervals of the results presented in Chapter 3.

be easily found. Radio galaxies may reach various sizes depending on their specific set of kinetic luminosity, lifetime and the gas density in which they expand; however, here it is assumed that the total injected power is evenly distributed over a sphere of $r_{\rm ICM} = 1$ Mpc. Obviously this is a simplified assumption as radio sources larger than this (i.e. larger than 2 Mpc) are observed and so they act on the ICM beyond the radius assumed here, but these giant radio galaxies form a relatively small fraction of the whole observed population (e.g. Schoenmakers *et al.*, 2000b). On the other hand, many radio galaxies will never reach total linear sizes of $1-2$ Mpc; however, after central engine switches off, that is after the jets stop supplying radio lobes with new material, the radio lobes will still expand buoyantly and hence they will act on the ICM. Finally, it is assumed that radio galaxies are centrally located and there exists some efficient energy – heat transfer[2]. Under these assumptions the total injected power, $Q\,t_{\rm max}$, of radio galaxies for the four chosen data sets is calculated. The

[2]The heat transport mechanisms which are usually invoked in the study of galaxy clusters are thermal conduction and weak shock enthalpy dissipation (see for instance Gitti *et al.*, 2007; Best *et al.*, 2007; Sanderson *et al.*, 2009; De Young, 2010, for some discussion on this topic). Here I will not focus on the efficiency of these mechanisms, and I will assume that whatever heat transfer mechanism takes place, it is very efficient and distributes the excess heat evenly between the ambient gas particles.

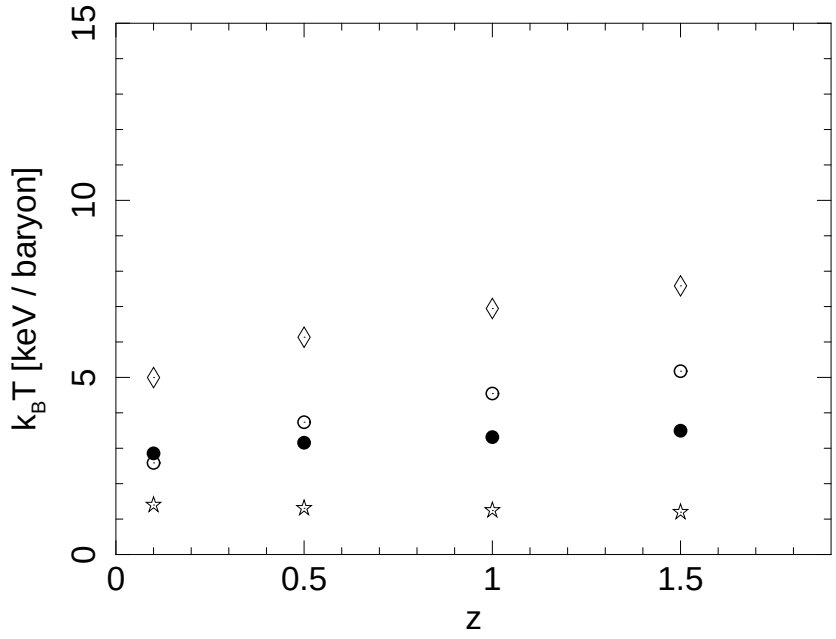

Figure 6.2: The total injected power per baryon over the lifetime of FR II radio galaxy estimated under the assumption that all of the radio galaxy power goes into heating the environment. The estimations are based on the total power being efficiently and evenly distributed over a sphere of a radius $r = 1$ Mpc. Each data point marker refers to different data set considered, where (i) data set 1*a* (filled circles) represents the case when the gas density redshift evolution is set to $n_{\rm r} = 4.0$ (Chapter 3: §3.8), (ii) data set 1*b* (open circles) is the best fit, (iii) data set 2 (diamonds) represents the case with high kinetic luminosity break, low central density and short maximum source lifetime, and (iv) data set 3 (stars) represents the case with low kinetic luminosity break, high central density, long maximum source lifetime. All data sets are within 90 per cent confidence intervals of the results presented in Chapter 3.

results are displayed in Figure 6.1.

Strikingly, the total injected power for each radio source over their respective lifetimes seems to be nearly the same in each case. Only data set 2 (marked as diamonds in Figure 6.1) shows signs of the departure from this trend at higher redshifts. However, this should not be considered as a contradiction of the postulated here robustness of the $Q\,t_{\rm max}$ quantity. As investigated in Chapter 3 (see §3.4.1 and Figure 3.21 in particular) for the highest kinetic luminosity breaks, the Schechter function (which is used to model the distribution of the kinetic luminosities) reaches an extremum and a power-law approximation can be used instead. In more precise words, the break of the Schechter function reaches very low probabilities and the vast majority of the radio source population is modelled by the power-law end of the Schechter function (defined by slope $\alpha_{\rm S}$, see also Eqn. 2.19). This is what happens here in the case of data set 2; already at redshift $z = 1.0$ its kinetic luminosity break reaches $\sim 2.5 \times 10^{42}$ W, but as can be deduced from the examples shown in Figure 3.21 despite the enormous $Q_{\rm B}$ the highest kinetic luminosities do not exceed 10^{42} W.

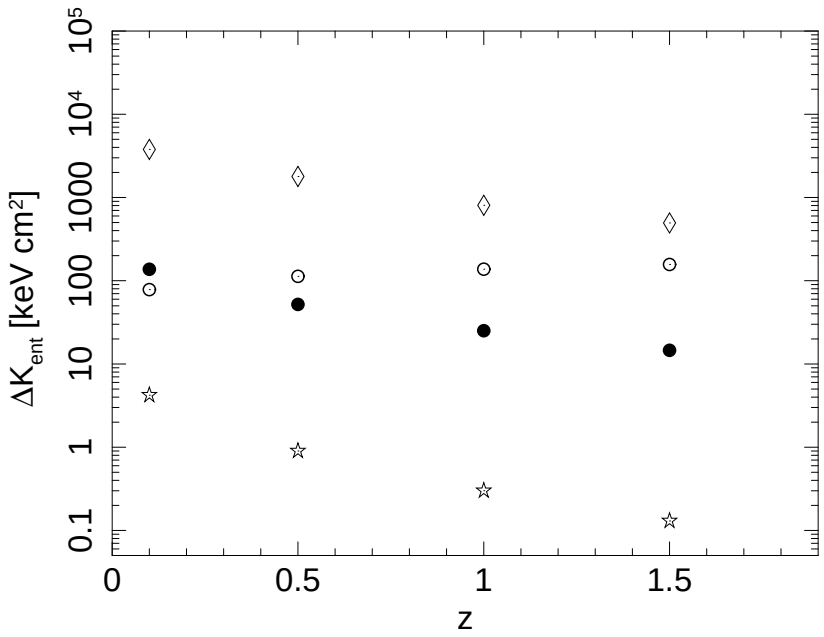

Figure 6.3: Change in cluster gas 'entropy' within the central core radius due to the impact of one episode of radio galaxy activity. The estimations of the change in 'entropy' are based on the injected power estimates presented in Figure 6.2. Each data point marker refers to different data set considered, where (i) data set 1*a* (filled circles) represents the case when the gas density redshift evolution is set to $n_{\rm r} = 4.0$ (Chapter 3: §3.8), (ii) data set 1*b* (open circles) is the best fit, (iii) data set 2 (diamonds) represents the case with high kinetic luminosity break, low central density and short maximum source lifetime, and (iv) data set 3 (stars) represents the case with low kinetic luminosity break, high central density, long maximum source lifetime. All data sets are within 90 per cent confidence intervals of the results presented in Chapter 3.

Because of this effect the total injected power is significantly overestimated in the case of data set 2 as $Q_{\rm B}$ does not represent the typical kinetic luminosities of radio galaxies in this case.

6.3.1 The entropy change and the gas heating rate

Since the total produced energy of different FR IIs is robust, I attempted to investigate the heating rates and change in entropy caused by the activity of these powerful radio galaxies. It has been assumed that all of the radio galaxy power goes into heating the environment and the total power is efficiently and evenly distributed over a sphere of a radius $r = 1$ Mpc. Clearly, due to the large linear extent of FR II radio galaxies one must expect that most of the energy will be deposited beyond the cooling radius (e.g. Gitti *et al.*, 2007; Mathews and Guo, 2011), where typically $r_{\rm cool} \sim 100$ kpc (e.g. Best *et al.*, 2007; Gitti *et al.*, 2007). Hence the use of 1 Mpc radius is justified. The results presenting the total power injected per baryon ($Q\,t_{\rm max}$ in units of keV/`baryon`) are displayed in Figure 6.2. Although spanning

a rather narrow range of possible values, and similarly suggesting mild, if any, redshift dependence, the results from separate data sets are somewhat different. One must remember that to estimate the energy injected per particle the total number of baryons within the considered volume must be known, and this is turn will depend on the cluster gas density. Also, the reason that there is nearly no redshift evolution in the heat rate can be explained by the fact that all three parameters used to determine the heat rates (Q, $t_{\rm max}$ and ρ) evolve with redshift and so may compensate for each other. That is, for higher redshifts the total injected energy is consistently higher (Figure 6.1), but the gas density also increases, and hence the total energy injected per particle stays roughly the same (with the exception of data set 1*b* where the strength of the redshift evolution of ρ_o is $n_{\rm n} = 0.0$ and so the change in $Q(z)\ t_{\rm max}(z)$ is not compensated by the change in $\rho_o(z)$, consult Table 6.1). One must keep in mind, however, that the reason there may be seen slight departure from this reasoning in the case of data set 2 may be the fact that the kinetic luminosities of this data sets are overestimated as discussed in previous section, and the increase in total produced energy for higher redshifts is stronger than the increase in the density of the ambient gas. To resolve this issue and to shed more light on the behaviour of radio sources in population from data set 2, the typical kinetic luminosity of these sources would need to be sought after and tested rather than $Q_{\rm B}$.

A much more discrepant picture comes from the estimations of the induced change in the 'entropy'. Since a radio source will inject a certain amount of energy into its environment, this excess energy (enthalpy) will increase the gas entropy. The entropy is dependent on the radius from the cluster core. Hence, results for three different radii are presented, i.e. change in the 'entropy' for gas density within core radius is displayed in Figure 6.3 and for gas densities at 500 kpc and 1 Mpc in Figure 6.4. The dependence on the gas number densities is much stronger than in the case of the estimated energy injected per baryon. Also, a redshift trend can be observed, although this is simply a reflection of the strength of the gas density evolution. At higher redshifts the gas density of the ICM is also higher (again with the exception of data set 1*b* in which the gas density does not undergo any redshift evolution), and so the same amount of energy injected per baryon must be allocated between more particles (consult also Eqn. 6.6). For reference, the gas number densities for each data set and plotted redshift are listed in Table 6.2. Since the 'entropy' is dependent on the gas density, the differences between the 'entropy' change of the tested data sets are significant, the scale of the impact of the AGN jets on this quantity can be only estimated once the gas density and its profile is constrained. It will be very interesting to incorporate these low redshift independent constraints on cluster gas density into the Monte Carlo simulations developed in this thesis.

Finally, it is important to stress here that these estimates are based on very strong assumptions as many concerns are not fully resolved yet. One of such issues is what fraction of the actual energy delivered by jets would actually contribute to heating the ICM. Perucho *et al.* (2011), for instance, suggest that the vast majority of the cocoon energy ($\geqslant$ 95 per

Table 6.2: Central gas number densities calculated according to the gas density profile (Chapter 2: Eqn. 2.5) with the assumed core radius $a_o = 2$ kpc and profile slope $\beta = 1.5$, and the gas density redshift evolution as listed in Table 6.1.

Redshift	Data set 1*a* [cm^{-3}]	Data set 1*b* [cm^{-3}]	Data set 2 [cm^{-3}]	Data set 3 [cm^{-3}]
$z = 0.1$	0.003	0.006	5×10^{-5}	0.19
$z = 0.5$	0.015	0.006	2×10^{-4}	1.76
$z = 1.0$	0.048	0.006	8×10^{-4}	8.60
$z = 1.5$	0.117	0.006	2×10^{-3}	29.30

cent) is transferred to the intracluster medium and goes into heating (see also Magliocchetti and Brüggen, 2007). While on the other hand Mathews and Guo (2011) point out that sizes of typical radio galaxies significantly exceed the cooling radius and raise a suggestion that only ~ 1 per cent of the total AGN kinetic feedback will reach the cluster cooling radius. Another issue that needs to be raised here is whether both morphological classes of radio galaxies have the same impact on the cluster environments. Due to the different interaction with the ambient medium of FR I and FR II radio galaxies, it has been suggested that it is FR I population that significantly contributes to the heating rates within the cooling radii especially at low redshifts (De Young, 2010). It is possible that the FR II sub-population of radio galaxies contributes much stronger to the overall AGN feedback especially at higher redshifts where these sources are expected to be much more numerous than to the cooling and heating problem of the cluster cores. This possible distinction should also be kept in mind while inspecting presented here results.

6.3.2 Deduced luminosities: cooling flow power and bremsstrahlung luminosity

It is also interesting to discuss the influence these results would exert on other cluster properties which can be measured. I will focus here on two such quantities, namely the cooling flow power and the bremsstrahlung luminosity.

Cooling flow power. The cooling luminosity, i.e. the cooling flow power (L_{cool}), is assumed to come from thermal energy of the medium and any 'pdV' work done on the gas

which enters the cooling radius. It can be estimated through the following relation

$$L_{\rm cool} = \left(\frac{\Gamma_{\rm ICM}}{\Gamma_{\rm ICM}-1}\right)\frac{\dot{M}_{\rm cool}k_{\rm B}T_i}{\mu m_{\rm p}}, \tag{6.7}$$

where $\Gamma_{\rm ICM}$ is the ICM adiabatic index, and $\dot{M}_{\rm cool}$ denotes the mass inflow rate, typical values of which are $\sim 10-300$ $M_\odot$ yr^{-1}. The mass inflow rate of the cooling flow can be calculated from the cluster X-ray luminosity so that $\dot{M}_{\rm cool} \approx (2\mu m_p/5k_{\rm B}T_{\rm vir})L_{\rm x}$ – this rate gives an estimate of the cluster cooling rate in the absence of any feedback. But one may also look at this quantity as the luminosity that must be compensated for by some means of heating to stop the cluster cooling. Typically, the cooling luminosities lie in the range of $\sim 10^{35}-10^{38}$ W (Fabian 1994; Rafferty *et al.* 2006; see also Gitti *et al.* 2012 and references therein). The kinetic luminosities of FR II radio galaxies are of order of, or may even significantly exceed, these cooling luminosities, and it had been suggested that they may balance out the cooling flows (e.g. Bîrzan *et al.*, 2004; Dunn *et al.*, 2005; Rafferty *et al.*, 2006; McNamara and Nulsen, 2007). As discussed by Churazov *et al.* (2002) the AGN feedback must be finely tuned; neither too much heating nor too little cooling can be accepted. However, as discussed by the same authors, the cooling flow may depend on the variation of the AGN heating. That is, there may occur either rare but very powerful outbursts, or less powerful but quasi-continuous supply of energy. Although the latter is usually favoured, some evidence for powerful outbursts exists (e.g. Jones *et al.*, 2002; McNamara *et al.*, 2005). The recently discovered one of the most powerful outbursts known ($\sim 6\times10^{54}$ J), which is located in MS0735 + 7421 galaxy cluster, can stop a cooling flow for few Gyr (McNamara *et al.*, 2005; Gitti *et al.*, 2007).

The kinetic luminosities estimated here with the Monte Carlo simulations indicate that radio galaxies are able to quench cooling flows at least for the time of their lifetimes. The range of possible values of these kinetic luminosities may suggest that the estimations of quenching the cooling flows with radio galaxies are less robust than those of total injected power of our degenerate results. However, one must bear in mind that the more powerful outbursts last for shorter time than the less powerful ones. Given that the activity in radio galaxies is recurrent, the galaxy cluster would undergo alternate periods of cooling and heating, but the recurrence timescales may be related to the power of the radio source, where the weaker outbursts are expected to occur more often (Soker *et al.*, 2001; David *et al.*, 2001). If this is the case, the estimates of the overall impact of radio sources on the evolving galaxy clusters based on our degenerate results would again be robust.

On the additional note, as suggested by Gitti *et al.* (2007), powerful AGN outbursts (such as the one of the MS0735 + 7421 galaxy cluster) would not cause any sudden and significant departures from most of cluster scaling relations, but such outbursts may play an important role in the global properties of clusters, and hence in similarity-breaking, if they are recurrent.

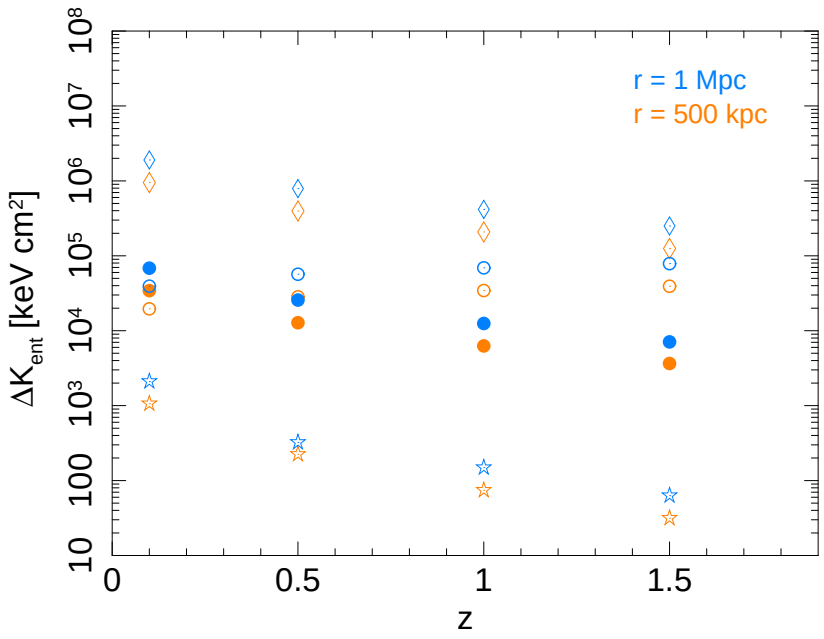

Figure 6.4: Change in cluster gas 'entropy' at the radius of 500 kpc (orange) and 1 Mpc (blue) from the central radio source due to the impact of one episode of radio galaxy activity. The estimated of the change in 'entropy' are based on the injected power estimates presented in Figure 6.2. Each data point marker refers to different data set considered, where (i) data set 1*a* (filled circles) represents the case when the gas density redshift evolution is set to $n_{\rm r} = 4.0$ (Chapter 3: §3.8), (ii) data set 1*b* (open circles) is the best fit, (iii) data set 2 (diamonds) represents the case with high kinetic luminosity break, low central density and short maximum source lifetime, and (iv) data set 3 (stars) represents the case with low kinetic luminosity break, high central density, long maximum source lifetime. All data sets are within 90 per cent confidence intervals of the results presented in Chapter 3.

Bremsstrahlung luminosity Another luminosity worth considering is the X-ray luminosity the injected energy would cause. Assuming that all of the injected power goes into heating, it might be observable as a thermal bremsstrahlung. The bremsstrahlung radiation is produced by free electrons which collide with ions in the surrounding plasma, and if it's strong enough the emission will be detectable in X-rays. In fact, thermal bremsstrahlung is the main radiation mechanism at temperatures $k_{\rm B}T >$ few keV. The X-ray luminosity is given by

$$L_{\rm x} = \left\{ \left(\frac{2\pi k_{\rm B}}{3m_{\rm e}} \right)^{1/2} \frac{2^5 \pi q^6 Z^2}{3hm_{\rm e}c^3} \right\} g_{ff} n_{\rm e} n_{\rm I} T^{1/2} V(t), \tag{6.8}$$

where $m_{\rm e}$, q and $n_{\rm e}$ are electron mass, charge and number density respectively, $n_{\rm I}$ is the number density of ions, h is the Planck constant, Z is atomic number, and g_{ff} is the so-called Gaunt factor which is a slowly varying function of Z, T and frequency (see e.g. Rybicki and Lightman, 1979). The Gaunt factor is usually of order of unity, hence one can neglect it

here in these approximate calculations, and Eqn. 6.8 becomes (in SI units of Watts)

$$L_{\rm x} \sim 2.5 \times 10^{31} n_{\rm e} n_{\rm i} T^{1/2} V(t), \tag{6.9}$$

where T is given in units of eV, the number densities of ions and electrons in m^{-3}, and volume in Mpc^3. Assuming that the typical X-ray luminosities of galaxy clusters are of order of $10^{36} - 10^{38}$ W and are integrated over central 100 kpc region then one can try to estimate what fraction of this observed luminosity our results would constitute. And so, for the local Universe ($z = 0.1$), the induced bremsstrahlung luminosity of both data set 1*a* and 1*b* would be of order of few – 40 per cent of the assumed typical X-ray luminosities, while data set 2 would contribute negligible amount of emission to the observed level and data set 3 would be significantly excessive. In these simple estimates made for the purpose of this discussion I again assumed that all the injected energy goes into heating the ICM gas. Eqn. 6.8 clearly shows that this thermal emission is dependent on the gas density of the medium and its temperature, and as shown already in § 6.3.1 it should not be expected to be robust for our degenerate results. On the contrary, it may be used, along with the gas density and entropy estimates, as independent constraint that will allow one to break the degeneracy of the fundamental parameters of FR II sources.

6.4 Summary

The impact of radio galaxies on their environments is investigated and discussed through simple estimations based on the results of Chapter 3. Specifically, the FR IIs' total injected power, their typical heating rates and induced change in entropy are explored for a few radio galaxy populations.

It is shown that the RG energetics compared to the available X-ray observations (and cluster gas density in particular) can provide diagnostics which may break degeneracies in the fundamental parameters of FR II radio sources, or at least narrow their uncertainties down. It will be interesting to attempt to include these diagnostics in the Monte Carlo simulations developed in this project. Strikingly, sets of two of the degenerate fundamental parameters, that is kinetic luminosity and the maximum lifetimes of the radio sources, provide particularly robust estimates of the total power produced by FR IIs during their lifetimes. This can be also used for robust estimations of the quenching of the cooling flows.

The scientist is not a person who gives the right answers, he's one who asks the right questions.

CLAUDE LÉVI-STRAUSS (1908 – 2009)

7
Conclusions

In the final chapter of this thesis I give a summary of the project undertaken during my doctorate candidature, the main findings are listed and any open issues are discussed. I draw to a close with listing some suggestions for the continuation of this work.

7.1 Summary

In this thesis I investigate the evolution of radio galaxies and radio-loud quasars, and the influence these radio sources exert on their environments, across cosmological epochs. I focus on sources with large scale radio structures of FR II morphology. I use the theoretical model of KA97/KDA97 for the intrinsic time evolution of an FR II morphology radio source, and apply it to populations of FR II sources. For the purpose of this study I develop the following:

- A new algorithm for multidimensional Monte Carlo simulations which explore the fundamental parameter space of radio galaxy populations is developed (Chapter 2). The method links the observable radio lobe luminosities, linear sizes and redshifts of FR II sources with their most plausible underlying kinetic luminosities, active lifetimes and environments in which radio sources are born (the fundamental parameters). Unlike previous studies, the method developed in this project compares radio luminosity functions found with the observed and simulated data to explore the underlying parameters; this approach allows one to directly link the results of this simulation to other radio source population studies which are most commonly expressed in terms of luminosity or mass functions. The simulation has been written in the *C* programming language, and has been executed on high performance supercomputer, the Iridis Compute Cluster, maintained by the University of Southampton, Southampton, U.K.

- A new low frequency (325 MHz) sample of FR II radio galaxies is constructed based on the the cross match of the WENSS survey and the available optically selected SDSS-FIRST-NVSS sample of radio-loud AGN (Chapter 4). The matching procedure is detailed and any possible observational biases are investigated. The resulting low frequency sample of radio galaxies is optically selected, so it is not radio complete, but it is argued that the sample is free from any significant biases and can be used in population studies.

The multidimensional Monte Carlo simulations are applied to two separate samples of FR II sources: a well known sample of the most powerful radio galaxies and radio-loud quasars extending up to redshift $z \approx 2$ (3CRR and BRL sample, Chapter 3), and the newly constructed low redshift ($z \leq 0.2$) sample of low luminosity radio galaxies (Chapter 4). It has been found that:

- For the powerful FR IIs the total lifetimes of the radio galaxies are found to be few $\times 10^7$ yr at low redshift and decrease for earlier epochs (Chapter 3). This is in agreement with independent studies on the 3CRR radio sources, but may be specific to these most powerful radio galaxies and quasars. With the current sample and its

strong flux limit I am unable to make definite statements about the evolution of the lifetimes of the sources which is suggested by our current results.

- The results suggest cosmological evolution of one or more source parameters (Chapter 3). In particular the mean density of the immediate source environments (or the $\rho_o a_o^\beta$ parameter if one allows core radius or β to change with redshift) is found to undergo evolution with redshift; the hypothesis that there is no evolution is ruled out with a probability of > 99 per cent. The central density of the FR II environments is found to undergo redshift evolution of approximately $(1+z)^4$; evolution stronger than the one expected from the Universe's expansion is possible if one considers additional effects from change of environment or core radius evolution.

- The estimated kinetic luminosities are in the range from 10^{38} to 10^{41} W for powerful FR II type sources, which is consistent with previous studies (Chapter 3). It is suggested that the kinetic luminosities of the local, low luminosity density FR IIs are significantly lower (10^{36} – few $\times 10^{38}$ W, Chapter 4); however, more work needs to be done on this low luminosity sample before any final conclusions can be drawn. In particular the morphological classification of the original SDSS-FIRST-NVSS sample of extended radio sources needs to be verified.

- It is observed that the kinetic luminosities depend on the cosmological epoch and the linear size of the source, where larger in linear size as well as higher redshift sources are more powerful (Chapter 3). The FR IIs' kinetic luminosity function undergoes cosmological evolution of the break luminosities of at least $(1+z)^3$ and may be as strong as $(1+z)^{10}$. The uncertainty originates from the strong degeneracy between $Q_{\rm B}$, $t_{\rm max}$ and ρ_o. Evolution stronger than $(1+z)^9$, however, is rather unlikely since as a consequence the black hole masses of the most luminous FR II sources would have to be $> 10^{11}$ $M_\odot$ assuming that there is no strong spin powering of the jets. These results suggest also that, at least at high redshifts, FR II sources most probably accrete at moderate/high Eddington ratios and the black hole spin may play a significant role in the jet production, as both effects seem to be necessary to explain the high estimated kinetic luminosities of FR II sources at higher z.

- An attempt has been made to estimate the duty cycles of FR II radio galaxies at the break in the kinetic luminosity function, finding them to decrease with redshift from $\sim 10^{-3}$ for $z_1 \leq 0.3$, to $\sim 10^{-4.5}$ at $0.3 < z_3 \leq 0.8$, to $\sim 10^{-5.5}$ at $0.8 < z_3 \leq 2.0$ (Chapter 3). The decrease in duty cycle at higher redshifts may be explained by a combination of the reduction in the lifetime of FR II radio galaxies together with evolution in the number density of massive black holes. The shift in kinetic luminosity break to higher values also indicates an intrinsic change in the population of kinetic powers. Interestingly, at low redshifts the duty cycle of powerful FR IIs exceeds that estimated for 10^9 $M_\odot$ AGN based on radiative luminosities. This difference can be

explained if the typical black hole mass of FR IIs shifts to lower masses at low z. Alternatively, the low-z FR II population may become dominated by a kinetically dominated, radiatively inefficient mode of accretion.

- The resulting radio galaxy energetics compared to quantities obtainable from X-ray observations, such as cluster gas densities, can provide diagnostics which may break degeneracies in the fundamental parameters or at least narrow their uncertainties down (Chapter 6).

- Strikingly, despite the strong degeneracy, sets of two of the fundamental parameters, the kinetic luminosities and the maximum lifetimes, provide particularly robust estimates of the total power produced by FR IIs during periods of their activity (Chapter 6). This can be also used for robust estimations of quenching of the cooling flows by radio galaxies.

It is noted here, however, that other theoretical models of radio galaxy time evolution, such as those of BRW99, MK02, or the modified models of Barai and Wiita (2006, 2007), might yield somewhat different results.

In addition to the numerical Monte Carlo investigations, I revisit the KA97/KDA97 theoretical model to investigate the radio lobe – kinetic luminosity scaling relation (Chapter 5). Through numerical exploration of the nonlinear model equations I find that the scaling relation is influenced mainly by the radio source age, aspect ratio, the injection index of the relativistic particles' initial distribution, and the radio source environment density and its profile. My predictions on the scaling relation agree well with earlier simplified theoretical predictions by Willott *et al.* (1999). I also contrast these results to the observationally found radio lobe – kinetic luminosity scaling relations reported in the literature.

7.2 Open issues

Although the study presented here sheds more light on the physical properties and evolution of FR II radio sources, it also unveils issues which needs to be investigated in more detail in order to resolve some of the uncertainties and degeneracies. In particular, the following three issues came into view in this project.

- One of the substantial limitations of any source population study is a survey's sensitivity which causes low luminosity, high redshift radio sources to remain undetected and unavailable for study. Although great care has been undertaken in the development of the Monte Carlo algorithm in this project to account for the sensitivity (Chapter 2), the availability of data observed to lower flux limits is crucial. In a study such as this one, low radio frequency (i.e. MHz frequencies) complete samples of radio sources are of particular importance. Such radio samples exist currently to a certain extent

(e.g. 6C, 7C catalogues, see §1.4), but real progress will be achieved with the state-of-the-art LOFAR facilities. It will be a great opportunity to revisit issues investigated in this study once new, low frequency LOFAR data become available.

- Moreover, although I attempt to shed more light on the strength of the assumptions set in the theoretical modelling of these radio sources, some of these assumptions are still ambiguous. One may attempt to use Bayesian evidence (Chapter 2) to investigate whether any of the assumptions are preferable (see also below), although observational constraints or deeper data may be nevertheless necessary to provide final answers. An emerging suggestion that these assumptions may need to be altered for lower luminosity density radio sources can already be noted in the results of Chapter 4. However, more work needs to be done on this low luminosity sample before any final conclusions can be drawn.

- Finally, due to the occurring degeneracies in the results (Chapter 3), many issues cannot be resolved. One way of breaking the degeneracy is to include data from more sensitive surveys as discussed above. However, as shown in Chapter 6 these degeneracies can be broken also through the analysis of the impact the simulated radio galaxies would have on their environments, and its correspondence to the actual X-ray observations.

7.3 Continuation of this work

There are many ways this project can be continued. Here I sketch only a few of those. First of all, the method developed in this project allows one not only to predict the underlying populations of extragalactic powerful radio sources (Chapter 3), but also to predict samples that would be observed by surveys of various flux limits. It will be of a great importance to verify predictions which can be provided with this Monte Carlo method. Initial test can be already done with currently available low radio frequency samples, such as 7C for instance. Once this is achieved, more reliable predictions for surveys planned for e.g. LOFAR can be estimated.

In this doctorate project I focused on radio sources of FR II morphology only, but no general conclusions can be made regarding the whole population of extragalactic extended radio sources if FR I morphology, and also hybrid (FR I/FR II) sources are not included. However, in order to take into account FR I radio sources general theoretical models of their time evolution must be developed. Another interesting path in the continuation of this project involves investigations of some of the peculiar radio sources which I came across while cross-matching the radio-loud AGN samples of Chapter 4. For instance, theoretical modelling of hybrid sources may lead to very interesting results. Moreover, the sample of Best et al. which I base my work presented in Chapter 4 on, includes a complete sub-sample of double-double radio galaxies. Again, theoretical modelling of these radio sources will

allow one to estimate their fundamental parameters and re-currency of their activity in more complete, population-oriented basis. It is particularly interesting as these radio sources can be used as probes of AGN duty cycles.

There are also a number of improvements to be made to the simulation itself. One of the most important advancements involves implementation of the MCMC algorithms (briefly discussed in Chapter 2) which will allow the simulation to be highly optimised. While at searching through four-dimensional parameter space via the grid minimisation (Chapter 4, independent-z fits in Chapter 3), the current version of my simulation is reasonably fast, the CPU (central processing unit) request rises significantly at higher dimensions; the seven-dimensional parameter space (combined-z fits in Chapter 3) is feasible, but require long processing time. Other improvements which I plan to work on concern for instance inclusion of radio sources of small linear sizes, that is radio sources which are smaller than 10 kpc. This will involve considering a changing density profile of the sources' environments instead of assuming the approximate relation given in Eqn. 2.5 (Chapter 2). Also, allowing for an intrinsic change in the radio source environments at various redshifts may improve the results; as discussed in Chapter 3 the implied evolution of central densities seem to be rather strong, but it can be explained if radio sources of different redshifts inhabit slightly different environments. Furthermore, the Bayes theorem, as discussed in Chapter 2, can be used to select between possible models regarding the results of Chapter 3. Since the frequentists approach, which I have been following in this work so far, is based on the hypothesis testing, one can only accept or reject the null-hypothesis being tested and no information is provided on alternative hypotheses at this point. Given that all tested models in my current work (models S and W, and the influence of the assumptions adopted) are not nested, one would need to turn to Bayesian approach to attempt to solve this issue. It will be of a great interest to investigate whether Bayesian evidence can provide us with definite statements on the tested here assumptions adopted in the theoretical models of FR IIs.

Two chapters of this thesis are currently open-ended. The discussion which I convey in Chapter 5 on the scaling relation between the radio lobe luminosity density and the kinetic luminosity of powerful radio sources induces even more questions on the subject. For instance, how much power does a radio source use on the expansion work? This can be also seen as an efficiency of the jet to inflate the radio cocoon. This issue has been tackled via X-ray observations of cavities in clusters, and attempts to estimate it on theoretical ground have also been made. However, given the method developed and used here this efficiency can be estimated for the whole, most likely populations of FR IIs, whether of complete underlying populations of these sources, or populations restricted by flux limit (the latter of which would provide an estimate which can be easily compared to the X-ray observations of cavities). Additionally, to avoid drawing conclusions which may be model dependent, I plan to perform such an investigation also with the use of the other theoretical models, such as the BRW99 and MK02 models. Furthermore, the scaling relation I considered here is modelled for the FR IIs only. As suggested in Chapter 6, the discrepancy between the the-

oretical predictions for the scaling relation and the estimates from X-ray observations may arise due to the possibility that different sources are considered in each method. Because of that, scaling relation for FR I radio sources should be theoretically investigated. Albeit, the lack of simple analytical models of FR I radio source growth may impede this intent.

Finally, Chapter 4 requires more analysis to be performed before any conclusions can be drawn. First of all, the morphological classification has to be revisited; it is crucial to estimate, as well as it is possible, above what linear size these extragalactic radio sources can be morphologically classified without doubt. Moreover, a fraction of radio sources of the full Best et al. sample is classified according to their affinity to LEG and HEG classes (Best and Heckman, 2012). I plan to cross match such FR II sources; if based on the two types (LEG, HEG) similarly sized sub-samples of FR II radio galaxies of each class can be obtained, the two sub-samples can be modelled separately. Such treatment will be invaluable to investigate whether there is any significant difference in the fundamental parameters between LEG and HEG FR II radio galaxies. This can further lead to a question whether the LEG/HEG classification of FR IIs is reminiscent of the state transitions known to take place in X-ray binary systems (e.g. Körding *et al.*, 2006; Merloni and Heinz, 2008). It will be of a great importance to shed more light on this issue.

APPENDICES

A

Influence of the Assumptions on the Results: Maps of the Confidence Intervals

---

The following appendix contains maps of the confidence intervals for all discussed cases of the influence of the secondary assumptions on the semi-analytical model of radio source growth and, what follows, the final results as discussed in detail in Chapter 2 and Chapter 3. The tests were done for the powerful FR II radio sample of 3C and BRL catalogues only. The best fitting parameters for each tested case are additionally listed. For in depth discussion regarding these tests see §3.10. This material has been submitted to the Monthly Notices of the Royal Astronomical Society as the Supplementary Online Material to A.D. Kapińska, P. Uttley & C.R. Kaiser, 'Fundamental properties of Fanaroff-Riley II radio galaxies investigated via Monte Carlo simulations' (MNRAS 2012, accepted, in press).

A.1 Maximum head advance speed

In the full, detailed simulation run it is assumed that the head advance speed may not exceed $0.4c$ (referred to as the 'initial' case). To test how strong an effect such an assumption can have on the results, the simulation has been re-run with $v_{\max} = 0.05c$, $v_{\max} = 0.15c$ and $v_{\max} = 0.8c$.

The results are displayed in Fig. A.1 and Fig. A.2, and the best-fitting parameters are listed in Table A.1. Only results for the non-evolving Model S for redshifts $z_1 < 0.3$ and $0.8 < z_3 < 2.0$ are presented. The results are discussed in §3.10.3.

Table A.1: The best-fitting parameters for the non-evolving Model S for two redshift ranges, where $0 < z_1 < 0.3$ and $0.8 < z_3 < 2.0$. For each case the one varying assumption, here the maximum head advance speed, is quoted. Due to occurring degeneracies (discussed in §3.5) one should always consult the corresponding confidence intervals (see Fig. A.1 and Fig. A.2). The following standard deviations of $\log_{10}(\rho_{\rm m})$ and $\log_{10}(t_{\rm max_m})$ log-normal distributions are used: $\log_{10}(\sigma_{\rho_o})$ = 0.15 and $\log_{10}(\sigma_{t_{\rm max}})$ = 0.05. 90 per cent errors are quoted.

z	$Q_{\rm B}$ [log(W)]	$\alpha_{\rm s}$	$\rho_{\rm m}$ [log(kg m^{-3})]	$t_{\rm max_m}$ [log(yr)]	$p-$value
initial					
$v_{\rm max} = 0.4c$					
z_1	$39.15^{+0.30}_{-0.30}$	$0.6^{+0.3}_{-0.6}$	$-23.4^{+0.6}_{-0.4}$	$7.23^{+0.30}_{-0.15}$	0.234
z_3	$39.90^{+0.60}_{-0.45}$	$-1.7^{+1.7}_{-8.3}$	$-20.0^{+2.0}_{-2.8}$	$7.13^{+0.60}_{-1.05}$	0.925
$v_{\rm max} = 0.05c$					
z_1	$38.55^{+0.30}_{-0.30}$	$0.7^{+0.4}_{-0.6}$	$-21.8^{+2.4}_{-0.6}$	$7.98^{+0.9}_{-0.15}$	0.166
z_3	$39.90^{+1.05}_{-0.30}$	$-3.1^{+2.9}_{-2.5\dagger}$	$-21.4^{+2.8}_{-0.2}$	$6.83^{+0.75}_{-(<0.15)\ddagger}$	0.910
$v_{\rm max} = 0.15c$					
z_1	$38.70^{+0.30}_{-0.15}$	$0.6^{+0.4}_{-0.5}$	$-22.4^{+1.4}_{-0.6}$	$7.68^{+0.6}_{-0.15}$	0.154
z_3	$40.05^{+0.75}_{-0.15}$	$-3.9^{+3.8}_{-1.7\dagger}$	$-22.4^{+3.2}_{-0.4}$	$6.38^{+1.05}_{-0.15}$	0.937
$v_{\rm max} = 0.8c$					
z_1	$39.45^{+0.30}_{-0.30}$	$0.6^{+0.3}_{-0.5}$	$-24.0^{+0.3}_{-0.3}$	$6.93^{+0.30}_{-0.30}$	0.233
z_3	$40.80^{+1.80}_{-0.30}$	$-3.7^{+2.9\dagger}_{-1.9}$	$-24.0^{+1.0}_{-(<0.2)\ddagger}$	$5.63^{+3.00}_{-(<0.15)\ddagger}$	0.940

Notes. The resolution of the results is $\Delta\log_{10}(\rho_o) = 0.2$, $\Delta\log_{10}(Q_B) = 0.15$, $\Delta\log_{10}(t_{\rm max}) = 0.15$, and $\Delta\alpha_s = 0.1$.
† For errors which may be extending beyond the searched ranges (see Table 3.2) value up to the range border is quoted.
‡ If errors are smaller than their respective resolution, value of $< \Delta$ is quoted.

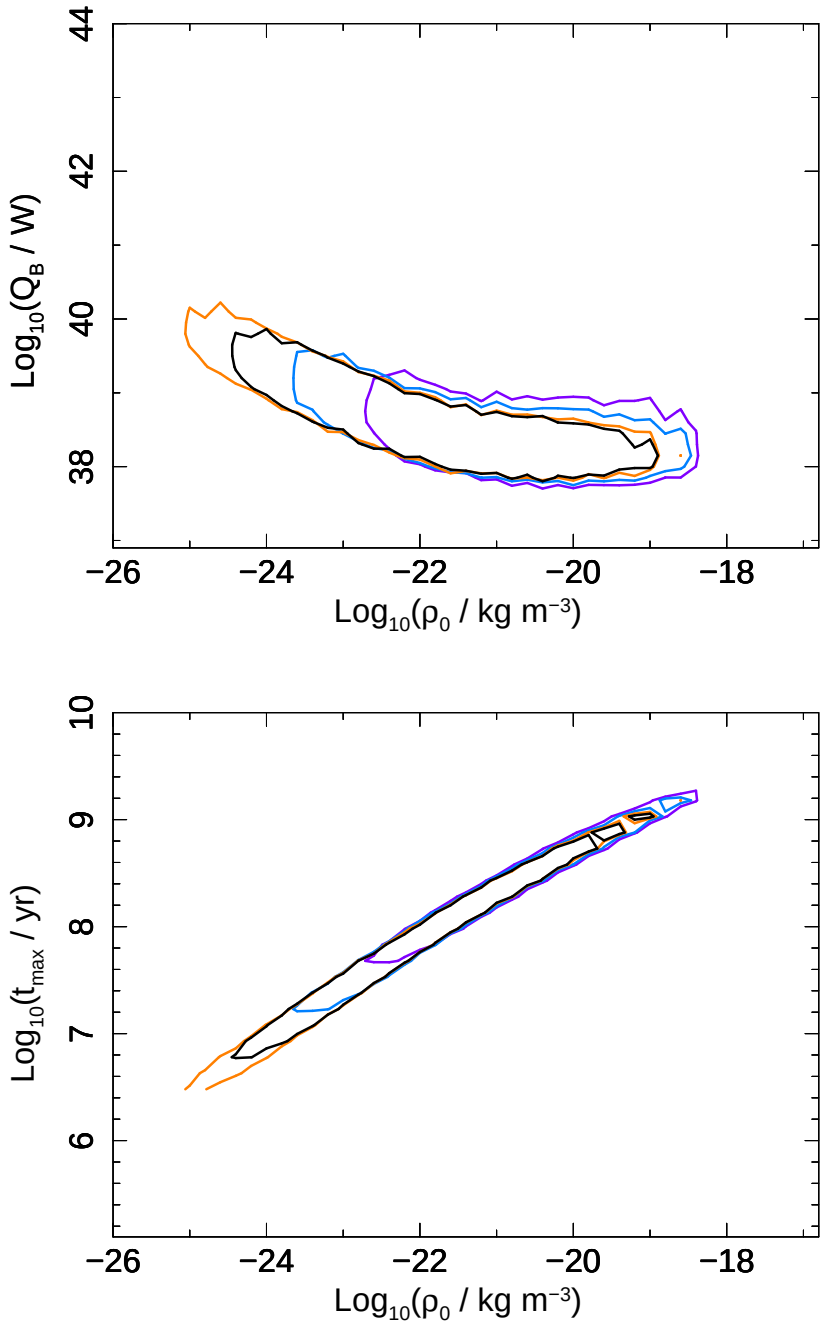

Figure A.1: 90 per cent confidence intervals for populations created with different assumptions of the maximum head advance speeds of jets: 0.8c (orange), 0.4c (black), 0.15c (blue), and 0.05c (violet) in units of the light speed c. Results shown for redshifts $0 < z_1 < 0.3$, and for Model S as described in Chapter 3. Findings are based on the 3CRR and BRL data fits. The case when the maximum head advance speed is assumed to be 0.4c is the initial, standard case analysed in depth in Chapter 3. The best fits, and goodness-of-fit test results for each case are listed in Table A.1

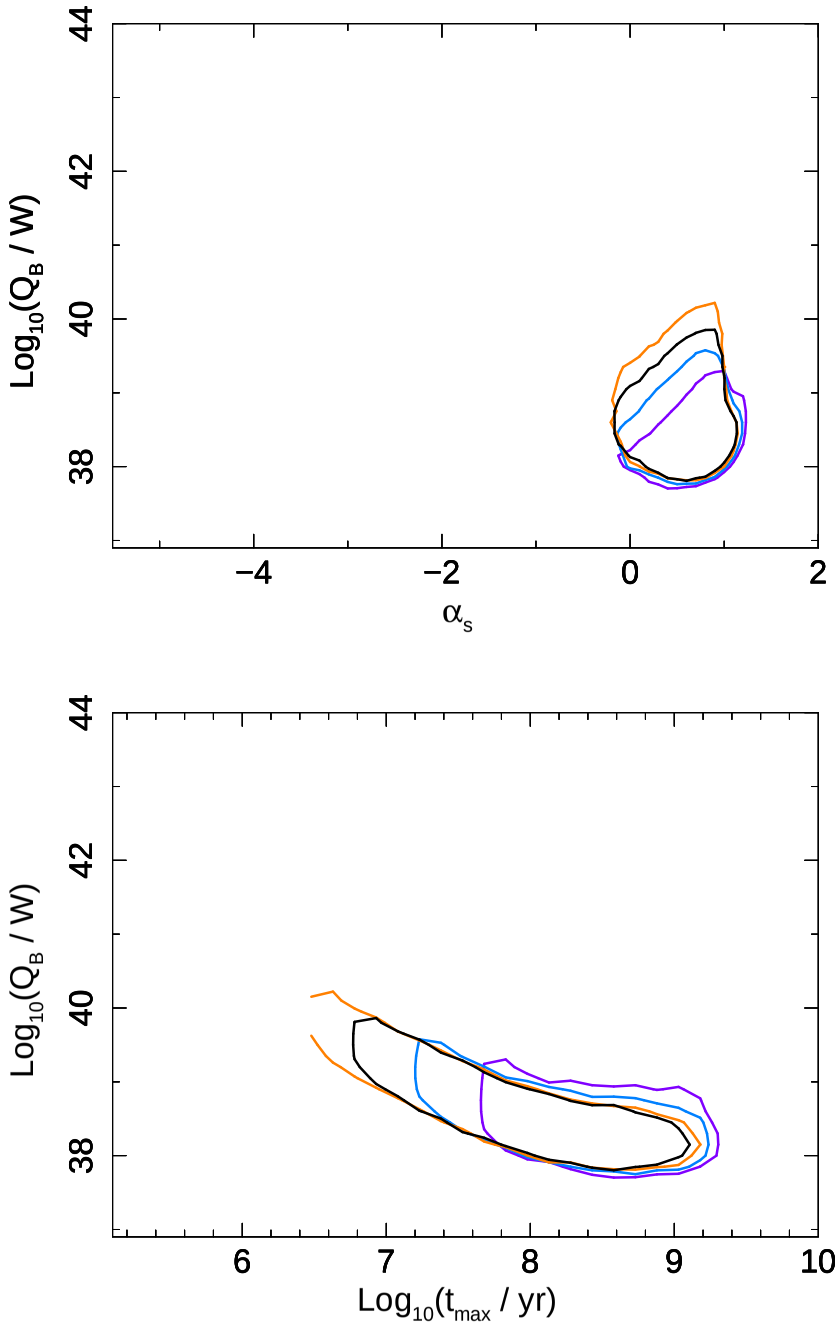

Figure A.1: *continued.*

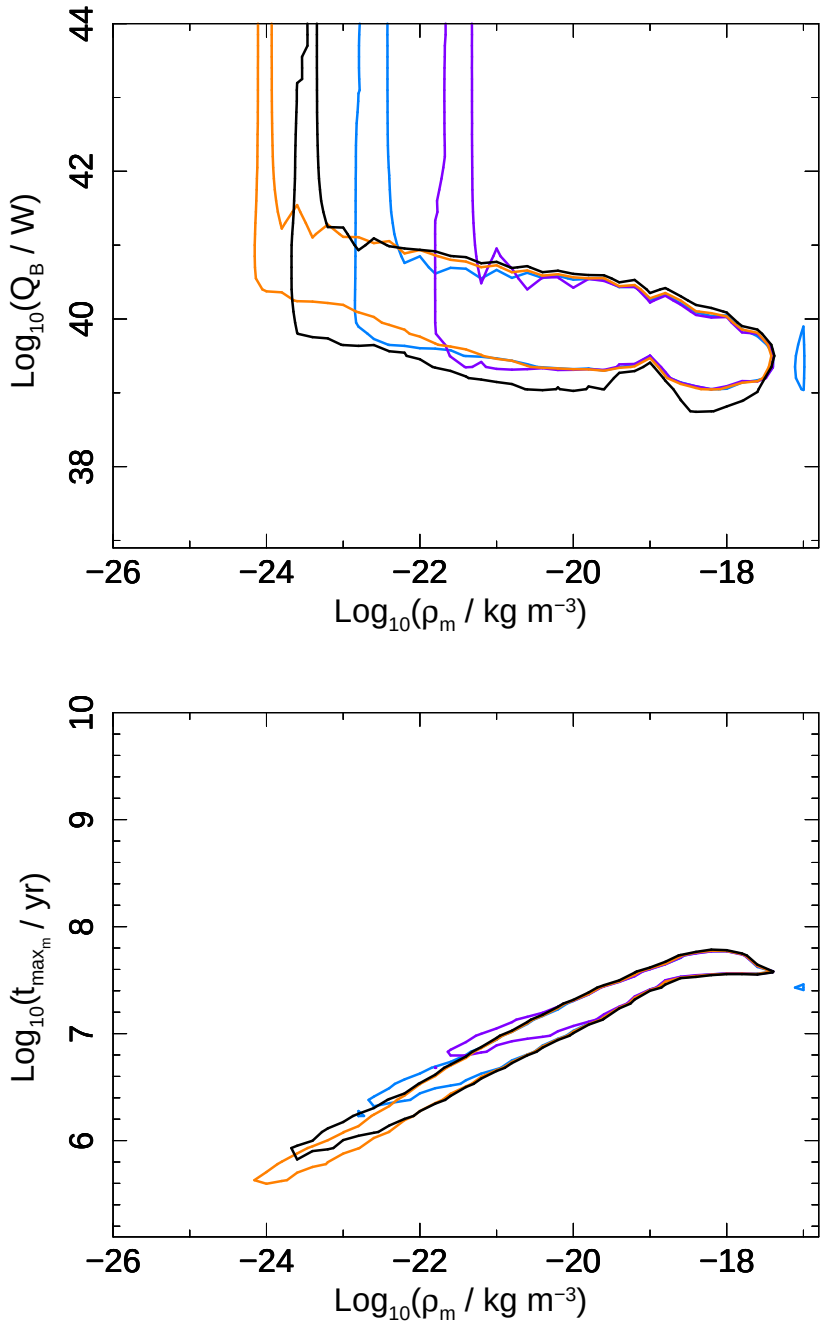

Figure A.2: 90 per cent confidence intervals for populations created with different assumptions of the maximum head advance speeds of jets: 0.8c (orange), 0.4c (black), 0.15c (blue), and 0.05c (violet) in units of the light speed c. Results shown for redshifts $0.8 < z_3 < 2.0$, and for Model S as described in Chapter 3. Findings are based on the 3CRR and BRL data fits. The case when the maximum head advance speed is assumed to be 0.4c is the initial, standard case analysed in depth in Chapter 3. The best fits, and goodness-of-fit test results for each case are listed in Table A.1

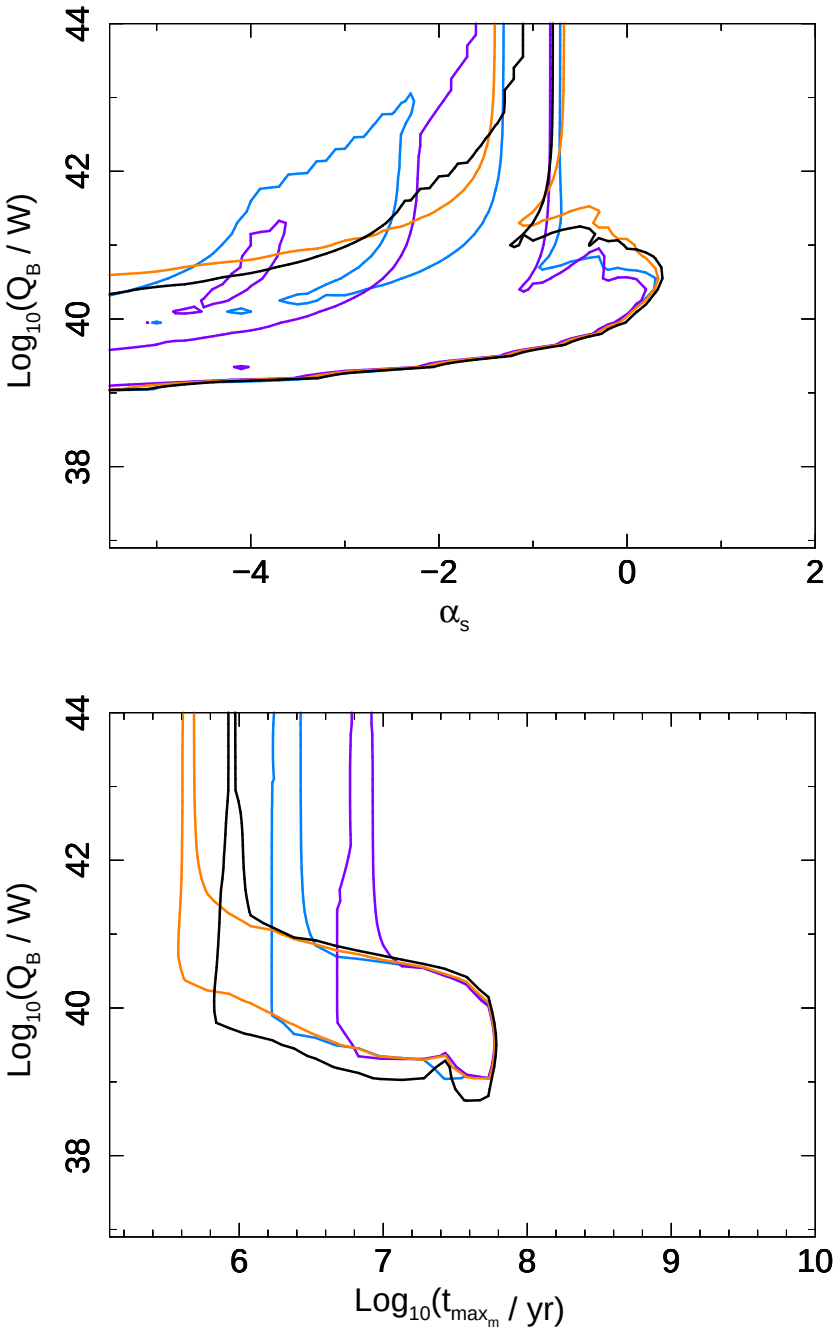

Figure A.2: *continued.*

A.2 Population central densities distribution

The density of the medium in which a radio source grows is defined by a central density, core radius and exponent β (Eqn. 2.5). However, in the generation of the whole source population it is assumed that the central densities are not the same for all sources, but are randomly chosen from log-normal distribution. The standard deviation of this distribution is investigated here.

It is initially assumed that the standard deviation of the log-normal central density distribution is $\sigma_{\log_{10}(\rho_o)} = 0.15$ (referred to as the 'initial' case). To test how strong an effect this assumption has on the results, the simulation has been re-run with $\sigma_{\log_{10}(\rho_o)} = 0.0$ (that is the central density distribution is a delta function, all galaxies in the population have the same central density ρ_o), $\sigma_{\log_{10}(\rho_o)} = 0.5$, $\sigma_{\log_{10}(\rho_o)} = 0.75$ and $\sigma_{\log_{10}(\rho_o)} = 1.0$. The results are displayed in Fig. A.3 and Fig. A.4, and the best-fitting parameters are listed in Table A.2. Only results for the non-evolving Model S for redshifts $z_1 < 0.3$ and $0.8 < z_3 < 2.0$ are presented. The results are discussed in detail in §3.10.1.

Table A.2: The best-fitting parameters for the non-evolving Model S for two redshift ranges, where $0 < z_1 < 0.3$ and $0.8 < z_3 < 2.0$. For each case the one varying assumption, here the standard deviation of the log-normal distribution of central densities, is quoted. Due to occurring degeneracies (discussed in §3.5) one should always consult the corresponding confidence intervals (see Fig. A.3 and Fig. A.4). The following standard deviation of $\log_{10}(t_{max_m})$ log-normal distribution is used: $\log_{10}(\sigma_{t_{max}})$ = 0.05. 90 per cent errors are quoted.

z	Q_B [log(W)]	α_s	ρ_m [log(kg m^{-3})]	t_{max_m} [log(yr)]	$p-$value
initial					
$\sigma_{\log_{10}(\rho_0)} = 0.15$					
z_1	$39.15^{+0.30}_{-0.30}$	$0.6^{+0.3}_{-0.6}$	$-23.4^{+0.6}_{-0.4}$	$7.23^{+0.30}_{-0.15}$	0.234
z_3	$39.90^{+0.60}_{-0.45}$	$-1.7^{+1.7}_{-8.3}$	$-20.0^{+2.0}_{-2.8}$	$7.13^{+0.60}_{-1.05}$	0.925
$\sigma_{\log_{10}(\rho_0)} = 0.50$					
z_1	$38.55^{+0.30}_{-0.30}$	$0.4^{+0.4}_{-0.6}$	$-23.4^{+0.60}_{-0.60}$	$7.38^{+0.3}_{-0.15}$	0.261
z_3	$40.35^{+0.45}_{-0.15}$	$-4.3^{+4.1}_{-1.3\dagger}$	$-24.4^{+4.2}_{-0.2}$	$5.93^{+1.20}_{-(<0.15)\ddagger}$	0.972
$\sigma_{\log_{10}(\rho_0)} = 0.75$					
z_1	$38.70^{+0.30}_{-0.30}$	$0.4^{+0.4}_{-1.4}$	$-23.8^{+1.0}_{-0.6}$	$7.53^{+0.30}_{-0.30}$	0.459
z_3	$40.65^{+(<0.15)\ddagger}_{-3.15}$	$0.6^{+(<0.1)\ddagger}_{-4.1}$	$-24.4^{+(<0.2)\ddagger}_{-0.2}$	$6.53^{+(<0.15)\ddagger}_{-0.6}$	0.884
$\sigma_{\log_{10}(\rho_0)} = 1.00$					
z_1	$38.40^{+0.15}_{-0.15}$	$0.4^{+0.2}_{-0.5}$	$-23.8^{+0.2}_{-(<0.2)\ddagger}$	$7.83^{+0.15}_{-(<0.15)\ddagger}$	0.684
z_3	$40.20^{+(<0.2)\ddagger}_{-(<0.2)\ddagger}$	$0.6^{+0.1}_{-(<0.1)\ddagger}$	$-24.00^{+(<0.2)\ddagger}_{-(<0.2)\ddagger}$	$6.08^{+(<0.15)\ddagger}_{-(<0.15)\ddagger}$	0.996
$\sigma_{\log_{10}(\rho_0)} = 0.00$					
z_1	$39.00^{+0.30}_{-0.30}$	$0.6^{+0.3}_{-0.5}$	$-23.0^{+0.60}_{-0.60}$	$7.38^{+0.30}_{-0.30}$	0.179
z_3	$39.90^{+0.45}_{-0.45}$	$-1.4^{+1.4}_{-4.2\dagger}$	$-19.6^{+1.6}_{-2.4}$	$7.28^{+0.45}_{-0.90}$	0.554

Notes. The resolution of the results is $\Delta\log_{10}(\rho_o) = 0.2$, $\Delta\log_{10}(Q_B) = 0.15$, $\Delta\log_{10}(t_{max})$ =0.15, and $\Delta\alpha_s = 0.1$.

† For errors which may be extending beyond the searched ranges (see Table 3.2) value up to the range border is quoted.

‡ If errors are smaller than their respective resolution, value of $< \Delta$ is quoted.

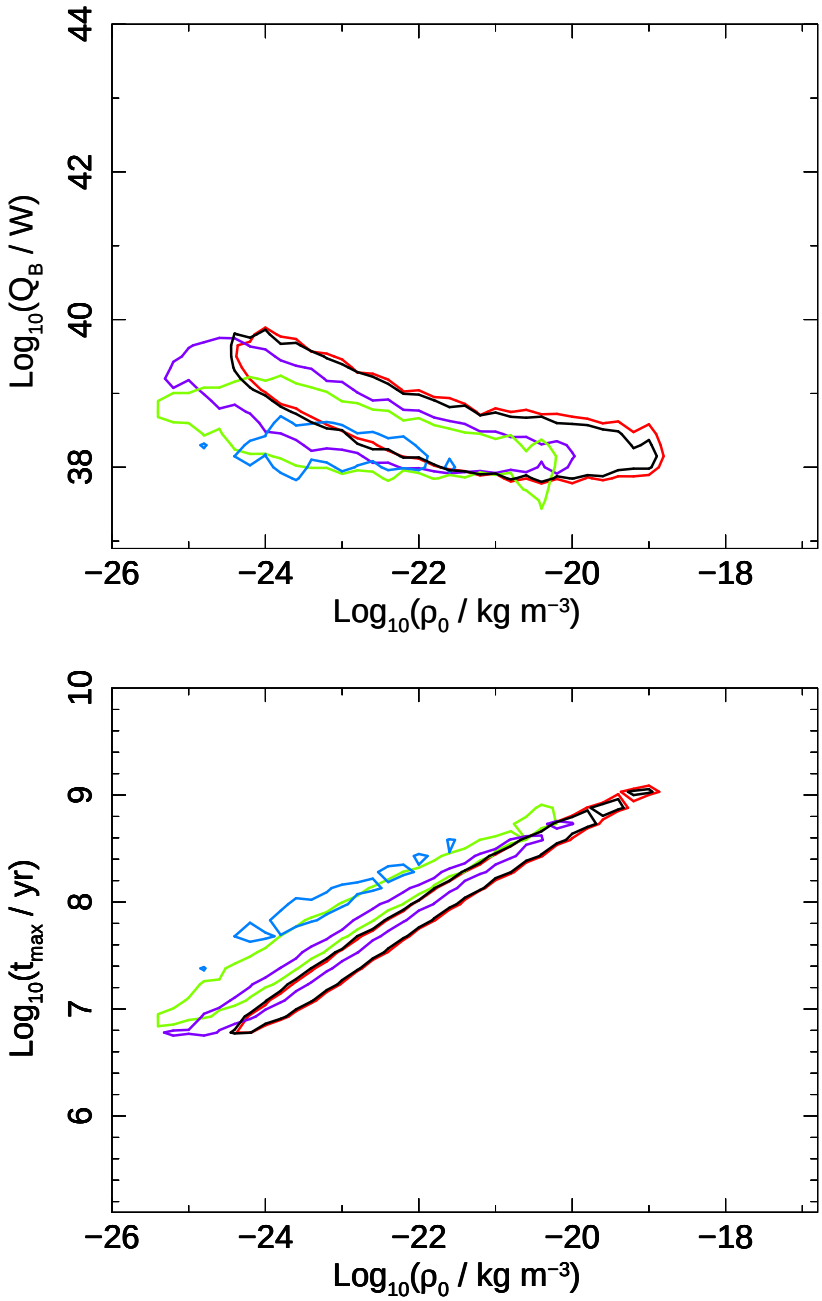

Figure A.3: 90 per cent confidence intervals for populations created with different assumptions on the standard deviation of the density log-normal distribution, where $\sigma_{\log_{10}(\rho_0)} = 0.0$ (i.e. ρ_o is a delta function, drawn in red), $\sigma_{\log_{10}(\rho_0)} = 0.15$ (black), $\sigma_{\log_{10}(\rho_0)} = 0.50$ (violet), $\sigma_{\log_{10}(\rho_0)} = 0.75$ (green), and $\sigma_{\log_{10}(\rho_0)} = 1.0$ (blue). Results shown for redshifts $0 < z_1 < 0.3$, and for Model S as described in Chapter 3. Findings are based on the 3CRR and BRL data fits. The case where the standard deviation is equal to $\sigma_{\log_{10}(\rho_0)} = 0.15$ is the initial, standard case analysed in depth in Chapter 3. The best fits, and goodness-of-fit test results for each case are listed in Table A.2

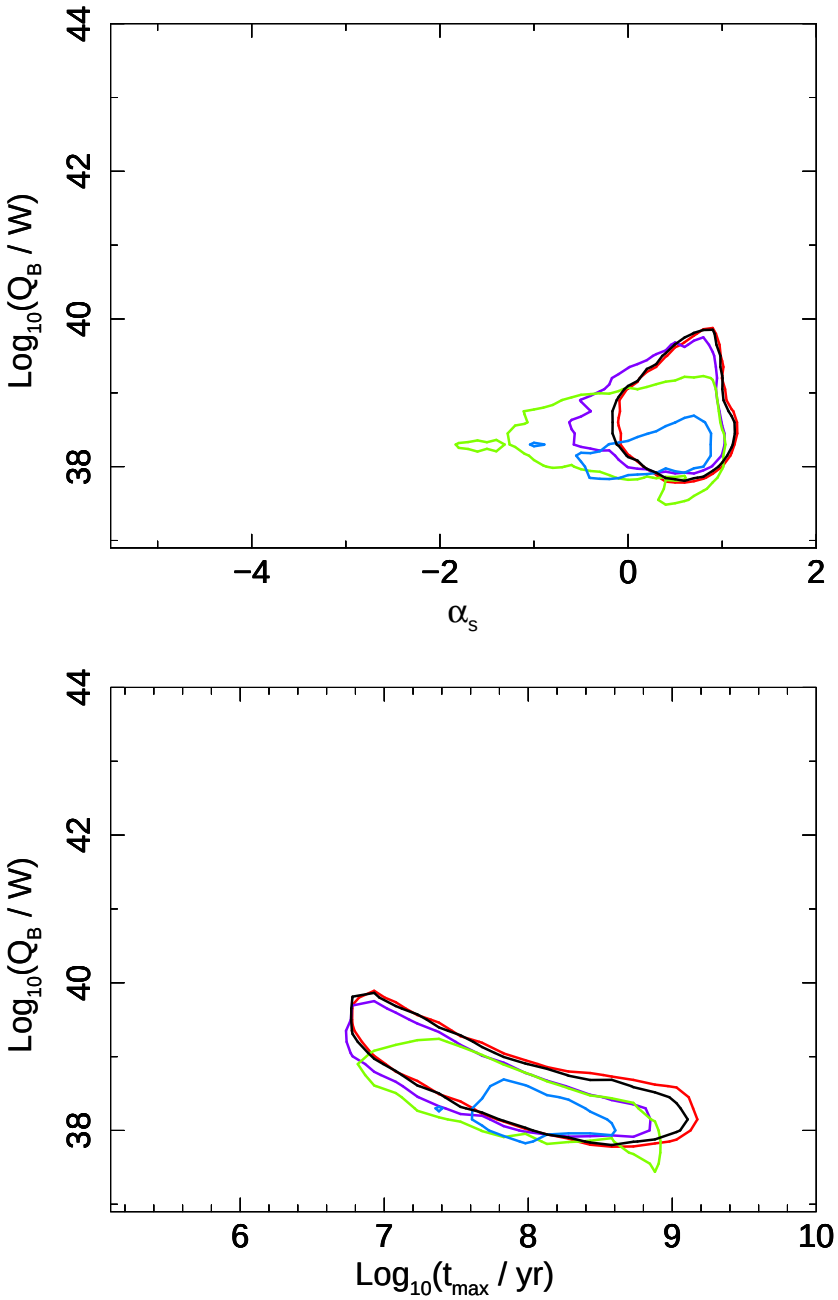

Figure A.3: *continued.*

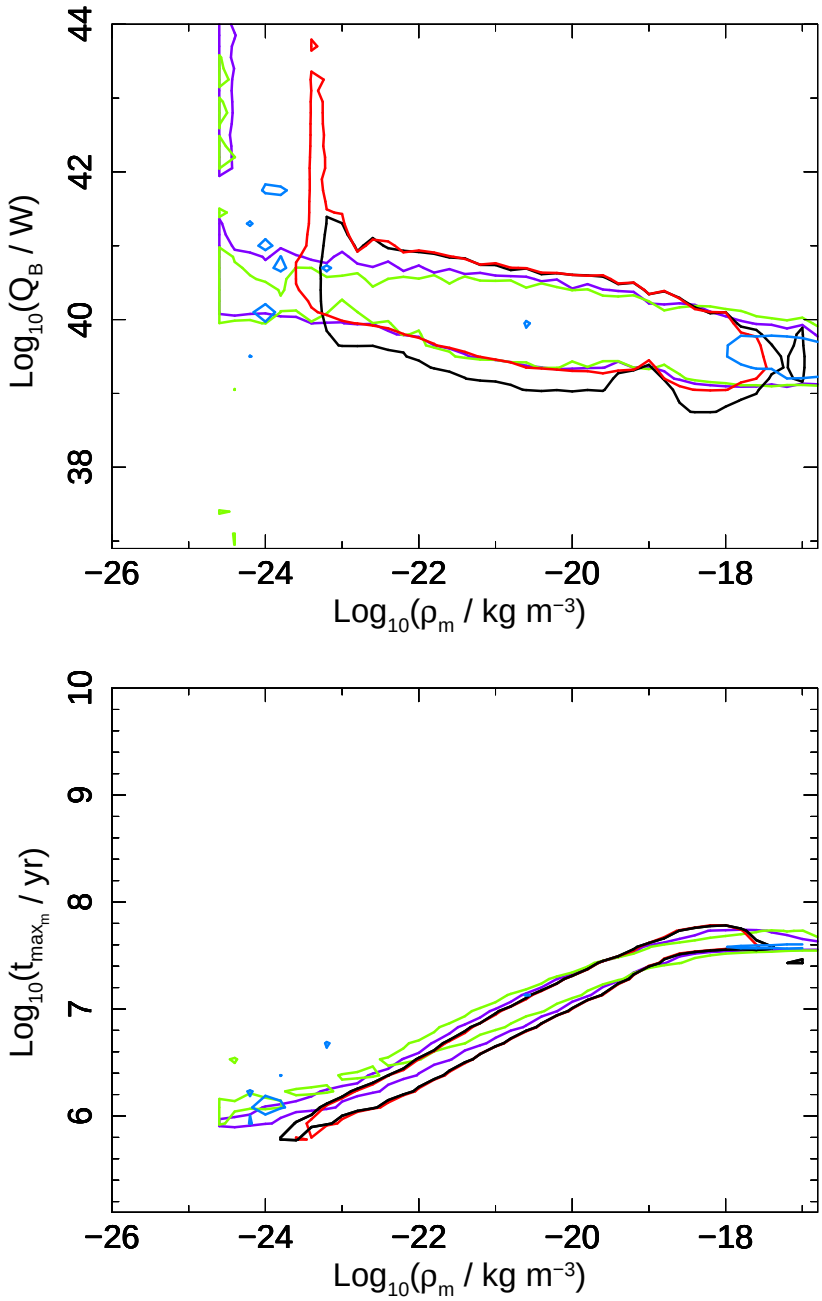

Figure A.4: 90 per cent confidence intervals for populations created with different assumptions on the standard deviation of the density log-normal distribution, where $\sigma_{\log_{10}(\rho_o)} = 0.0$ (i.e. ρ_o is a delta function, drawn in red), $\sigma_{\log_{10}(\rho_o)} = 0.15$ (black), $\sigma_{\log_{10}(\rho_o)} = 0.50$ (violet), $\sigma_{\log_{10}(\rho_o)} = 0.75$ (green), and $\sigma_{\log_{10}(\rho_0)} = 1.0$ (blue). Results shown for redshifts $0.8 < z_3 < 2.0$, and for Model S as described in Chapter 3. Findings are based on the 3CRR and BRL data fits. The case where the standard deviation is equal to $\sigma_{\log_{10}(\rho_o)} = 0.15$ is the initial, standard case analysed in depth in Chapter 3. The best fits, and goodness-of-fit test results for each case are listed in Table A.2

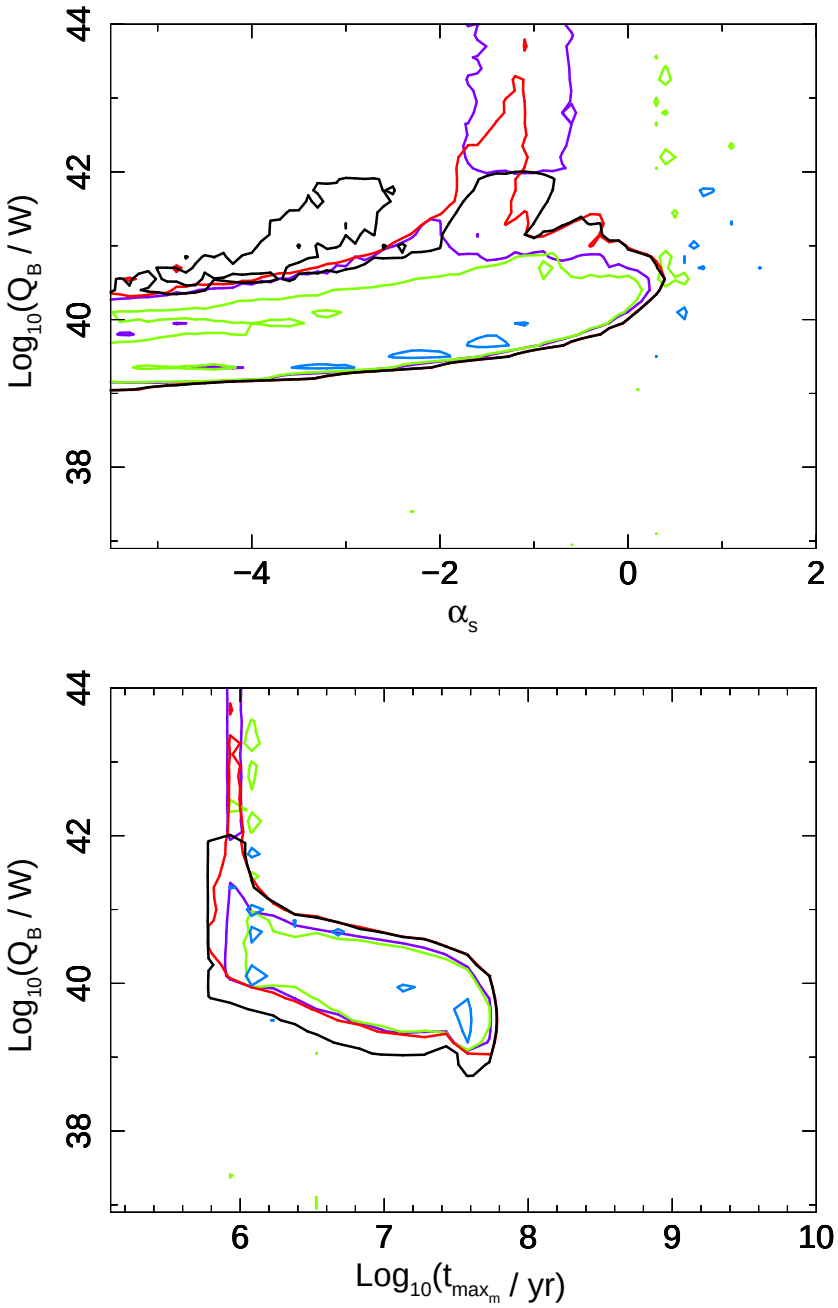

Figure A.4: *continued.*

A.3 Jet particle content

The jet particle content, represented by the parameter k' which is defined as a ratio of the energy density of thermal particles to the energy density of the electrons (see Chapter 2), is initially set to $k' = 0$ in the simulations. This implies that jet is composed of lightweight electron-positron plasma. To investigate how strong an effect an introduction of thermal heavy particles to the radio source outflows has on the final results the simulation is re-run with $k' \in [0;10]$, $k' \in [0;100]$, and finally with $k' = 100$.

The results are displayed in Fig. A.5 and Fig. A.6, and the best-fitting parameters are listed in Table A.3. Only results for the non-evolving Model S for redshifts $z_1 < 0.3$ and $0.8 < z_3 < 2.0$ are presented. The results are discussed in detail in §3.10.5.

Table A.3: The best-fitting parameters for the non-evolving Model S for two redshift ranges, where $0 < z_1 < 0.3$ and $0.8 < z_3 < 2.0$. For each case the one varying assumption, here the particle content of the jet, is quoted. Due to occurring degeneracies (discussed in §3.5) one should always consult the corresponding confidence intervals (see Fig. A.5 and Fig. A.6). The following standard deviations of $\log_{10}(\rho_{\rm m})$ and $\log_{10}(t_{\rm max_m})$ log-normal distributions are used: $\log_{10}(\sigma_{\rho_{\rm o}})$ = 0.15 and $\log_{10}(\sigma_{t_{\rm max}})$ = 0.05. 90 per cent errors are quoted.

z	$Q_{\rm B}$ [log(W)]	$\alpha_{\rm s}$	$\rho_{\rm m}$ [log(kg m^{-3})]	$t_{\rm max_m}$ [log(yr)]	$p-$value
initial					
$k = 0$					
z_1	$39.15^{+0.30}_{-0.30}$	$0.6^{+0.3}_{-0.6}$	$-23.4^{+0.6}_{-0.4}$	$7.23^{+0.30}_{-0.15}$	0.234
z_3	$39.90^{+0.60}_{-0.45}$	$-1.7^{+1.7}_{-8.3}$	$-20.0^{+2.0}_{-2.8}$	$7.13^{+0.60}_{-1.05}$	0.925
$k \in [0,10]$					
z_1	$39.30^{+0.30}_{-0.30}$	$0.4^{+0.4}_{-0.9}$	$-23.2^{+0.8}_{-0.6}$	$7.23^{+0.30}_{-0.30}$	0.284
z_3	$43.20^{+0.90\dagger}_{-2.25}$	$-3.0^{+0.9}_{-2.6\dagger}$	$-23.4^{+(<0.2)\ddagger}_{-0.2}$	$5.78^{+(<0.15\ddagger}_{-(<0.15)\ddagger}$	0.610
$k \in [0,100]$					
z_1	$38.70^{+0.75}_{-0.15}$	$-1.8^{+2.4}_{-3.8\dagger}$	$-22.8^{+2.6}_{-0.6}$	$7.38^{+0.9}_{-0.3}$	0.339
z_3	$41.10^{+0.75}_{-0.75}$	$-1.0^{+1.1}_{-4.6\dagger}$	$-17.6^{+(<0.2)\ddagger}_{-5.8}$	$6.98^{+(<0.15)\ddagger}_{-1.05}$	0.765
$k = 100$					
z_1	$40.50^{+0.30}_{-0.30}$	$0.6^{+0.3}_{-0.5}$	$-22.6^{+0.8}_{-0.4}$	$7.08^{+0.3}_{-0.15}$	0.193
z_3	$41.85^{+0.60}_{-0.45}$	$-2.2^{+2.2}_{-3.4\dagger}$	$-21.6^{+3.2}_{-0.6}$	$6.08^{+0.75}_{-0.15}$	0.946

Notes. The resolution of the results is $\Delta\log_{10}(\rho_{\rm o}) = 0.2$, $\Delta\log_{10}(Q_{\rm B}) = 0.15$, $\Delta\log_{10}(t_{\rm max})$ =0.15, and $\Delta\alpha_{\rm s} = 0.1$.

† For errors which may be extending beyond the searched ranges (see Table 3.2) value up to the range border is quoted.

‡ If errors are smaller than their respective resolution, value of $< \Delta$ is quoted.

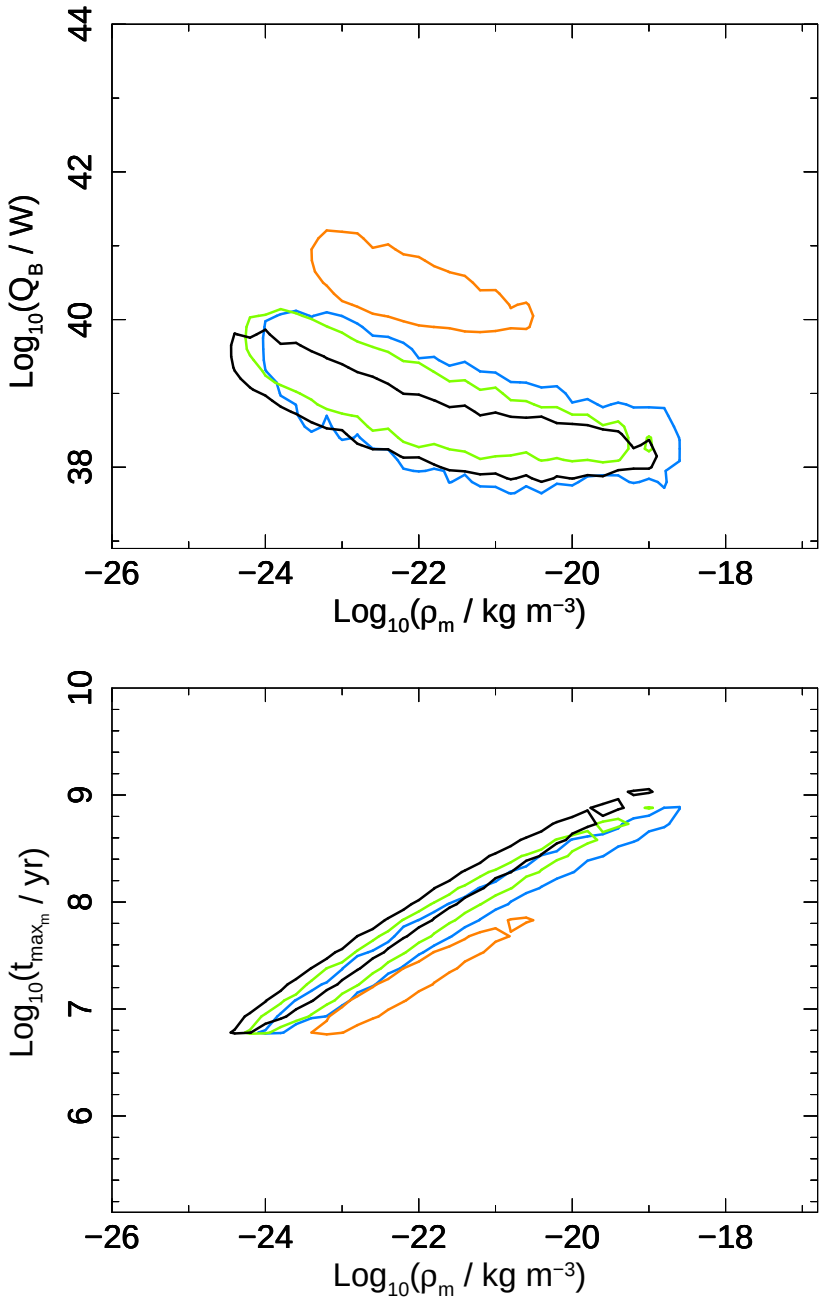

Figure A.5: 90 per cent confidence intervals for populations created with different assumptions on the particle content of the jet, where $k = 0$ (lightweight jets, black), $k' \in [0;10]$ (modest inclusion of protons in the jet, light green), $k' \in [0;100]$ (heavy jets, blue), and $k' = 100$ (heavy jets, orange). Results shown for redshifts $0 < z_1 < 0.3$, and for Model S as described in Chapter 3. Findings are based on the 3CRR and BRL data fits. The case where $k' = 0$ is the initial, standard case analysed in depth in Chapter 3. The best fits, and goodness-of-fit test results for each case are listed in Table A.3

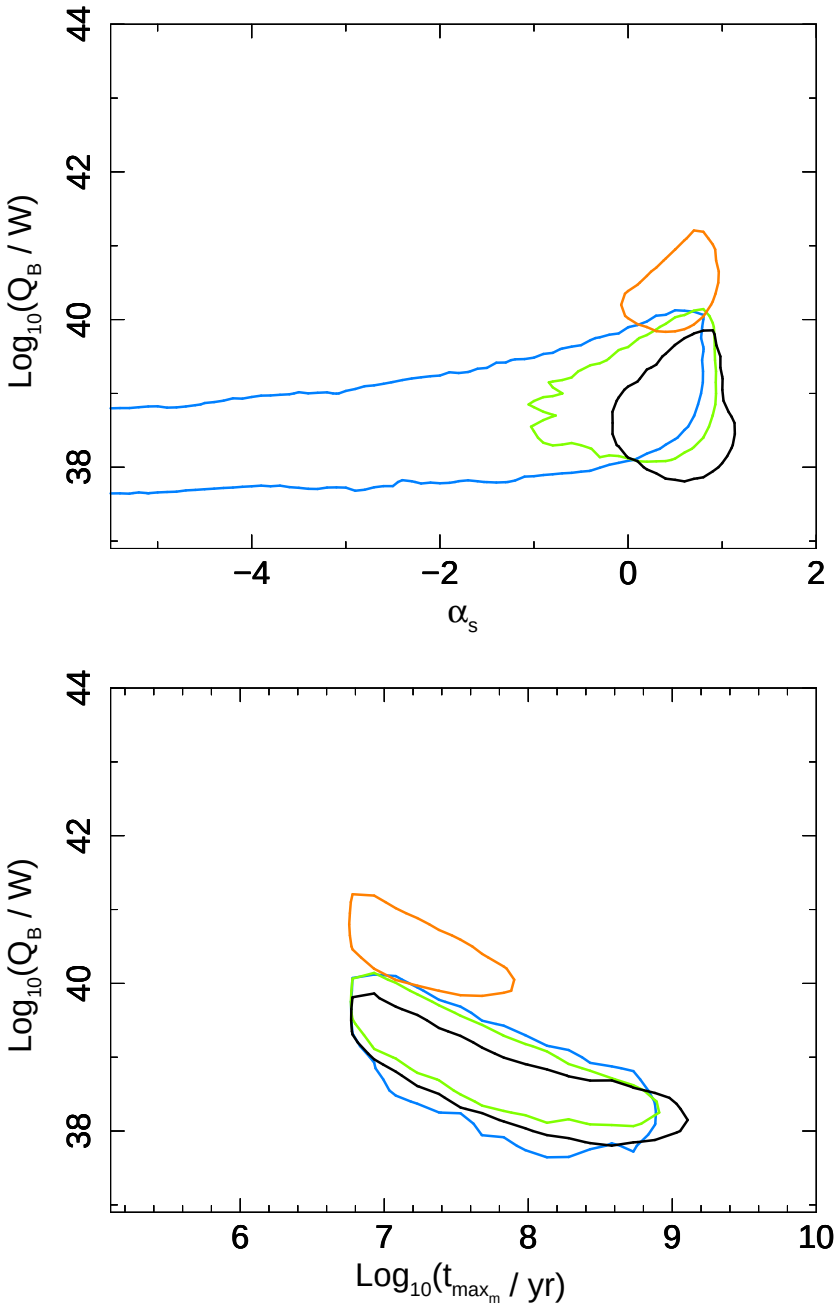

Figure A.5: *continued.*

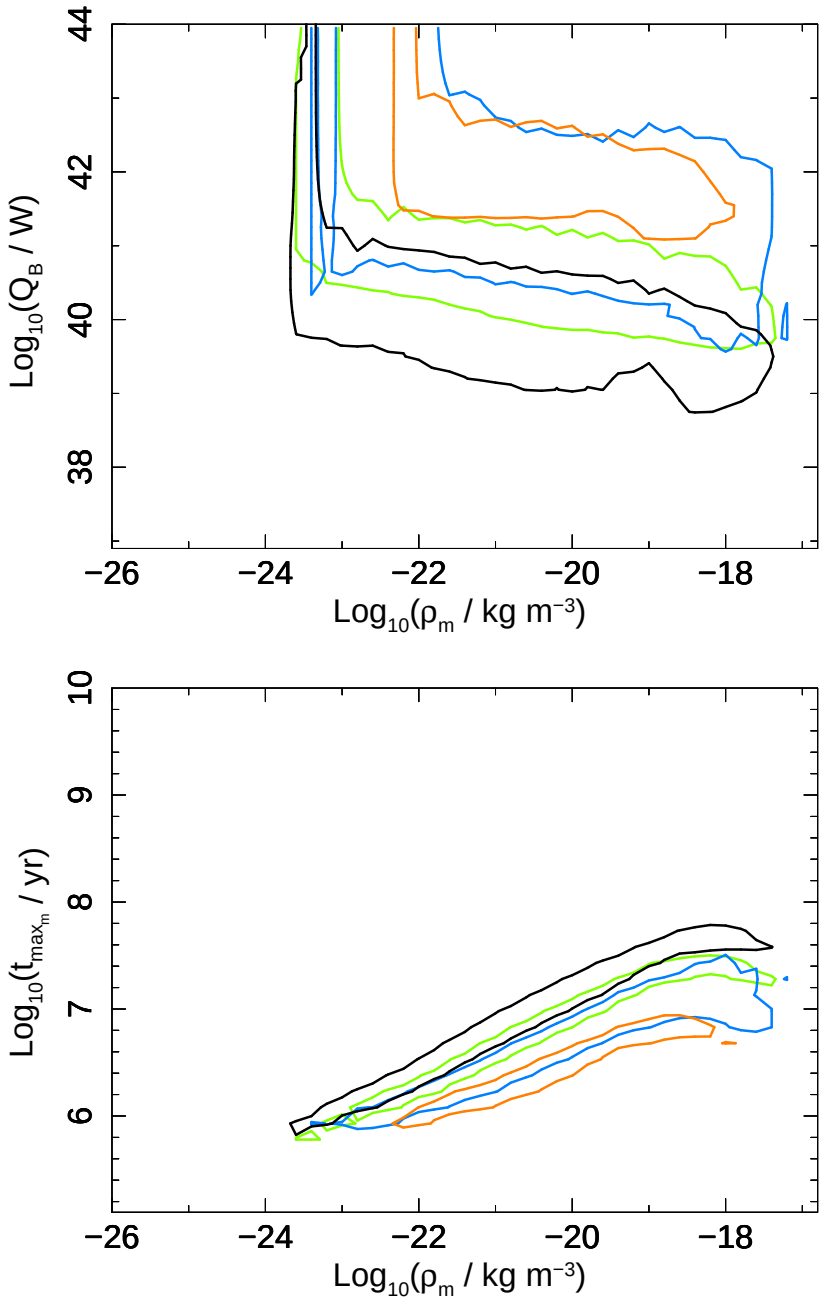

Figure A.6: 90 per cent confidence intervals for populations created with different assumptions on the standard deviation of the density log-normal distribution, where $k' = 0$ (lightweight jets, black), $k' \in [0;10]$ (modest inclusion of protons in the jet, light green), and $k' \in [0;100]$ (heavy jets, blue), and $k' = 100$ (heavy jets, orange). Results shown for redshifts $0.8 < z_3 < 2.0$, and for Model S as described in Chapter 3. Findings are based on the 3CRR and BRL data fits. The case where $k' = 0$ is the initial, standard case analysed in depth in Chapter 3. The best fits, and goodness-of-fit test results for each case are listed in Table A.3.

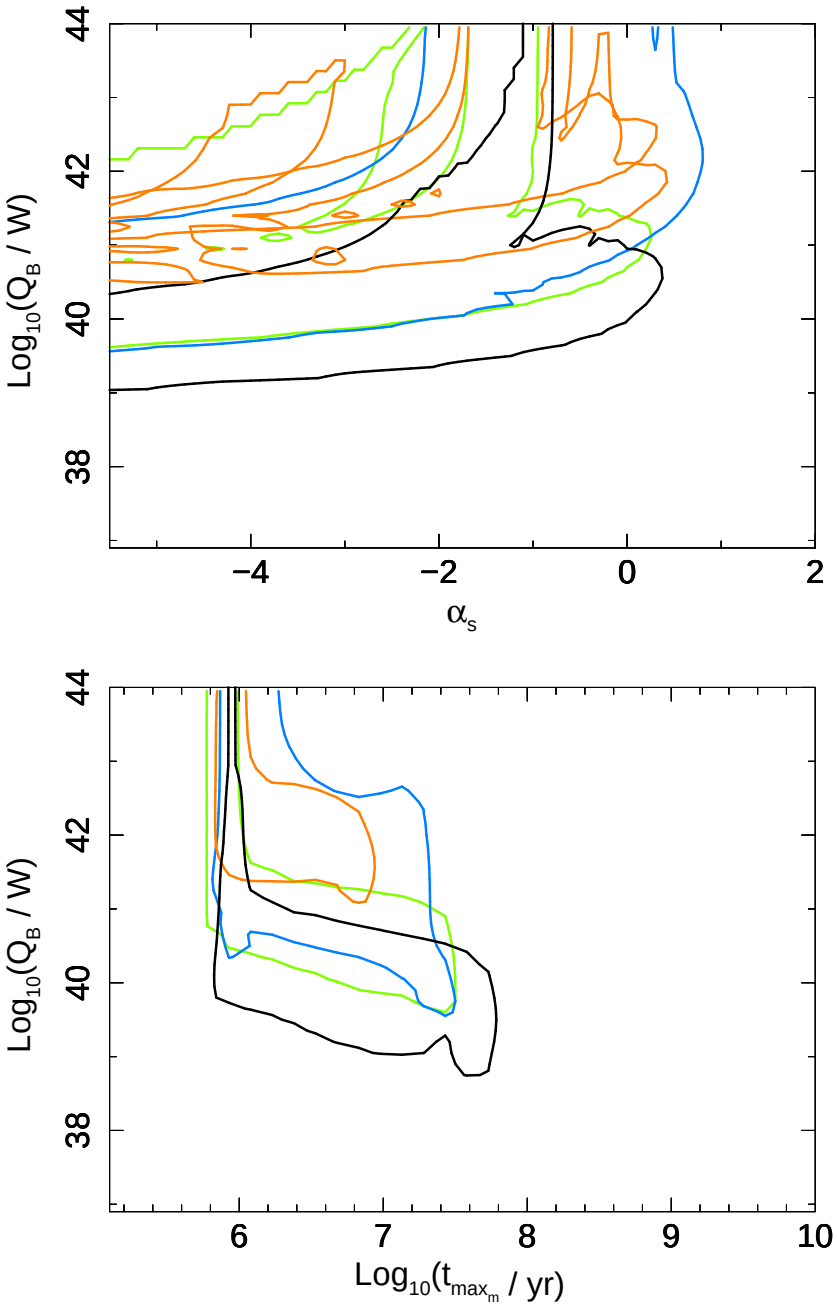

Figure A.6: *continued.*

A.4 Lorentz factors

It is initially assumed that the minimum Lorentz factor is $\gamma_{\rm min} = 1$, and the maximum is $\gamma_{\rm max} = 10^{10}$. Further, subsequently to the discussion in Chapter 2 and Chapter 3, the following combinations of the Lorentz factors were tested:
(1) $\gamma_{\rm min} = 10^2$ and $\gamma_{\rm max} = 10^{10}$,
(2) $\gamma_{\rm min} = 10^4$ and $\gamma_{\rm max} = 10^{10}$,
(3) $\gamma_{\rm min} = 10^1$ and $\gamma_{\rm max} = 10^5$.

The results are displayed in Fig. A.7 and Fig. A.8, and the best-fitting parameters are listed in Table A.4. Only results for the non-evolving Model S for redshifts $z_1 < 0.3$ and $0.8 < z_3 < 2.0$ are presented. The results are discussed in detail in §3.10.4.

Table A.4: The best-fitting parameters for the non-evolving Model S for two redshift ranges, where $0 < z_1 < 0.3$ and $0.8 < z_3 < 2.0$. For each case the one varying assumption, here the minimum and maximum Lorentz factors of the electron distribution, is quoted. Due to occurring degeneracies (discussed in §3.5) one should always consult the corresponding confidence intervals (see Fig. A.7 and Fig. A.8). The following standard deviations of $\log_{10}(\rho_{\rm m})$ and $\log_{10}(t_{\rm max_m})$ log-normal distributions are used: $\log_{10}(\sigma_{\rho_{\rm o}})$ = 0.15 and $\log_{10}(\sigma_{t_{\rm max}})$ = 0.05. 90 per cent errors are quoted.

z	$Q_{\rm B}$ [log(W)]	$\alpha_{\rm s}$	$\rho_{\rm m}$ [log(kg m^{-3})]	$t_{\rm max_m}$ [log(yr)]	$p-$value
initial					
$\gamma_{\rm min} = 1$					
$\gamma_{\rm max} = 10^{10}$					
z_1	$39.15^{+0.30}_{-0.30}$	$0.6^{+0.3}_{-0.6}$	$-23.4^{+0.6}_{-0.4}$	$7.23^{+0.30}_{-0.15}$	0.234
z_3	$39.90^{+0.60}_{-0.45}$	$-1.7^{+1.7}_{-8.3}$	$-20.0^{+2.0}_{-2.8}$	$7.13^{+0.60}_{-1.05}$	0.925
$\gamma_{\rm min} = 10^2$					
$\gamma_{\rm max} = 10^{10}$					
z_1	$37.95^{+0.45}_{-0.30}$	$0.8^{+0.3}_{-0.6}$	$-21.2^{+1.0}_{-1.0}$	$8.43^{+0.45}_{-0.45}$	0.192
z_3	$40.35^{+0.60}_{-0.30}$	$-1.8^{+1.4}_{-3.3}$	$-23.4^{+1.0}_{-0.4}$	$6.08^{+0.30}_{-0.15}$	0.954
$\gamma_{\rm min} = 10^4$					
$\gamma_{\rm max} = 10^{10}$					
z_1	$37.95^{+0.30}_{-0.30}$	$0.6^{+0.6}_{-0.8}$	$-24.0^{+1.2}_{-0.6}$	$7.53^{+0.6}_{-0.3}$	0.398
z_3	$39.15^{+0.6}_{-(<0.15)\ddagger}$	$-5.6^{+4.5}_{-(<0.1)\ddagger}$	$-24.6^{+0.6}_{-(<0.2)\ddagger}$	$5.93^{+0.15}_{-(<0.15)\ddagger}$	0.917
$\gamma_{\rm min} = 1$					
$\gamma_{\rm max} = 10^5$					
z_1	$39.00^{+0.30}_{-0.15}$	$0.4^{+0.4}_{-0.4}$	$-23.4^{+0.6}_{-0.4}$	$7.23^{+0.30}_{-0.15}$	0.160
z_3	$40.20^{+0.60}_{-(<0.15)\ddagger}$	$-5.6^{+5.6}_{-(>0.15)\dagger}$	$-23.4^{+4.0}_{-(<0.2\ddagger)}$	$5.93^{+1.50}_{-(<0.15)\ddagger}$	0.920

Notes. The resolution of the results is $\Delta\log_{10}(\rho_{\rm o}) = 0.2$, $\Delta\log_{10}(Q_{\rm B}) = 0.15$, $\Delta\log_{10}(t_{\rm max})$ =0.15, and $\Delta\alpha_{\rm s} = 0.1$.

† For errors which may be extending beyond the searched ranges (see Table 3.2) value up to the range border is quoted.

‡ If errors are smaller than their respective resolution, value of $< \Delta$ is quoted.

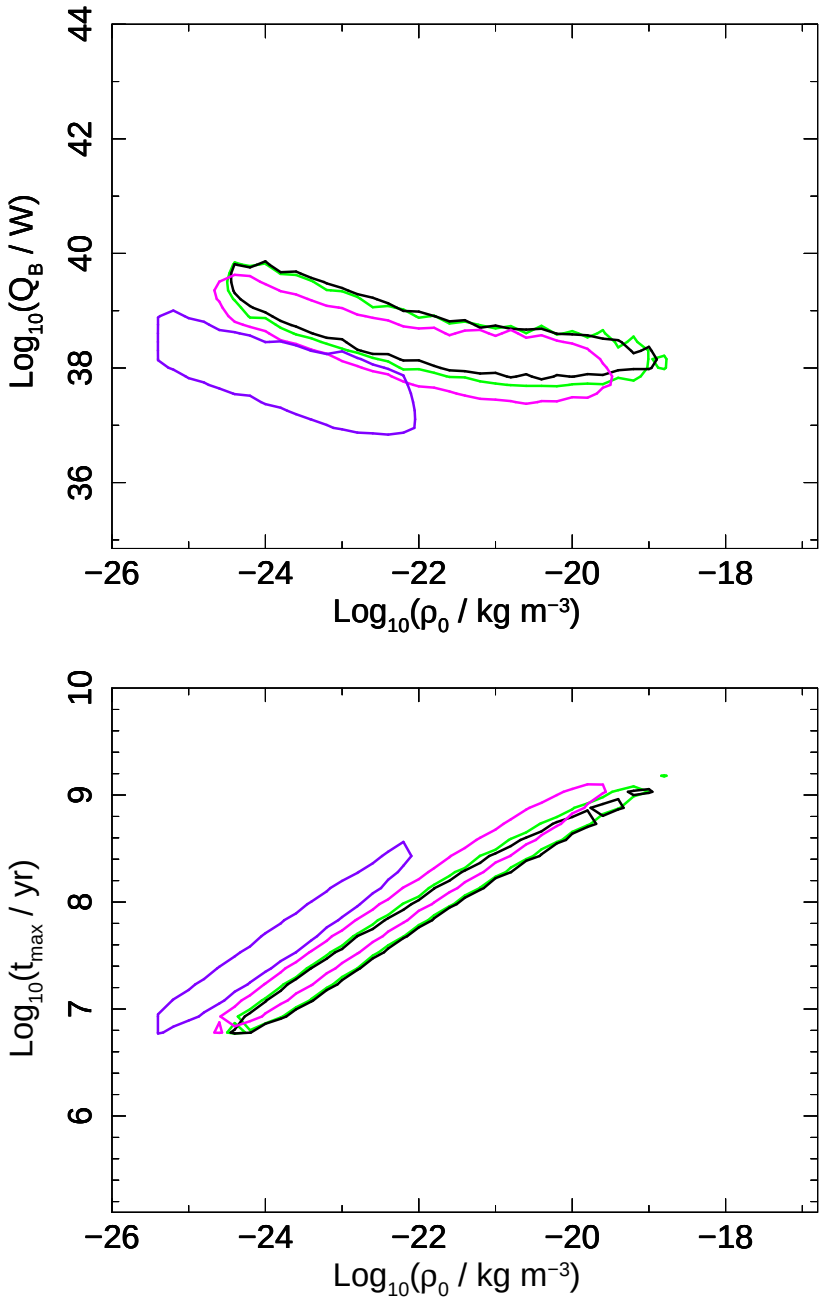

Figure A.7: 90 per cent confidence intervals for populations created with different assumptions on the standard deviation of the density log-normal distribution, where (i) $\gamma_{min} = 1$ and $\gamma_{max} = 10^{10}$ (black), (ii) $\gamma_{min} = 10^2$ and $\gamma_{max} = 10^{10}$ (magenta), (iii) $\gamma_{min} = 10^4$ and $\gamma_{max} = 10^{10}$ (violet), and(iv) $\gamma_{min} = 1$ and $\gamma_{max} = 10^5$ (green). Results shown for redshifts $0 < z_1 < 0.3$, and for Model S as described in Chapter 3. Findings are based on the 3CRR and BRL data fits. The case where the Lorentz factors are set to $\gamma_{min} = 1$ and $\gamma_{max} = 10^{10}$ is the initial, standard case analysed in depth in Chapter 3. The best fits, and goodness-of-fit test results for each case are listed in Table A.4.

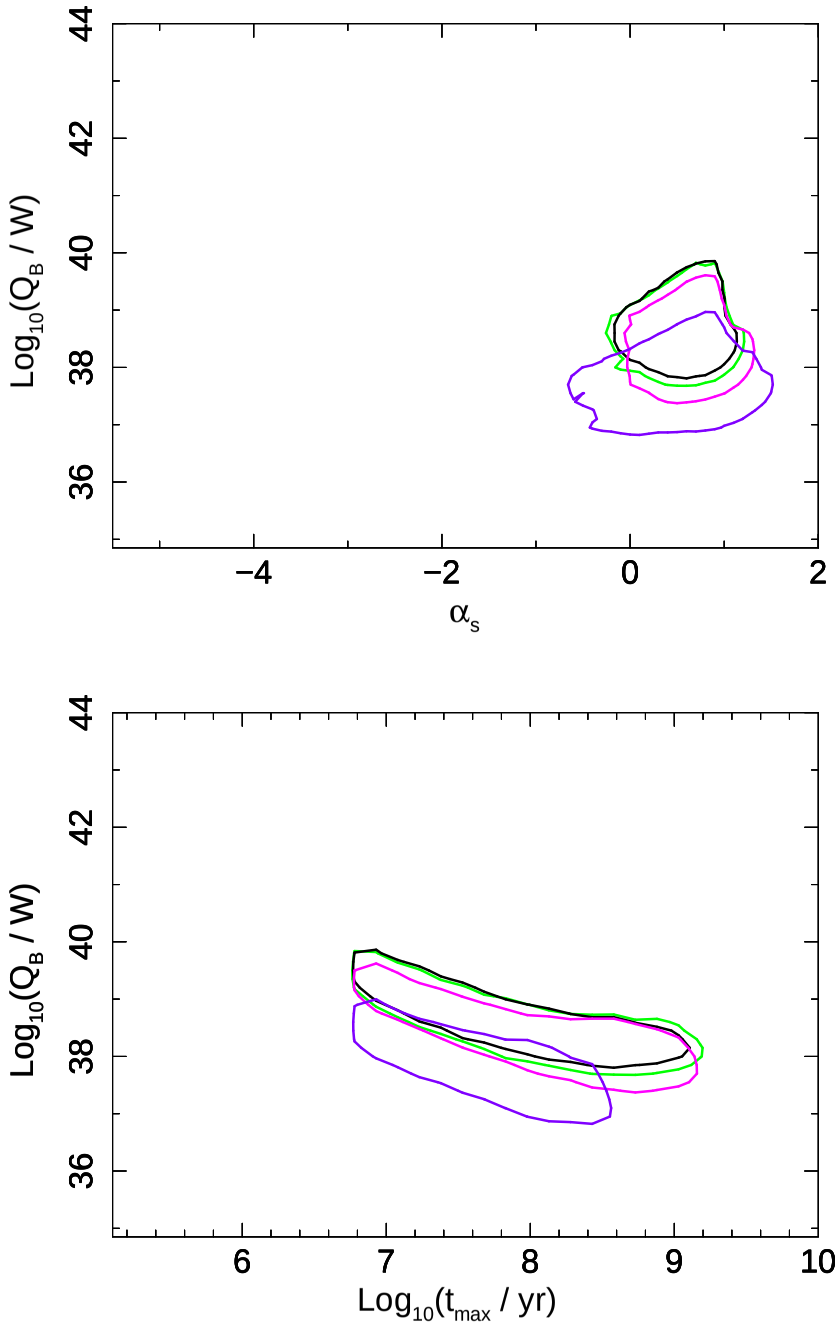

Figure A.7: *continued*

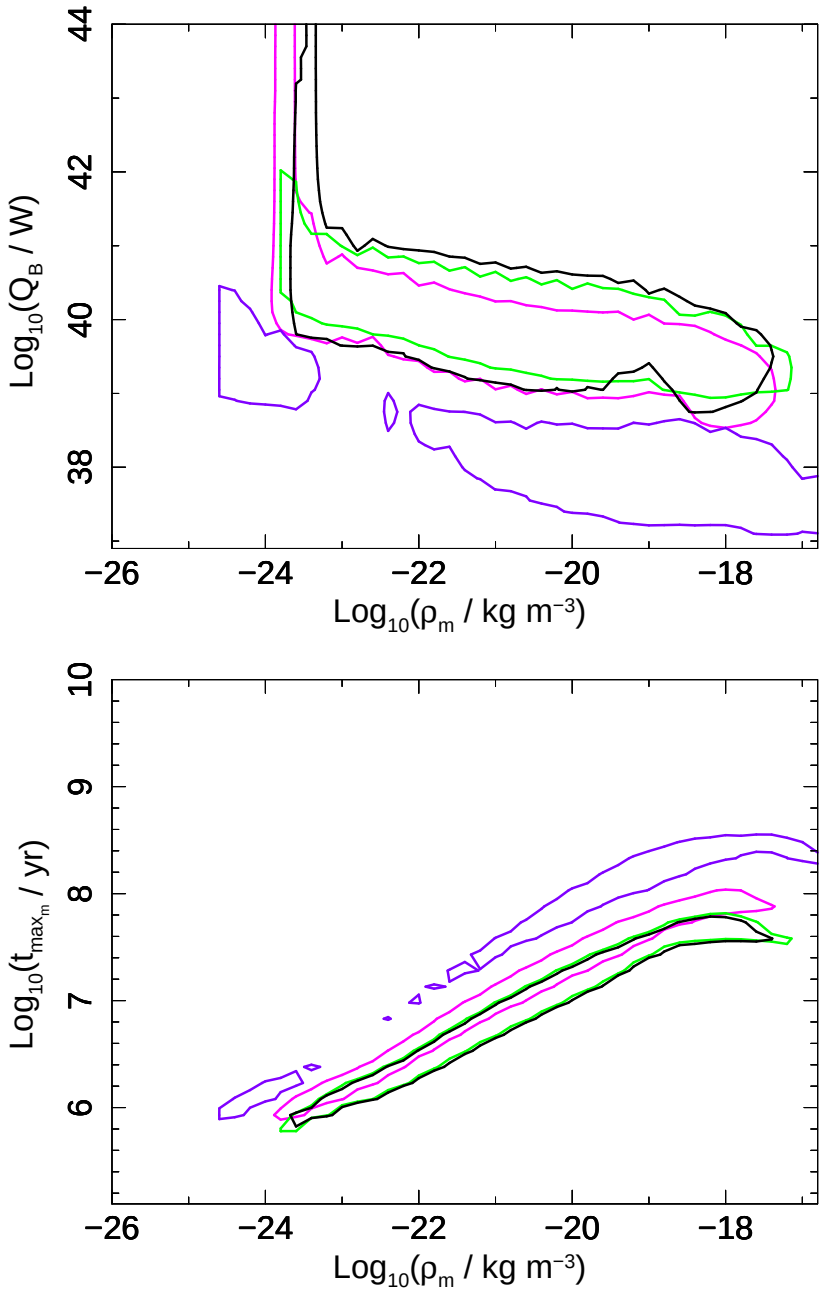

Figure A.8: 90 per cent confidence intervals for populations created with different assumptions on the standard deviation of the density log-normal distribution, where (i) $\gamma_{\rm min} = 1$ and $\gamma_{\rm max} = 10^{10}$ (drawn in black), (ii) $\gamma_{\rm min} = 10^2$ and $\gamma_{\rm max} = 10^{10}$ (magenta), (iii) $\gamma_{\rm min} = 10^4$ and $\gamma_{\rm max} = 10^{10}$ (violet), and(iv) $\gamma_{\rm min} = 1$ and $\gamma_{\rm max} = 10^5$ (green). Results shown for redshifts $0.8 < z_3 < 2.0$, and for Model S as described in Chapter 3. Findings are based on the 3CRR and BRL data fits. The case where the Lorentz factors are set to $\gamma_{\rm min} = 1$ and $\gamma_{\rm max} = 10^{10}$ is the initial, standard case analysed in depth in Chapter 3. The best fits, and goodness-of-fit test results for each case are listed in Table A.4.

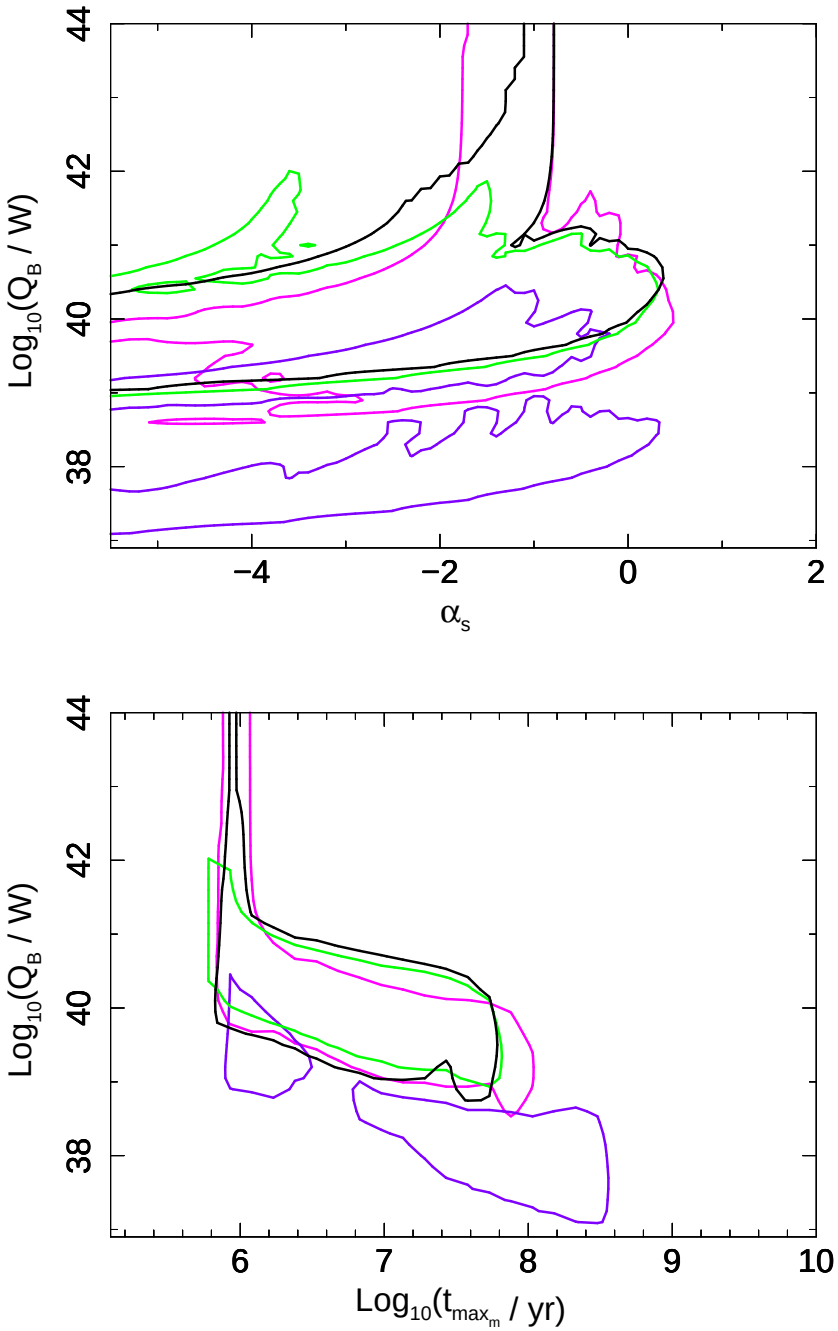

Figure A.8: *continued*

A.5 Particle injection index

In the initial, full simulation run it is assumed that the initial particle injection index m is randomly generated for each source in a population from a uniform distribution of $m \in [2;3]$ (see §2.3.4 and §3.10.4 for discussion). The simulation has been re-run to test the accuracy of this assumption, and the following values of the parameter m have been considered:
(1) $m = 2.3$ (single value for all sources), and
(2) $m_o = 2.4$ and $\sigma_{m_o} = 0.3$ (Gaussian distribution with mean m_o and standard deviation σ_{m_o}, note however that this distribution is taken as valid only between values 2 and 3).

The results are displayed in Fig. A.9 and Fig. A.10, and the best-fitting parameters are listed in Table A.5. Only results for the non-evolving Model S for redshifts $z_1 < 0.3$ and $0.8 < z_3 < 2.0$ are presented. The results are discussed in detail in §3.10.4.

Table A.5: The best-fitting parameters for the non-evolving Model S for two redshift ranges, where $0 < z_1 < 0.3$ and $0.8 < z_3 < 2.0$. For each case the one varying assumption, here the particle injection index, is quoted. Due to occurring degeneracies (discussed in §3.5) one should always consult the corresponding confidence intervals (see Fig. A.9 and Fig. A.10). The following standard deviations of $\log_{10}(\rho_{\rm m})$ and $\log_{10}(t_{\rm max_m})$ log-normal distributions are used: $\log_{10}(\sigma_{\rho_{\rm o}})$ = 0.15 and $\log_{10}(\sigma_{t_{\rm max}})$ = 0.05. 90 per cent errors are quoted.

z	$Q_{\rm B}$ [log(W)]	$\alpha_{\rm s}$	$\rho_{\rm m}$ [log(kg m^{-3})]	$t_{\rm max_m}$ [log(yr)]	$p-$value
initial uniform distribution $m \in [2;3]$					
z_1	$39.15^{+0.30}_{-0.30}$	$0.6^{+0.3}_{-0.6}$	$-23.4^{+0.6}_{-0.4}$	$7.23^{+0.30}_{-0.15}$	0.234
z_3	$39.90^{+0.60}_{-0.45}$	$-1.7^{+1.7}_{-8.3}$	$-20.0^{+2.0}_{-2.8}$	$7.13^{+0.60}_{-1.05}$	0.925
single value $m = 2.3$					
z_1	$39.15^{+0.30}_{-0.15}$	$0.6^{+0.3}_{-0.3}$	$-23.4^{+0.6}_{-0.4}$	$7.23^{+0.30}_{-0.15}$	0.195
z_3	$40.05^{+0.45}_{-0.30}$	$-0.6^{+0.8}_{-2.2}$	$-19.8^{+1.8}_{-2.0}$	$7.28^{+0.45}_{-0.75}$	0.940
Gaussian distribution $m_o = 2.4$, $\sigma_{m_o} = 0.3$					
z_1	$38.85^{+0.30}_{-0.30}$	$0.6^{+0.3}_{-0.6}$	$-22.8^{+1.0}_{-0.6}$	$7.53^{+0.45}_{-0.30}$	0.210
z_3	$42.45^{+0.90}_{-1.80}$	$-3.3^{+0.8}_{-2.3\dagger}$	$-23.8^{+(<0.2)\ddagger}_{-(<0.2)\ddagger}$	$5.78^{+(<0.15)\ddagger}_{-(<0.15)\ddagger}$	0.685

Notes. The resolution of the results is $\Delta\log_{10}(\rho_{\rm o}) = 0.2$, $\Delta\log_{10}(Q_{\rm B}) = 0.15$, $\Delta\log_{10}(t_{\rm max}) = 0.15$, and $\Delta\alpha_{\rm s} = 0.1$.
† For errors which may be extending beyond the searched ranges (see Table 3.2) value up to the range border is quoted.
‡ If errors are smaller than their respective resolution, value of $< \Delta$ is quoted.

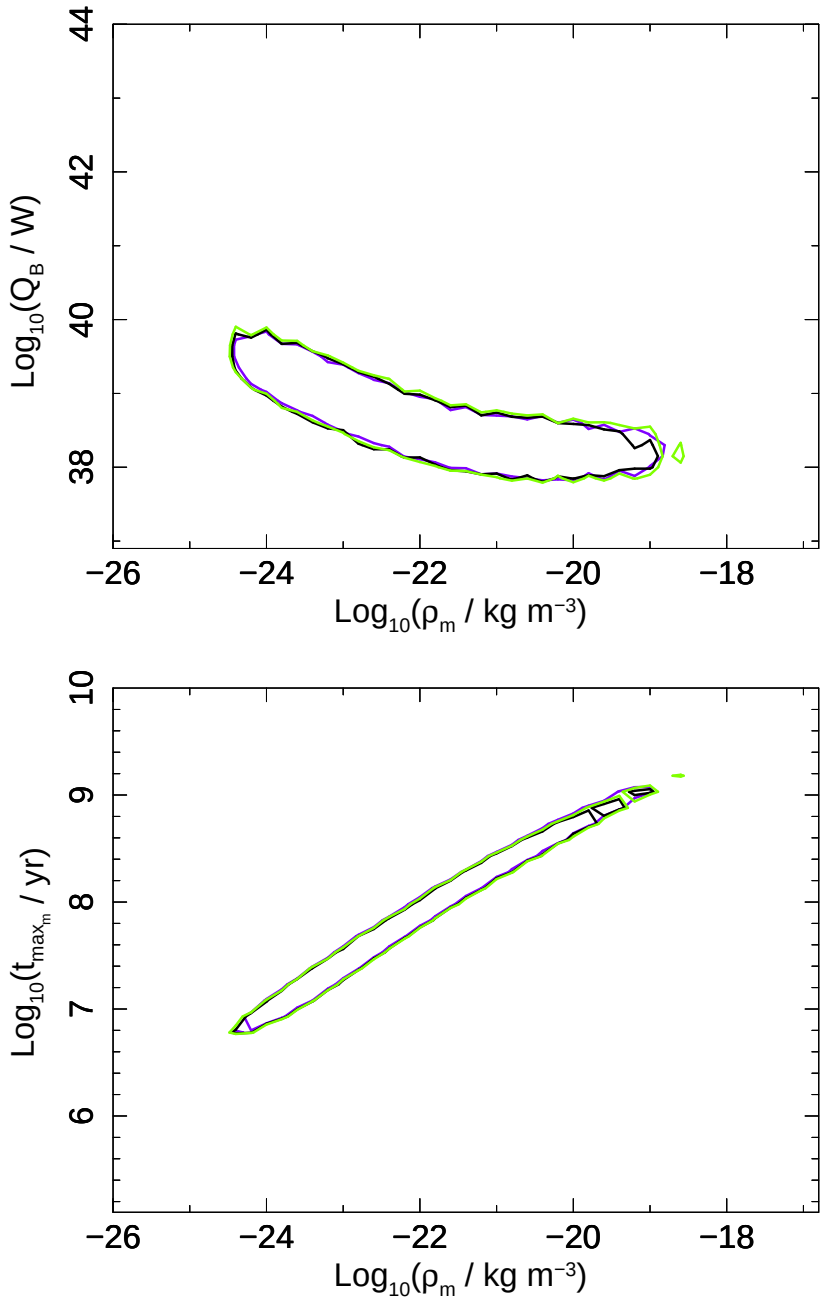

Figure A.9: 90 per cent confidence intervals for populations created with different assumptions on the particle injection index, where (i) $m \in [2;3]$ (uniform distribution, drawn in black), (ii) $m = 2.3$ (single value, violet), and (iii) $m_o = 2.4$ and $\sigma_{m_o} = 0.3$ (green). Results shown for redshifts $0 < z_1 < 0.3$, and for Model S as described in Chapter 3. Findings are based on the 3CRR and BRL data fits. The case where the particle injection index is assumed to be a uniform distribution, the case (i) above, is the initial, standard case analysed in depth in Chapter 3. The best fits, and goodness-of-fit test results for each case are listed in Table A.5

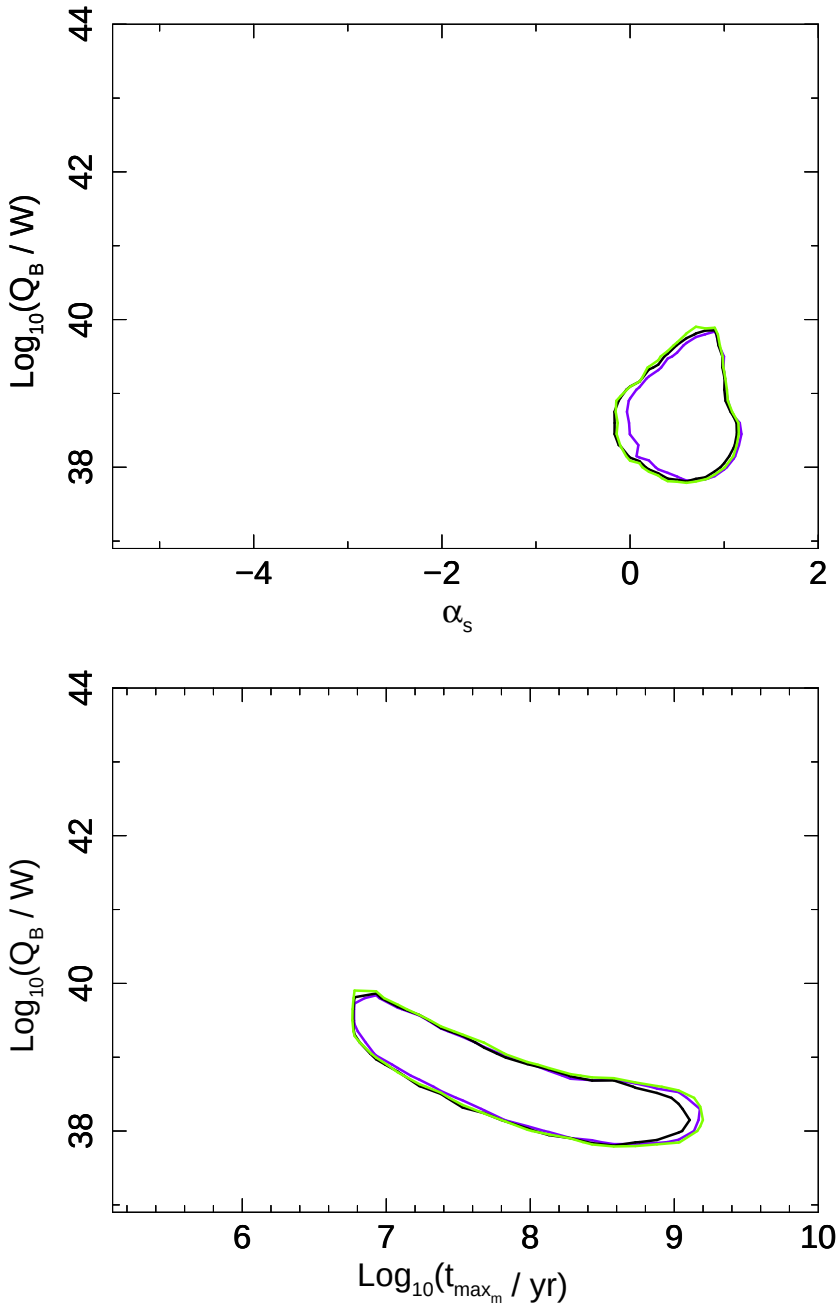

Figure A.9: *continued*

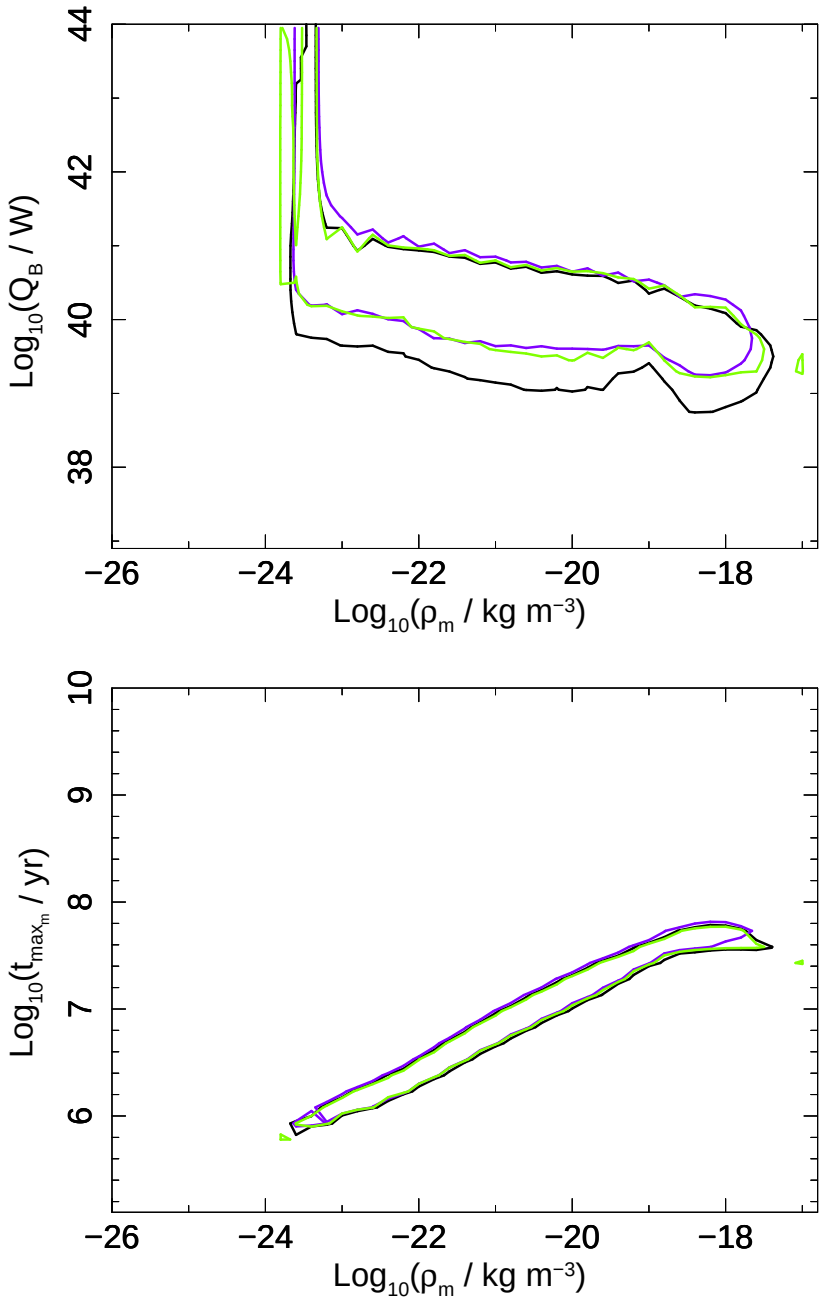

Figure A.10: 90 per cent confidence intervals for populations created with different assumptions on the particle injection index, where (i) $m \in [2;3]$ (uniform distribution, drawn in black), (ii) $m = 2.3$ (single value, violet), and (iii) $m_o = 2.4$ and $\sigma_{m_o} = 0.3$ (green). Results shown for redshifts $0.8 < z_3 < 2.0$, and for Model S as described in Chapter 3. Findings are based on the 3CRR and BRL data fits. The case where the particle injection index is assumed to be a uniform distribution, the case (i) above, is the initial, standard case analysed in depth in Chapter 3. The best fits, and goodness-of-fit test results for each case are listed in Table A.5.

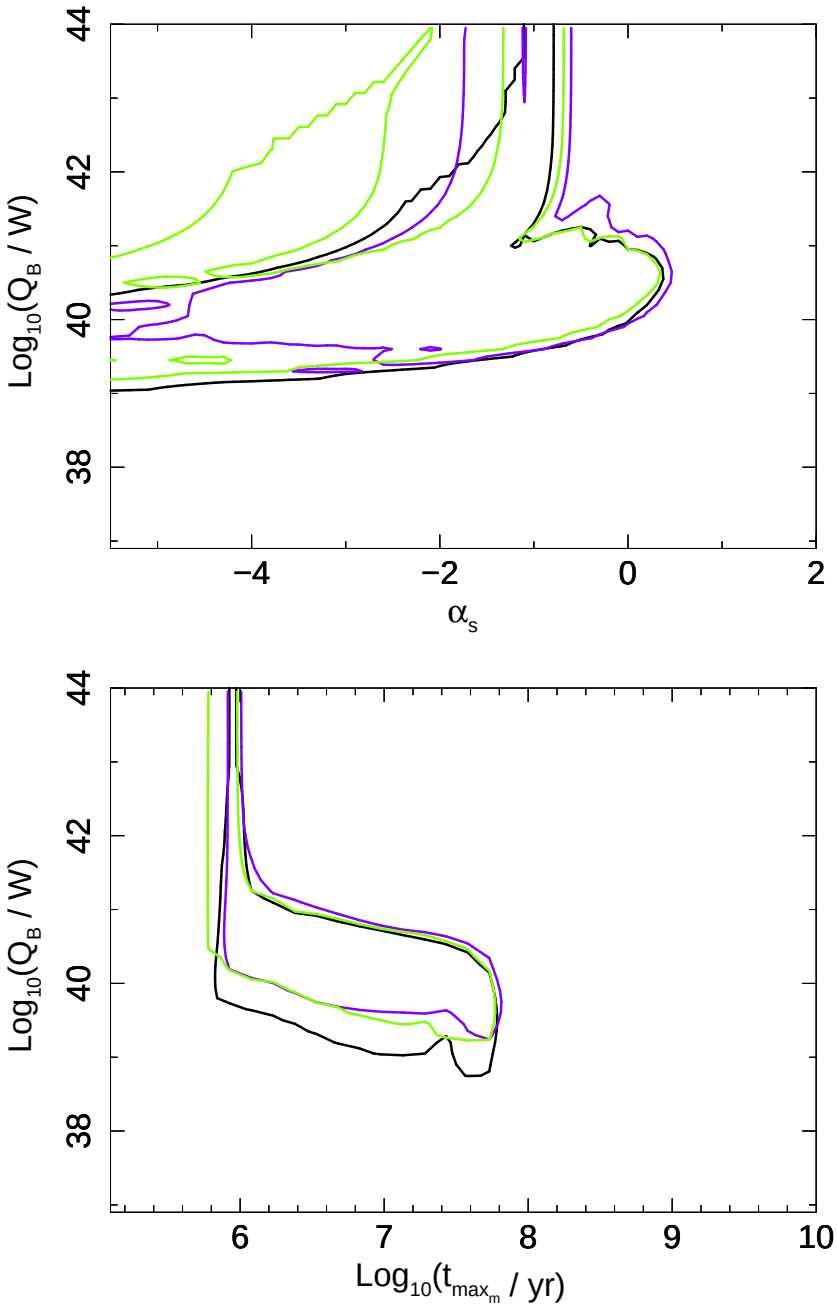

Figure A.10: *continued*

A.6 Population maximum lifetimes distribution

The maximum age of that sources may reach during their lifetime is defined by $t_{\rm max}$. However, in the generation of the whole population of sources it is assumed that the maximum lifetime is not the same for each source, but are rather randomly chosen from log-normal distribution. The standard deviation of this distribution is investigated here.

Initially it is assumed that standard deviation of the log-normal distribution of source maximum ages is $\sigma_{\log_{10}(t_{\rm max})} = 0.05$ (referred to as the 'initial' case). Further, the following cases were tested:
(1) $\sigma_{\log_{10}(t_{\rm max})} = 0.3$, and
(2) $\sigma_{\log_{10}(t_{\rm max})} = 0.6$.

The results are displayed in Fig. A.11 and Fig. A.12, and the best-fitting parameters are listed in Table A.6. Only results for the non-evolving Model S for redshifts $z_1 < 0.3$ and $0.8 < z_3 < 2.0$ are presented. The results are discussed in detail in §3.10.2.

Table A.6: The best-fitting parameters for the non-evolving Model S for two redshift ranges, where $0 < z_1 < 0.3$ and $0.8 < z_3 < 2.0$. For each case the one varying assumption, here the standard deviation of the population maximum ages, is quoted. Due to occurring degeneracies (discussed in §3.5) one should always consult the corresponding confidence intervals (see Fig. A.11 and Fig. A.12). The following standard deviation of $\log_{10}(\rho_{\rm m})$ log-normal distribution is used: $\log_{10}(\sigma_{\rho_{\rm o}}) = 0.15$. 90 per cent errors are quoted.

z	$Q_{\rm B}$ [log(W)]	$\alpha_{\rm s}$	$\rho_{\rm m}$ [log(kg m^{-3})]	$t_{\rm max_m}$ [log(yr)]	$p-$value
initial					
$\sigma_{\log_{10}(t_{\rm max})} = 0.05$					
z_1	$39.15^{+0.30}_{-0.30}$	$0.6^{+0.3}_{-0.6}$	$-23.4^{+0.6}_{-0.4}$	$7.23^{+0.30}_{-0.15}$	0.234
z_3	$39.90^{+0.60}_{-0.45}$	$-1.7^{+1.7}_{-8.3}$	$-20.0^{+2.0}_{-2.8}$	$7.13^{+0.60}_{-1.05}$	0.925
$\sigma_{\log_{10}(t_{\rm max})} = 0.30$					
z_1	$39.15^{+0.30}_{-0.30}$	$0.6^{+0.3}_{-0.5}$	$-23.4^{+1.0}_{-0.6}$	$7.23^{+0.45}_{-0.30}$	0.201
z_3	$40.50^{+0.45}_{-(<0.15)\ddagger}$	$-5.4^{+4.1}_{-0.2\dagger}$	$-23.8^{+1.0}_{-(<0.15)\ddagger}$	$5.33^{+0.75}_{-(<0.15)\ddagger}$	0.801
$\sigma_{\log_{10}(t_{\rm max})} = 0.60$					
z_1	$39.30^{+0.30}_{-0.30}$	$0.6^{+0.3}_{-0.4}$	$-23.6^{+0.4}_{-0.6}$	$7.23^{+0.15}_{-0.45}$	0.073
z_3	$39.60^{+0.45}_{-0.30}$	$-2.5^{+2.0}_{-3.1\ddagger}$	$-17.4^{+(<0.2)\ddagger}_{-(<0.2\ddagger)}$	$6.23^{+0.30}_{-(<0.15\ddagger)}$	0.677

Notes. The resolution of the results is $\Delta\log_{10}(\rho_{\rm o}) = 0.2$, $\Delta\log_{10}(Q_{\rm B}) = 0.15$, $\Delta\log_{10}(t_{\rm max}) = 0.15$, and $\Delta\alpha_{\rm s} = 0.1$.
† For errors which may be extending beyond the searched ranges (see Table 3.2) value up to the range border is quoted.
‡ If errors are smaller than their respective resolution, value of $< \Delta$ is quoted.

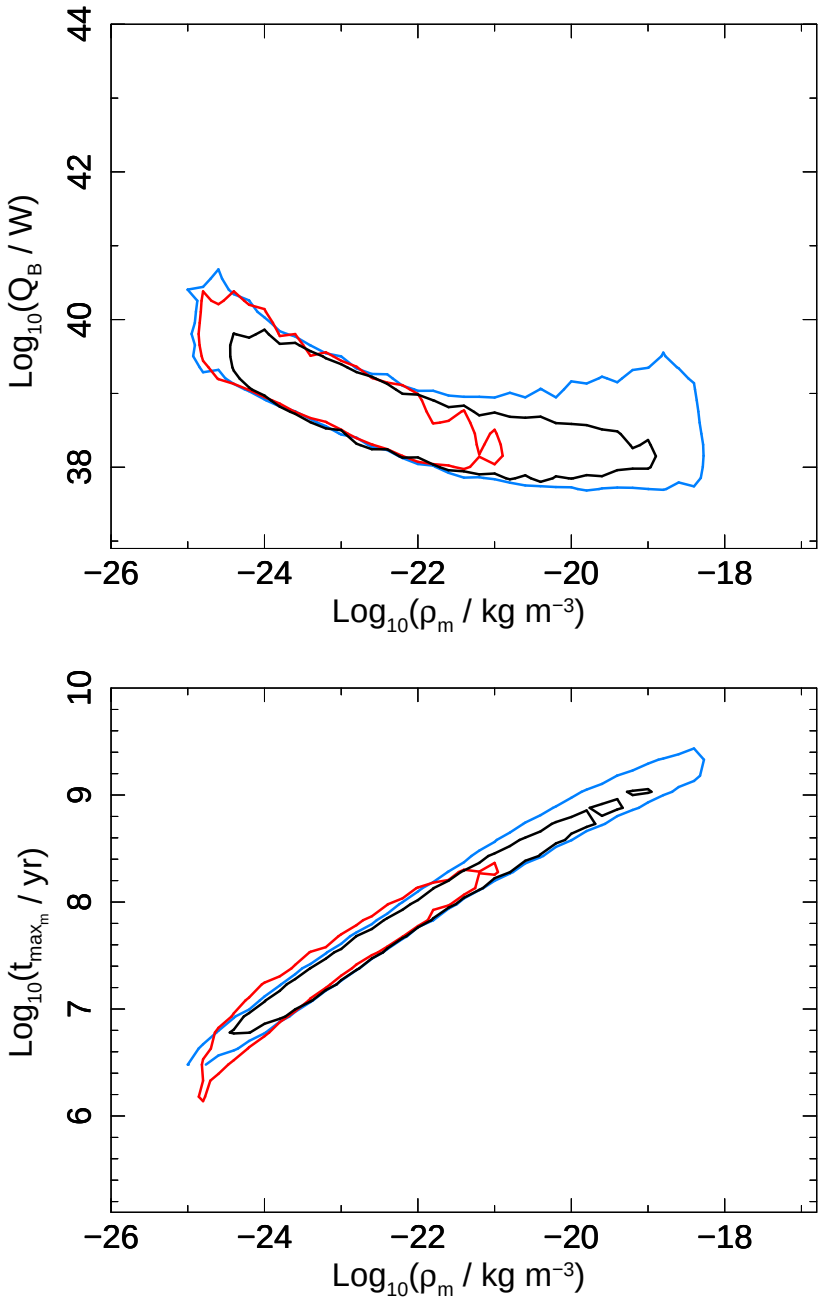

Figure A.11: 90 per cent confidence intervals for populations created with different assumptions on the standard deviation of the log-normal maximum lifetimes distribution of the sources, where $\sigma_{\log_{10}(t_{max})} = 0.05$ (black), $\sigma_{\log_{10}(t_{max})} = 0.3$ (yellow), and $\sigma_{\log_{10}(t_{max})} = 0.6$ (red). Results shown for redshifts $0 < z_1 < 0.3$, and for Model S as described in Chapter 3. Findings are based on the 3CRR and BRL data fits. The case where the standard deviation is equal to $\sigma_{\log_{10}(t_{max})} = 0.05$ is the initial, standard case analysed in depth in Chapter 3. The best fits, and goodness-of-fit test results for each case are listed in Table A.6.

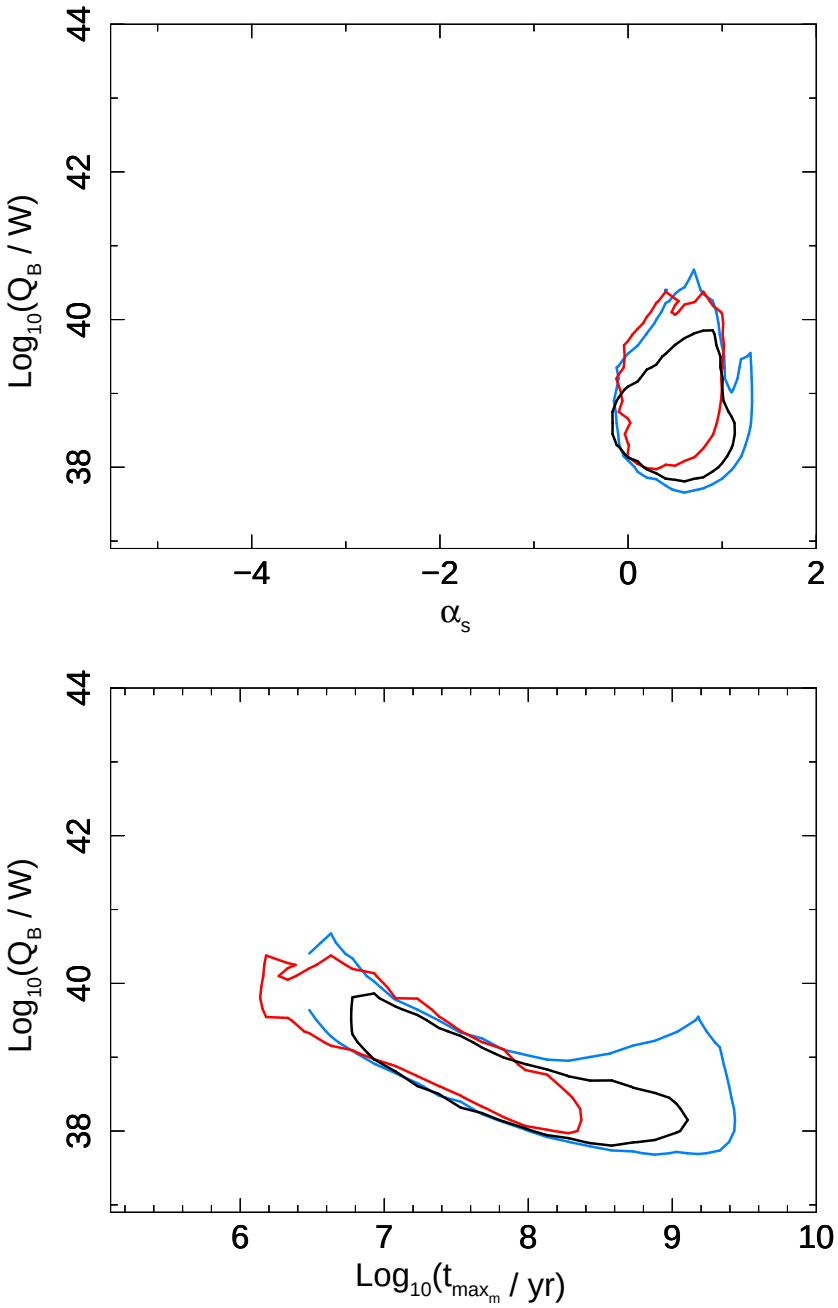

Figure A.11: *continued.*

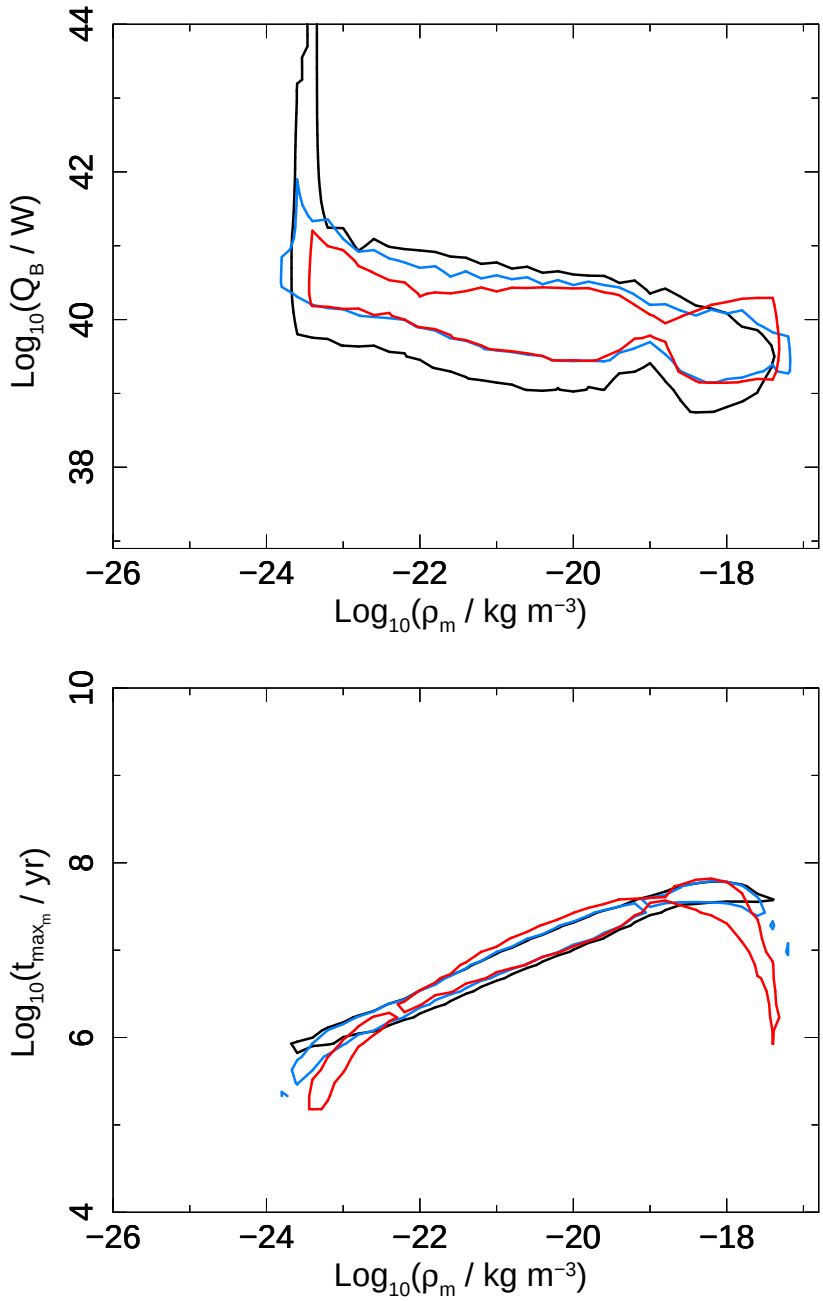

Figure A.12: 90 per cent confidence intervals for populations created with different assumptions on the standard deviation of the log-normal maximum lifetimes distribution of the sources, where $\sigma_{\log_{10}(t_{max})} = 0.05$ (black), $\sigma_{\log_{10}(t_{max})} = 0.3$ (yellow), and $\sigma_{\log_{10}(t_{max})} = 0.6$ (red). Results shown for redshifts $0.8 < z_3 < 2.0$, and for Model S as described in Chapter 3. Findings are based on the 3CRR and BRL data fits. The case where the standard deviation is equal to $\sigma_{\log_{10}(t_{max})} = 0.05$ is the initial, standard case analysed in depth in Chapter 3. The best fits, and goodness-of-fit test results for each case are listed in Table A.6.

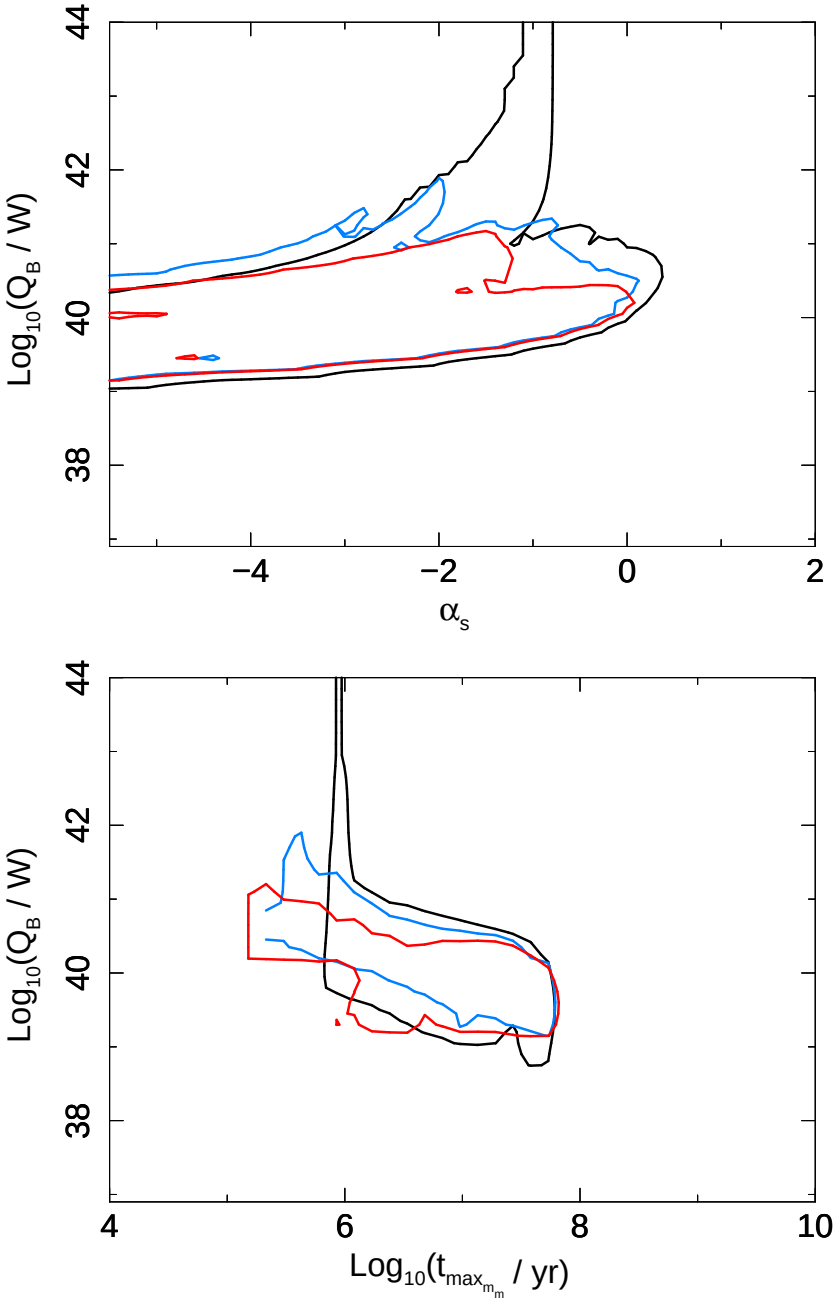

Figure A.12: *continued.*

A.7 A special case: combination of the minimum Lorentz factor values and the case of heavy jets

It is initially assumed that the minimum Lorentz factor is $\gamma_{\rm min} = 1$, and the maximum is $\gamma_{\rm max} = 10^{10}$, and that the jets are lightweight, that is contain only electrons and positrons ($k' = 0$). Subsequently to the discussion in Chapter 2 and Chapter 3, the following combinations of the Lorentz factors and the possible particle content of the outflow were tested:
(i) $k' \in (0, 100)$, $\gamma_{\rm min} = 10^2$ and $\gamma_{\rm max} = 10^{10}$,
(ii) $k' = 100$, $\gamma_{\rm min} = 10^2$ and $\gamma_{\rm max} = 10^{10}$,
(iii) $k' \in (0, 100)$, $\gamma_{\rm min} = 10^4$ and $\gamma_{\rm max} = 10^{10}$,
(iv) $k' = 100$, $\gamma_{\rm min} = 10^4$ and $\gamma_{\rm max} = 10^{10}$.

The results are displayed in Fig. A.13 and Fig. A.14, and the best-fitting parameters are listed in Table A.4. Only results for the non-evolving Model S for redshifts $z_1 < 0.3$ and $0.8 < z_3 < 2.0$ are presented. The results are discussed in detail in §3.10.5.

Table A.7: The best-fitting parameters for the non-evolving Model S for two redshift ranges, where $0 < z_1 < 0.3$ and $0.8 < z_3 < 2.0$. For each case the one varying assumption, here the standard deviation of the population maximum ages, is quoted. Due to occurring degeneracies (discussed in §3.5) one should always consult the corresponding confidence intervals (see Fig. A.11 and Fig. A.12). The following standard deviations of $\log_{10}(\rho_{\rm m})$ and $\log_{10}(t_{\max_{\rm m}})$ log-normal distributions are used: $\log_{10}(\sigma_{\rho_{\rm o}}) = 0.15$ and $\log_{10}(\sigma_{t_{\max}}) = 0.05$. 90 per cent errors are quoted.

z	$Q_{\rm B}$ [log(W)]	$\alpha_{\rm s}$	$\rho_{\rm m}$ [log(kg m^{-3})]	$t_{\max_{\rm m}}$ [log(yr)]	$p-$value
initial					
$\gamma_{\rm min} = 1, k' = 0$					
z_1	$39.15^{+0.30}_{-0.30}$	$0.6^{+0.3}_{-0.6}$	$-23.4^{+0.6}_{-0.4}$	$7.23^{+0.30}_{-0.15}$	0.234
z_3	$39.90^{+0.60}_{-0.45}$	$-1.7^{+1.7}_{-8.3}$	$-20.0^{+2.0}_{-2.8}$	$7.13^{+0.60}_{-1.05}$	0.925
$\gamma_{\rm min} = 10^2, k' \in (0,100)$					
z_1	$38.85^{+0.45}_{-0.45}$	$-0.3^{+1.0}_{-1.6\dagger}$	$-23.0^{+1.4}_{-0.8}$	$7.38^{+0.60}_{-0.45}$	0.390
z_3	$40.65^{+0.45}_{-0.45}$	$-1.1^{+0.8}_{-2.5}$	$-17.2^{+(<0.2\ddagger)}_{-(<0.2\ddagger)}$	$7.13^{+(<0.15\ddagger)}_{-(<0.15\ddagger)}$	0.824
$\gamma_{\rm min} = 10^2, k' = 100$					
z_1	$40.05^{+0.30}_{-0.30}$	$0.6^{+0.3}_{-0.5}$	$-22.6^{+0.6}_{-0.6}$	$7.23^{+0.30}_{-0.15}$	0.240
z_3	$41.55^{+0.6}_{-0.45}$	$-1.5^{+1.6}_{-2.7}$	$-22.2^{+2.8}_{-0.2}$	$6.08^{+0.9}_{-(<0.15)\ddagger}$	0.970
$\gamma_{\rm min} = 10^4, k' \in (0,100)$					
z_1	$37.80^{+0.9}_{-0.15}$	$-5.0^{+5.7\dagger}_{-0.6\dagger}$	$-24.6^{+2.6}_{-(<0.2)\ddagger}$	$7.08^{+1.2}_{-(<0.15)\ddagger}$	0.312
z_3	$38.85^{+1.2}_{-0.45}$	$-2.9^{+3.2}_{-2.7\dagger}$	$-18.2^{+0.8}_{-3.4}$	$7.88^{+0.15}_{-0.90}$	0.901

..continued on page 232.

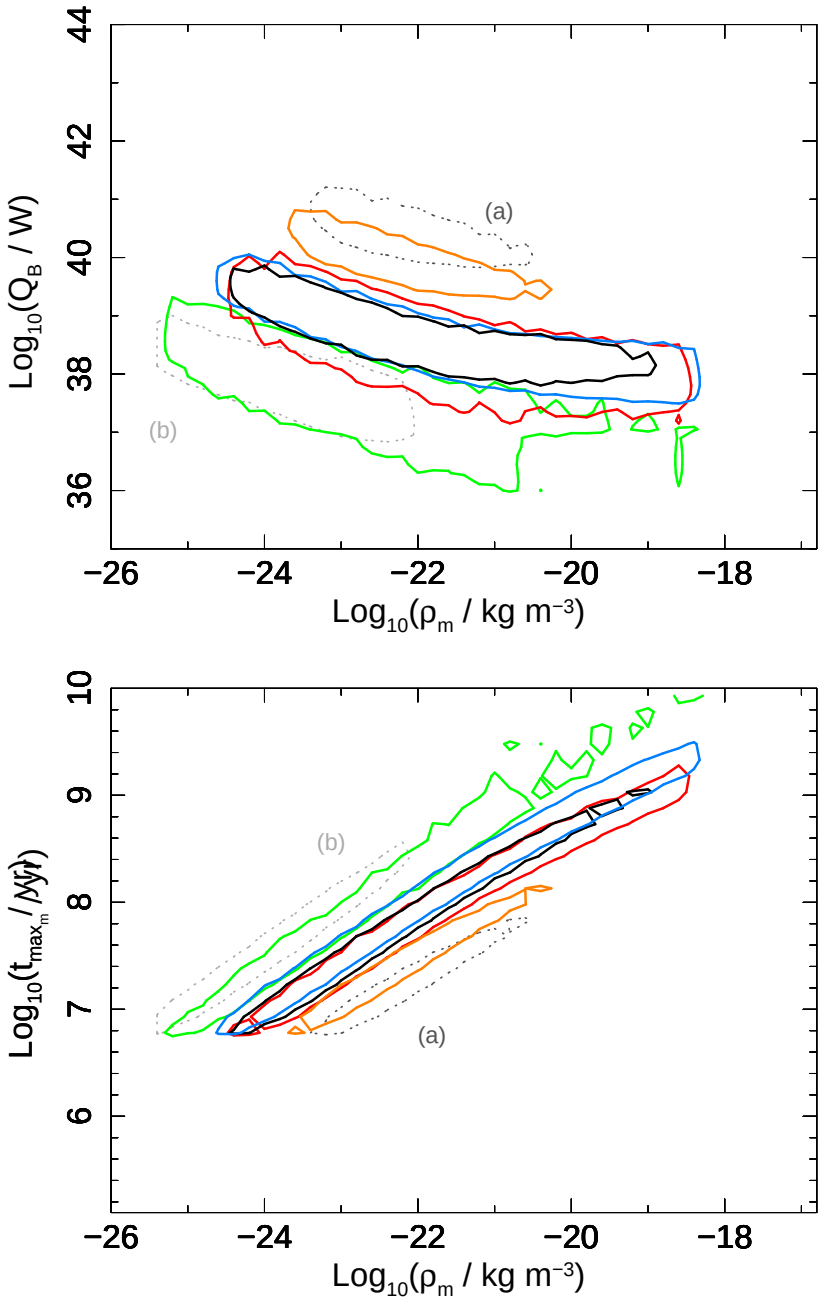

Figure A.13: 90 per cent joint confidence intervals for radio galaxy populations created with various assumptions on the minimum energy of the initial particle distribution and the particle content of the jet. The following cases are plotted: (i) $k' = 0$, $\gamma_{\rm min} = 1$ and $\gamma_{\rm max} = 10^{10}$ (solid, black, the default case), (ii) $k' \in (0,100)$, $\gamma_{\rm min} = 10^2$ and $\gamma_{\rm max} = 10^{10}$ (solid, red), (ii) $k' = 100$, $\gamma_{\rm min} = 10^2$ and $\gamma_{\rm max} = 10^{10}$ (solid, orange), (iv) $k' \in (0,100)$, $\gamma_{\rm min} = 10^4$ and $\gamma_{\rm max} = 10^{10}$ (solid, green), and (v) $k' = 100$, $\gamma_{\rm min} = 10^4$ and $\gamma_{\rm max} = 10^{10}$ (solid, blue). For reference plotted are the cases where (a) $k' = 100$, $\gamma_{\rm min} = 1$ and $\gamma_{\rm max} = 10^{10}$ (dotted, dark grey, see also Figure A.7), and (b) $k' = 0$, $\gamma_{\rm min} = 10^4$ and $\gamma_{\rm max} = 10^{10}$ (dotted, light grey, see also Figure A.9). Results shown for redshifts $0 < z_1 < 0.3$, and for Model S as described in Chapter 3. Findings are based on the 3CRR and BRL data fits. The best fits, and goodness-of-fit test results for each case are listed in Table A.7.

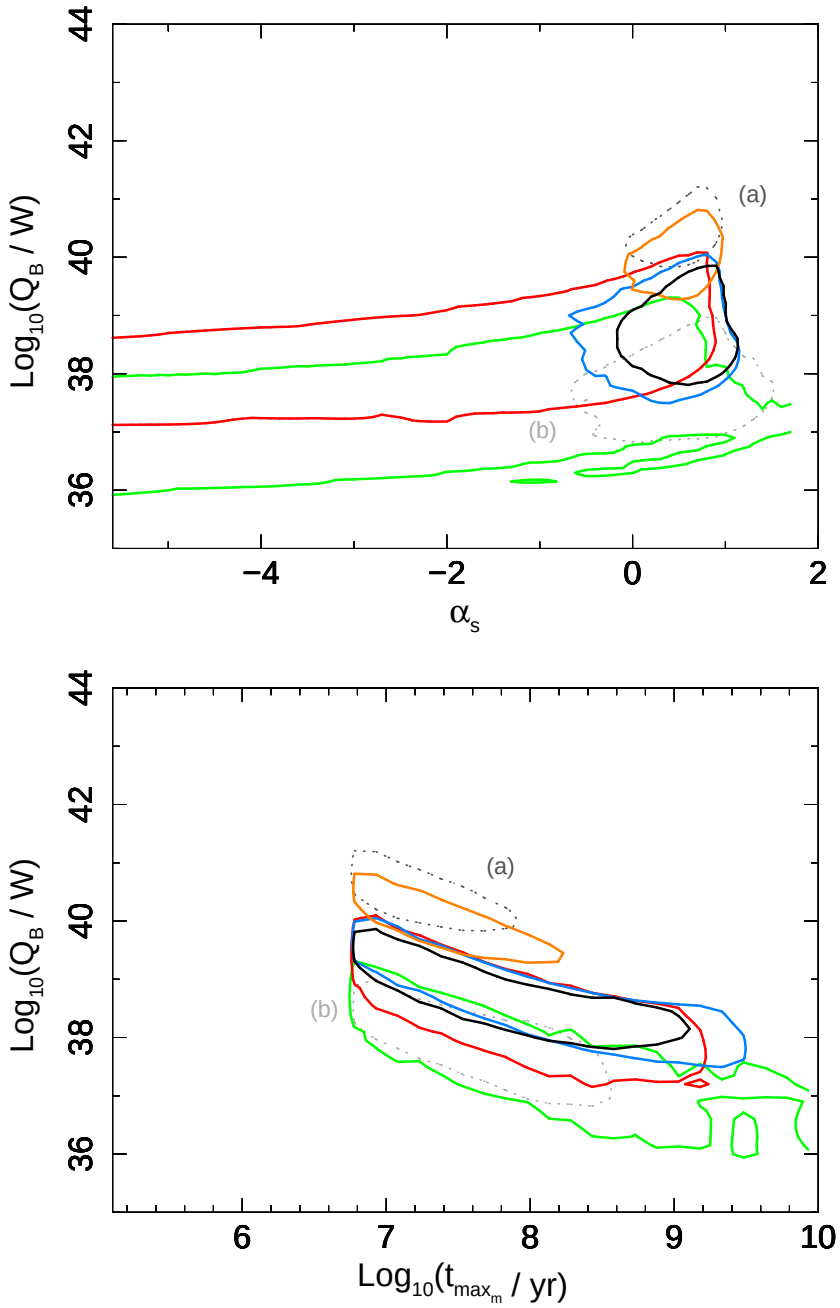

Figure A.13: *continued.*

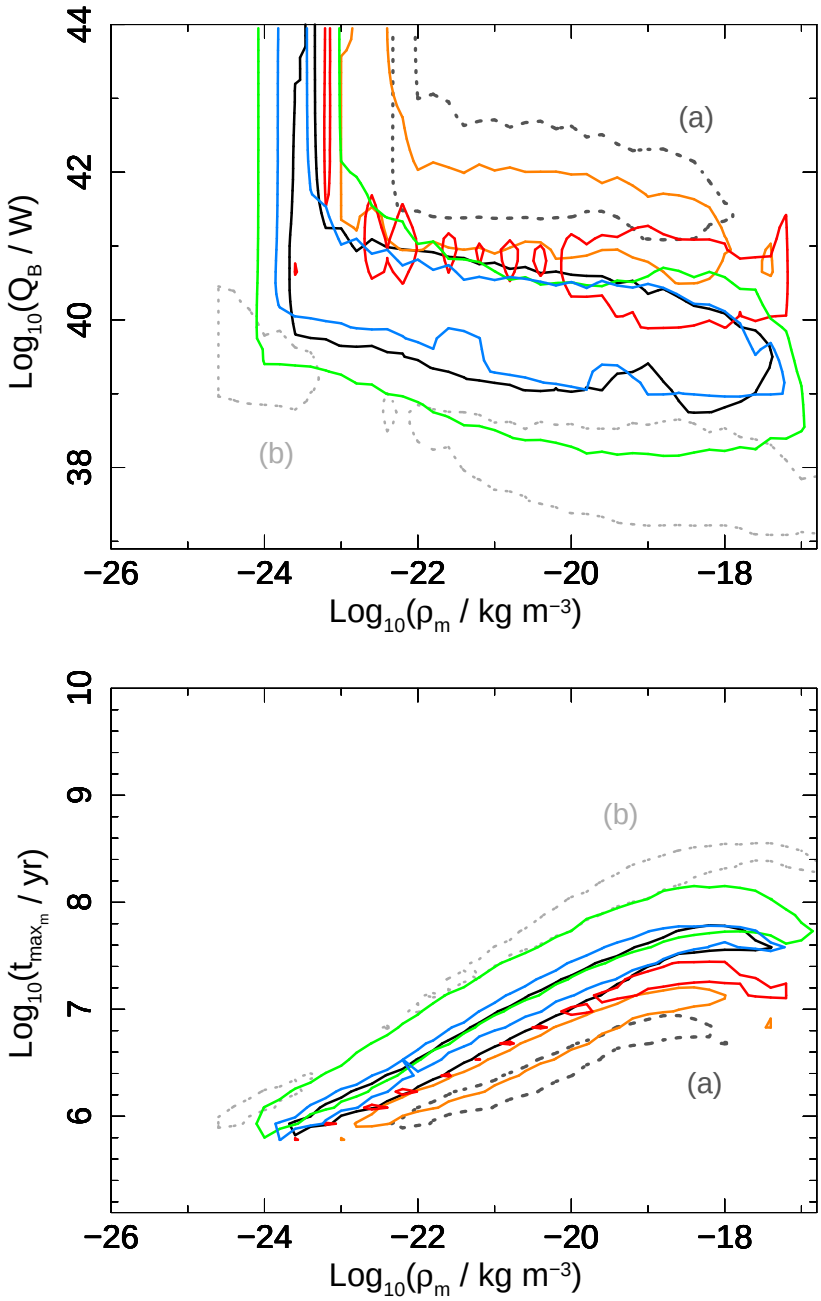

Figure A.14: 90 per cent joint confidence intervals for radio galaxy populations created with various assumptions on the minimum energy of the initial particle distribution and the particle content of the jet. The following cases are plotted: (i) $k' = 0$, $\gamma_{\rm min} = 1$ and $\gamma_{\rm max} = 10^{10}$ (solid, black, the default case), (ii) $k' \in (0,100)$, $\gamma_{\rm min} = 10^2$ and $\gamma_{\rm max} = 10^{10}$ (solid, red), (ii) $k' = 100$, $\gamma_{\rm min} = 10^2$ and $\gamma_{\rm max} = 10^{10}$ (solid, orange), (iv) $k' \in (0,100)$, $\gamma_{\rm min} = 10^4$ and $\gamma_{\rm max} = 10^{10}$ (solid, green), and (v) $k' = 100$, $\gamma_{\rm min} = 10^4$ and $\gamma_{\rm max} = 10^{10}$ (solid, blue). For reference plotted are the cases where (a) $k' = 100$, $\gamma_{\rm min} = 1$ and $\gamma_{\rm max} = 10^{10}$ (dotted, dark grey, see also Figure A.8), and (b) $k' = 0$, $\gamma_{\rm min} = 10^4$ and $\gamma_{\rm max} = 10^{10}$ (dotted, light grey, see also Figure A.10). Results shown for redshifts $0.8 < z_3 < 2.0$, and for Model S as described in Chapter 3. Findings are based on the 3CRR and BRL data fits. The best fits, and goodness-of-fit test results for each case are listed in Table A.7.

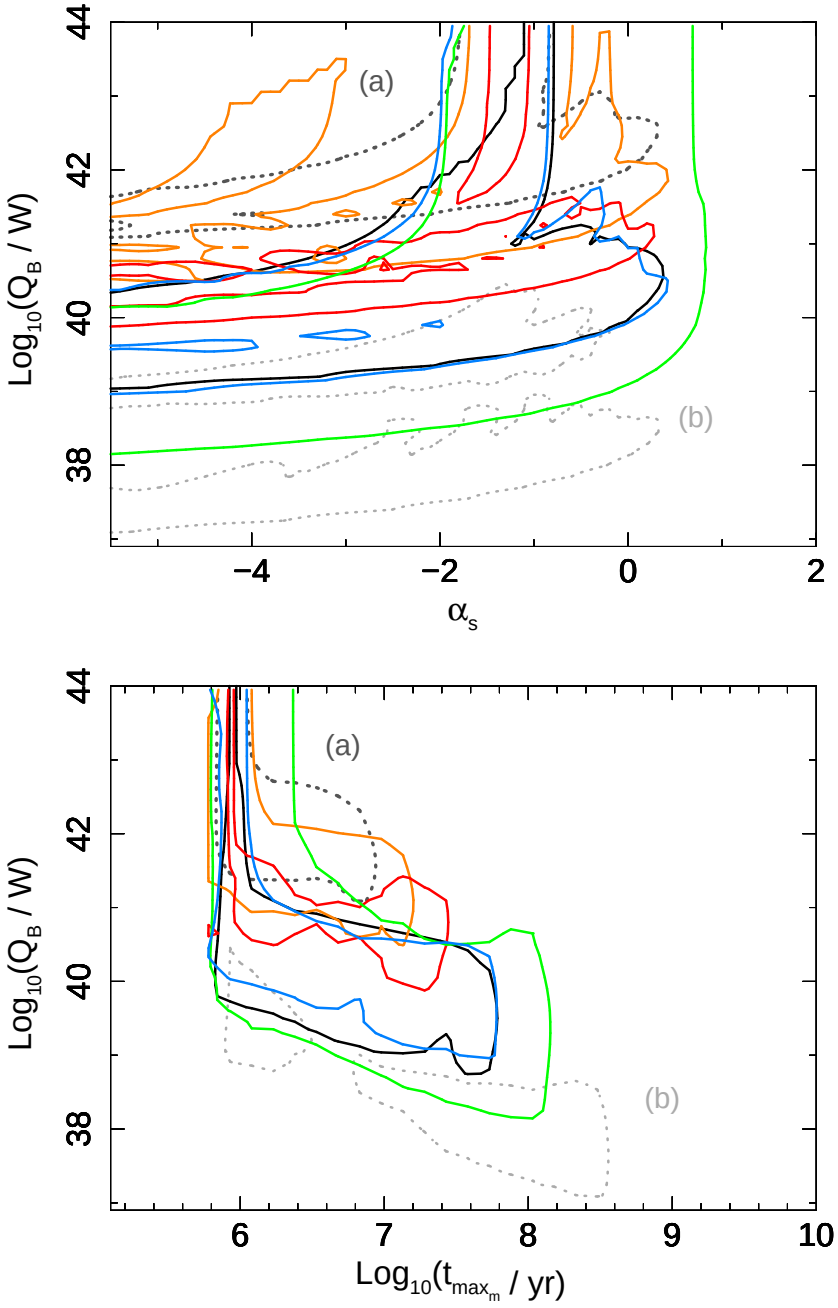

Figure A.14: *continued.*

Table A.8: *Continued*.

z	Q_{B} [log(W)]	α_{s}	ρ_{m} [log(kg m^{-3})]	$t_{\mathrm{max_m}}$ [log(yr)]	$p-$value
$\gamma_{\mathrm{min}} = 10^4$, $k' = 100$					
z_1	$39.3^{+0.30}_{-0.30}$	$0.4^{+0.4}_{-0.7}$	$-23.8^{+0.6}_{-0.4}$	$7.08^{+0.30}_{-0.15}$	0.288
z_3	$40.20^{+1.35}_{-(<0.15)\ddagger}$	$-5.4^{+5.5}_{-0.2\dagger}$	$-23.6^{+4.0}_{-(<0.2\ddagger)}$	$5.93^{+1.5}_{-(<0.15\ddagger)}$	0.867

Notes. The resolution of the results is $\Delta\log_{10}(\rho_{\mathrm{o}}) = 0.2$, $\Delta\log_{10}(\mathrm{Q_B}) = 0.15$, $\Delta\log_{10}(\mathrm{t_{max}})$ =0.15, and $\Delta\alpha_{\mathrm{s}} = 0.1$.
† For errors which may be extending beyond the searched ranges (see Table 3.2) value up to the range border is quoted.
‡ If errors are smaller than their respective resolution, value of $< \Delta$ is quoted.

B

Multicomponent Sources in the WENSS Catalogue

The following appendix contains a list of multicomponent sources which were attempted to be matched to the SDSS-FIRST-NVSS sample and were mislabelled in the WENSS catalogue. For details see §4.3.2 in Chapter 4.

Table B.1: Multicomponent sources in the WENSS survey catalogue. Column 6 (*Comm.*) gives information whether the sources have been marked as multicomponent source (M) in the WENSS catalogue, or a single source (S). A 'match' means that a radio galaxy from Best et al. FR II sub-sample has been matched to a particular component(s) or single source(s). 'Yes/No' indicates whether the multicomponent or single source label has been applied correctly in the WENSS survey catalogue, or whether not. Only these sources which are erroneously labelled as multicomponent in the WENSS catalogue and which have been attempted to be matched to the Best et al. FR II sub-sample are listed. The quoted redshifts are taken from the Best et al. FR II sub-sample. For details see §4.3.2 in Chapter 4.

Source name (based on B1950 coordinates)	Redshift (z)	RA (J2000) [WENSS]	Dec (J2000) [WENSS]	Flux density [mJy]	*Comm.*
WNB1523.0+2951		15 25 07.01	+29 40 31.2		M, Yes†
WNB1523.0+2951A	0.1114	15 25 05.06	+29 40 59.3	124	match
WNB1523.0+2951B	0.1114	15 25 07.55	+29 39 36.1	121	match
WNB1523.0+2951C		15 25 11.37	+29 41 48.4	54	
WNB0836.9+2959		08 40 01.71	+29 48 58.9		M, No
WNB0836.9+2959A		08 40 00.63	+29 49 47.2	280	
WNB0836.9+2959B	0.0648	08 40 01.77	+29 48 54.5	1790	match
WNB1512.0+3021		15 14 06.28	+30 10 26.4		M, No
WNB1512.0+3021A	0.0932	15 14 04.06	+30 08 50.5	215	match
WNB1512.0+3021B		15 14 08.44	+30 11 58.7	210	
WNB1428.0+3059		14 30 12.1	+30 45 56.1		M, No
WNB1428.0+3059A	0.1292	14 30 10.5	+30 44 31.0	110	match
WNB1428.0+3059B		14 30 13.0	+30 46 44.3	161	
WNB1510.1+3101	0.0896	15 12 12.06	+30 50 22.6	82	S, No – match
WNB1509.9+3101	0.0896	15 11 58.85	+30 50 17.0	106	S, No – match
WNB0828.3+3229		08 31 27.40	+32 19 29.9		M, Yes†
WNB0828.3+3229A	0.0512	08 31 22.08	+32 18 43.7	2543	match
WNB0828.3+3229B		08 31 22.66	+32 23 49.5	280	
WNB0828.3+3229C	0.0512	08 31 34.79	+32 20 26.4	2039	match
WNB0828.3+3229D		08 31 46.66	+32 19 19.8	34	

continued on next page

Table B.1: *Continued.*

Source name (based on B1950 coordinates)	Redshift (z)	RA (J2000) [WENSS]	Dec (J2000) [WENSS]	Flux density [mJy]	*Comm.*
WNB1309.5+4114		13 11 46.82	+40 58 51.2		M, Yes†
WNB1309.5+4114A	0.1103	13 11 42.00	+40 56 26.8	610	match
WNB1309.5+4114B	0.1103	13 11 43.95	+41 00 11.9	465	match
WNB1309.5+4114C		13 11 44.05	+41 01 42.2	518	
WNB1309.5+4114D		13 12 01.35	+40 57 08.1	392	
WNB0912.6+4140		09 15 49.83	+41 28 24.6		M, No
WNB0912.6+4140A		09 15 44.42	+41 27 59.2	436	
WNB0912.6+4140B	0.1510	09 15 57.89	+41 29 02.6	300	match
WNB0827.7+4157		08 31 09.15	+41 47 15.1		M, Yes†
WNB0827.7+4157A	0.1320	08 31 01.82	+41 47 54.5	170	match
WNB0827.7+4157B		08 31 03.04	+41 45 16.1	50	
WNB0827.7+4157C	0.1320	08 31 13.19	+41 47 09.6	323	match
WNB1513.1+4212		15 14 55.09	+42 01 03.3		M, No
WNB1513.1+4212A	0.1349	15 14 53.91	+42 00 48.1	616	match
WNB1513.1+4212B		15 15 04.00	+42 02 58.7		
WNB1015.4+4624		10 18 31.45	+46 09 02.2		M, Yes†
WNB1015.4+4624A	0.1654	10 18 24.84	+46 09 01.3	69	match
WNB1015.4+4624B	0.1654	10 18 37.35	+46 09 21.4	56	match
WNB1015.4+4624C		10 18 38.49	+46 07 57.3	19	
WNB0926.2+4639		09 29 30.27	+46 26 03.0		M, Yes†
WNB0926.2+4639A		09 29 24.96	+46 24 48.0	44	
WNB0926.2+4639B	0.1679	09 29 30.15	+46 26 01.7	24	match
WNB0926.2+4639C	0.1679	09 29 35.84	+46 27 31.0	29	match
WNB0823.7+4645		08 27 17.03	+46 35 40.9		M, Yes†
WNB0823.7+4645A		08 27 06.42	+46 36 14.8	31	
WNB0823.7+4645B	0.1249	08 27 12.82	+46 35 25.9	121	match
WNB0823.7+4645C	0.1249	08 27 22.20	+46 35 46.9	130	match
WNB1023.2+5444		10 26 24.54	+54 29 11.7		M, No
WNB1023.2+5444A		10 26 24.50	+54 29 08.6	609	match
WNB1023.2+5444B		10 26 26.71	+54 31 06.7	31	

continued on next page

Table B.1: *Continued.*

Source name (based on B1950 coordinates)	Redshift (z)	RA (J2000) [WENSS]	Dec (J2000) [WENSS]	Flux density [mJy]	*Comm.*
WNB1043.4+5451		10 46 31.76	+54 36 02.3		M, Yes†
WNB1043.4+5451A	0.1447	10 46 22.01	+54 37 46.8	166	match
WNB1043.4+5451B	0.1447	10 46 25.75	+54 37 07.8	292	match
WNB1043.4+5451C		10 46 31.59	+54 33 02.9	31	
WNB1043.4+5451D	0.1447	10 46 39.39	+54 34 45.0	417	match
WNB1333.1+5858		13 35 00.67	+58 43 02.7		M, No
WNB1333.1+5858A	0.1567	13 34 51.73	+58 41 21.5	33	
WNB1333.1+5858B		13 35 00.78	+58 43 04.4	1277	match
WNB1218.4+6356		12 20 48.66	+63 39 59.9		M, Yes†
WNB1218.4+6356A	0.1875	12 20 26.59	+63 42 56.0	391	match
WNB1218.4+6356B	0.1875	12 20 47.39	+63 40 40.6	125	match
WNB1218.4+6356C	0.1875	12 20 53.77	+63 40 25.8	258	match
WNB1218.4+6356D		12 21 03.58	+63 37 19.4	481	
WNB1713.0+6407		17 13 23.5	+64 03 47.3		M, No
WNB1713.0+6407A		17 13 06.7	+64 06 43.8	216	
WNB1713.0+6407B	0.0784	17 13 29.2	+64 02 51.2	602	match

Notes. † A multicomponent source, but too many components declared. Some of the components may be separate sources.

C

Fourier Transform and its Application to Radio Interferometry

---

Radio interferometry has been born in 1940s, when difficulty in reaching high resolutions of radio observations while using only single dish telescopes lead to development of technique called aperture synthesis. In this appendix I briefly outline the mathematical foundations of the Fourier transformations which the technique of aperture synthesis is based on. I also briefly highlight the relationships between the observing radio frequencies, interferometer configurations, radio source models and the resolution. The following discussion is based predominantly on Bracewell (1979), Taylor et al. *(1999) and Sasao and Fletcher (2005).*

C.1 Mathematical foundations

The Fourier transform originates in the generalisation of the so-called Fourier series, which, studied by Joseph Fourier in 19th century, is an expression of a periodic function $f(x)$ represented in terms of summation (integration) of simple sine and cosine functions. The Fourier series of a function $f(x)$ is given by

$$f(x) = \frac{a_{n=0}}{2} + \sum_{n=1}^{\infty} a_n \cos(nx) + \sum_{n=1}^{\infty} b_n \sin(nx), \tag{C.1}$$

where the terms a_n and b_n, the Fourier sine and cosine coefficients, are defined such that $a_n = \pi^{-1} \int_{-\pi}^{\pi} f(x) \cos(nx)\, \mathrm{d}x$ and $b_n = \pi^{-1} \int_{-\pi}^{\pi} f(x) \sin(nx)\, \mathrm{d}x$.

For simplification reasons and to allow for inclusion of complex coefficients, the Euler's formula given by

$$e^{2\pi i\theta} = \cos(2\pi\theta) + i\sin(2\pi\theta) \tag{C.2}$$

is often used to express the Fourier series and the Fourier transform. Hence, in general terms, the Fourier transform, $F(\xi)$, of the periodic function $f(x) \in \mathbb{R}$, where $x \in (-\infty, \infty)$, is defined as follows

$$F(\xi) = \int_{-\infty}^{\infty} f(x) e^{-2\pi i \xi x} \mathrm{d}x, \tag{C.3}$$

and its inverse is given by

$$f(x) = \int_{-\infty}^{\infty} F(\xi) e^{2\pi i \xi x} \mathrm{d}\xi. \tag{C.4}$$

One must bear in mind that through the use of the Euler's formula the Fourier coefficients become of complex type. The Fourier transform allows one to covert function of x into a function of ξ, whatever the two parameters represent. Examples of the Fourier transform applications are discussed in the next section.

To present how the Fourier transform works, below I consider two examples: the Fourier transform of a delta function and of a Gaussian function. These examinations will be further referred to in the discussion of §C.2.1.

Delta function. The Dirac's delta function ($\delta(x)$, $\delta-$function) for any $x \in \mathbb{R}$ is defined such that

$$\delta(x) = \begin{cases} +\infty & \text{for } x = 0 \\ 0 & \text{for } x \neq 0, \end{cases} \tag{C.5}$$

and the following is also satisfied

$$\int_{-\infty}^{\infty} \delta(x)\mathrm{d}x = 1. \tag{C.6}$$

Formally the function is a distribution or a measure rather than a mathematical function. In signal processing the delta function is referred to as the impulse symbol, while in image processing it represents the ideal point source.

The Fourier transform of the $\delta-$function is well defined and is given by

$$F(\xi) = \int_{-\infty}^{\infty} e^{-2\pi i\xi x}\delta(x)\mathrm{d}x = 1. \tag{C.7}$$

Hence the resulting spectrum of this special function is uniform and independent of the ξ parameter.

Gaussian function. For any $a, \mu, \sigma \in \mathbb{N}$, the Gaussian function is given by

$$g(x) = ae^{-\frac{(x-\mu)^2}{2\sigma^2}}. \tag{C.8}$$

The Fourier transform of such general Gaussian function, $G(\xi)$, can be easily derived, as it is presented below.

$$\begin{aligned} G(\xi) &= \int_{-\infty}^{\infty} g(x)e^{-2\pi i\xi x}\mathrm{d}x && \text{(C.9)} \\ &= a\int_{-\infty}^{\infty} e^{-\frac{(x-\mu)^2}{2\sigma^2}} e^{-2\pi i\xi x}\mathrm{d}x && \text{(C.10)} \\ &= a\int_{-\infty}^{\infty} e^{-\left(\frac{x-\mu}{\sqrt{2}\sigma}+\sqrt{2}\pi i\xi\sigma\right)^2} e^{\sqrt{2}\pi i\xi\mu-2(\pi\xi\sigma)^2}\mathrm{d}x && \text{(C.11)} \end{aligned}$$

Changing the differential from dx to dz, where $z = \left(\frac{x-\mu}{2\sigma} + \sqrt{2}\pi i\xi\sigma\right)$, one gets $\mathrm{d}x = 2\sigma\mathrm{d}z$, and thus the transform becomes

$$\begin{aligned} G(\xi) &= 2\sigma a e^{\sqrt{2}\pi i\xi\mu-2(\pi\xi\sigma)^2}\int_{-\infty}^{\infty} e^{-z^2}\mathrm{d}z && \text{(C.12)} \\ &= 2\sqrt{\pi}\sigma a e^{\sqrt{2}\pi i\xi\mu-2(\pi\xi\sigma)^2}. && \text{(C.13)} \end{aligned}$$

That is, for a Gaussian function of a form $g(x) = e^{-x^2/\sigma^2}$, where $a = 1$ and $\mu = 0$, its Fourier transform will be $G(\xi) = \sqrt{\pi}\sigma e^{-\pi^2\xi^2\sigma^2}$. The Fourier transform of a Gaussian function is another Gaussian function but with width parameter different from the original by $1/(\sigma\sqrt{\pi})$. Examples of this particular transform are plotted in Figure C.1 along the discussion of §C.2.1 on the implications of using this transform in radio interferometry.

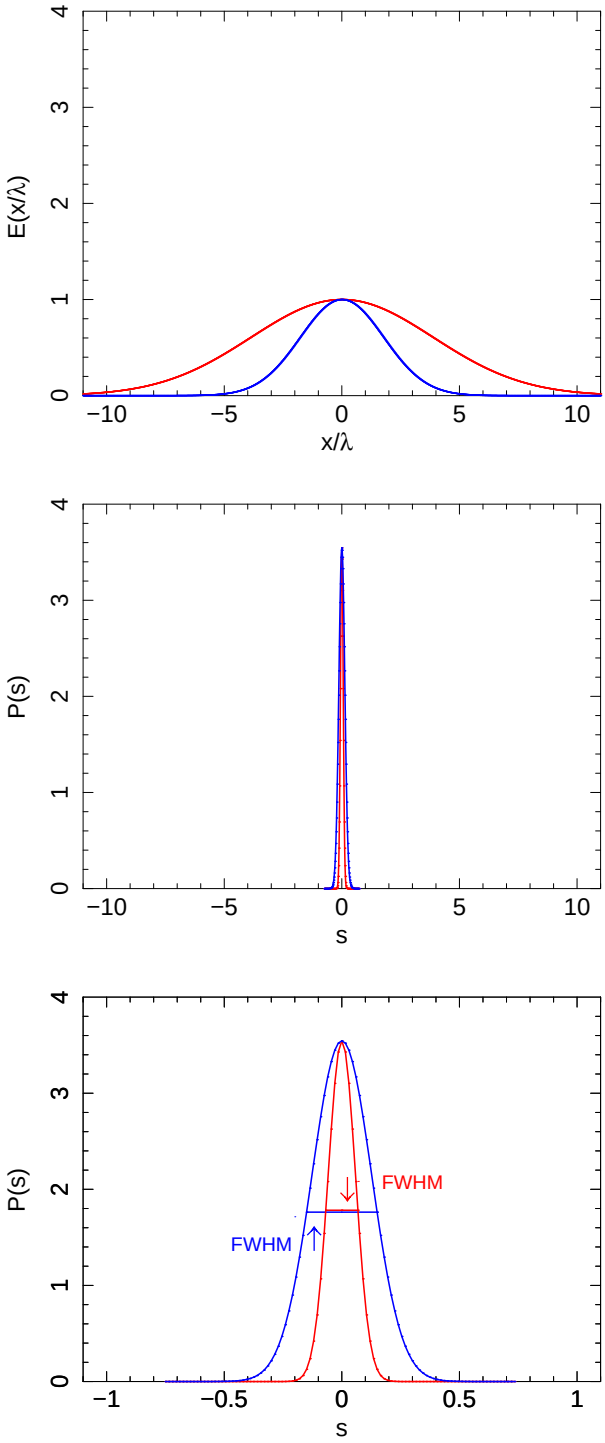

Figure C.1: Two sample Gaussian aperture field distributions (*top*) and their Fourier transforms (*middle*). The two Gaussian distributions differ only in their assumed variance σ^2, where $\sigma^2_{\rm red} > \sigma^2_{\rm blue}$, and for both cases $a = 1$ and $\mu = 0$ (Eqn. C.8). The resolution is then defined as the full width at half maximum power of the resulting beam, that is the Fourier transformed distributions (*bottom*), and will be different for each of the analysed here Gaussians. Note that the *bottom* panel is the same as the *middle* one, but replotted to allow for more detailed investigation. Note, that only amplitudes are plotted and the sidelobe problem is ignored in this example.

C.2 Application to radio interferometry

In signal processing the Fourier transform is defined in terms of time (t) and frequency (ν) domain (the time-frequency analysis), that is $x = t$ and $\xi = \nu$. For a signal $f(t)$ sampled over a given time interval its Fourier transformed representation is known as the frequency spectrum (or power spectrum). The complex form of the Fourier coefficients is interpreted here as an amplitude of the wave (cosines, $\Re[F(\nu)]$) and its phase (sines, $\Im[F(\nu)]$).

Below I focus specifically on the image processing, often referred to as the synthesis imaging or the aperture synthesis, which is directly applied to radio interferometry.

C.2.1 Image processing

Image processing is a part of a subset of large family of signal processing applications. Once the radio signal has been recorded, and the data is collected from the radio telescopes, ideally one would like to image the observations. In this special case again the Fourier transform is used. In the conventional notation of Fourier transform of signal processing one transforms the waveform $F(t)$ measured at times t_i into the frequency spectrum $f(\nu)$ over the frequencies ν_i. The Fourier transform works analogically for the case of radio antennae, where the aperture field distribution $E(x/\lambda)$ measured over the aperture distances $(x/\lambda)_i$ (in units of wavelengths) is transformed into the so-called field radiation pattern $P(s)$ measured over the direction sine $s = \sin(\Theta)$.

The Fourier transform of an aperture distribution $E(x/\lambda)$ is of the following form

$$E(x/\lambda) = P(s)e^{2\pi ixs/\lambda}, \tag{C.14}$$

where s is a direction function, and specifically $s = \sin\Theta$. Θ is interpreted as the angle at which a radio source is observed (see also Chapter 1: §1.4) and, unlike in the case of the conventional frequency domain of the Fourier transform, is periodic over the interval $T_\theta \in [0, 2\pi]$. The amplitude component of the resulting distribution is constant over the whole aperture; however, the phase changes. Two examples of such Fourier transforms are shown in Figure C.1. The aperture field distribution is arbitrarily chosen to be Gaussian, and the two examples differ only in their assumed variance σ^2, where specifically $\sigma^2_{\rm red} > \sigma^2_{\rm blue}$ in Figure C.1. The Fourier transforms of the two distributions will be Gaussian distributions but much narrower than the original functions. As already shown in the derivation of the Fourier transform for a Gaussian function, if the aperture dimensions are scaled up/down (e.g. by introducing $x = ax_{\rm a1}$) while no change to the aperture distribution pattern is done ($E(ax_{\rm a1}/\lambda)$), then the field radiation pattern is compressed by the magnitude of that scaling factor ($P(s/a)/|a|$). Clearly, the wider the aperture the narrower the beam. (Note, that only amplitudes are plotted and I ignored the sidelobe problems in this example). The resolution ($\theta_{\rm res}$) of the interferometer is then defined as the full width at half maximum (FWHM) power of the resulting beam, and is marked in the bottom panel of Figure C.1.

The response of radio interferometer is a convolution of the beam (power/radiation pattern) with the signal recorder from the radio source. The measurements of the radio interferometer are then traced on the (u,v) plane, which is the measured visibility domain (see Chapter 1: §1.4 for brief discussion on measuring the visibilities by radio interferometers and the coordinate systems used). Radio imaging is at this point an inverse process, where the distribution of measured visibilities is known and one wants to find the true sky brightness. One of the techniques used in this inverse problem for a single source at the phase centre is model fitting[1] where, given the visibility distribution, one attempts to fit to it a parametric model of the sky brightness distribution (intensity distribution). Let us consider two of such model components, a point source, which is represented by a delta function, and an extended radio source that can be fitted with a symmetric Gaussian. If such a model component is centred at the origin of the (l,m) plane and is a function of $\sqrt{l^2+m^2}$, its Fourier transform will be measured on the (u,v) plane as a function of $\sqrt{u^2+v^2}$. For a point source, its Fourier transform will be constant, and so independent of the u,v distance (§C.1). However, in the case of the extended source which can be fitted with a Gaussian, the amplitude of the visibility function (the Fourier transformed model distribution) will depend on the u,v distance, that is the interferometer baseline. This effect causes that for the longest baselines of the interferometer array, the visibility amplitudes of the considered source will be significantly weaker as compared to the shortest baselines of the array, and the source may be resolved out if its angular size is larger than the visibility spacing which is given by $\lambda/D_{\text{baseline}}\sin(\Theta)$ (refer also to Chapter 1: §1.4).

Two outcomes of the above discussion should be highlighted here. Firstly, for the same interferometer observing at the same radio frequencies but at different configurations (which will lead to different maximum baselines) the resulting resolution of the final radio images will be different. Secondly, if two sets of observations are performed at two different frequencies, but allowing for different maximum baseline in each case so that the resolutions of their respective final radio images will be similar, the flux densities of their observed radio sources must be corrected as some of the flux density at one of these frequencies may be missed (resolved out). The latter issue is particularly relevant to the work done in Chapter 4, where samples from two radio surveys have been matched together (the NVSS and WENSS surveys)

[1]Note however, that for problems more complex than a single source field, typically a range of deconvolution techniques is used. These techniques include for example CLEAN deconvolution procedure (Högbom, 1974) and its modifications (e.g. Clark, 1980; Schwab, 1984), maximum entropy method (MEM; Cornwell and Evans, 1985; Narayan and Nityananda, 1986), as well as recently developed adaptive scale pixel (ASP) algorithm (Bhatnagar and Cornwell, 2004).

D

Maximum Likelihood Method

Cash (1979) showed that using the popular χ^2 minimisation estimator to find the best fitting parameters of a model is erroneous if dealing with sparse binned data; the method required at least 10 data counts in each considered bin. In this study one often must deal with empty data bins and hence the standard χ^2 method is not applicable. In this appendix I introduce the basics of the method of maximum likelihood estimation, and present a derivation of its form for Poisson distributed data. The derivation is trivial and can be easily reproduced (consult relevant textbooks). The maximum likelihood method (MLM) is considered to be robust, and is applicable to most models and different types of data.

D.1 The principles of Maximum Likelihood Estimator

Let x be a variable, a sample of N observations, coming from an unknown probability density function $f_o(x)$. However, $f_o(x)$ is part of a parametric family of distributions $f(x|\theta)$, and $\theta \in \Theta$, so that $f_o(x) = f(x|\theta_o)$, and Θ denotes the set of all allowed values for the considered parameter (here θ). A parametric families of distributions, by definition, can be described with a finite number of constant parameters (which are to be estimated) denoted as an m-dimensional parameter $\theta = (\theta_1, \theta_2, ..., \theta_m)$. Then θ_o is the unknown 'true value' of the parameter, and the aim is, by varying θ, to find the maximum likelihood estimator (MLE) θ_{mle} which is going to be as close to the true value as possible.

The joint density function for all observations is

$$f(x_1, x_2, ..., x_N|\theta) = f(x_1|\theta) \times f(x_2|\theta) \times ... \times f(x_N|\theta). \tag{D.1}$$

If, at this point, observations x are considered to be 'fixed', the parameter θ is the one to be estimated. It is done by allowing θ to vary freely in order to maximise the product in Eqn. (D.1). Hence the likelihood function is given by

$$\mathcal{L} = \mathcal{L}(\theta|x) = \prod_{i=1}^{N} f(x_i|\theta), \qquad i = 1, 2, ...N. \tag{D.2}$$

Often the maximum likelihood method is used in its logarithmic form, where

$$\ln(\mathcal{L}) = \ln[\mathcal{L}(\theta|x)] = \sum_{i=1}^{N} f(x_i|\theta), \qquad i = 1, 2, ...N, \tag{D.3}$$

and is referred to as the log-likelihood.

The MLE is found by finding θ that maximises $\mathcal{L}$ or $\ln(\mathcal{L})$, that is

$$\theta_{\text{mle}} = \arg\max[\mathcal{L}(\theta|x_1, ..., x_N)] \tag{D.4}$$

or

$$\theta_{\text{mle}} = \arg\max\{\ln[\mathcal{L}(\theta|x_1, ..., x_N)]\}. \tag{D.5}$$

D.2 Application to Poisson distributed data

The Poisson distribution is defined such that

$$f(k; \lambda) = \frac{\lambda_k e^{-\lambda}}{k!}, \tag{D.6}$$

where λ denotes the mean of the distribution, and it is equal to the expected number of occurrences of an event, and k denotes the actual number of occurrences of the event. Note that λ is always positive, $\lambda > 0$, and k is non-negative, that is $k \in 0, 1, ..., N$, where N is the

maximum of occurrences that has happened in an experiment.

Applying this distribution to Equation D.3 one gets

$$\begin{aligned}\ln(\mathcal{L}) &= ln\left(\prod_{i=1}^{N} f(k_i;\lambda)\right) \\ &= \sum_{i=1}^{N} \ln\left(\frac{\lambda^{k_i} e^{-\lambda}}{k_i!}\right) \\ &= \sum_{i=1}^{N} \left[\ln(\lambda^{k_i}) + \ln(e^{-\lambda}) - \ln(k_i!)\right] \\ &= -N\lambda + \ln(\lambda)\sum_{i=1}^{N}(k_i) - \sum_{i=1}^{N}\ln(k_i!).\end{aligned} \tag{D.7}$$

Hence, for a continuous function, where the probability density function $f(k;\lambda)$ is known, the MLE λ can be found by equating the first derivative of Eqn. D.7 to zero, that is

$$\frac{\partial(\ln(\mathcal{L}))}{\partial\lambda} = \frac{\partial}{\partial\lambda}\left(-N\lambda + \ln(\lambda)\sum_{i=1}^{N}(k_i) - \sum_{i=1}^{N}\ln(k_i!)\right) = 0. \tag{D.8}$$

Solving the equation one gets

$$\frac{\partial(\ln(\mathcal{L}))}{\partial\lambda} = -N + \frac{1}{\lambda}\sum_{i=1}^{N}(k_i) = 0, \tag{D.9}$$

and finally

$$\lambda_{mle} = \frac{1}{N}\sum_{i=1}^{N}(k_i). \tag{D.10}$$

If, however, the probability density function of the data set is not known, which is the case in this project, one needs to investigate the so-called binned MLM. In such a case, a likelihood histogram needs to be constructed. This likelihood histogram has the same form as the likelihood given in Eqn. D.7. Rewriting and re-organising the equation one may get

$$\ln(\mathcal{L}) = \sum_{i=1}^{N}\left[k_i\ln(\lambda_i) - \lambda_i - \ln(k_i!)\right], \tag{D.11}$$

but now N is the number of bins, k_i is the number of occurrences of the event in each i bin, and λ_i is the expected number of occurrences (the true value, which in such a modelling will come from some underlying model) in each bin. The maximum likelihood is found through re-calculation of Eqn. D.11 with a range of different values of λ_i.

E

Cosmology

In the following appendix I give a summary of the cosmological background that has been silently assumed in this work. Cosmological equations used in some of the calculations of this thesis are listed and briefly discussed, and the most important parameters are defined. The following appendix contains advance textbook physics, and the reader is referred to any cosmology textbook, e.g. Peacock (1999), Ryden (2003).

E.1 Some fundamental formulae

The cosmological model assumed in this work is the Λ Cold Dark Matter (ΛCDM) model (often referred to as standard model). The model assumes flat spatial geometry of the Universe, non-zero cosmological constant (Λ), the existence of cold dark non-baryonic matter which dominates the total mass of the Universe, and a small baryonic matter component. The ΛCDM model uses the Friedmann-Lemaître-Robertson-Walker (FLRW) metric.

The Friedmann equation, expressed in terms of Hubble parameter (H), states that

$$H_0^2 = \frac{8\pi G\varepsilon_0}{3c^2} - \frac{kc^2}{a(t_0)^2} + \frac{\Lambda}{3} \tag{E.1}$$

where G is the Newton's gravitational constant, ε_0 is the critical energy density, k describes the curvature of the Universe (if $k=0$ the Universe is flat, if $k=-1$ it is closed, and if $k=1$ it is open), $a(t)$ is a scale factor, and c denotes the speed of light. The subscript 0 indicates that the value of the relevant parameter is at the redshift $z=0$. The Hubble parameter is defined as

$$H_0 \equiv \left(\frac{\dot{a}(t_0)}{a(t_0)}\right), \tag{E.2}$$

and the scale factor represents the relative expansion of the Universe

$$a(t) = \frac{1}{1+z}. \tag{E.3}$$

Clearly, at $z=0$, the scale factor is $a(t_0)=1$.

The second Friedmann equation, sometimes called the Friedmann acceleration equation, states that

$$\dot{H_0} + H_0^2 = \frac{\ddot{a}(t_0)}{a(t_0)} = -\frac{4\pi G}{3c^2}(\varepsilon_0 + 3p) + \frac{\Lambda}{3}, \tag{E.4}$$

where $\ddot{a}$ is scale factor's second derivative, and p denotes pressure.

The Friedmann equations describe the expansion of the Universe, assuming that the Universe is homogeneous and isotropic (the cosmological principle). They are derived from the Einstein's field equations of gravitation (refer to physics textbooks on the general theory of relativity).

Often, the so-called density parameter (Ω) is introduced, which is defined as a ratio of the actual density (ρ) to the critical density (ρ_{crit}). The overall density parameter may be further divided into the matter density parameter (Ω_{M}, includes both dark and baryonic matter density), the vacuum density parameter (the cosmological constant, Ω_Λ), the spatial curvature density parameter (Ω_{k}), and the radiation density parameter (Ω_{R}), where

$$\Omega_{\text{R}} \equiv \frac{\rho_{\text{R}}}{\rho_{\text{crit}}}, \qquad \Omega_{\text{M}} \equiv \frac{\rho_{\text{M}}}{\rho_{\text{crit}}}, \qquad \Omega_\Lambda \equiv \frac{\rho_\Lambda}{\rho_{\text{crit}}}, \qquad \Omega_{\text{k}} = 1 - \Omega, \tag{E.5}$$

and

$$\Omega = \Omega_{\rm R} + \Omega_{\rm M} + \Omega_{\Lambda} + \Omega_{\rm k}. \tag{E.6}$$

The values given for all of these parameters refer to the density ratios as of today (i.e. $z = 0$). The current measurements of the parameters are reported to be as follows $H_0 = 70.4^{+1.5}_{-1.6}$ km s^{-1} Mpc^{-3}, $\Omega_{\rm M} = 0.268 \pm 0.018$, $\Omega_{\rm b} = 0.0044 \pm 0.0007$ (baryonic density), where a model that assumes $\Omega_{\Lambda} = 1 - \Omega_{\rm M}$, $\Omega_{\rm k} = 0$ and $\Omega_{\rm R} = 0$ is adopted (quoted values are based on the three-year WMAP[1] results only, Spergel *et al.*, 2007).

The critical density can be found from the Friedmann equation. Assuming that the Universe is flat ($k = 0$), and that $\Lambda = 0$ (one will obtain the most basic from the Friedmann universes, which is ideal for comparison), the critical density becomes

$$\rho_{\rm crit,0} = \frac{3H_0^2}{8\pi G}. \tag{E.7}$$

And allowing for redshift evolution in our Universe, the expression becomes

$$\rho_{\rm crit} = \frac{3H^2(z)}{8\pi G}. \tag{E.8}$$

It is can be seen now that the Friedmann equation can be expressed in terms of density parameters such that

$$H^2(z) = H_0^2(\Omega_{\rm R}(1+z)^4 + \Omega_{\rm M}(1+z)^3 + \Omega_{\rm k}(1+z)^2 + \Omega_{\Lambda})^{1/2}. \tag{E.9}$$

E.2 Luminosity at cosmological distances

The observed radio luminosity ($L_{\nu_{\rm obs}}$) of a source is found with

$$L_{\nu_{\rm obs}} = 4\pi d_{\rm L}^2(z) S_{\nu_{\rm obs}}, \tag{E.10}$$

where $S_{\nu_{\rm obs}}$ is the source's observed flux density, and $d_{\rm L}$ denotes the so-called luminosity distance of the source at the redshift z. The luminosity distance is related to the metric ($d_{\rm M}$) and angular ($d_{\rm A}$) distance measures through

$$d_{\rm L}(z) = d_{\rm M}(z)(1+z) = d_{\rm A}(z)(1+z)^2. \tag{E.11}$$

[1] Wilkinson Microwave Anisotropy Probe (http://map.gsfc.nasa.gov/).

Further, the metric distance can be found with the comoving distance ($d_{\rm C}$)

$$d_{\rm M}(z) = \begin{cases} \frac{d_{\rm H}}{\Omega_{\rm k}^{1/2}} sinh\left(\frac{\Omega_{\rm k}^{1/2} d_{\rm C}(z)}{d_{\rm H}}\right) & \text{if } \Omega_{\rm k} > 0 \\ d_{\rm C}(z) & \text{if } \Omega_{\rm k} = 0 \\ \frac{d_{\rm H}}{(-\Omega_{\rm k})^{1/2}} sin\left(\frac{(-\Omega_{\rm k})^{1/2} d_{\rm C}(z)}{d_{\rm H}}\right) & \text{if } \Omega_{\rm k} < 0, \end{cases} \tag{E.12}$$

and where $d_{\rm H} = c/H(z)$ denotes the Hubble distance. The comoving distance ($d_{\rm C}$), on the other hand, is defined as

$$d_{\rm C}(z) = d_{\rm H} \int_0^{z'} \frac{z}{E(z)} dz = \frac{c}{H_0} \int_0^{z'} \frac{z}{E(z)} dz, \tag{E.13}$$

where $E(z)$ is expressed as

$$E(z) = (\Omega_{\rm M}(1+z)^3 + \Omega_{\rm k}(1+z)^2 + \Omega_\Lambda)^{1/2}. \tag{E.14}$$

Hence, for the special case of the flat matter-dominated Universe ($\Omega_k = 0$) one gets the luminosity distance in the following form

$$d_{\rm L}(z) = \frac{c(1+z)}{H_0} \int_0^{z'} \frac{z}{(\Omega_{\rm M}(1+z)^3 + \Omega_\Lambda)^{1/2}} dz \tag{E.15}$$

The radio luminosity of Eqn. E.10 is the observed radio luminosity of a source at a frequency ν. However, if the source is at a redshift z, the observed luminosity will correspond to different wavelength in the rest frame of that source. To correct for this effect the standard $K-correction$ is used. In radio regime the correction has two terms, the bandwidth correction $(1+z)^{-1}$ due to the spectral shifts and the 'colour' correction $(1+z)^{\alpha}$ which relates to the radio flux and radio spectral index relation[2] (terms used after Morrison *et al.*, 2003). Hence, the *absolute* radio luminosity of a radio source is found with

$$L_{\nu_{\rm em}} = 4\pi d_{\rm L}^2(z) S_{\nu_{\rm obs}} (1+z)^{\alpha-1}. \tag{E.16}$$

The linear size of a source (D) can be found with

$$D = \theta_{\rm size} d_{\rm A}(z), \tag{E.17}$$

where $\theta_{\rm size}$ is the source's angular size as defined in §1.4. Hence, using the luminosity distance, one may obtain the linear size of a radio source in the following form

$$D = \frac{\theta_{\rm size} d_{\rm L}(z)}{(1+z)^2}. \tag{E.18}$$

[2] $S_\nu \propto \nu^{-\alpha}$ as defined in §3.2 (Eqn. 3.1).

E.3 Cosmic Microwave Background

Cosmic microwave background (CMB) radiation is thermal radiation that permeate the observable Universe. CMB is the relic radiation which remained after the initial phases of the Universe development, namely directly after the so-called 'last scattering' of the photons. The current ($z = 0$) temperature of the CMB is approximately $T \approx 2.7$K, and has a spectrum of a black body.

The fundamental Einstein-Planck equation (also called the Planck relation) relates the energy of a photon (E) and its wavelength

$$E = h\nu, \tag{E.19}$$

where h is the Planck constant. It can be shown that the number density of photons emitted by a perfect black body is given by

$$n_\gamma(\nu)d\nu = \left(\frac{8\pi}{c^3}\right)\frac{\nu^2}{e^{h\nu/k_\mathrm{B}T}-1}d\nu, \tag{E.20}$$

where k_B is the Boltzmann constant. Further, the CMB radiation density is given by the Stefan-Boltzmann law, which given the total energy density for black body radiation, that is

$$\begin{aligned}\varepsilon_{\gamma,0} &= \int_0^\infty h\nu n(\gamma)d\nu \\ &= \sigma_\mathrm{SB}T^4.\end{aligned} \tag{E.21}$$

σ_SB is the Stefan-Boltzmann constant, and $\sigma_\mathrm{SB} = (2\pi^5 k_\mathrm{B}^2)/(15h^3c^2)$.

Now, under the assumption of the number of photons being preserved in the expanding Universe the following is valid

$$N_\gamma = N_{\gamma,0}a^{-3} = N_{\gamma,0}(1+z)^3. \tag{E.22}$$

And since the energy of each photon changes with redshift as

$$h\nu = h\nu(1+z), \tag{E.23}$$

the energy density of the CMB radiation (ε_γ) varies as

$$\varepsilon_\gamma = \varepsilon_{\gamma,o}a^{-4} = \varepsilon_{\gamma,o}(1+z)^4, \tag{E.24}$$

where $\varepsilon_{\gamma,o}$ is the energy density of the radiation at the redshift $z = 0$.

BIBLIOGRAPHY

Alexander P., 1987, MNRAS, 225, 27

Alexander P., 2000, MNRAS, 319, 8

Alexander P., 2006, MNRAS, 368, 1404

Alexander P., Leahy J. P., 1987, MNRAS, 225, 1

Alfvén H., Herlofson N., 1950, Physical Review, 78, 616

Allington-Smith J. R., Ellis R., Zirbel E. L., Oemler Jr. A., 1993, ApJ, 404, 521

Angel J. R. P., Stockman H. S., 1980, ARA&A, 18, 321

Antonucci R., 1993, ARA&A, 31, 473

Arnaud M., 2005, in F. Melchiorri & Y. Rephaeli (ed.), *Background Microwave Radiation and Intracluster Cosmology*, pp. 77–+

Arnaud M., Evrard A. E., 1999, MNRAS, 305, 631

Arshakian T. G., Longair M. S., 2000, MNRAS, 311, 846

Baade W., 1956, ApJ, 123, 550

Baade W., Minkowski R., 1954, ApJ, 119, 206

Baldwin J. E., 1982, in Heeschen D. S., Wade C. M. (eds.), *Extragalactic Radio Sources*, vol. 97 of *IAU Symposium*, pp. 21–24

Barai P., Wiita P. J., 2006, MNRAS, 372, 381

Barai P., Wiita P. J., 2007, ApJ, 658, 217

Barthel P. D., 1989, ApJ, 336, 606

Barthel P. D., Miley G. K., 1988, Nature, 333, 319

Barthel P. D., Miley G. K., Jagers W. J., Schilizzi R. T., Strom R. G., 1985, A&A, 148, 243

Baum S. A., Heckman T. M., van Breugel W., 1992, ApJ, 389, 208

Baum S. A., Zirbel E. L., O'Dea C. P., 1995, ApJ, 451, 88

Becker R. H., White R. L., Helfand D. J., 1995, ApJ, 450, 559

Begelman M. C., 1986, Nature, 322, 614

Begelman M. C., Blandford R. D., Rees M. J., 1984, Reviews of Modern Physics, 56, 255

Begelman M. C., Rees M. J., 1984, MNRAS, 206, 209

Bell A. R., 1978, MNRAS, 182, 443

Belsole E., Worrall D. M., Hardcastle M. J., Croston J. H., 2007, MNRAS, 381, 1109

Bennett A. S., 1962, MNRAS, 125, 75

Best P. N., Bailer D. M., Longair M. S., Riley J. M., 1995, MNRAS, 275, 1171

Best P. N., Heckman T. M., 2012, MNRAS, 421, 1569

Best P. N., Kaiser C. R., Heckman T. M., Kauffmann G., 2006, MNRAS, 368, L67

Best P. N., Kauffmann G., Heckman T. M., Ivezić Ž., 2005, MNRAS, 362, 9

Best P. N., Peacock J. A., Brookes M. H., Dowsett R. E., Röttgering H. J. A., Dunlop J. S., Lehnert M. D., 2003, MNRAS, 346, 1021

Best P. N., Röttgering H. J. A., Lehnert M. D., 1999, MNRAS, 310, 223

Best P. N., Röttgering H. J. A., Lehnert M. D., 2000, MNRAS, 315, 21

Best P. N., von der Linden A., Kauffmann G., Heckman T. M., Kaiser C. R., 2007, MNRAS, 379, 894

Bhatnagar S., Cornwell T. J., 2004, A&A, 426, 747

Bialek J. J., Evrard A. E., Mohr J. J., 2001, ApJ, 555, 597

Bicknell G. V., 1994, ApJ, 422, 542

Bicknell G. V., 1995, ApJS, 101, 29

Bicknell G. V., Dopita M. A., O'Dea C. P. O., 1997, ApJ, 485, 112

Bicknell G. V., Wagner S. J., Groves B. A., 2001, in R. A. Laing & K. M. Blundell (ed.), *Particles and Fields in Radio Galaxies Conference*, vol. 250 of *Astronomical Society of the Pacific Conference Series*, pp. 80–+

Binney J., Alouani Bibi F., Omma H., 2007, MNRAS, 377, 142

Bird J., Martini P., Kaiser C., 2008, ApJ, 676, 147

Biretta J. A., Stern C. P., Harris D. E., 1991, AJ, 101, 1632

Bîrzan L., McNamara B. R., Nulsen P. E. J., Carilli C. L., Wise M. W., 2008, ApJ, 686, 859

Bîrzan L., Rafferty D. A., McNamara B. R., Wise M. W., Nulsen P. E. J., 2004, ApJ, 607, 800

Biviano A., Salucci P., 2004, in R. Dettmar, U. Klein, & P. Salucci (ed.), *Baryons in Dark Matter Halos*

Blandford R. D., Payne D. G., 1982, MNRAS, 199, 883

Blandford R. D., Pringle J. E., 1976, MNRAS, 176, 443

Blandford R. D., Rees M. J., 1974, MNRAS, 169, 395

Blandford R. D., Znajek R. L., 1977, MNRAS, 179, 433

Blundell K. M., Fabian A. C., Crawford C. S., Erlund M. C., Celotti A., 2006, ApJ, 644, L13

Blundell K. M., Rawlings S., 1999, Nature, 399, 330

Blundell K. M., Rawlings S., Eales S. A., Taylor G. B., Bradley A. D., 1998, MNRAS, 295, 265

Blundell K. M., Rawlings S., Willott C. J., [BRW99], 1999, AJ, 117, 677

Bodo C., Massaglia S., Feretti L., Ferrari A., Dall'anese D., 1996, in R. D. Ekers, C. Fanti, & L. Padrielli (ed.), *Extragalactic Radio Sources*, vol. 175 of *IAU Symposium*, p. 463

Bodo G., Ferrari A., Massaglia S., Trussoni E., 1990, MNRAS, 244, 530

Böhringer H., Voges W., Fabian A. C., Edge A. C., Neumann D. M., 1993, MNRAS, 264, L25

Borgani S., Governato F., Wadsley J., Menci N., Tozzi P., Quinn T., Stadel J., Lake G., 2002, MNRAS, 336, 409

Bornancini C. G., O'Mill A. L., Gurovich S., Lambas D. G., 2010, MNRAS, 406, 197

Bracewell R. N., 1979, *The Fourier transform and its applications*, McGraw-Hill

Bremer M. A. R., 1994, in D. R. Crabtree, R. J. Hanisch, & J. Barnes (ed.), *Astronomical Data Analysis Software and Systems III*, vol. 61 of *Astronomical Society of the Pacific Conference Series*, p. 175

Brent R. P., 1973, *Algorithms for Minimization without Derivatives*, Prentice-Hall, Inc., Englewood Cliffs N.J.

Bridle A. H., Fomalont E. B., Byrd G. G., Valtonen M. J., 1989, AJ, 97, 674

Brocksopp C., Kaiser C. R., Schoenmakers A. P., de Bruyn A. G., 2007, MNRAS, 382, 1019

Brocksopp C., Kaiser C. R., Schoenmakers A. P., de Bruyn A. G., 2011, MNRAS, 410, 484

Broderick J. W., Fender R. P., 2011, MNRAS, 417, 184

Brüggen M., Kaiser C. R., 2001, MNRAS, 325, 676

Burbidge G., Perry J., 1976, ApJ, 205, L55

Burbidge G. R., 1956, ApJ, 124, 416

Burch S. F., 1979, MNRAS, 186, 519

Carilli C. L., Perley R. A., Dreher J. W., Leahy J. P., 1991, ApJ, 383, 554

Carvalho J. C., 1985, MNRAS, 215, 463

Cash W., 1976, A&A, 52, 307

Cash W., 1979, ApJ, 228, 939

Cassen P., Pettibone D., 1976, ApJ, 208, 500

Caswell J. L., Crowther J. H., 1969, MNRAS, 145, 181

Cattaneo A., Best P. N., 2009, MNRAS, 395, 518

Cattaneo A., Faber S. M., Binney J., Dekel A., Kormendy J., Mushotzky R., Babul A., Best P. N., Brüggen M., Fabian A. C., Frenk C. S., Khalatyan A., Netzer H., Mahdavi A., Silk J., Steinmetz M., Wisotzki L., 2009, Nature, 460, 213

Cavaliere A., Menci N., Tozzi P., 1999, MNRAS, 308, 599

Celotti A., Fabian A. C., 1993, MNRAS, 264, 228

Cheung C. C., 2007, AJ, 133, 2097

Cheung C. C., Healey S. E., Landt H., Verdoes Kleijn G., Jordán A., 2009, ApJS, 181, 548

Chiaberge M., Marconi A., 2011, MNRAS, 416, 917

Churazov E., Sunyaev R., Forman W., Böhringer H., 2002, MNRAS, 332, 729

Clark B. G., 1980, A&A, 89, 377

Clarke D. A., Bridle A. H., Burns J. O., Perley R. A., Norman M. L., 1992, ApJ, 385, 173

Clarke D. A., Burns J. O., 1991, ApJ, 369, 308

Cleary K., Lawrence C. R., Marshall J. A., Hao L., Meier D., 2007, ApJ, 660, 117

Cohen A. S., Lane W. M., Cotton W. D., Kassim N. E., Lazio T. J. W., Perley R. A., Condon J. J., Erickson W. C., 2007, AJ, 134, 1245

Condon J. J., 1999, Proceedings of the National Academy of Science, 96, 4756

Condon J. J., Cotton W. D., Greisen E. W., Yin Q. F., Perley R. A., Taylor G. B., Broderick J. J., 1998, AJ, 115, 1693

Cornwell T. J., Evans K. F., 1985, A&A, 143, 77

Cowie L. L., Binney J., 1977, ApJ, 215, 723

Cowie L. L., Songaila A., Hu E. M., Cohen J. G., 1996, AJ, 112, 839

Croston J. H., Hardcastle M. J., Birkinshaw M., Worrall D. M., Laing R. A., 2008a, MN-

RAS, 386, 1709

Croston J. H., Hardcastle M. J., Harris D. E., Belsole E., Birkinshaw M., Worrall D. M., 2005, ApJ, 626, 733

Croston J. H., Hardcastle M. J., Mingo B., Evans D. A., Dicken D., Morganti R., Tadhunter C. N., 2011, ApJ, 734, L28

Croston J. H., Kraft R. P., Hardcastle M. J., 2007, ApJ, 660, 191

Croston J. H., Kraft R. P., Hardcastle M. J., Birkinshaw M., Worrall D. M., Nulsen P. E. J., Penna R. F., Sivakoff G. R., *and 14 co-suthors*, 2009, MNRAS, 395, 1999

Croston J. H., Pratt G. W., Böhringer H., Arnaud M., Pointecouteau E., Ponman T. J., Sanderson A. J. R., Temple R. F., , Bower R. G., Donahue M., 2008b, A&A, 487, 431

Croton D. J., Springel V., White S. D. M., De Lucia G., Frenk C. S., Gao L., Jenkins A., Kauffmann G., Navarro J. F., Yoshida N., 2006, MNRAS, 365, 11

Curran P. A., Evans P. A., de Pasquale M., Page M. J., van der Horst A. J., 2010, ApJ, 716, L135

Curtis H., Campbell W., Moore J., Wilson R., Wright W., Observatory L., 1918, *Studies of the nebulae: made at the Lick Observatory, University of California, at Mount Hamilton, California, and Santiago, Chile*, Publications, University of California Press

Daly R. A., 1995, ApJ, 454, 580

David L. P., Nulsen P. E. J., McNamara B. R., Forman W., Jones C., Ponman T., Robertson B., Wise M., 2001, ApJ, 557, 546

De Young D. S., 2010, ApJ, 710, 743

della Ceca R., Lamorani G., Maccacaro T., Wolter A., Griffiths R., Stocke J. T., Setti G., 1994, ApJ, 430, 533

Deltorn J.-M., Le Fevre O., Crampton D., Dickinson M., 1997, ApJ, 483, L21+

Di Matteo T., Springel V., Hernquist L., 2005, Nature, 433, 604

Domainko W., Gitti M., Schindler S., Kapferer W., 2004, A&A, 425, L21

Dopita M. A., Reuland M., van Breugel W., de Vries W., Stanford S. A., Röttgering H., Miley G., Venemans B., *and 6 co-authors*, 2007, Ap&SS, 311, 305

Dressler A., 1980, ApJ, 236, 351

Dressler A., Oemler Jr. A., Couch W. J., Smail I., Ellis R. S., Barger A., Butcher H., Poggianti B. M., Sharples R. M., 1997, ApJ, 490, 577

Dunlop J. S., McLure R. J., Kukula M. J., Baum S. A., O'Dea C. P., Hughes D. H., 2003, MNRAS, 340, 1095

Dunlop J. S., Peacock J. A., 1990, MNRAS, 247, 19

Dunn R. J. H., Fabian A. C., 2004, MNRAS, 355, 862

Dunn R. J. H., Fabian A. C., Taylor G. B., 2005, MNRAS, 364, 1343

Eales S. A., 1985, MNRAS, 217, 149

Edge A. C., Frayer D. T., 2003, ApJ, 594, L13

Edge D. O., Shakeshaft J. R., McAdam W. B., Baldwin J. E., Archer S., 1959, MmRAS, 68, 37

Eilek J. A., Arendt P. N., 1996, ApJ, 457, 150

Eilek J. A., Caroff L. J., 1979, ApJ, 233, 463

Ekers R. D., Fanti R., Lari C., Parma P., 1978, Nature, 276, 588

Elvis M., Wilkes B. J., McDowell J. C., Green R. F., Bechtold J., Willner S. P., Oey M. S., Polomski E., Cutri R., 1994, ApJS, 95, 1

Ettori S., Tozzi P., Borgani S., Rosati P., 2004, A&A, 417, 13

Fabian A. C., 1994, ARA&A, 32, 277

Fabian A. C., 2006, in A. Wilson (ed.), *The X-ray Universe 2005*, vol. 604 of *ESA Special Publication*, p. 463

Fabian A. C., Nulsen P. E. J., 1977, MNRAS, 180, 479

Fabian A. C., Rees M. J., Stoeger W. R., Maccagni D., 1976, Nature, 260, 683

Fabian A. C., Sanders J. S., Ettori S., Taylor G. B., Allen S. W., Crawford C. S., Iwasawa K., Johnstone R. M., 2001, MNRAS, 321, L33

Fabian A. C., Voigt L. M., Morris R. G., 2002, MNRAS, 335, L71

Falle S. A. E. G., 1991, MNRAS, 250, 581

Fan J. H., Cheng K. S., Zhang L., 2001, PASJ, 53, 201

Fan J. H., Xie G. Z., 1996, A&A, 306, 55

Fanaroff B. L., Riley J. M., 1974, MNRAS, 167, 31P

Fanti C., Fanti R., Dallacasa D., Schilizzi R. T., Spencer R. E., Stanghellini C., 1995, A&A, 302, 317

Feigelson E. D., Jogesh Babu G., 2012, ArXiv e-prints

Fermi E., 1949, Physical Review, 75, 1169

Ferrari A., 1998, ARA&A, 36, 539

Ferrari A., Bodo G., Massaglia S., Trussoni E., 1995, in *American Institute of Physics Conference Series*, vol. 345 of *American Institute of Physics Conference Series*, pp. 457–464

Ferrari A., Tzeferacos P., Zanni C., 2009, Ap&SS, 322, 3

Fomalont E. B., Miley G. K., 1975, Nature, 257, 99

Fomalont E. B., Miley G. K., Bridle A. H., 1979, A&A, 76, 106

Fossati G., Maraschi L., Celotti A., Comastri A., Ghisellini G., 1998, MNRAS, 299, 433

Fukugita M., Ichikawa T., Gunn J. E., Doi M., Shimasaku K., Schneider D. P., 1996, AJ, 111, 1748

Gadotti D. A., Kauffmann G., 2009, MNRAS, 399, 621

Gaibler V., Krause M., Camenzind M., 2009, MNRAS, 400, 1785

Ghisellini G., Celotti A., 2001, A&A, 379, L1

Ghisellini G., Celotti A., George I. M., Fabian A. C., 1992, MNRAS, 258, 776

Gitti M., Brighenti F., McNamara B. R., 2012, Advances in Astronomy, 2012

Gitti M., McNamara B. R., Nulsen P. E. J., Wise M. W., 2007, ApJ, 660, 1118

Gopal-Krishna, 1988, A&A, 192, 37

Gopal-Krishna, Biermann P. L., Gergely L. Á., Wiita P. J., 2010, ArXiv e-prints

Gopal-Krishna, Biermann P. L., Wiita P. J., 2003, ApJ, 594, L103
Gopal-Krishna, Wiita P. J., 2000, A&A, 363, 507
Gopal-Krishna, Wiita P. J., 2001, ApJ, 560, L115
Gopal-Krishna, Wiita P. J., Barai P., 2004, Journal of Korean Astronomical Society, 37, 517
Gopal-Krishna, Wiita P. J., Saripalli L., 1989, MNRAS, 239, 173
Gower J. F. R., Scott P. F., Wills D., 1967, MmRAS, 71, 49
Graham A. W., Driver S. P., Petrosian V., Conselice C. J., Bershady M. A., Crawford S. M., Goto T., 2005, AJ, 130, 1535
Greenstein J. L., Matthews T. A., 1963, AJ, 68, 279
Grimes J. A., Rawlings S., Willott C. J., 2004, MNRAS, 349, 503
Hardcastle M. J., Birkinshaw M., Cameron R. A., Harris D. E., Looney L. W., Worrall D. M., 2002, ApJ, 581, 948
Hardcastle M. J., Croston J. H., 2010, MNRAS, 404, 2018
Hasinger G., Miyaji T., Schmidt M., 2005, A&A, 441, 417
Heavens A., 2009, ArXiv e-prints
Heckman T. M., Baum S. A., van Breugel W. J. M., McCarthy P., 1989, ApJ, 338, 48
Heinz S., Merloni A., Schwab J., 2007, ApJ, 658, L9
Hill G. J., Lilly S. J., 1991, ApJ, 367, 1
Ho L. C., 1999, ApJ, 516, 672
Ho L. C., 2002a, in R. Maiolino, A. Marconi, & N. Nagar (ed.), *Issues in Unification of Active Galactic Nuclei*, vol. 258 of *Astronomical Society of the Pacific Conference Series*, p. 165
Ho L. C., 2002b, ApJ, 564, 120
Ho L. C., Peng C. Y., 2001, ApJ, 555, 650
Hodges-Kluck E. J., Reynolds C. S., 2011, ApJ, 733, 58
Högbom J. A., 1974, 15, 417
Hooper E. J., Impey C. D., Foltz C. B., Hewett P. C., 1996, ApJ, 473, 746
Hopkins P. F., Hernquist L., Cox T. J., Robertson B., Krause E., 2007a, ApJ, 669, 67
Hopkins P. F., Richards G. T., Hernquist L., 2007b, ApJ, 654, 731
Hutchings J. B., Campbell B., 1983, Nature, 303, 584
Istomin Y. N., Sol H., 2011, A&A, 527, A22+
Ivezić Ž., Menou K., Knapp G. R., Strauss M. A., Lupton R. H., Vanden Berk D. E., Richards G. T., Tremonti C., Weinstein M. A., Anderson S., et al., 2002, AJ, 124, 2364
Jackson C. A., Wall J. V., 1999, MNRAS, 304, 160
Jamrozy M., Konar C., Saikia D. J., Stawarz L., Mack K.-H., Siemiginowska A., 2007, MNRAS, 378, 581
Jarvis M. J., Rawlings S., 2000, MNRAS, 319, 121
Jarvis M. J., Rawlings S., Willott C. J., Blundell K. M., Eales S., Lacy M., 2001, MNRAS, 327, 907

Jones C., Forman W., Vikhlinin A., Markevitch M., David L., Warmflash A., Murray S., Nulsen P. E. J., 2002, ApJ, 567, L115

Jovanović P., Popović L. Č., 2009, ArXiv e-prints

Jovanović P., Zakharov A. F., Popović L. Č., Petrović T., 2008, MNRAS, 386, 397

Kaastra J. S., Tamura T., Peterson J. R., Bleeker J. A. M., Ferrigno C., Kahn S. M., Paerels F. B. S., Piffaretti R., Branduardi-Raymont G., Böhringer H., 2004, A&A, 413, 415

Kaiser C. R., Alexander P., 1997, MNRAS, 286, 215

Kaiser C. R., Alexander P., 1999, MNRAS, 302, 515

Kaiser C. R., Best P. N., 2007, MNRAS, 381, 1548

Kaiser C. R., Best P. N., 2008, MNRAS, 384, 1742

Kaiser C. R., Binney J. J., 2004, in T. Reiprich, J. Kempner, & N. Soker (ed.), *The Riddle of Cooling Flows in Galaxies and Clusters of galaxies*, p. 249

Kaiser C. R., Dennett-Thorpe J., Alexander P., [KDA97], 1997, MNRAS, 292, 723

Kaiser C. R., Schoenmakers A. P., Röttgering H. J. A., 2000, MNRAS, 315, 381

Kaiser N., 1986, MNRAS, 222, 323

Kaiser N., 1991, ApJ, 383, 104

Kapahi V. K., 1989, AJ, 97, 1

Kapahi V. K., Subrahmanya C. R., Kulkarni V. K., 1987, Journal of Astrophysics and Astronomy, 8, 33

Kawakatu N., Kino M., Nagai H., 2009, ApJ, 697, L173

Kellermann K. I., Sramek R., Schmidt M., Shaffer D. B., Green R., 1989, AJ, 98, 1195

Kelly B. C., Vestergaard M., Fan X., Hopkins P., Hernquist L., Siemiginowska A., 2010, ApJ, 719, 1315

King I. R., 1972, ApJ, 174, L123+

Kinman T. D., Grasdalen G. L., Rieke G. H., 1974, ApJ, 194, L1

Kino M., Takahara F., 2004, MNRAS, 349, 336

Kirk J. G., Guthmann A. W., Gallant Y. A., Achterberg A., 2000, ApJ, 542, 235

Koide S., Shibata K., Kudoh T., 1998, ApJ, 495, L63

Koide S., Shibata K., Kudoh T., 1999, ApJ, 522, 727

Körding E. G., Jester S., Fender R., 2006, MNRAS, 372, 1366

Körding E. G., Jester S., Fender R., 2008, MNRAS, 383, 277

Kormendy J., Djorgovski S., 1989, ARA&A, 27, 235

Kormendy J., Richstone D., 1995, ARA&A, 33, 581

Kraft R. P., Vázquez S. E., Forman W. R., Jones C., Murray S. S., Hardcastle M. J., Worrall D. M., Churazov E., 2003, ApJ, 592, 129

Kronberg P. P., Dufton Q. W., Li H., Colgate S. A., 2001, ApJ, 560, 178

La Franca F., Melini G., Fiore F., 2010, ApJ, 718, 368

Laing R. A., Bridle A. H., Parma P., Feretti L., Giovannini G., Murgia M., Perley R. A., 2008, MNRAS, 386, 657

Laing R. A., Guidetti D., Bridle A. H., Parma P., Bondi M., 2011, MNRAS, 417, 2789

Laing R. A., Jenkins C. R., Wall J. V., Unger S. W., 1994, in G. V. Bicknell, M. A. Dopita, & P. J. Quinn (ed.), *The Physics of Active Galaxies*, vol. 54 of *Astronomical Society of the Pacific Conference Series*, pp. 201–+

Laing R. A., Peacock J. A., 1980, MNRAS, 190, 903

Laing R. A., Riley J. M., Longair M. S., 1983, MNRAS, 204, 151

Lampton M., Margon B., Bowyer S., 1976, ApJ, 208, 177

Laor A., 2000, ApJ, 543, L111

Large M. I., Mills B. Y., Little A. G., Crawford D. F., Sutton J. M., 1981, MNRAS, 194, 693

Lazio T. J. W., Kassim N. E., Weiler K., Gross C. A., 1999, in *American Astronomical Society Meeting Abstracts*, vol. 31 of *Bulletin of the American Astronomical Society*, pp. 1498–+

Leahy J. P., Parma P., 1992, in J. Roland, H. Sol, & G. Pelletier (ed.), *Extragalactic Radio Sources. From Beams to Jets*, pp. 307–308

Leahy J. P., Williams A. G., 1984, MNRAS, 210, 929

Ledlow M. J., Owen F. N., 1995, AJ, 109, 853

Ledlow M. J., Owen F. N., 1996, AJ, 112, 9

Ledlow M. J., Owen F. N., Keel W. C., 1998, ApJ, 495, 227

Leismann T., Antón L., Aloy M. A., Müller E., Martí J. M., Miralles J. A., Ibáñez J. M., 2005, A&A, 436, 503

Lelievre G., Nieto J.-L., Horville D., Renard L., Servan B., 1984, A&A, 138, 49

Lin Y.-T., Shen Y., Strauss M. A., Richards G. T., Lunnan R., 2010, ApJ, 723, 1119

Liu R., Pooley G., Riley J. M., 1992, MNRAS, 257, 545

Longair M. S., 1992, *High energy astrophysics. Vol.1: Particles, photons and their detection*, High Energy Astrophysics, by Malcolm S. Longair, pp. 436. ISBN 0521387736. Cambridge, UK: Cambridge University Press, March 1992.

Longair M. S., 1994, *High energy astrophysics. Vol.2: Stars, the galaxy and the interstellar medium*, Cambridge: Cambridge University Press, —c1994, 2nd ed.

Longair M. S., Seldner M., 1979, MNRAS, 189, 433

Lovelace R. V. E., 1976, Nature, 262, 649

Luo Q., Sadler E. M., 2010, ApJ, 713, 398

Machalski J., Chyzy K. T., Jamrozy M., 2004a, 54, 249

Machalski J., Chyzy K. T., Jamrozy M., 2004b, 54, 391

Machalski J., Chyży K. T., Stawarz L., Kozieł D., 2007, A&A, 462, 43

Machalski J., Jamrozy M., Stawarz L., Kozieł-Wierzbowska D., 2011, Astrophys. J., 740, 58

Machalski J., Kozieł-Wierzbowska D., Jamrozy M., Saikia D. J., 2008, ApJ, 679, 149

Mack K.-H., Klein U., O'Dea C. P., Willis A. G., 1997, 123, 423

MacKay D. J. C., 2003, *Information theory, inference and learning algorithms*, Cambridge: Cambridge University Press, —c2003

Magliocchetti M., Brüggen M., 2007, MNRAS, 379, 260

Magorrian J., Tremaine S., Richstone D., Bender R., Bower G., Dressler A., Faber S. M., Gebhardt K., Green R., Grillmair C., Kormendy J., Lauer T., 1998, AJ, 115, 2285

Malmquist K. G., 1922, *On some relations in stellar statistics*, Arkiv för matematik, astronomi och fysik, Almqvist & Wiksells

Manolakou K., Kirk J. G., 2002, A&A, 391, 127

Markevitch M., 1998, ApJ, 504, 27

Markevitch M., Vikhlinin A., 2001, ApJ, 563, 95

Markoff S., Falcke H., Fender R., 2001, A&A, 372, L25

Marshall H. L., Miller B. P., Davis D. S., Perlman E. S., Wise M., Canizares C. R., Harris D. E., 2002, ApJ, 564, 683

Martí J. M., Müller E., 2003, Living Reviews in Relativity, 6, 7

Martí J. M. A., M uller E., Font J. A., Ibáñez J. M. A., Marquina A., 1997, ApJ, 479, 151

Massaro F., Ajello M., 2011, ApJ, 729, L12+

Mathews W. G., Bregman J. N., 1978, ApJ, 224, 308

Mathews W. G., Guo F., 2011, ApJ, 738, 155

Maughan B. J., Jones L. R., Ebeling H., Scharf C., 2006, MNRAS, 365, 509

McGilchrist M. M., Baldwin J. E., Riley J. M., Titterington D. J., Waldram E. M., Warner P. J., 1990, MNRAS, 246, 110

McHardy I. M., 1979, MNRAS, 188, 495

McLure R. J., Dunlop J. S., 2004, MNRAS, 352, 1390

McLure R. J., Jarvis M. J., 2004, MNRAS, 353, L45

McNamara B. R., Nulsen P. E. J., 2007, ARA&A, 45, 117

McNamara B. R., Nulsen P. E. J., Wise M. W., Rafferty D. A., Carilli C., Sarazin C. L., Blanton E. L., 2005, Nature, 433, 45

McNamara B. R., Wise M., Nulsen P. E. J., David L. P., Sarazin C. L., Bautz M., Markevitch M., Vikhlinin A., Forman W. R., Jones C., Harris D. E., 2000, ApJ, 534, L135

Meier D. L., 1999, ApJ, 522, 753

Meier D. L., 2001, in R. A. Laing & K. M. Blundell (ed.), *Particles and Fields in Radio Galaxies Conference*, vol. 250 of *Astronomical Society of the Pacific Conference Series*, p. 10

Meier D. L., 2002, NewAR, 46, 247

Meier D. L., Edgington S., Godon P., Payne D. G., Lind K. R., 1997, Nature, 388, 350

Meier D. L., Koide S., Uchida Y., 2001, Science, 291, 84

Meisenheimer K., R oser H.-J., Hiltner P. R., Yates M. G., Longair M. S., Chini R., Perley R. A., 1989, A&A, 219, 63

Meli A., Mastichiadis A., 2008, Nuclear Instruments and Methods in Physics Research A, 588, 193

Merloni A., Heinz S., 2007, MNRAS, 381, 589

Merloni A., Heinz S., 2008, MNRAS, 388, 1011

Merloni A., Heinz S., di Matteo T., 2003, MNRAS, 345, 1057

Mezcua M., Lobanov A. P., Chavushyan V. H., León-Tavares J., 2011, A&A, 527, A38

Miley G. K., Overzier R. A., Tsvetanov Z. I., Bouwens R. J., Benítez N., Blakeslee J. P., Ford H. C., Illingworth G. D., *and 30 co-authors*, 2004, Nature, 427, 47

Mingo B., Hardcastle M. J., Croston J. H., Evans D. A., Hota A., Kharb P., Kraft R. P., 2011, ApJ, 731, 21

Moderski R., Sikora M., Lasota J.-P., 1998, MNRAS, 301, 142

Morrison G. E., Owen F. N., Ledlow M. J., Keel W. C., Hill J. M., Voges W., Herter T., 2003, ApJS, 146, 267

Mortlock D. J., Warren S. J., Venemans B. P., Patel M., Hewett P. C., McMahon R. G., Simpson C., Theuns T., Gonzáles-Solares E. A., Adamson A., Dye S., Hambly N. C., Hirst P., Irwin M. J., Kuiper E., Lawrence A., Röttgering H. J. A., 2011, Nature, 474, 616

Mullin L. M., Riley J. M., Hardcastle M. J., 2008, MNRAS, 390, 595

Mutel R. L., Phillips R. B., 1988, in Reid M. J., Moran J. M. (eds.), *The Impact of VLBI on Astrophysics and Geophysics*, vol. 129 of *IAU Symposium*, pp. 73–+

Narayan R., Nityananda R., 1986, ARA&A, 24, 127

Natarajan P., Treister E., 2009, MNRAS, 393, 838

Neal R. M., 1993, *Probabilistic inference using Markov chain Monte Carlo methods*, Technical Report CRG-TR-93-1, Department of Computer Science, University of Toronto

Nulsen P. E. J., Hambrick D. C., McNamara B. R., Rafferty D., Birzan L., Wise M. W., David L. P., 2005, ApJ, 625, L9

O'Dea C. P., 1998, PASP, 110, 493

O'Dea C. P., 2002, NewAR, 46, 41

O'Dea C. P., Baum S. A., Maloney P. R., Tacconi L. J., Sparks W. B., 1994, ApJ, 422, 467

O'Dea C. P., Daly R. A., Kharb P., Freeman K. A., Baum S. A., 2009, A&A, 494, 471

O'Dea C. P., Koekemoer A. M., Baum S. A., Sparks W. B., Martel A. R., Allen M. G., Macchetto F. D., Miley G. K., 2001, AJ, 121, 1915

Ohsuga K., Kato Y., Mineshige S., 2005, ApJ, 627, 782

Ohsuga K., Mineshige S., 2007, ApJ, 670, 1283

Omma H., Binney J., Bryan G., Slyz A., 2004, MNRAS, 348, 1105

Oort J. H., Walraven T., 1956, Bull. of the Astron. Instit. of the Netherlands, 12, 285

Oort M. J. A., Katgert P., Windhorst R. A., 1987, Nature, 328, 500

Orr M. J. L., Browne I. W. A., 1982, MNRAS, 200, 1067

O'Sullivan E., Giacintucci S., David L. P., Gitti M., Vrtilek J. M., Raychaudhury S., Ponman T. J., 2011, ApJ, 735, 11

Owen F. N., Ledlow M. J., 1994, in G. V. Bicknell, M. A. Dopita, & P. J. Quinn (ed.), *The Physics of Active Galaxies*, vol. 54 of *Astronomical Society of the Pacific Conference Series*, p. 319

Owen F. N., White R. A., 1991, MNRAS, 249, 164

Paczyńsky B., Wiita P. J., 1980, A&A, 88, 23

Padovani P., 1993, MNRAS, 263, 461

Peacock J. A., 1999, *Cosmological Physics*

Penrose R., Floyd G. R., 1971, Nature, 229, 177

Perley R. A., Roser H.-J., Meisenheimer K., 1997, A&A, 328, 12

Perucho M., 2011, ArXiv e-prints

Perucho M., Quilis V., Martí J.-M., 2011, ApJ, 743, 42

Peterson J. R., Fabian A. C., 2006, 427, 1

Peterson J. R., Kahn S. M., Paerels F. B. S., Kaastra J. S., Tamura T., Bleeker J. A. M., Ferrigno C., Jernigan J. G., 2003, ApJ, 590, 207

Peterson J. R., Paerels F. B. S., Kaastra J. S., Arnaud M., Reiprich T. H., Fabian A. C., Mushotzky R. F., Jernigan J. G., Sakelliou I., 2001, A&A, 365, L104

Pilkington J. D. H., Scott P. F., 1965, MmRAS, 69, 183

Poggianti B. M., De Lucia G., Varela J., Aragon-Salamanca A., Finn R., Desai V., von der Linden A., White S. D. M., 2010, MNRAS, 405, 995

Ponman T. J., Cannon D. B., Navarro J. F., 1999, Nature, 397, 135

Press W. H., Teukolsky S. A., Vetterling W. T., Flannery B. P., 1992, *Numerical Recipes in C. The Art of Scientific Computing.*, Cambridge: Cambridge University Press, —c1992, 2nd ed.

Rafferty D. A., McNamara B. R., Nulsen P. E. J., Wise M. W., 2006, ApJ, 652, 216

Rawlings S., 2002, in A. Pramesh Rao, G. Swarup, & Gopal-Krishna (ed.), *The Universe at Low Radio Frequencies*, vol. 199 of *IAU Symposium*, p. 34

Rawlings S., Jarvis M. J., 2004, MNRAS, 355, L9

Rawlings S., Saunders R., 1991, Nature, 349, 138

Rees M. J., Begelman M. C., Blandford R. D., Phinney E. S., 1982, Nature, 295, 17

Rengelink R. B., Tang Y., de Bruyn A. G., Miley G. K., Bremer M. N., Roettgering H. J. A., Bremer M. A. R., 1997, 124, 259

Richards G. T., Lacy M., Storrie-Lombardi L. J., Hall P. B., Gallagher S. C., Hines D. C., Fan X., Papovich C., *and 9 co-authors*, 2006, ApJS, 166, 470

Richstone D., Ajhar E. A., Bender R., Bower G., Dressler A., Faber S. M., Filippenko A. V., Gebhardt K., Green R., Ho L. C., Kormendy J., Lauer T. R., Magorrian J., Tremaine S., 1998, Nature, 395, A14

Rosner R., Tucker W. H., 1989, ApJ, 338, 761

Rowan-Robinson M., 1972, Nature, 236, 112

Rybicki G. B., Lightman A. P., 1979, *Radiative processes in astrophysics*, New York, Wiley-Interscience, 1979. 393 p.

Ryden B., 2003, *Introduction to cosmology*

Sand D. J., 2006, *On the distribution of dark matter in clusters of galaxies*, Ph.D. thesis, California Institute of Technology, California, USA

Sanderson A. J. R., O'Sullivan E., Ponman T. J., 2009, MNRAS, 395, 764

Sarazin C. L., 1988, *X-ray emission from clusters of galaxies*

Sargent W. L. W., Young P. J., Lynds C. R., Boksenberg A., Shortridge K., Hartwick F. D. A., 1978, ApJ, 221, 731

Saripalli L., Subrahmanyan R., 2009, ApJ, 695, 156

Saripalli L., Subrahmanyan R., Hunstead R. W., 1994, MNRAS, 269, 37

Sasao T., Fletcher A. B., 2005, Lecture notes for KVN students, URL `http://www.astro.sci.yamaguchi-u.ac.jp/jvn/reduction/kvnlecnote/kchap3.pdf`

Scannapieco E., Silk J., Bouwens R., 2005, ApJ, 635, L13

Schechter P., 1976, ApJ, 203, 297

Scheuer P. A. G., 1974, MNRAS, 166, 513

Scheuer P. A. G., 1987, in J. A. Zensus & T. J. Pearson (ed.), *Superluminal Radio Sources*, pp. 104–113

Scheuer P. A. G., 1995, MNRAS, 277, 331

Scheuer P. A. G., 1996, in P. E. Hardee, A. H. Bridle, & J. A. Zensus (ed.), *Energy Transport in Radio Galaxies and Quasars*, vol. 100 of *Astronomical Society of the Pacific Conference Series*, p. 1

Schilizzi R. T., Tian W. W., Conway J. E., Nan R., Miley G. K., Barthel P. D., Normandeau M., Dallacasa D., Gurvits L. I., 2001, A&A, 368, 398

Schilizzi R. T., van Ardenne A., Miley G. K., Baud B., Baath L., Ronnang B. O., Pauliny-Toth I. I. K., 1979, A&A, 77, 1

Schmidt M., 1963, Nature, 197, 1040

Schmidt M., 1968, ApJ, 151, 393

Schnitzeler D. H. F. M., Katgert P., Haverkorn M., de Bruyn A. G., 2007, A&A, 461, 963

Schoenmakers A. P., de Bruyn A. G., Röttgering H. J. A., van der Laan H., Kaiser C. R., 2000a, MNRAS, 315, 371

Schoenmakers A. P., Mack K.-H., de Bruyn A. G., Röttgering H. J. A., Klein U., van der Laan H., 2000b, A&AS, 146, 293

Schoenmakers A. P., Mack K.-H., Lara L., Röttgering H. J. A., de Bruyn A. G., van der Laan H., Giovannini G., 1998, A&A, 336, 455

Schreier E. J., Gorenstein P., Feigelson E. D., 1982, ApJ, 261, 42

Schwab F. R., 1984, AJ, 89, 1076

Shabala S. S., Kaviraj S., Silk J., 2011, MNRAS, 413, 2815

Shankar F., Weinberg D. H., Miralda-Escudé J., 2009, ApJ, 690, 20

Shklovskii I. S., 1963, Soviet Astronomy, 6, 465

Shlosman I., Begelman M. C., Frank J., 1990, Nature, 345, 679

Sijacki D., Springel V., Di Matteo T., Hernquist L., 2007, MNRAS, 380, 877

Sikora M., Begelman M. C., Madejski G. M., Lasota J.-P., 2005, ApJ, 625, 72

Sikora M., Stawarz L., Lasota J.-P., 2007, ApJ, 658, 815

Silk J., 2005, MNRAS, 364, 1337

Singal A. K., 1988, MNRAS, 233, 87

Singal A. K., 1993, MNRAS, 263, 139

Smith E. P., Heckman T. M., Bothun G. D., Romanishin W., Balick B., 1986, ApJ, 306, 64

Smith F. G., 1967, Nature, 213, 967

Smith S., 1936, ApJ, 83, 23

Soker N., White III R. E., David L. P., McNamara B. R., 2001, ApJ, 549, 832

Soltan A., 1982, MNRAS, 200, 115

Spergel D. N., Bean R., Doré O., Nolta M. R., Bennett C. L., Dunkley J., Hinshaw G., Jarosik N., Komatsu E., Page L., Peiris H. V., Verde L., *and 10 co-authors*, 2007, ApJS, 170, 377

Spitkovsky A., 2008, ApJ, 682, L5

Sramek R. A., Weedman D. W., 1980, ApJ, 238, 435

Steinhardt C. L., Elvis M., 2010, MNRAS, 402, 2637

Steinhardt C. L., Elvis M., 2011, MNRAS, 410, 201

Stiavelli M., Moller P., Zeilinger W. W., 1991, Nature, 354, 132

Stoughton C., Lupton R. H., Bernardi M., Blanton M. R., Burles S., Castander F. J., Connolly A. J., Eisenstein D. J., Frieman J. A., Hennessy G. S., et al., 2002, AJ, 123, 485

Strauss M. A., Weinberg D. H., Lupton R. H., Narayanan V. K., Annis J., Bernardi M., Blanton M., Burles S., Connolly A. J., Dalcanton J., et al., 2002, AJ, 124, 1810

Strittmatter P. A., Hill P., Pauliny-Toth I. I. K., Steppe H., Witzel A., 1980, A&A, 88, L12

Strom R. G., Willis A. G., 1980, A&A, 85, 36

Tadhunter C., 2008, NewAR, 52, 227

Tamura T., Kaastra J. S., den Herder J. W. A., Bleeker J. A. M., Peterson J. R., 2004, A&A, 420, 135

Taylor G. B., Carilli C. L., Perley R. A. (eds.), 1999, *Synthesis Imaging in Radio Astronomy II*, vol. 180 of *Astronomical Society of the Pacific Conference Series*

Thompson A. R., Moran J. M., Swenson Jr. G. W., 2001, *Interferometry and Synthesis in Radio Astronomy, 2nd Edition*

Tozzi P., Norman C., 2001, ApJ, 546, 63

Tremblay G. R., O'Dea C. P., Baum S. A., Koekemoer A. M., Sparks W. B., de Bruyn G., Schoenmakers A. P., 2010, ApJ, 715, 172

Ueda Y., Akiyama M., Ohta K., Miyaji T., 2003, ApJ, 598, 886

Urry C. M., Padovani P., 1995, PASP, 107, 803

Voigt L. M., Schmidt R. W., Fabian A. C., Allen S. W., Johnstone R. M., 2002, MNRAS, 335, L7

Voit G. M., 2005, Reviews of Modern Physics, 77, 207

Voit G. M., Bryan G. L., 2001, Nature, 414, 425

Voit G. M., Bryan G. L., Balogh M. L., Bower R. G., 2002, ApJ, 576, 601

Voit G. M., Donahue M., 1995, ApJ, 452, 164

Waldram E. M., Pooley G. G., Grainge K. J. B., Jones M. E., Saunders R. D. E., Scott P. F.,

Taylor A. C., 2003, MNRAS, 342, 915
Wang Y., Kaiser C. R., 2008, MNRAS, 388, 677
Wang Y., Kaiser C. R., Laing R., Alexander P., Pavlovski G., Knigge C., 2009, MNRAS, 397, 1113
Wang Y., Knigge C., Croston J. H., Pavlovski G., 2011, MNRAS, 418, 1138
Wardle J. F. C., Homan D. C., Ojha R., Roberts D. H., 1998, Nature, 395, 457
Weingartner J. C., Draine B. T., 2001, ApJ, 548, 296
White R. L., Becker R. H., Helfand D. J., Gregg M. D., 1997, ApJ, 475, 479
Willis A. G., Strom R. G., Wilson A. S., 1974, Nature, 250, 625
Willott C. J., Rawlings S., Blundell K. M., Lacy M., 1999, MNRAS, 309, 1017
Willott C. J., Rawlings S., Blundell K. M., Lacy M., Eales S. A., 2001, MNRAS, 322, 536
Wilson A. S., Colbert E. J. M., 1995, ApJ, 438, 62
Wilson J. R., 1972, ApJ, 173, 431
Wing J. D., Blanton E. L., 2011, AJ, 141, 88
Wold M., Lacy M., Lilje P. B., Serjeant S., 2000, MNRAS, 316, 267
Wolfe A. M., Burbidge G. R., 1970, ApJ, 161, 419
Wu K. K. S., Fabian A. C., Nulsen P. E. J., 2001, MNRAS, 324, 95
Wu X.-B., Liu F. K., Zhang T. Z., 2002, A&A, 389, 742
Wu X.-P., Xue Y.-J., 2002, ApJ, 572, L19
York D. G., Adelman J., Anderson Jr. J. E., Anderson S. F., Annis J., Bahcall N. A., Bakken J. A., Barkhouser R., *and 136 co-authors*, 2000, AJ, 120, 1579
Yu Q., Tremaine S., 2002, MNRAS, 335, 965
Zirbel E. L., 1997, ApJ, 476, 489
Zubko V., Dwek E., Arendt R. G., 2004, ApJS, 152, 211
Zwicky F., 1933, Helvetica Physica Acta, 6, 110
Zwicky F., 1937, ApJ, 86, 217

INDEX

The greater the sphere of our knowledge, the larger is the surface of its contact with the infinity of our ignorance.

ANONYMOUS

This thesis was typeset in LaTeX.